UNIVERSITY OF CAPE TOWN
IYUNIVESITHI YASEKAPA • UNIVERSITEIT VAN KAAPSTAD

Experimental and Numerical Study on the Effect of Strain Rate to Ductile Damage

Andrew Scott Bowden

Thesis presented in partial fulfilment of the requirements
of the degree MSc(Engineering)

Blast Impact and Survivability Research Centre
Department of Mechanical Engineering
University of Cape Town
December 2009

Declaration

I hereby grant the University of Cape Town free license to reproduce for the purpose of research either the whole or any portion of the contents in any manner whatsoever of the above dissertation.

I know the meaning of plagiarism and declare that all the work in this document, save for that which is properly acknowledged, is my own. I also declare that this material has not been submitted for any purpose or examination to any other Department or University.

Signed on the 14$^{\text{th}}$ of December 2009

. . . . . .

Andrew Scott Bowden

Abstract

Ductile fracture modelling is extensively used in the automotive, aerospace, aluminium and steel industries. However, these models are often only validated in a limited region of stress states, for example tensile failure by void growth but not shear. In addition, the predictions generally do not include strain rate or temperature effects. Quasistatic tests are often used in calibration, even though many applications such as automotive accidents and ballistic impact operate in the dynamic range.

Thus the aims of this thesis were to develop a system to test the damage properties of materials at both quasistatic ($\approx 1\,\mathrm{s}^{-1}$) and dynamic ($> 1 \times 10^3\,\mathrm{s}^{-1}$) strain rates, and then to determine the influence of strain rate to ductile fracture.

From the literature the Bai-Wierzbicki damage model was identified as being applicable to the widest range of loading conditions. Thus tests to calibrate this failure locus were conducted on sheet specimens with notches cut into each to introduce non-axial stresses, resulting in a range of loading conditions. This testing procedure involved experimental testing combined with finite element analysis (FEA) to determine the stress and strain state at the position of fracture initiation. All specimens used material from the same sheet of mild steel.

To break the dynamic specimens a tensile split Hopkinson pressure bar, or TSHB, was optimized and built. Hopkinson bars are the standard method of conducting high strain rate characterisation tests, however, there is no universal design to examine tensile deformation. The apparatus built used a tubular striker and produced a square input pulse with low noise as desired. Sheet specimens were glued into slotted sections of threaded bar, which in turn screwed into the split Hopkinson bars. This method was successful as in every case the specimens broke before the epoxy.

FEA modelling techniques were optimized to minimize computation time. The most important was the use of infinite elements to simulate the bars which, when calibrated, were found to be the ideal method of modelling split Hopkinson bars.

Ultimately it was found that strain rate does influence ductile damage. The dynamic specimens failed at a lower strain than the quasistatic equivalents. This indicates that, at high strain rates, fracture strain decreases with strain rate. In contrast, in the quasistatic range strain rate tends to decrease displacement to fracture and thus it is proposed that at quasistatic strain rates, fracture strain increases with strain rate. It is speculated that the degree that strain rate influences ductile fracture is related to the Lode angle, which is a measure of the third deviatoric stress invariant.

Acknowledgements

It is a pleasure to recognize those who made this thesis possible.

First and foremost I would like to thank my supervisor, Trevor Cloete, for his support, advice, funding and encouragement. We both manage to distract each other far too easily, but have made a good team.

My sincere thanks go to Professor Gerald Nurick for his help in organising funding, for his advice, and especially for his role in making BISRU a great place to work.

For their help in the experimental and modelling work I am incredibly grateful to the support crew of Reuben Govender, Vic Balden, Matt Theobald and Steve Chung.

My thanks go to the Mechanical Engineering workshop staff especially Glen Newins, Charles Nicholas, Horst Emrich and Len Watkins for manufacturing the apparatus and specimens. Their patience, advice and good humour are almost unlimited.

Finally to my office mates Carlo Geretto, Yolande Iyer and Patrick Smith for providing distractions when I needed them and when I didn't. The group provided the perfect environment for discussions and encouragement which helped me tremendously.

Contents

List of Figures

List of Tables

Nomenclature

Roman

A	cross-sectional area
A, B, C, D, k, n, m	Zhao plasticity constants
c	wave propagation speed
C_p	specific heat
$D_1, \ldots, D_6$	Bai-Wierzbicki failure locus constants
E_{ij}	strain tensor
G	shear modulus
m	mass
N	averaging weight factor
N_{ij}	normal direction tensor
p	pressure
q	heat flux per unit volume
s	yield surface
S_{ij}	deviatoric stress tensor
T	temperature
t	time
T_{ij}	Cauchy stress tensor
u	displacement
V	volume
E	Young's modulus

Greek

$\bar{\theta}$	normalized Lode angle
$\dot{\epsilon}$	equivalent strain rate
ϵ	equivalent strain
η	triaxiality

$\hat{\eta}$	plastic work to heat ratio
λ	1st Lamé parameter
ν	poisson's ratio
ρ	density
σ	equivalent stress
$\tilde{\epsilon}$	equivalent measure of old elastic strain and current increment

Subscripts

f	failure
i	incident
i, j	tensor indices
$melt$	melting
r	reflected
s	striker
t	transmitted
$trans$	transition
v	von mises

Superscripts

D	deviatoric
el	elastic
new	state at current step
old	state at previous step
pl	plastic
$trial$	approximated current state

Abbreviations

BISRU	Blast Impact and Survivability Research Unit
SHB	split Hopkinson pressure bar
TSHB	tensile split Hopkinson pressure bar
VDLOAD	vectorised user defined pressure load subroutine (Abaqus)
VUMAT	vectorised user defined material subroutine (Abaqus)

Variables used only in the literature review are defined where used.

Chapter 1

Introduction

Damage is defined in this work as a discontinuous deformation and is evident in the initiation and propagation of cracks in a crack free body. Simulations trying to predict this phenomena are extensively used in the automotive, aerospace, aluminium and steel industries [1]. However, little consensus exists as to which fracture prediction method to use in general applications. In many situations loading conditions vary significantly, but damage models are generally accurate only for specific conditions [1].

The difficulty in studying damage is that unlike yield, ductile fracture is history dependent [2]. Furthermore, yield in ductile materials is closely related to the equivalent deviatoric stress, while recent work has shown that no single parameter accurately predicts fracture [3].

Coupled with the difficulty in predicting damage in controlled conditions is the limited understanding of the effect strain rate and temperature have on the process. Indeed, many dynamic simulations are conducted using fracture models calibrated using quasistatic data, see for example [4]. However, the application for dynamic modelling is extensive and includes automotive accidents, ballistic impact and explosives testing.

1.1 Motivation

Research at the Blast Impact and Survivability Research Unit (BISRU) of the University of Cape Town is focused on dynamic testing. This is primarily in the form of blast impact loading, drop weight experiments and split Hopkinson pressure bar characterisation. A damage model that covers a wide range of strain rates is vital to simulate these events and hence the motivation for this thesis.

This work is a first stage in developing a damage model valid across a wide range of strain rates, from quasistatic ($\approx 1 \times 10^{-3}\,\mathrm{s}^{-1}$) to dynamic ($> 1 \times 10^{3}\,\mathrm{s}^{-1}$), and loading conditions. To reduce the complexity, the scope is limited to tensile testing of mild steel, a material which has high strain rate dependence in plastic deformation. Ultimately the test program needs to be expanded to include shear and compression and thus damage models implemented in this thesis need to be valid within those regions.

1.2 Objectives and Method

The central aims of this study, together with the method to achieve each, can be summarized as follows:

1. Develop a procedure to study failure across a wide range of strain rates.
   (a) Analyse existing damage models and select the optimal method that is accurate over a wide range of loading conditions.
   (b) Optimize and build a tensile split Hopkinson pressure bar (TSHB) apparatus for the dynamic experiments.
   (c) Conduct quasistatic and dynamic experiments on specimens with differing geometries to produce a range of stress states.
   (d) Write a user defined plasticity and damage model to implement in the Abaqus finite element package.

2. Determine trends in the influence of strain rate to fracture strain.
   (a) Perform finite element analysis to determine the stress state and strain at failure.
   (b) Compare the failure strains at equivalent stress states for the specimens deformed at different rates.
   (c) Calibrate and implement a damage model in Abaqus.

1.3 Outline of the Report

This report begins with a literature review in chapter 2. Of prime importance is an analysis of well-known failure models. This is followed by a review of the split Hopkinson bar method and the adaptation that have been developed for tensile testing. Various specimen designs used to analyse damage are then considered followed by modelling techniques used to simulate tensile specimens and the TSHB.

Chapter 3 covers the design of both the TSHB and specimens. Also included is an outline of the specimen assembling process and jig design.

The simulation procedure is developed in chapter 4, which begins by detailing the theory behind the plasticity and damage model implementation. This is followed by an analysis to assess and optimize model stability. Finally the modelling techniques developed to simulate the experiments are detailed.

Chapter 5 shows the results from all the dynamic and quasistatic tests. The simulations for these follow in chapter 6. The plasticity model is calibrated to correspond closely to the experimental results and then the damage parameters are found.

Chapter 7 discusses the effectiveness of the tensile split Hopkins bar apparatus and the specimen attachment techniques as well as the methods used to model the experiments. This is followed by a detailed analysis of the influence of strain rate to damage.

Finally chapter 8 summarizes the significant conclusions, while the recommendations in chapter 9 give an assessment of the improvements still required.

Chapter 2

Literature Review

2.1 Introduction

This chapter provides a summary of the literature relating to failure modelling and analysis.

The first section details the development of the common damage models with emphasis placed on the more recent developments. Damage modelling is a relatively young field with several models developed as recently as 2008 and thus the main purpose is to assess which model is most applicable for this work.

The next section deals with the split Hopkinson bar (SHB) apparatus and methods developed to adapt the conventional compressive test for tensile experiments. The SHB is the most widely accepted method for material characterisation under dynamic conditions[5].

A basic analysis of tensile testing is included, followed by a review of specimen designs used in failure analysis as well as methods implemented to secure these to the SHB. Finally, finite element modelling techniques are considered relating to the SHB as well as specimen-bar interactions. Emphasis is placed on techniques that reduce computation time, while maintaining accuracy.

2.2 Damage Modelling

2.2.1 Fracture Definition

In this work fracture, or damage, is defined as a discontinuous description of deformation and is evident as the initiation of cracks within a material. This is distinct from material separation as under extreme conditions materials can separate simply due to plastic deformation by necking to a point as found in the classic work by Bridgman [6].

Ductile fracture refers to damage occurring after significant plastic deformation, in contrast to brittle fracture. Two competing forms exist:

1. Fracture due to void nucleation and coalescence.
2. Fracture due to shear decohesion.

The former occurs after large tensile axial strains. In the case of a round tensile specimen, the localization process of necking[1] results in non-axial tensile stresses. When these are large enough small holes form near the axis, referred to as *void nucleation*. With further strain these voids expand and join with one another (*void coalescence*) leaving only the outer perimeter remaining. However, as this region is too small to withstand the load, cracks form and the material fractures.

Fracture due to void nucleation and coalescence results in the classic *cup and cone* fracture shown in figure 2.1a. Note the distinction between the central region, where void nucleation results in a pitted surface, and the smooth outer perimeter, where the cracks propagate.

Figure 2.1 shows the extreme contrast between fracture due to void growth and that formed by shear decohesion. For the latter failure occurs along the slip lines, shearing the atomic bonds along one plane [8]. In a homogeneous material with no impurities such as voids, this results in a smooth failure surface as the material fractures along a plane parallel to the shear load applied.

[1] Detailed in section 2.4.

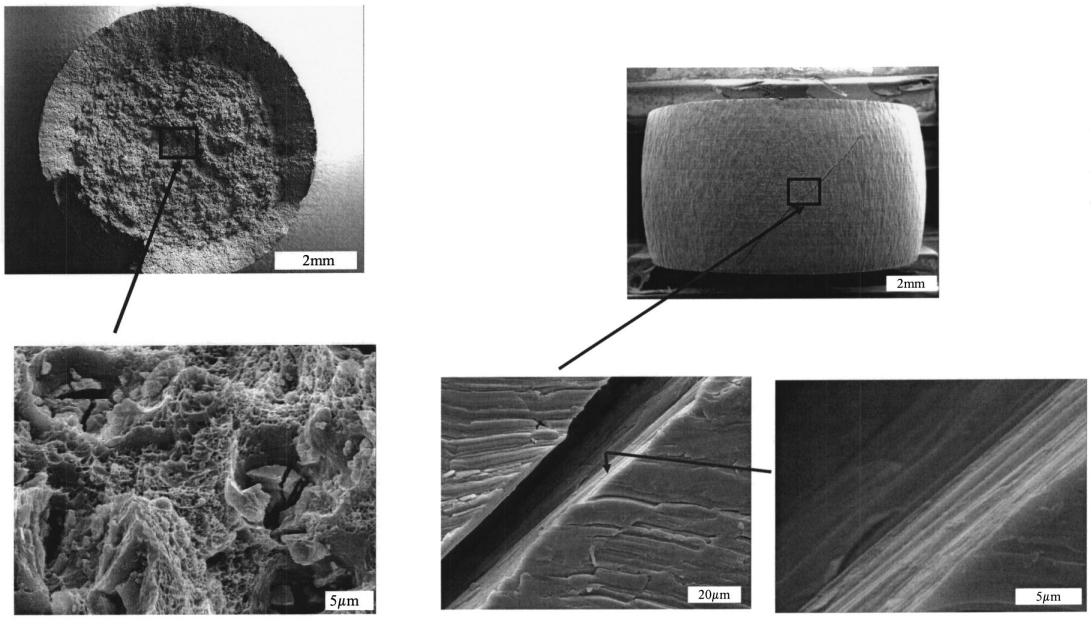

(a) Void nucleation and coalescence. (b) Shear decohesion.

Figure 2.1: Scanning electron microscope pictures showing the fracture zones in a tensile and upsetting test [7].

Two issues complicate damage analysis. Firstly as a finite amount of time is required for voids to form and join together, fracture is history dependent. Secondly failure may occur due to a combination of shear decohesion and void growth [3]. Thus if a model is to be accurate across a wide range of loading configurations both of these phenomena need to be considered.

2.2.2 Bridgman High Pressure Testing

In 1944 Bridgman [6] conducted a series of tensile tests in an environment pressurized up to 2.8 GPa. Bridgman found that specimens attained far greater strain before fracture when high pressure was applied. He argued that the principal mechanism for fracture in ductile tensile tests is hydrostatic tension on the axis as this promotes void nucleation. Thus a high applied pressure tends to decrease the non-axial tension and hence delay the onset of failure.

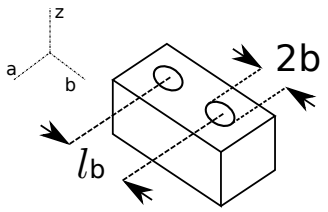

Figure 2.2: Cell used by McClintock [2] to study the growth of voids.

2.2.3 McClintock Model

One of the earliest theoretical studies on void growth and nucleation was conducted by McClintock [2] in 1968. McClintock knew that in contrast to plastic yield or brittle fracture, which relies only on the current material state, the growth of holes in ductile fracture depend on the entire history of stress, strain and rotation. This makes ductile damage far harder to analyse and explains the lack of theoretical work on the subject up until this point.

In McClintock's analysis, the problem was simplified to include only situations in which the principal stress components do not rotate relative to the material. Thus failure due to shear decohesion was neglected and the effect of the deviatoric stress components ignored[2].

The study considered the growth of cylindrical holes in a plastic deforming material. Each cell contained three sets of perpendicular holes (one set is shown in figure 2.2) with the criterion that failure would occur when the hole grew to the extent that it touched a pair of edges on the cell boundary (void coalescence). Thus if a hole stretched along the b direction as shown in the figure, failure would occur with a growth factor of,

$$F^f_{zb} = \frac{1/2}{b^0/l^0_b} \tag{2.1}$$

with b^0 initial hole width in the b direction and, l^0_b initial separation.

The resulting failure locus is described as follows,

$$\frac{\delta\eta_{zb}}{\delta\epsilon} = \frac{\sinh[(1-n)(\sigma_a+\sigma_b)/(2\sigma/\sqrt{3})]}{(1-n)\ln F^f_{zb}} \tag{2.2}$$

where η_{zb} is damage accumulation factor along plane z-b, σ_a and σ_b are the stresses

in directions a and b and n is the material hardening constant. ϵ and σ refer to the equivalent strain and stress respectively. The damage accumulation factor predicts failure once unity is reached.

Agreeing with the earlier results of Bridgman [6], McClintock found that a high transverse tensile stress reduces ductility. In contrast, at low tensile transverse stresses the holes are required to remain open for the steady state damage rate to be positive [2]. This has several implications, firstly due to hole growth fracture is not predicted to occur in a conventional tensile test with straight specimens (i.e. no notches cut into the surface) prior to necking as the non-axial tensile stress through the region is minimal and thus no voids form. Secondly this mode of fracture will not occur in loading states of pure torsion or uniaxial compression as in these cases the holes would close.

A convenient measure of transverse stress is *triaxiality*, η, which is the hydrostatic stress, σ_m normalized by the equivalent von Mises stress,

$$\eta = \frac{\sigma_m}{\sigma} \tag{2.3}$$

This ratio is used extensively in the damage models considered in this review as well as in the numerical analyses in chapter 6. Negative triaxialities occur in cases of compression, pure shear results in a triaxiality of zero, while positive values occur in tension.

2.2.4 Rice-Tracey Model

Rice and Tracey [9] extended the theoretical work by McClintock to cover the growth of isolated spherical voids as these refer more closely to the physical voids which occur in practice than the cylindrical holes used previously. The aim was to determine the relationship between void growth and stress triaxiality.

Rice and Tracey found that hole growth rates increased with superimposed hydrostatic tension, which corresponds to an increase in triaxiality. The parameter used to explain the relationship was D, which describes the degree of deformation on the void boundary to that of the surrounding material and is defined by $D = \dot{R}_0/\dot{\epsilon}R_0$, where $\dot{R}_0$ is the average radial velocity on the void boundary.

An exponential relationship between the strain rate ratio and triaxiality was found, which could be approximated as,

$$D = Ce^{\frac{\sqrt{3}}{2}.\eta} \tag{2.4}$$

with η the triaxiality and C a constant.

However, as a continuum analysis was used, the calculations are independent of void size and spacing, while dependent on the volume fraction. Thus the model cannot apply to fracture at a crack tip where the void size has a significant effect[9].

It seems reasonable to suggest that the ratio D would have an inverse relationship with strain to failure as a high D indicates that the material around the void is deforming at a much greater rate than the remainder of the material. Thus to put the relationship in a form used by the fracture loci in the subsequent models,

$$\epsilon_f = Ae^{-B\eta} \tag{2.5}$$

where ϵ_f refers to the equivalent strain to failure and A and B are material constants.

2.2.5 Gurson Model

The final continuum mechanics based model considered here is that developed by Gurson [10] in 1977 and modified by Needleman and Tvergaard [11] in 1984. Gurson developed the model using a similar approach to McClintock and Rice-Tracey by considering the growth of cylindrical and spherical voids.

It is described as a function equal to zero at failure,

$$\Phi = \left(\frac{\sigma}{\sigma_y}\right)^2 + 2q_1 f^* \cosh\left(\frac{[T_{ii}]}{2\sigma_y}\right) - 1 - (q_1 f^*)^2 = 0 \tag{2.6}$$

with q_1 a material constant, σ_y the yield stress and T_{ii} the trace of the Cauchy stress tensor. f^* is a measure of the void volume fraction and needs to be determined for each strain increment.

An inherent advantage with the Gurson technique is that the model is based on a physically plausible mechanism. However, it requires many tests to calibrate. Furthermore, only one form of damage is considered, that of void growth and coalescence, and is thus only valid for regions of tensile triaxiality.

2.2.6 Cockcroft-Latham Model

In contrast to the continuum approach used in the McClintock and Rice-Tracey models, Cockcroft and Latham [12] developed a phenomenological prediction method.

It was proposed that the damage criterion should be a combination of both stress and strain, as metals fail at different strains depending on the loading conditions. A criteria that fitted this option was that of total plastic work, W, defined as,

$$W = \int_0^{\epsilon_f} \sigma d\epsilon \tag{2.7}$$

Cockroft and Latham observed that the shape of the neck in a tensile test had a major influence over the fracture strain. As the yield stress is not affected by the neck shape, a normalized stress was suggested of the form,

$$\sigma^* = \frac{\sigma_1}{\sigma} \tag{2.8}$$

with σ_1 the maximum principal stress.

The final model is simply the product between that for plastic work and the normalized principle stress. Fracture is predicted when the value C reaches a calibrated value.

$$C = \int_0^{\epsilon_f} \sigma \left(\frac{\sigma_1}{\sigma}\right) d\epsilon = \int_0^{\epsilon_f} \sigma_1 d\epsilon \tag{2.9}$$

The Cockcroft-Latham model has been commonly used in the metal bulk forming processes [13]. Wierzbicki et al. [1] argued that the method is only applicable in the range of small to negative triaxialities. However, it was developed by considering tensile specimens that have mid to high positive triaxialities. Thus Cockcroft and Latham's intention was clearly for a far wider application.

2.2.7 Johnson-Cook Model

In 1985, Johnson and Cook [14] introduced a damage model that takes into account triaxiality as well as the effect of strain rate and temperature. It is simple, experimentally based, and easy to implement numerically and thus has been extensively used and is included in the commercial finite element packages Abaqus, LS-DYNA and Autodyn [1].

The model is as follows,

$$\begin{aligned}\epsilon_f &= f(\eta) \cdot f(\dot{\epsilon}) \cdot f(T) \\ &= \left[D_1 + D_2 e^{D_3 \cdot \eta}\right] \left[1 + D_4 \ln \dot{\epsilon}^*\right] \left[1 + D_5 T^*\right]\end{aligned} \tag{2.10}$$

where D_1 through D_5 are material constants and,

$$\dot{\epsilon}^* = \frac{\dot{\epsilon}}{\dot{\epsilon}_0} \qquad T^* = \frac{T - T_0}{T_{\text{melt}} - T_0}$$

The terms $\dot{\epsilon}_0$ and T_0 refer to the reference quasistatic strain rate and transient temperature respectively.

Johnson and Cook calibrated three materials to test the model; copper, Armco iron and 4340 steel. For each of these, three sets of experiments were completed; quasi-static tensile tests, Split-Hopkinson Bar tensile tests and quasistatic torsion tests.

The triaxiality term, $f(\eta)$, has the greatest influence, and describes an exponential decrease in ductility with increasing pressure. This is similar to the early findings by McClintock [2] and Rice and Tracey [9]. A major discrepancy was noted for the steel torsion test, with the predicted strain to fracture being far lower than the extrapolated curve from the tensile data would suggest. However, Johnson and Cook argued that as the torsion data from the iron and copper specimens agreed with the curve, the steel torsion data was an anomaly and could be ignored[14]. Later work by Bao and Wierzbicki [3] proposed that the low torsion data point was correct and that errors are simply due to the invalid technique of extrapolating data from regions where void growth failure dominates to that of shear decohesion[2].

[2]This is covered in section 2.2.13 on page 18.

Of lesser influence in this model, but of distinct importance for the work in this thesis, is the strain rate function $f(\dot{\epsilon})$. This has the same form as used in the Johnson-Cook plasticity model [15], and describes how an increase in strain rate leads to an increase in fracture strain. Finally, the temperature term, $f(T)$, increases ductility with an increase in temperature. This is opposite to its effect on plastic yield in decreasing the strain required.

The combined effect of strain rate and temperature to increase fracture strain reported by Johnson and Cook [14] is in direct contrast to the research in this thesis. This work found that dynamic specimens fail at a lower strain than the quasistatic equivalents. The strain rate analysis is dealt with in detail in chapter 7, but needs consideration throughout the analysis.

Johnson and Cook calibrated the triaxiality constants, D_1 to D_3, using the quasistatic tension and torsion tests. The torsion data had a low triaxiality of zero, compared to that of the tensile from 0.7 upwards. The strain rate and temperature constants, D_4 and D_5, were be found by comparing the data from Hopkinson Bar tests at high strain rates conducted with specimens preheated to various temperatures to that from the quasistatic experiments. The dynamic fracture strains had to be estimated by measuring the final cross-sectional area of the fractured specimens.

An example of the fracture locus for 4340 steel is included in figure 2.3. Note that the dynamic calibration tests were conducted at strain rates in the order of $500\,\mathrm{s}^{-1}$, while an extreme value of $10^5\,\mathrm{s}^{-1}$ is shown. Thus for 4340 steel, strain rate clearly has only a very minor influence. Armco iron and copper had greater strain rate dependence, however, the difference between a rate of $1\,\mathrm{s}^{-1}$ and $10^5\,\mathrm{s}^{-1}$ was still less than 20%.

Johnson and Cook used compressive impact tests on short cylinders to validate the technique. Although damage was evident around the edges of each specimen, the model failed to predict any failure with the strains in the model lower than that required. It was suggested that the model may not extrapolate well into the extreme regions of strain rate, temperature and pressure. This agrees with the findings of Bao and Wierzbicki [3] in which separate equations were used to describe the high, mid and low triaxiality ranges instead of extrapolating from tensile data.

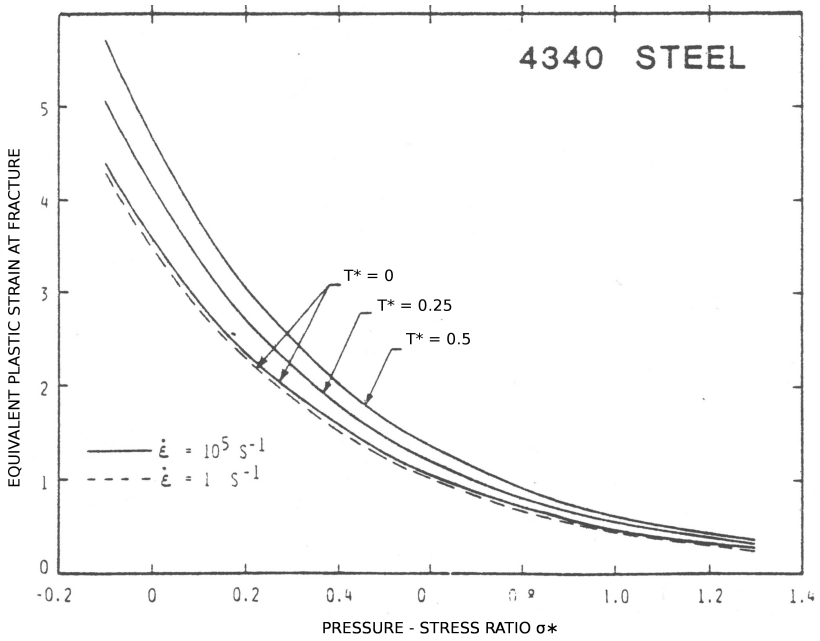

Figure 2.3: Johnson-Cook fracture model for 4340 Steel[14].

2.2.8 Constant Fracture Strain Model

Possibly the simplest fracture model defines material failure to occur when a specified equivalent strain is reached. The equivalent strain is defined simply by,

$$\epsilon = \sqrt{\frac{2}{3}\left(\epsilon_1^2 + \epsilon_2^2 + \epsilon_3^2\right)} \tag{2.11}$$

where ϵ_1 through ϵ_3 are the principal strains.

This method was first suggested in the early 20th century[1] and is still commonly used due to its ease in implementation. A further advantage is that possible fracture locations can be found simply by analysing the resulting strains in a finite element model. Thus the constant fracture strain criterion is found in almost all nonlinear finite element codes [1].

However, fracture strain is strongly dependent on the calibration test. For example, a pure shear test will result in significantly different failure strain to a uniaxial tension test. Thus the model is only valid if the loading used in the application is closely related to that of the calibration tests. In cases where complex loading occurs, in which the type of dominant loading changes, this approach is unsuitable.

2.2.9 Fracture Forming Limit Diagram

An experimentally derived method applicable to plane stress applications involves a combination of the principle strains adding to a damage constant in the form,

$$\epsilon_1 + \epsilon_2 = -\epsilon_3 = C \tag{2.12}$$

where ϵ_1 through ϵ_3 are the principal strains at failure.

The advantage is that only one test is required to calibrate the model. However, it is only used in the narrow loading range between uniaxial and biaxial tension. The model was developed and is still used in the metal forming industry. [1].

2.2.10 Maximum Shear Stress Model

The *maximum shear stress* model is similar to the Tresca yield condition and predicts that a material will fail when the equivalent deviatoric stress reaches a critical value[13].

The model is commonly used in cases where shear decohesion failure is dominant, such as in an upsetting test in which fracture occurs along a plane with the maximum shear stress. A major application is brittle materials, for example in soil and rock mechanics[1].

It can be expected that inaccuracies will occur in cases dominated by failure due to ductile void growth as this is a different fracture mode to shear decohesion. Wierzbicki et al. [1] conducted calibration tests for various fracture models on aluminium 2024-T351 and compared the calibrated fracture locus generated by each model with all the experimental data points. At high tensile triaxialities the failure strain was severely overestimated. However, excellent correlation occurred with the plane stress tests at low triaxialities, dominated by shear decohesion. This makes the model an excellent choice if the application is within the shear and compressive region as only one test is required for calibration.

2.2.11 Wilkins Model

Wilkins et al. [16] in 1980 was the first to consider the effect of the deviatoric stress invariants, J_1, J_2 and J_3. Wilkins found that both hydrostatic tension and asymmetric strain, which relates to the deviatoric invariants, enhanced strain damage. This is reasonable as damage can occur due to a combination of void growth, related to hydrostatic tension, and shear decohesion, related to deviatoric stress.

The influence of each was described in separable terms as follows,

$$D = \int w_1 w_2 d\epsilon \tag{2.13}$$

in which w_1 relates to the hydrostatic pressure, and w_2 relates to the deviatoric stress.

$$w_1 = \left(\frac{1}{1 + a\sigma_m}\right)^{\alpha} \qquad w_2 = (2 - A_s)^{\beta} \qquad A_s = \max\left(\frac{J_2}{J_3}, \frac{J_2}{J_1}\right)$$

with a, α and β material constants.

The model has been widely used due to its simplicity and easy calibration. It is included in the commercial codes PAM-CRASH and LS-DYNA[13]

The asymmetry parameter A_s relates closely to the Lode angle, used extensively in this thesis. This is defined by,

$$\theta = \frac{1}{3}\arccos\left(\frac{r}{\sigma}\right) \tag{2.14}$$

where r relates to the determinant of the deviatoric stress tensor, S_{ij} and to the third deviatoric invariant through [17],

$$r = \left[\frac{27}{2}\det\left[S_{ij}\right]\right]^{1/3} = 3\left(\frac{J_3}{2}\right)^{1/3}$$

In several models a normalized Lode angle is used. This is defined simply as,

$$\bar{\theta} = 1 - \frac{6\theta}{\pi}$$

with a range from -1 to 1.

2.2.12 CrachFEM Model

A more recent criteria that takes both hydrostatic and a deviatoric effects into account is the *CrachFEM* model. This was developed in combination by the BMW R&D Centre and MATFEM Co. to be used in modelling thin sheet metal and extrusions [1].

CrachFEM utilizes two competing failure criteria; ductile failure and shear decohesion with failure being defined when either is reached. The ductile locus is only dependent on triaxiality and is of the form,

$$\epsilon_f^{ductile} = d_0 e^{-3c\eta} + d_1 e^{3c\eta} \tag{2.15}$$

with three constants, d_0, d_1 and c.

The shear model includes both hydrostatic and deviatoric terms,

$$\epsilon_f^{shear} = d_2 e^{-f\Theta} + d_3 e^{f\Theta} \tag{2.16}$$

with Θ defined by

$$\Theta = \frac{\sigma}{\tau_{max}} (1 - 3k_s\eta) \tag{2.17}$$

The parameter τ_{max} refers to the maximum shear stress. Note that Θ should not be confused with the Lode angle θ.

The shear model introduces four new constants d_2, d_3, f and k_s, leaving a large total of 7 material constants to be found. However, by considering two separate damage criteria it is claimed to be valid though a wide range of loading conditions.

2.2.13 Bao - Wierzbicki Damage Model

Triaxiality Locus

In 2004 Bao and Wierzbicki [7] conducted a comparative study on damage models. These were evaluated by conducting quasistatic upsetting and tensile tests and then using finite element analysis to simulate the experiments.

Upsetting tests involve the uniaxial compression of short cylindrical specimens with damage occurring due to the build up of tensile circumferential stresses near the specimen equator [7]. As fracture initiation occurs on the outer surface, the displacement to fracture was found by compressing cylinders to differing degrees and visually inspecting for cracks.

Round specimens were used for the tensile tests. These involved both smooth specimens and ones with circumferential notches cut out of the gauge section[3]. By adding notches, Bao and Wierzbicki were able to increase the degree of hydrostatic stress, or triaxiality, at the fracture locations. In the tensile tests, fracture initiation occurs in the centre of the specimen and thus cannot be seen visually without slicing the specimen. Instead, a sudden load drop in force-displacement response occurs and this was taken to be the point of fracture.

All the damage models considered are of the form [7],

$$C = \int_0^{\epsilon_f} f d\epsilon \tag{2.18}$$

with C the material damage parameter and f a measure of damage accumulation. By using finite element analysis to model each test Bao and Wierzbicki were able to determine the stress state at each point in the deformation and thus evaluate C for all the models with each configuration.

The study found that for each failure model, the damage parameters varied considerably when calculated using specimens of differing geometries. For example using the McClintock criterion [2], parameters four times lower are required for the upsetting tests compared to the tensile. These upsetting tests correspond to an average triaxiality of approximately $\eta \approx -0.25$ compared to that for the tensile varying from 0.4 to 0.95.

However, although not applicable in compression, the general Rice-Tracey model [9] and the Hydrostatic stress model were found to use similar parameters for each of the tensile tests, indicating that the prediction is adequate in the region. In contrast the Cockcroft-Latham-Oh model calibrates significantly different parameters for each of the tensile tests, but similar ones amongst the upsetting tests and is thus acceptable within this region.

[3]Examples of these are included in section 2.5

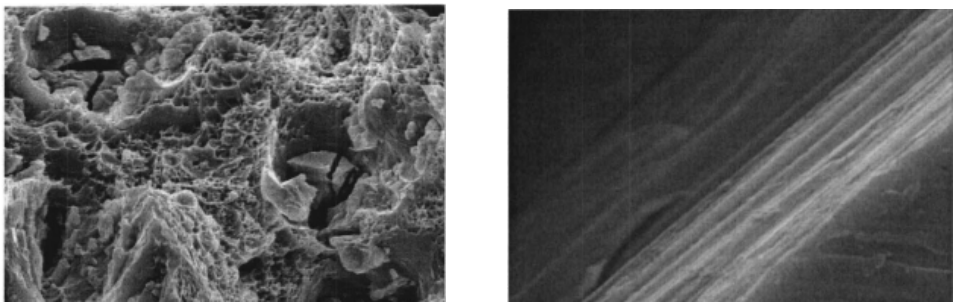

(a) Tensile Specimen (b) Upsetting Specimen

Figure 2.4: Scanning electron microscope pictures showing the fracture zones in a tensile and upsetting test found by Bao and Wierzbicki [7].

Bao and Wierzbicki explained the large difference in constants between the upsetting and tensile tests by considering the fracture mechanism occurring in both situations. Failure due to void nucleation and coalescence results in a rough dimpled damage surface, such as that in figure 2.4a. In contrast failure due to shear decohesion results in a smooth surface. Thus to apply a method calibrated and developed for only a limited range of loading conditions to a wider scenario is dubious. The different failure mechanisms explain the good prediction the Rice-Tracey and Hydrostatic stress models give for tensile tests as these are based on this mechanism.

Bao and Wierzbicki noted that despite this fact Johnson and Cook [14], among other authors, extrapolated the results from the Rice-Tracey model based on void growth to low triaxialities in which nucleation and coalescence is not the prime cause of fracture.

Bao and Wierzbicki proposed an alternative fracture locus in which three zones, each described by a different equation, are used. This is explained in detail in [3] and included here as figure 2.5. At low triaxialities of $-\frac{1}{3}$ shear fracture dominates, while at high values of greater than 0.4 void nucleation occurs. In between a transition zone exists where both contribute.

Damage is a time history dependent property and thus the triaxiality is described in an average sense as,

$$\left(\frac{\sigma_m}{\sigma}\right)_{av} = \frac{1}{\epsilon_f}\int_0^{\epsilon_f} \frac{\sigma_m}{\sigma} d\epsilon \tag{2.19}$$

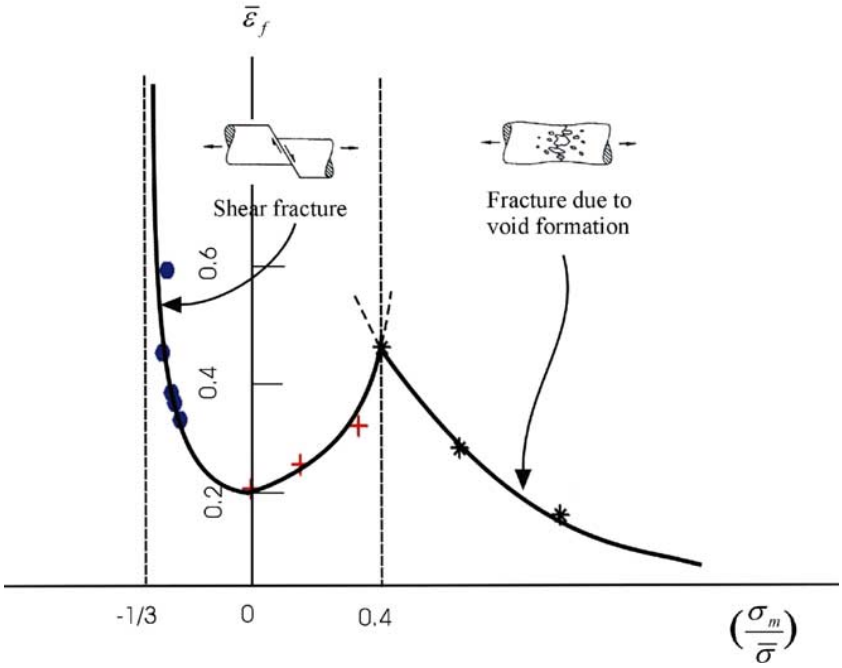

Figure 2.5: Fracture locus based on stress triaxiality proposed by Bao and Wierzbicki [7]. Note that although the diagram depicting shear fracture is shown as tensile, negative triaxialities result from compressive experiments.

It was proposed that the local peak around the triaxiality of 0.4 would be greater than that at zero for a material in which the strain to fracture is smaller in shear than in void growth. However, it would be lower if the strain to fracture in shear is larger [7].

This locus explains the discrepancy in the torsion data point in the development of the Johnson-Cook model that was previously ignored[4]. The major advantage is that it is calibrated through a wide range of loading conditions and thus is intended to be used in cases where the stress state changes significantly. However, in implementation three separate loci must be implemented.

[4]See section 2.2.7 on page 13

Triaxiality Cut-off Value

An interesting aspect of the model is the negative cut-off value of $\eta_{av} = -\frac{1}{3}$. Bao and Wierzbicki released a paper in 2005 [18] which proposed that below this value fracture initiation will never occur. Three approaches were followed, the first considered classic experimental data reported by Bridgman [19], while the second considered upsetting tests conducted by Bao and Wierzbicki in [3]. The third used a finite element analysis approach to study the effect of hydrostatic pressure to tensile tests, in effect using the same approach as Bridgman, but using only simulations.

Bridgman conducted tensile tests on steel subjected to various constant hydrostatic pressures. Thus his results were convenient to study the effect of triaxiality as the parameter is a normalized measure of hydrostatic stress. Included in the data are the applied pressure, the final strain and final stress as well as the neck profile.

As only the final true stress is given, the average triaxiality was estimated as,

$$\eta_{\text{av}} = \frac{1}{2}\left(\eta_i + \eta_f\right) \tag{2.20}$$

with η_i and η_f referring to the initial and final triaxiality respectively. This would be far more efficient computationally than determining the average from the integral of triaxiality and strain. However, no analysis was presented to show the error in average triaxiality due to using this simplified method.

The initial value can be calculated from the applied pressure, while the final was found using a modified Bridgman formula found using simulations,

$$\eta_f = -\frac{p}{\sigma} + \frac{1}{3} + 1.4\ln\left(1 + \frac{a}{2R}\right)$$

where a refers to the specimen diameter in the necked region and R refers to the neck radius.

The average triaxiality for all tests is shown in figure 2.6. Bao and Wierzbicki realized that no specimens with an average triaxiality of lower than approximately -0.3 fractured.

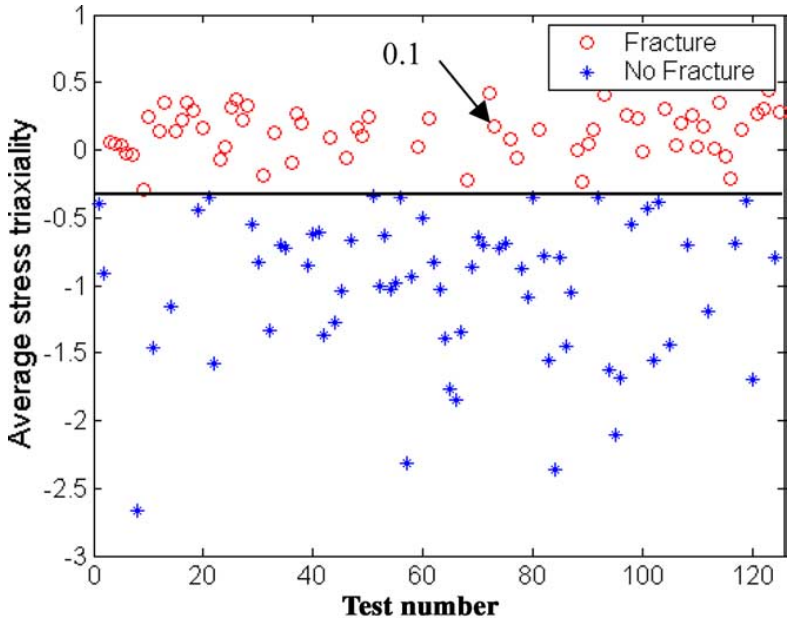

Figure 2.6: Bridgman experimental data showing the average triaxiality for each specimen [18].

Similarly in the upsetting tests the fracture locus was found to be related to the hoop and axial strains through,

$$E_{\theta\theta} + \frac{1}{2}E_{zz} = C \tag{2.21}$$

which, when written in terms of equivalent strain to failure and triaxiality, results in an infinite strain for a triaxiality of $-\frac{1}{3}$.

Finally, the numerical simulations on both aluminium and steel under constant applied pressure showed the stress triaxiality would increase positively with strain as the neck grew. The example for aluminium is shown in figure 2.7. In the cases where the applied pressure was of sufficient magnitude, the triaxiality never increased above $-\frac{1}{3}$ and no failure occurred, instead specimens necked to a point before separating. However, in the remainder fracture is evident shortly after increasing above the cut-off. Note that in this figure there is no mention of using the average triaxiality and thus one must assume that the instantaneous value is presented. As triaxiality is increasing for each specimen, the average value would be lower that shown if the assumption is correct.

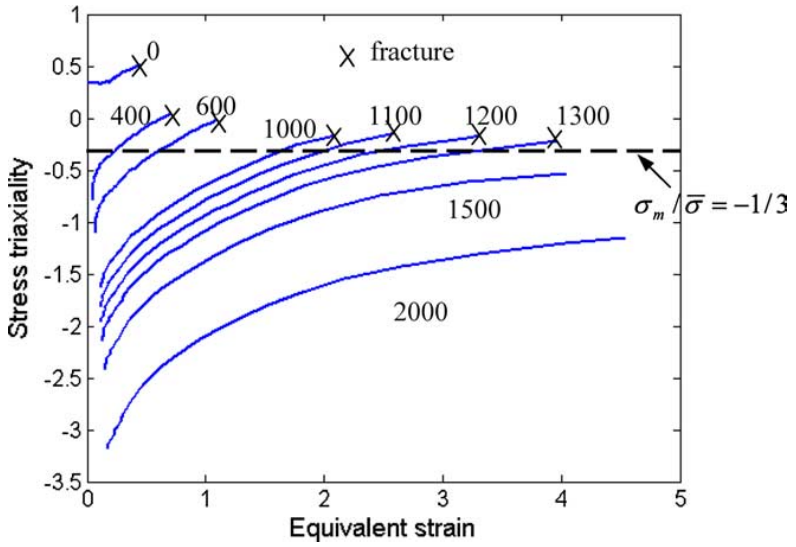

Figure 2.7: Stress triaxiality versus equivalent strain found using finite element analysis on aluminium found by Bao and Wierzbicki [18]. The triaxiality is assumed to be instantaneous, not the average.

The fact that failure did not occur directly after passing the threshold indicates the history dependence as the voids need a finite amount of time to nucleate, grow and join. This gives credence to the method of using the average triaxiality, and not the final value, at fracture.

2.2.14 Xue - Wierzbicki Model

In the same year, Wierzbicki and Xue [20] extended the Bao-Wierzbicki model to include the effects of the deviatoric stress components. The additional components were introduced in the form of the normalized third deviatoric stress invariant, ξ, related to the Lode Angle, θ though,

$$\xi = \frac{27}{2}\frac{J_3}{\sigma^3} = \cos(3\theta) \tag{2.22}$$

where J_3 is the third deviatoric invariant.

As damage is history dependent, the mean value of ξ was taken. This was calculated as,

$$\xi_{av} = \frac{1}{\epsilon_f}\int_0^{\epsilon_f} \xi(\epsilon)\mathrm{d}\epsilon \tag{2.23}$$

In his work on the fracture initiation of ductile solids, Xue [21] found that the equivalent strain to fracture was bounded by a lower curve corresponding to plane strain, $\xi = 0$ and an upper corresponding to axisymmetric stress, $\xi = \pm 1$. This is indicated in figure 2.8a

Wierzbicki and Xue proposed to describe the two limiting curves with simple exponential functions,

$$\epsilon_f^{axi} = C_1 e^{-C_2 \eta} \qquad \xi = 1 \tag{2.24}$$

$$\epsilon_f^{ps} = C_3 e^{-C_4 \eta} \qquad \xi = 0; \tag{2.25}$$

where ϵ_f^{axi} is the strain to fail under a pure axisymmetric load and ϵ_f^{ps} is that under plane strain. In combination, four constants, C_1 through C_4 are required.

The deviatoric parameter was described by an ellipse, shown in figure 2.8b. Of the form

$$\left(\frac{\Delta \bar{\epsilon}_f}{\epsilon_f^{axi} - \epsilon_f^{ps}} \right)^{1/m} + \xi^{1/m} = 1 \tag{2.26}$$

m was chosen to be the closest even integer to $1/n$, for n the plasticity hardening exponent.

Note that the exponential functions are the same form as that used by Rice and Tracey [9] and the locus reduces to the Rice and Tracey model if the deviatoric stress effect is neglected.

By noting from figure 2.8b that $\Delta \epsilon_f = \epsilon_f^{axi} - \epsilon_f$. Equations 2.24 and 2.25 were substituted into eq. 2.26 resulting in

$$\epsilon_f = C_1 e^{-C_2 \eta} - \left(C_1 e^{-C_2 \eta} - C_3 e^{-C_4 \eta} \right) \left(1 - \xi^{1/n} \right)^n \tag{2.27}$$

shown in figure 2.8c

For $\xi = 1$ the resulting form is equation 2.24, similarly $\xi = 0$ reduces to equation 2.25.

A negative value of ξ results in an imaginary value for strain. Thus one must assume from the symmetric form of the locus that the magnitude of ξ should be used.

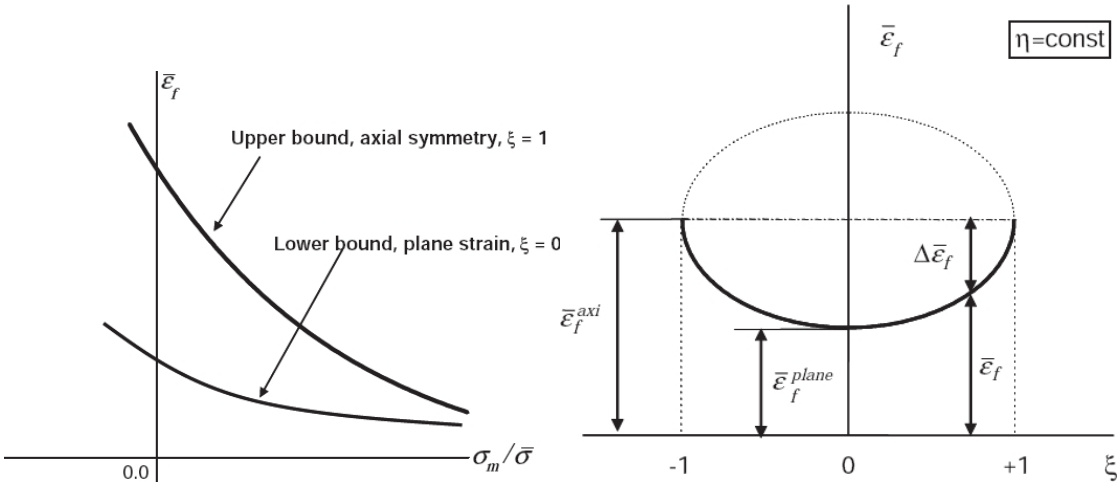

(a) Triaxiality (b) Lode angle

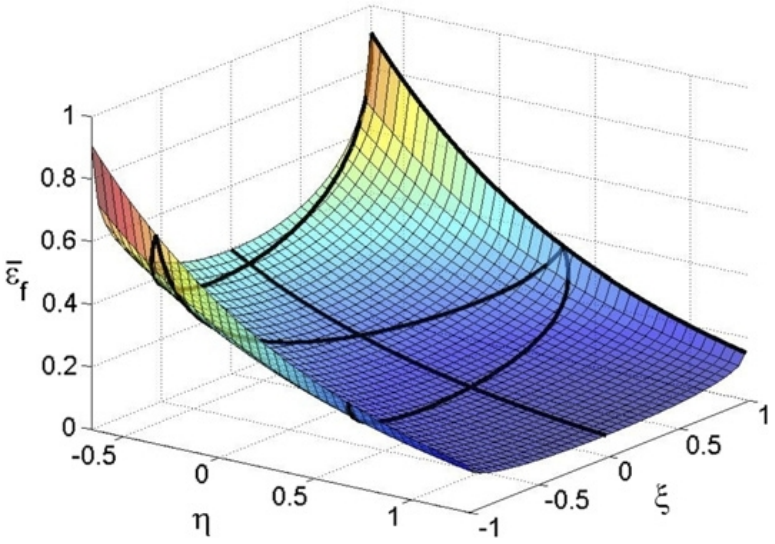

(c) Fracture Locus

Figure 2.8: Xue-Wierzbicki fracture locus with triaxiality and symmetric Lode angle dependence [1].

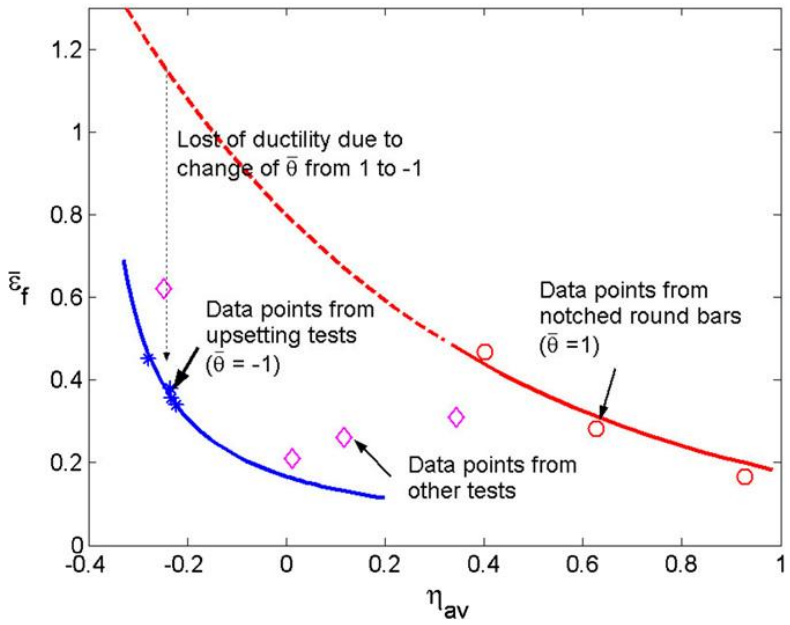

Figure 2.9: Ductility change between $\bar{\theta} = -1$ and 1 [17].

Interestingly, the new form has no triaxiality cut-off value. However, the strain required for fracture to occur at $\eta = -\frac{1}{3}$ is very high and unlikely to occur[1]. In total four damage constants are required and thus four separate calibration experiments are used.

This new form agrees closely with the Bao-Wierzbicki model and is more general as the previous model depends on the path chosen through the triaxiality-Lode angle space. A further advantage over the Bao-Wierzbicki locus and indeed the CrachFEM model is that one equation describes the entire fracture locus.

2.2.15 Bai - Wierzbicki Model

In studying upsetting tests, with a deviatoric parameter of $\xi = -1$, Bai and Wierzbicki [17] noted the ductility was lower than that in tensile axisymmetric tests with a value of $\xi = 1$ for the same triaxiality. This is shown in figure 2.9. According to the Xue-Wierzbicki model, the locus should be symmetric about $\xi = 0$ and thus should be the same in axial symmetry compression or tension.

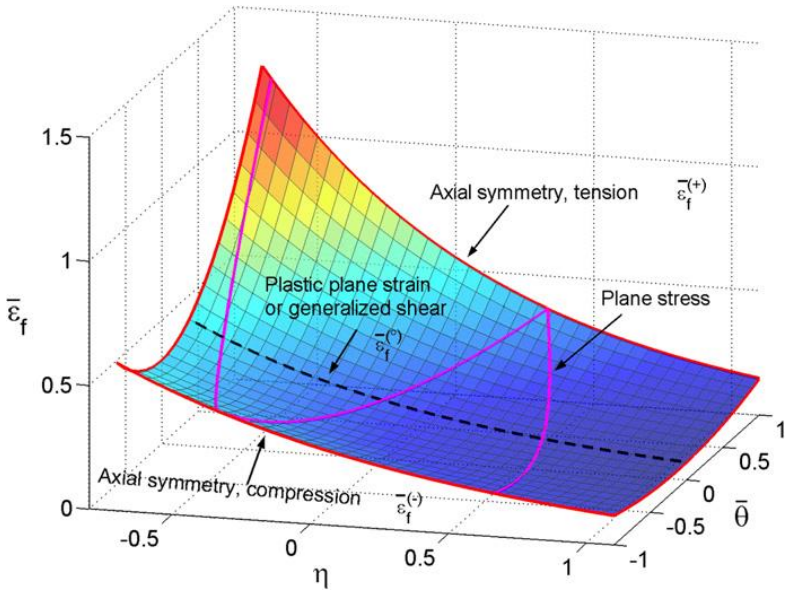

Figure 2.10: Fracture locus for the Bai-Wierzbicki damage model [17].

Thus the Bai-Wierzbicki model was proposed, a more general description than the Xue-Wierzbicki model as symmetry is not imposed. The locus is shown in figure 2.10. Note that in the figure, the normalized Lode Angle, $\bar{\theta}$ is used in place of the normalized third deviatoric stress invariant. However, the Lode Angle is also a measure of the third deviatoric stress invariant and has the same range from -1 to 1. It is defined by

$$\bar{\theta} = 1 - \frac{6\theta}{\pi} = 1 - \frac{2}{\pi}\arccos\xi \tag{2.28}$$

Instead of the elliptic function, used previously to describe the Lode angle influence, in this case a parabolic function is implemented based on the failure strain for an experiment in axisymmetric tension, $\epsilon_f^{(+)}$, axisymmetric compression, $\epsilon_f^{(-)}$ and plane strain, $\epsilon_f^{(o)}$.

The reason for Bai and Wierzbicki to change from an elliptical function to a parabolic is not discussed. However, the implication is that in the case of the ellipse the gradient $\dfrac{d\epsilon_f}{d\bar{\theta}}$ is infinite at $\bar{\theta} = \pm 1$, but finite in the parabolic case.

The locus is described by

$$\epsilon_f = \left[\frac{1}{2}\left(\epsilon_f^{(+)} + \epsilon_f^{(-)}\right) - \epsilon_f^{(o)}\right]\bar{\theta}^2 + \frac{1}{2}\left(\epsilon_f^{(+)} - \epsilon_f^{(-)}\right)\bar{\theta} + \epsilon_f^{(o)} \tag{2.29}$$

In the case of symmetry about the Lode Angle, the model reduces to a form very similar to the Xue-Wierzbicki model. In the symmetric case, the actual normalized Lode, not only the absolute, can be used.

$$\epsilon_f = \left[\epsilon_f^{(axi)} - \epsilon_f^{(o)}\right]\bar{\theta}^2 + \epsilon_f^{(o)} \tag{2.30}$$

The same exponential form as the Xue-Wierzbicki model describes the triaxiality influence. Thus

$$\epsilon_f^{(+)} = D_1 e^{-D_2\eta} \qquad \xi = +1 \tag{2.31}$$

$$\epsilon_f^{(o)} = D_3 e^{-D_4\eta} \qquad \xi = 0 \tag{2.32}$$

$$\epsilon_f^{(-)} = D_5 e^{-D_6\eta} \qquad \xi = -1 \tag{2.33}$$

Equations 2.31 to 2.33 can be substituted into eq 2.29 for the final form:

$$\begin{aligned}\epsilon_f\left(\eta, \bar{\theta}\right) = &\left[\frac{1}{2}\left(D_1 e^{-D_2\eta} + D_5 e^{-D_6\eta}\right) - D_3 e^{-D_4\eta}\right]\bar{\theta}^2 \\ &+ \frac{1}{2}\left(D_1 e^{-D_2\eta} - D_5 e^{-D_6\eta}\right)\bar{\theta} \\ &+ D_3 e^{-D_4\eta}\end{aligned} \tag{2.34}$$

2.2.16 Damage Model Comparisons

Quasistatic Calibration Tests

Recently, Wierzbicki, Bao, Lee and Bai[1] conducted a comparison of 7 commonly used damage models. These were Constant Equivalent Strain, Fracture Forming Limit Diagrams, Maximum Shear Stress, Johnson-Cook, Xue-Wierzbicki, Wilkins, CrachFEM and finally Cockcroft-Latham.

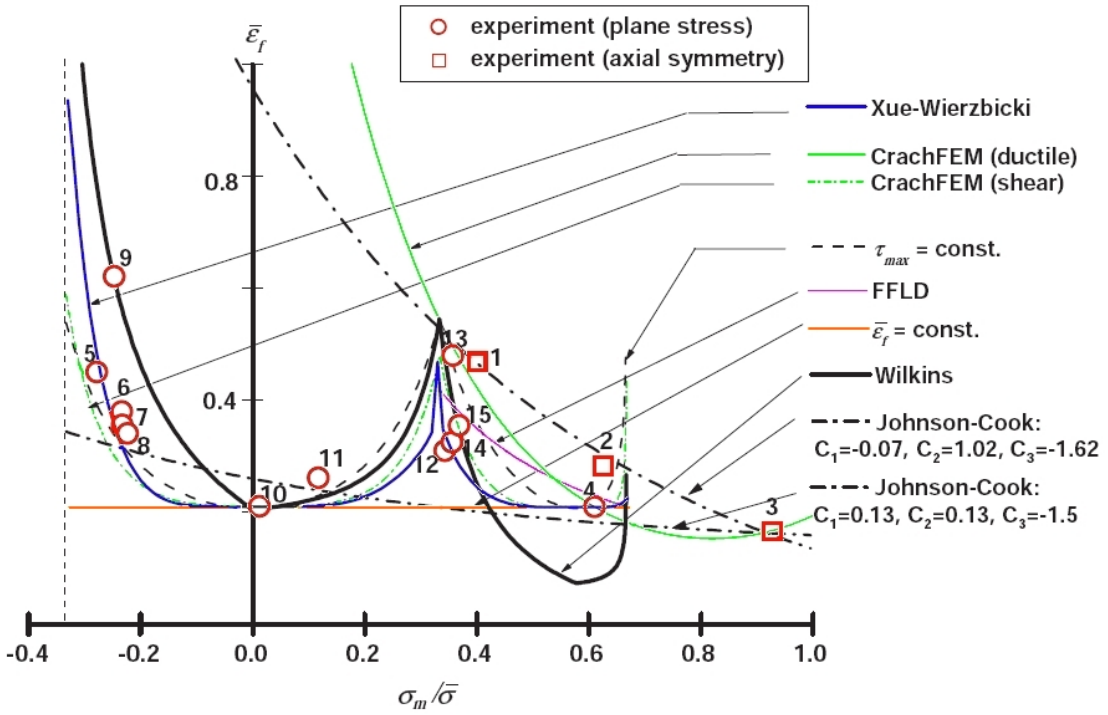

Figure 2.11: Calibrated Wierzbicki-Xue model plotted with all experimental test points and compared against several different models [1]. The colours have been added to differentiate between each.

The models were evaluated using specimens of aluminium 2024-T351, with three tensile tests on notched and unnotched round bars used in calibration and then evaluated against specimens loaded under plane stress conditions. The latter were chosen as with plane stress it is trivial to convert from a locus in stress space to that of strain. The resulting fracture loci plotted against the test failure points is shown in figure 2.11.

The constant strain locus is shown as a straight line towards the bottom of the plot. Conventionally unnotched bars are used to determine the failure strain. However, as failure strain is low for high triaxialities this method vastly underestimates failure strain for lower triaxialities. Wierzbicki et al. [1] proposed that a more consistent option would be to use a test with a similar stress state to the application. In this case the transverse plain strain test was used which corresponded closely to two points, but resulted in large underestimation in failure strain for most of the range.[1]

The fracture forming limit diagram requires only one test to calibrate, but is limited to plane stress situations between uniaxial and biaxial tension. In this region it gives an acceptable approximation in the plane stress case. However, the limit diagram cannot be used in complex loading situations in which the stress state changes drastically.

Similarly, although not shown in the figure, the Cockcroft-Latham model provided excellent approximation in the negative triaxial region, but significantly underestimated failure strain elsewhere. Wierzbicki et al. [1] used an upsetting test to calibrate resulting in accurate predictions of other upsetting tests in the region. However, the model is based on tensile testing and thus, presumably, if a tensile test was used to calibrate, it should be reasonable in the higher triaxial regions. Even in this case it would still only apply to a narrow band of stress states.

In contrast, using the maximum shear criterion also requires only a single calibration test, but results in reasonable correlation to the evaluation points. At high triaxialities over 0.7 fracture due to void growth dominates and thus it is predictable that the model vastly overestimates the failure strain within this region and would not predict failure for axisymmetric cases. However, as long as the intended application stays within the low to mid triaxialities it is an excellent model to use industrially as the cost to test only one specimen is low[1].

Two loci were developed to evaluate the Johnson-Cook model. The first used material constants from the literature[22] which resulted in the lower curve. The second used the calibration data points from high triaxialities. There is a massive difference between the resulting loci, which indicates that the Johnson-Cook model is only applicable to a narrow range of stress states close to that used in calibration.

The Wilkins model takes both triaxiality and the deviatoric stress state into account, but requires four calibration tests. Reasonable correlation is evident in the negative to low triaxial range below $\frac{1}{3}$, but between $\frac{1}{3}$ and $\frac{2}{3}$ it under-predicts fracture strain and in the high triaxial range greater than $\frac{2}{3}$ failure is not predicted. Wierzbicki et al. [1] argues that this is due to the separable form of the model which results in good correlation in either low triaxialities or mid range triaxial stresses, but never in both.

The CrashFEM technique requires three tests to calibrate the shear dominated region and three for the ductile failure locus. However, Wierzbicki et al. [1] used only four in total as two were used to calibrate both loci. The correlation through the ductile region is good, while the model marginally underestimates failure strain through the shear locus region. This model is very promising as it provides a reasonable prediction through different stress states.

Finally, the model developed by Xue and Wierzbicki resulted in impressive accuracy for all stress states. Four tests are required to calibrate, which is three more than using the maximum shear criterion. However, this cost is acceptable for complex loading situations which require accuracy throughout the triaxiality and deviatoric stress range. The testing cost is the same as that for the CrachFEM model, but the correlation to the evaluation points is more precise. The more general Bai-Wierzbicki model which does not assume symmetry about the triaxiality of zero may improve this accuracy even further, but requires an extra two calibration tests.

Applicability to High Strain Rate Testing

Teng and Wierzbicki [13] considered the application of six fracture models to high strain rate testing. The paper was based on high velocity perforation tests conducted by Børvik et al. [23, 24] in which cylindrical projectiles were shot using a gas gun at 12mm Weldox 460 E steel plate.

Teng and Wierzbicki used the experimental data in a set of finite element simulations to determine whether the damage models would follow the qualitative form of damage occurring in the tests. This was quantified by determining the modelled residual projectile velocity and comparing to that found in the experiments. A typical experimental result is shown in figure 2.12, note that no spalling occurred to the plug.

Perforation tests were chosen as these involve complex loading starting with compression when the projectile hits, with a negative triaxiality and developing shear through the thickness as the triaxiality increases to around zero. This is followed by bending and finally axial strain as the triaxiality increases positively.

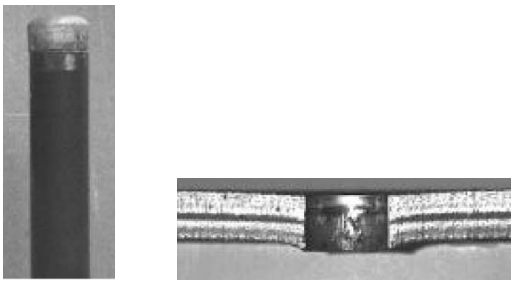

Figure 2.12: Perforation test showing a cylindrical projectile and plate conducted by Børvik et al. [23].

The simplest criterion for failure is using a constant fracture strain. This may be sufficient for processes involving a narrow load band. However, problems could be expected for complex loading scenarios as the fracture strain varies drastically depending on the loading condition. The assumption was proved correct when using a low fracture strain resulted in artificial erosion under compression within the impact zone, shown in figure 2.13a.

The artificial erosion was corrected by using a higher fracture strain, but the residual velocity of the projectile in the numerical results exceeded that of the experimental. It was suggested that increasing the fracture strain to a high, but false value would produce close correlation, but that would only be valid for that specific case [13]. In a second attempt, artificial erosion was easily corrected by imposing a cut-off value of $\eta = -\frac{1}{3}$ as found by Bao and Wierzbicki [18]. However, this did not correct the errors in the residual velocities.

The maximum shear stress criterion was investigated due to its applicability in modelling the cracks that form due to shear around the plug perimeter [13]. However, Teng and Wierzbicki found it difficult to determine the exact critical shear stress with a value slightly too low resulting in premature failure and too high in severely distorted elements but no damage. This difficulty in calibration makes the technique unsuitable.

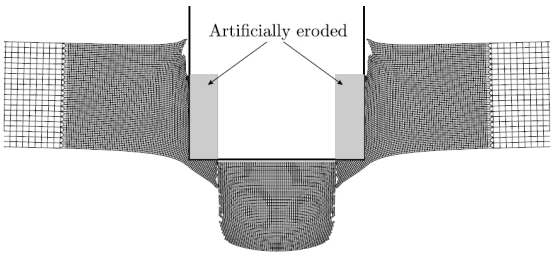

(a) Constant Strain

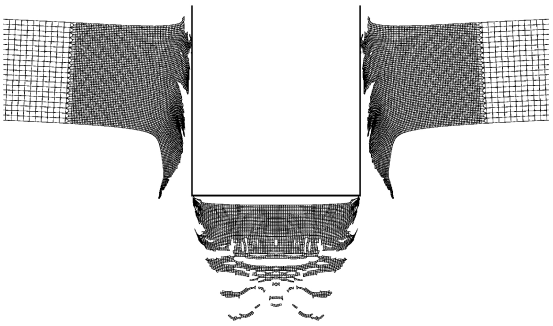

(b) Wilkins

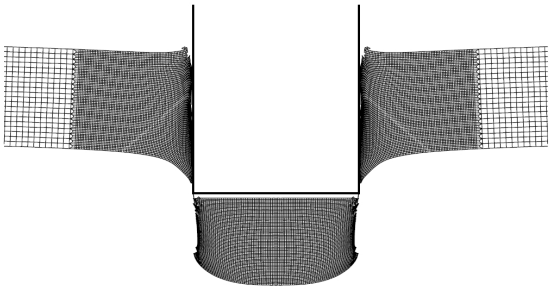

(c) Johnson-Cook

Figure 2.13: Perforation simulation results using the constant fracture strain, Wilkins and Johnson-Cook damage models conducted by Teng and Wierzbicki [13].

The model by Wilkins includes both triaxiality and Lode angle effects. However, in contrast to the experimental results, the model predicted severe spalling in the impact zone. This was due to the compressive impact stress wave reflecting against the free surface and returning as tensile. Damage due to the hydrostatic pressure term tends to infinity as the pressure approaches a critical value. Thus at the position the tensile stress wave meets the compressive, the high pressure difference results in instant failure. The result is shown in figure 2.13b.

The modified Cockroft-Latham fracture criterion also suffered from calibration problems. The complication came in using one damage parameter for the entire model. This parameter can be calibrated for the shear decohesion zone of $-\frac{1}{3} < \eta \leq 0$ and separately for high triaxialities however, over the whole range the curve cannot be fitted adequately. This problem was identified by Bao and Wierzbicki [18] leading to the development of a model consisting of three zones described by different criteria.

In the simulations, two Cockroft-Latham damage values were chosen to test, corresponding to low and high triaxiality respectively. Both are relevant as the material experiences a full range of triaxial loading. The model had a fracture pattern similar to the experiments with a solid plug of material being ejected for both damage parameters. In addition no artificial erosion occurred as a positive principal stress is required to add to the damage integral. However, there were large errors in the residual velocity due to the damage parameter only being applicable to a one region of pressure.

A vast improvement is evident when using the Johnson-Cook fracture model, shown in 2.13c. In this case the form of failure is consistent with the experimental results with the impacted zone forming a clean plug. Part of the success is due to the calibration yielding a high fracture strain in uniaxial compression, similar to the cut-off value of $\eta = -\frac{1}{3}$ found by Bao and Wierzbicki [18]. This prevents elements being artificially eroded under the impact zone as evident in the constant fracture strain model.

This technique proved successful in modelling the perforation as the residual velocities also compared well with the experimental results. However, a caution when using Johnson-Cook, or indeed any model calibrated in the high triaxiality tensile region, is that artificial erosion may occur if the calibrated failure strain in uniaxial compression is low.

A second set of simulations were conducted based on material damage parameters for aluminium 2024-T351 found by Wierzbicki et al. [1]. These results yielded similar results for the models detailed above and in this case the Bao-Wierzbicki damage criterion[3] could be evaluated. The model performed well resulting in a very similar fracture pattern to that using the Johnson-Cook criterion. However, as the model is separated into three distinct regions, the prediction should be accurate throughout the triaxiality range. In contrast a Johnson-Cook model calibrated for high triaxialities results in an excessive failure strain for low to negative triaxialities.

It should be highlighted that although these simulations were based on a dynamic experiment, the material properties were found using quasistatic tests. These models, with the exception of Johnson-Cook do not take strain rate into account which is the focus of this thesis.

2.2.17 Final Evaluation

The core of the research by the BISRU group is blast testing, involving complex loading over a wide band of triaxiality and deviatoric stresses. Thus, one of the priorities for this study is to evaluate or develop a damage model that could characterize materials to be used in blasting.

For this reason the Cockcroft-Latham, fracture forming limit diagram and constant strain models cannot be considered as these are only applicable to a narrow range of triaxial loading.

The continuum based models of McClintock, Rice-Tracey and Gurson were developed by studying the growth of voids and thus are only truly applicable to ductile fracture. Further, the Gurson model, which is the latest iteration of the three, is difficult to calibrate.

The Johnson-Cook model, while simple to calibrate has been shown to exhibit substantially different properties depending on which tests are used for calibration. This results in it only being applicable to a small range of triaxialities despite its success in the perforation tests.

The Wilkins model was shown to correspond reasonably closely to test points, but in high strain rate testing it resulted in false forms of damage developing. Similarly, although the maximum shear model followed its evaluation points closely, it failed under the dynamic loading in the perforation tests.

Thus the two applicable models are the CrachFEM and that developed by Wierzbicki et al. In the evaluation point comparison, the CrachFEM model had marginally worse accuracy than the Wierzbicki-Xue and in application two different fracture loci need to be evaluated at each strain iteration. Thus the Wierzbicki set of models was chosen. These are based on experimental observations and are designed to be relatively easy to calibrate. It was shown to be accurate through all stress states and applicable to high strain rate testing.

The latest iteration, the Bai-Wierzbicki locus is the most general as in contrast to the Wierzbicki-Xue model, symmetry about a triaxiality of zero is not assumed. However, in this case six tests are required for evaluation as opposed to the four used in the symmetry case. As the tests used in this thesis are all of positive triaxiality, the symmetric model is applicable. An additional consideration is whether to use a parabola to model the Lode effect such as used in the Bai-Wierzbicki locus, or to rather use the ellipse implemented in the Wierzbicki-Xue technique. Ultimately the symmetric version of the Bai-Wierzbicki model, with the parabolic function, is implemented as can readily be converted to an asymmetric form if desired.

2.3 Split Hopkinson Pressure Bar

Split Hopkinson pressure bars are used to test material behaviour under high loading rates of between 100 and 10 000 s^{-1} [25]. Certain materials, such as steel, have properties that vary considerably for differing strain rates. These properties cannot be obtained from standard quasistatic tests that typically have strain rates in the order of $10^{-3}\,s^{-1}$. Thus, experimental data is vital in order to properly understand material response under dynamic loading. The split Hopkinson pressure bar has emerged as the standard experimental technique due to its ability to maintain relatively constant strain rates of the order of 1000 s^{-1} [5].

The apparatus development began with Hopkinson [26] in 1914 who developed a method to measure the peak pressure and duration of a stress wave travelling through a long metal rod. The bar was impacted with a projectile and short bars placed at the end to capture momentum. Forty years later Davies [27] improved this technique by replacing the additional short bars with capacitors.

In 1949 Kolsky [28] modified the Hopkinson bar to study the effect of high strain rates on material properties. The design split the Hopkinson bar into two lengths: the 'input bar', onto which the stress wave was applied using a striker, and the 'output bar'. Kolsky placed capacitors around the side of the input bar as well as at the end of the output bar and sandwiched cylindrical specimens between the two. In this way he was able to determine the changes in the stress wave as it passed through the specimen and thus deduce specimen deformation. This apparatus is referred to as the 'Kolsky bar' in some work but, as labelled by Kolsky himself, it is called the 'split Hopkinson pressure bar', or SHB, in this thesis.

This technique has since been refined. High-precision strain gauges have replaced the capacitors and loading is achieved with the use of gas-guns as opposed to detonators. Further, advances in electronics have allowed the use of high-speed digital oscilloscopes and signal conditioners all of which increase the precision of the measurements. However, in essence the compressive split Hopkinson bar as developed by Kolsky remains the same.

2.3.1 Compressive Pulse to Generate Tensile Deformation

Several methods have been developed to create a tensile split Hopkinson pressure bar, or TSHB. The early attempts used a striker to generate a compressive pulse within the input bar. This compressive pulse was then used to create tensile deformation within the specimen.

Tube and Yoke Apparatus

In an initial apparatus designed by Harding, Wood and Campbell [29] in 1960, the input bar was designed as a hollow tube with the specimen attached to the tube via a yoke. A striker was fired at the far end of the tube creating a compressive wave that travelled through the bar. The yoke converted this compressive wave into a tensile wave that travelled through the specimen.

The configuration, shown in figure 2.14, is compact, but at the time two tests were required for each experiment: one to capture the input wave and a second to deform the specimen. Today, with the correct application of strain gauges only one test should be required. However, this complication together with the complex geometry required has led to the development of subsequent techniques.

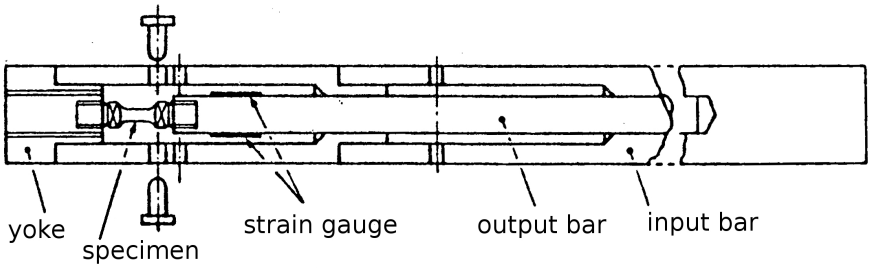

Figure 2.14: Tube and Yoke TSHB designed by Harding et al. [29]. The load is applied to the free end of the input bar, or tube, on the right.

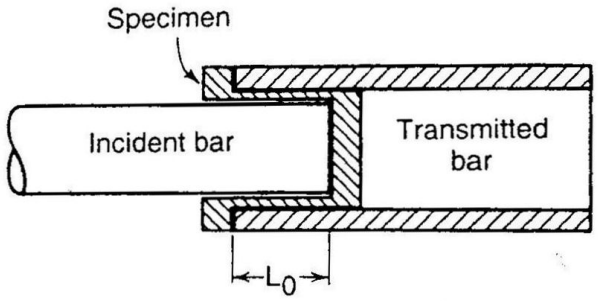

Figure 2.15: 'Hat' shaped specimen proposed by Lindholm and Yeakley [31].

Hat Specimens

Several methods have been developed that are able to use the same striker/gas gun configurations as used in compression tests. However, this has often come at the disadvantage of specimens with complicated geometries that are expensive to machine and introduce additional sources of error [30].

An example is the 'hat' shaped specimens introduced by Lindholm and Yeakley [31]. The setup used is shown in figure 2.15, with the geometry chosen so that the major deformation occurs within the gauge section tube. Complications include the stress concentration zones that form at the fillets as well as friction effects between the specimen gauge section and bars. Although the striker and incident bar can be used in both tension and compression tests, the tension test requires a hollow transmitted bar.

Modified Compression-Collar Bar

Nicholas [32] and Ellwood [33] independently developed a system that utilized the fact that when a compressive wave is reflected at the end of a bar, it returns as a tensile pulse. In the original apparatus the specimen was threaded into the bars, a collar was then fitted around the specimen against both bars as shown in figure 2.16.

When the striker hits the first bar, a compressive wave forms. This wave travels through the collar and specimen, with the collar ensuring that the specimen only strains elastically. The wave then travels through the second bar, reflecting off the

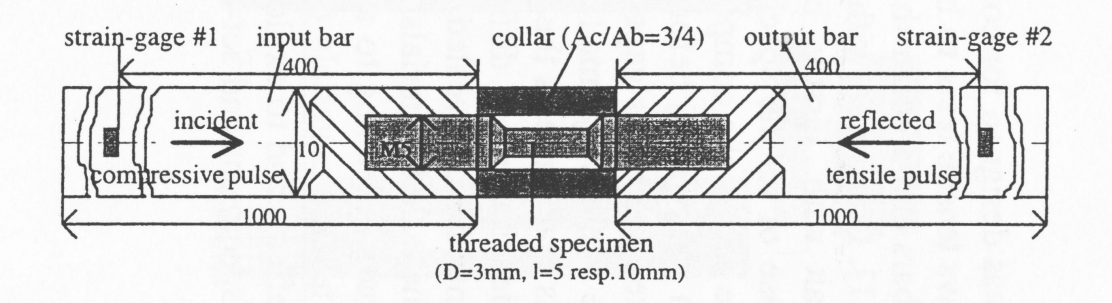

Figure 2.16: Modified compression bar as used by Nicholas [32].

end and returning as a tensile pulse. The specimen is thus subjected to the tensile pulse and strained. Note that the collar is not rigidly connected to the bars and hence cannot support a tensile load.

Ellwood noted that problems with the technique include aligning the collar with the bars and ensuring there is no slack in the threading as errors here create additional oscillations in the reflected pulse [33]. Incorrect alignment may also lead to permanent specimen deformation in compression. These complications make the technique difficult to implement. There is a lack of recent publications using the collar method and thus it is assumed that it is not implemented any more.

2.3.2 Generating a Tensile Pulse Directly

In recent work, the direct tensile bar is the most common approach for TSHB experiments [5]. With this technique a tensile pulse is applied to the input bar and interacts with the specimen in a similar way to that in the compression test.

Stored Energy

One implementation of the direct tensile bar approach is to release a tensile pulse stored in the input bar my means of a clamp as used by Staab and Gilat [34]. In this method, the tensile pulse is steadily generated in a section of the bar by using a hydraulic actuator. Once the stress in the bar reaches a predefined level a bolt breaks releasing the clamp and the tensile stress propagates towards the specimen.

This apparatus was used in the study by Li and Ramesh [35] whose setup is shown in figure 2.17.

An advantage of the design is the constant amplitude of the input pulse. This is relatively free from oscillations as the pulse is 'ramped' over a region of 30 to 40μs. Oscillations are generated due to wave dispersion and this occurs to a greater degree with low rise times[5]. However, as the clamp bolt breaks during each experiment, these have to be replaced.

Tubular Striker with Parallel Gas Gun

An alternative approach to the clamp technique generates the tensile pulse by impacting a flange at the end of the incident bar with a hollow striker. The complication inherent in this method is designing the gas gun/striker combination so that it does not interfere with the incident bar.

A possible configuration was used in the experimental work by Verleysen and Diegrieck [36]. This is referred to as the 'parallel gas gun' technique as the gas gun is placed alongside the input bar, facing in the direction of the flange as shown in figure 2.18. Only the specimens are deformed and thus no parts need replacing. However, the gas gun is placed in parallel with the input bar and not in line as used in compression tests. Hence a major adjustment is required to change between compressive and tensile testing and thus a dedicated tensile SHB station may be required.

Tubular Striker with Reversed Gas Gun

In 2007, Cloete and Downey [37] designed a SHB for the testing of round tensile specimens, depicted in figure 2.19. The novelty of the design lies in its simplicity and compatibility with the gas gun firing rigs of conventional compressive hopkinson bars.
A tensile experiment is run by pressurizing a tubular striker with the gas gun. The pressure is maintained by a plug at the far end of the barrel, inside the striker, and a seal attached to the striker. As the barrel plug is fixed, the pressure acting on the striker forces it to accelerate back towards the gun.

[5]Detailed in section 2.3.3 on page 44.

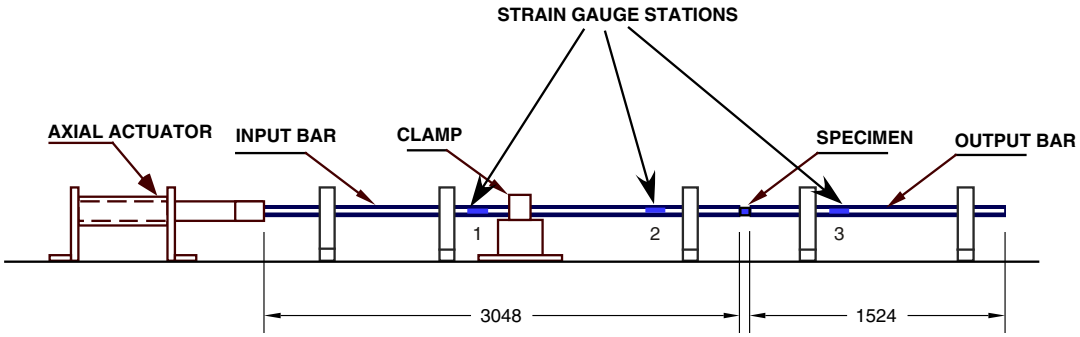

Figure 2.17: Direct tension apparatus using a stored tensile pulse [35].

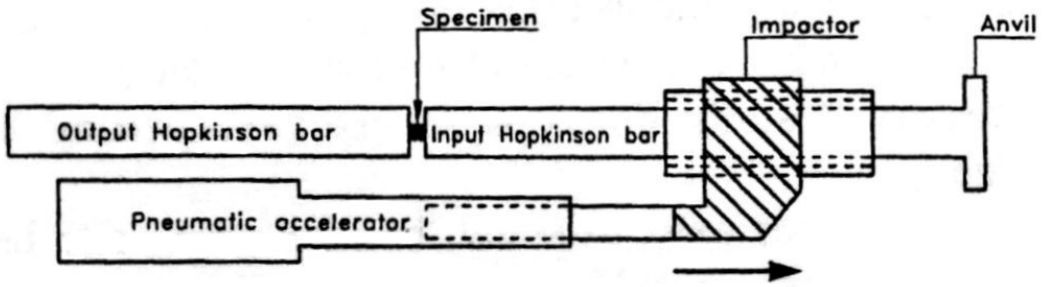

Figure 2.18: Direct tension apparatus using a flanged incident bar [36].

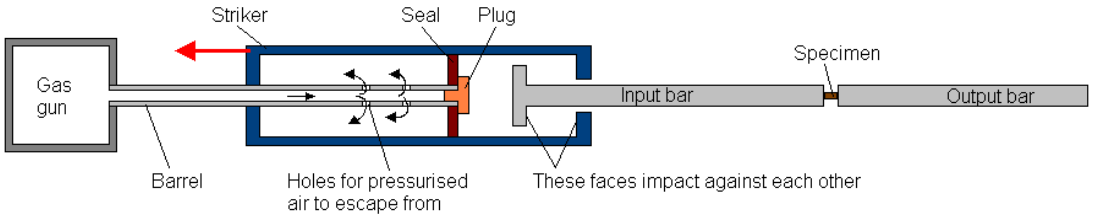

Figure 2.19: Tensile Split Hopkinson Bar designed by Cloete and Downey [37].

A *transfer cap* is attached at the other end of the striker, while a flange of similar size is screwed onto the input bar. Thus when the striker has attained its required velocity the cap collides with the flange, creating a tensile incident pulse.

This design has a significant advantage over the parallel technique as changing between compressive and tensile testing is relatively simple. All that is required is for the striker and barrel to be replaced and the tensile bars aligned and thus a dedicated tensile SHB station is not required.

Tubular Striker Numerical Analysis

A concern with using tubular strikers with either the parallel or reversed gas gun technique is the influence the flanges and caps have on the pulse shape. Thus to quantify this effect a finite element analysis was conducted by Bowden [38]. The study showed that acceptable input pulses could be obtained by using tubular strikers. There are several critical components that need optimization. The first is the size of the transfer cap relative to the flange. If the endcap is too heavy a stress peak occurs at the start of the pulse due to the additional inertia of the component. This problem is exacerbated by using a material with a high density for the transfer cap.

A similar effect was noted for the pressure cap which seals the striker at the gas gun end. If the mass of this component is too large a stress peak occurs at the end of the pulse. In contrast smaller pressure caps have the positive effect of increasing the pulse length. Thus the mass of the endcap, flange and pressure cap should be minimized for an ideal pulse shape.

2.3.3 Dispersion in the SHB

Dispersion in waves travelling along long bars is due to the signals containing components with differing frequencies. The wave propagation velocity, c, is related to the component frequency and thus the pulse shape changes as it travels down the bar [39].

Pochammer[40] and Chree[41] independently found the solution to the equation of motion in an infinite cylindrical solid. This solution showed that the closer the bar radius is to the wavelength, the slower the phase velocity. Thus high frequency components travel at a lower velocity than those at lower frequencies.

Tyas and Watson[42] found that in signals containing only frequency components of low wavelength, dispersion will be low and thus the waves will propagate almost one dimensionally at $c_0 = \sqrt{E/\rho}$. To ensure that pulse propagation is roughly one dimensional, the wavelength, L, and radius, R, are related and limited to $R/L < 0.05 - 0.1$ [42]. Thus the frequency needs to be kept lower for bars with larger diameters.

Many experiments, such as those with impact tests, create higher frequency components. This creates a problem as the component wavelength becomes close to the bar radius. Thus radial inertia begins to have a noticeable influence on component velocity as described by Pochammer and Chree[42]. In terms of the SHPB experiments, this dispersion is evident in oscillations within the strain gauge reading and these oscillations are undesirable as these indicate a variation in loading. This problem is worse at higher strain rates in which the period of oscillation is significant relative to the total strain [5].

A simple method to reduce dispersion is to introduce softened contact. This is implemented by placing a small quantity of soft material such as putty on the impact surface to absorb the high frequency components. However, pulse softening does lead to a longer pulse rise time and thus a compromise needs to be made between the degree of oscillations and the rise time.

2.4 Tensile Test

Tensile testing is complicated by the process of 'necking', a process in which an instability causes localized thinning in the material.

As a neck is formed, the bar radius through the neck decreases significantly. However, material past the neck boundary tends to inhibit this decrease in cross sectional area and thus tensile non-axial stresses arise. Bridgman [6] proposed that as an applied hydrostatic pressure increases material ductility, this hydrostatic

tension due to the non-axial forces decreases ductility, leading to brittle fracture on the axis. This in turn leads to the classic *cup and cone* fracture as the break at the axis spreads outwards until the specimen is sufficiently deformed and shear failure begins to dominate towards the outer surface.

The condition for necking is presented succinctly in the Considère criterion[43], published in 1885. This states that necking occurs when the true hardening rate equals the true stress

$$\frac{d\sigma}{d\epsilon} = \sigma \tag{2.35}$$

In essence, as a material hardens due to plastic deformation the hardening rate decreases and the minimum cross-sectional area is reduced. The load is related to the area through,

$$\sigma = \frac{F}{A}$$

with F the reaction force and A the area. Thus for a constant force and perfectly plastic material the load decreases with the reduction in area. However, for a non-perfectly plastic material, hardening results in an increase in load. Eventually the load reduction rate due to the change in area exceeds the increase due to hardening. At this stage the maximum load is reached and an unstable situation exists. Localization occurs with elastic recovery in the regions not affected.

In ductile tensile tests four points can be identified, plastic yield, diffuse necking, localized necking and finally fracture. The process is shown in figure 2.20. Diffuse necking occurs when the Considère criterion is met, while local necking occurs just prior to fracture[44].

Hydrostatic tension within the necked region complicates the stress measurement and calculation as it leads to an overestimation of flow stress and thus of hardening. However, Bridgeman was able to develop a simple correction formula, based on the geometry of the neck, to determine true tress.

$$f_{bridgman} = \left[\left(1 + 2\frac{R}{a}\right)\log\left(1 + \frac{a}{2R}\right)\right]^{-1} \tag{2.36}$$

where a is the bar radius at the neck centre and R is the radius of the neck groove as shown in figure 2.21.

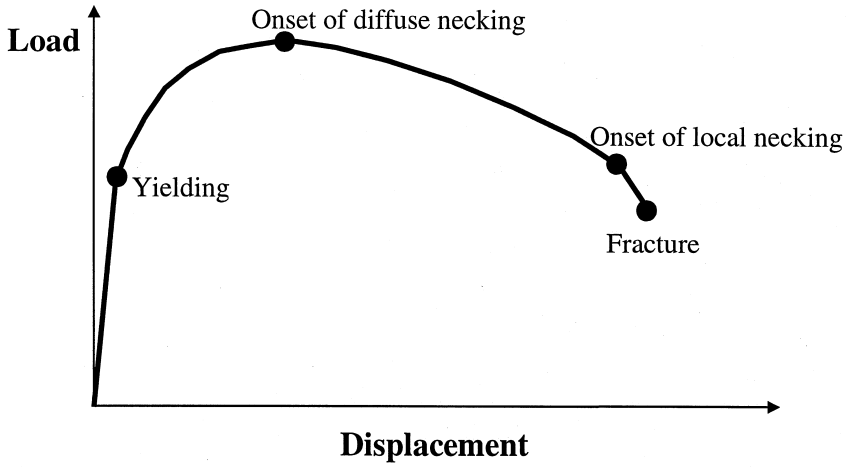

Figure 2.20: Load displacement graph for a typical tension test[44].

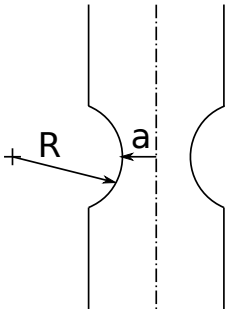

Figure 2.21: Neck dimensions used for the Bridgeman correction factor.

Implementation was simplified by the estimation of the geometric ratio by Roy et al. [45], which related it to the current strain and the strain at maximum load, ϵ_{Pmax},

$$\frac{a}{R} = 1.1\,(\epsilon - \epsilon_{Pmax}) \tag{2.37}$$

More recently, Zhang et al. [44], in 1999, attempted to address the same issue for sheet specimens which have rectangular cross sections and unlike round specimens undergo cross-section shape changes during deformation. In a numerical study on sheet specimens, Zhang et al. noticed two forms of localized necking related to the aspect ratio of width, w to thickness, t,

$$S = \frac{w}{t}$$

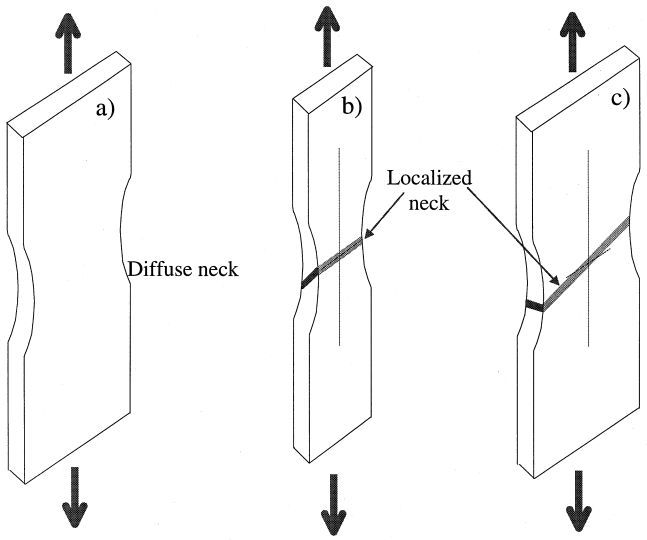

Figure 2.22: Tensile neck formation beginning with (a) diffuse necking followed by (b) localized necking with low aspect ratio and strong hardening or (c) high aspect ratio and low hardening[44].

For a specimen with a low ratio and strong hardening, the localization occurs at an angle across the thickness, shown in figure 2.22. In contrast, wider specimens with a high aspect ratio, but low hardening localized across the width. Thus the geometry of the cross section plays a key role in the form damage takes.

All specimens with different aspect ratios produced the same average true stress-true strain profile before necking as round bars and thus it was concluded that the Bridgman correction is still applicable. The problem is determining the shape of the cross section post necking.

Zhang et al. proposed that the shape change could be split into a proportional volume change, A_p and a non-proportional shape change, A_s

$$\frac{\Delta A}{A_o} = \frac{\Delta A_p}{A_o} - \frac{\Delta A_s}{A_o} \tag{2.38}$$

with the proportional term given by

$$\frac{\Delta A_p}{A_o} = 2\left(\frac{\Delta t}{t_o}\right) - \left(\frac{\Delta t}{t_o}\right)^2 \tag{2.39}$$

and the non-proportional by

$$\frac{\Delta A_s}{A_o} = f_s(S) \cdot f_t(x) \cdot f_m(y) \tag{2.40}$$

A_o and t_o refer to the initial area and thickness respectively, while x and y are related to the current thickness ratio and that at maximum load

$$x = \frac{\Delta t}{t_o} - \left(\frac{\Delta t}{t_o}\right)_{Pmax} \qquad\qquad y = \left(\frac{\Delta t}{t_o}\right)_{Pmax}$$

The function f_s relates the area ratio to the aspect ratio, f_t relates the area ratio to the thickness ratio and f_m is related to the material properties. These functions have been found through curve fitting in [44]. However, the reliance on the latter two to the change in thickness is problematic. This can be determined in a quasistatic tests using an extensiometer, but not in a dynamic Split Hopkinson Bar test.

An alternative approach was taken by Bao and Wierzbicki [7] in a 2004 study. In this case, instead of attempting to estimate the change in specimen shape during necking, an iterative simulation process was used in which the material properties were altered until the deformed shape as well as the reaction force versus displacement of the model matched that in the experiments. The method is time consuming as several simulation runs are required, but allows flexibility for specimens with complex designs such as notches to be tested without knowing the materials hardening characteristics beforehand.

2.5 Specimen Design

To calibrate and analyse a damage model, tests are required from several different regions of triaxiality and Lode angle. For example the Xue-Wierzbicki requires tests from four positions and the more general Bai-Wierzbicki model uses six. Figure 2.23 is a useful diagram that shows a range of tests plotted against Lode Angle and triaxiality. Ideally tests should be taken from a wide range of these points.

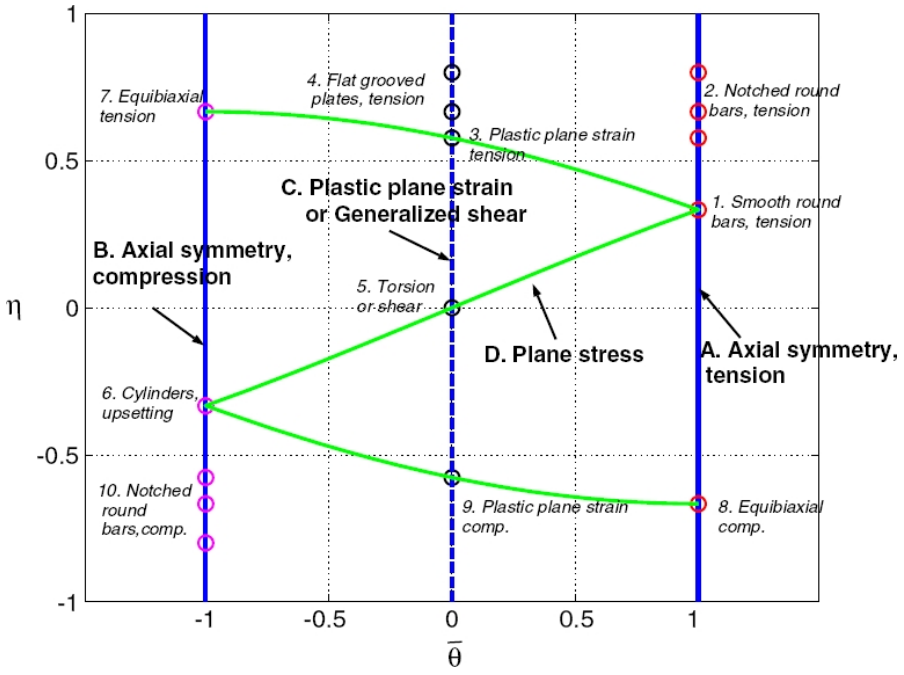

Figure 2.23: Calibration tests plotted relative to triaxiality and Lode angle [17].

2.5.1 Tension

In calibrating the Bai-Wierzbicki model, Bai and Wierzbicki [17] used two sets of tensile tests. The first were round specimens which have a normalized Lode angle of $\bar{\theta} = 1$, shown in figure 2.24a. Straight round specimens have an initial triaxiality of $\frac{1}{3}$, but this can be increased by machining notches into the cross-section [3]. The material outside the notch limits radial deformation, creating non-axial stress and thus increased triaxiality. Although not mentioned, a similar effect should be able to be achieved with dogbone sheet specimens.

The second set used flat, grooved specimens with $\bar{\theta} = 0$ shown in 2.24b. These have a large lateral dimension, which tends to limit transverse deformation. Thus the loading condition is approximately plane strain. To vary the triaxiality angle, the grooves were made with differing radii[17].

(a) Tensile round

(b) Tensile flat

(c) Upsetting

(d) Pure Shear

(e) Combined loading

(f) Butterfly

Figure 2.24: Specimens used to calibrate the Bai-Wierzbicki model [17].

2.5.2 Compression

Cylindrical compression tests have a normalized Lode of -1 and negative triaxialities. In damage testing the experiments are termed *'upsetting tests'*. In these friction between the compressive platens and the short specimens causes barrelling to occur. This creates tensile circumferential stresses that result in failure on the specimen outer surface [3]. However, the test is not practical with sheet metal because the specimens would have to be too small.

2.5.3 Shear

From figure 2.23 it is clear that a pure shear test is useful as it is located at the origin of both the triaxiality and Lode axes. Bao and Wierzbicki [3] developed a specimen designed to test for pure shear. These involved a central shear zone with a grip section attached on either side and pulled in opposite directions as shown in figure 2.24d. These were then modified by angling the shear zone, imposing a combined tensile-shear load. The combined tensile-shear concept is particularly useful as it allows for tests in the transition triaxialities of 0 to 0.4 as detailed in section 2.2.13.

2.5.4 Combined

The configuration suggested by Bai and Wierzbicki [17] is the *'butterfly specimen'* shown in 2.24f. The main advantage is that the specimen can be placed under several different loading conditions, with the fracture location constant for all. In total Bai and Wierzbicki tested 8 different loading conditions on a biaxial test rig with successful results. A further advantage is that it does not correspond only to the limiting Lode angle cases of -1, 0 and 1 as occurs in the conventional specimens. However, this specimen would be difficult to test using a SHB rig.

2.5.5 Tensile Specimen Design Issues

Geometry

Unlike in compression, tensile specimens undergo a large degree of stress localization through the process of necking. This provides a complication for Hopkinson tests as only the axial displacement history of the specimen ends are known from the tests[6]. The complications can be broadly split into two groups, which relate to measuring the correct load and strain.

Load Measurement
One consideration may be to allow necking to develop fully as the Bridgman correction factor can then be applied. In 1915, Upton (as reported by Davis et al. [46]) found that round specimens with aspect ratios of length to diameter, $\frac{L}{D}$, two and greater had the same area reduction within the localized zone. With lower aspect ratios lateral restraint is placed on the gauge section by the transition zone which is the region between where the specimen is gripped and the gauge section.

In a more recent study Matic, Kirby and Jones [47] conducted experimental and numerical tests on steel with similar findings. It was reported that specimens with an aspect ratio of 1.67 and greater followed same stress strain profile up to necking, while lower ratios resulted in an overestimation of material strength. This again is due to the non-axial stresses caused by the lateral restraint of the transition zones.

In 2007 Bowden [38] conducted a finite element analysis of the Tensile Split Hopkinson Test. The round tensile specimens provided similar results to the quasistatic tests of Davis and Matic et al. with an aspect ratio of two or greater required to prevent a large overestimation of material strength. In this study it was shown that the error was due to non-axial stresses within the transition zone.

Strain Measurement
A further problem relates to the size of the transition zone as with low aspect ratios the strain within this region became significant. As a Hopkinson test calculates the displacement at the specimen ends, it is impossible to determine strain in the gauge section relative to the transition zone without running parallel numerical simulations. Ideally this transition zone effect should be minimized, which occurs

[6]Explained fully in section 2.4 on page 45

with $\frac{L}{D} \geq 1.6$ [38]. The influence of the transition zone radius size was also considered, but was found not to have nearly as significant an effect.

Verleysen et al. [48] conducted a similar study and found that with sheet specimens the transition radius had a far greater effect . For specimens 5mm long by 4mm wide a 1mm radius accounted for 17% of total strain increasing rapidly with a 2mm radius resulting in 29%. This was supported by experimental work conducted by Verleysen and Degrieck [36] which, using a high speed camera to track specimen deformation, found that the strain along the specimen was not constant due to strain within the transition zones. Thus the TSHB test overestimates strain prior to necking due to the transition round and then underestimates post necking due to localization.

A caution with using too small radii was included in a later study by Verleysen et al. [49]. This noted that non-axial stresses caused by the transition zone, which are greater for sharper transition radii, tend to decrease strain through the material. However, with a large gauge section this should not be restrictive on necking, as Upton found (reported by Davis et al. [46]).

If parallel numerical work is conducted, the material properties obtained from the TSHB data can be iteratively adjusted until the bar displacements in the simulation match those of the test. This process was followed by Bao and Wierzbicki [3] among others who reported success. A further advantage is that the material characteristics can be obtained from specimens with complex geometries. However, there is the possibility that by tailoring material parameters to fit the experimental data, errors due to the mesh or modelled geometry could be hidden. If the fitted model applies well to a range of different specimens, the risk of a major calibration error is minimal.

Securing the Specimen

The methods to secure the specimen refer here to the dynamic SHB tests as standard clamps are used to grip quasistatic specimen. Downey [50] tested axisymmetric specimens with threaded attachment zones as shown in figure 2.25. This is a conventional method used successfully by Li and Ramesh [35] and Rodríguez et al. [51] among others.

Figure 2.25: Tensile specimen used by Downey [50].

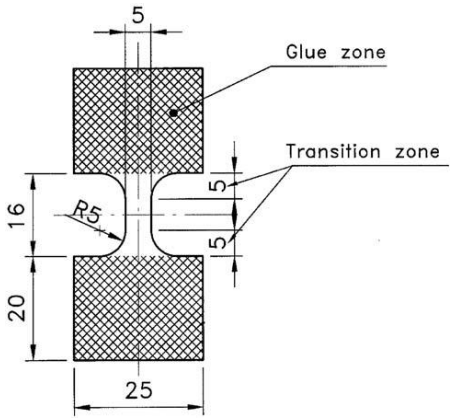

Figure 2.26: Tensile sheet specimen design used by Verleysen and Degrieck [36].

Close to the transition zone, flats were machined to allow the specimens to be gripped easily and screwed into the Split Hopkinson bars. Parallel finite element analysis on the design by Bowden [38] showed that the effect of the flats on capturing material properties was insignificant for flat lengths less than 5mm on a $\phi 10\,\text{mm}$ specimen. However, large oscillations due to wave reflections within the region were evident for a specimen with a 15mm flat.

In the FEA model, the thread interaction was simplified as simply a nodal tie between the specimen and bars. With this method, the length of the thread did not have a significant effect on the results with only an unrealistic length of 2mm altering the resulting material stress strain curve drastically. Oscillations were noted when steel specimens were placed in aluminium bars, but these were minimized with thread lengths of around 15mm and over. However, although it was not studied, the interaction of the thread itself may reduce the quality of the results further.

In the series of tests on sheet specimens, Verleysen and Degrieck [36] glued the specimens directly into slots in the bars. To ensure that the glue bond was strong enough, the glue zone was significantly larger than the specimen gauge zone as

illustrated in figure 2.26. The advantage of the method is that no end fixtures other than the slots cut into the bars are required. However, the setup time between experiments is presumably significant as each specimen needs to be glued into the bars, tested and then removed in series.

2.6 Numerical Simulation

2.6.1 Tensile Split Hopkinson Tests

Basic Setup

Verleysen et al. [49, 52] modelled the split Hopkinson bar experiment to determine the influence of tensile specimen geometry. The models used bars long enough to prevent the reflected stress from interfering with the specimens, with a 2m length required. $\frac{1}{4}$ symmetry reduced the number of elements and hence computation time. The applicable integration scheme for dynamic experiments such as these is an explicit analysis as the computational cost for each step is low. The disadvantage is that small time steps are required. However, as the simulations need to run for only a short time period it is by far the most efficient.

Emphasis was placed on keeping a high mesh density in the region surrounding the specimen while leaving the remainder of the bars relatively coarse. This was deemed acceptable as the bars were only required to transmit the load onto the specimen [49]. Verleysen et al. used eight noded continuum elements with reduced integration and hourglass control and argued that these are relevant type for modelling a highly dynamic process with 3D elements [49]. A similar system was used by Rodríguez et al. [51] among others.

Infinite Elements

The stable time increment is dependent on the size of the smallest elements in the specimen and this affects all elements including those of the long bars. Despite this complication, most of the published work on simulating the SHB test report modelling the entire bars (see for example [49]). However, a promising technique

was implemented by Kammerer and Neme [53]. In the work 'semi-infinite' elements replaced the bars by absorbing the reflected waves. The major advantage is that the simulation only has to run for the time required to deform the specimen, not for that taken by the stress waves to move along the bars. Furthermore the element count is significantly reduced.

This technique is successfully implemented in this thesis and is covered in chapter 4.

Applying the Load

Instead of simulating a striker to create the input pulse, Rodríguez et al. [51] loaded the specimen directly by placing a simplified velocity profile modelled on that recorded experimentally onto one specimen edge. The pulse was shaped as a trapezoid with a rise and fall time of 60 and 40μs respectively and a total duration of 220μs. Allowing for a rise and fall reduces dispersion as the wave travels along the bars. Dispersion results in oscillations within the stress wave and thus should be minimized[7].

Applying a load directly to the specimen is simple and minimizes the element count and computational cost. However, the method is flawed as it does not take into account the stress waves generated due to the velocity boundary condition. Thus any error in material properties results in significant oscillations in the specimen loading stress. Chapter 4 considers the technique in detail and found it to be unsuitable for an accurate simulation.

A far better technique was implemented Bowden [38] in which a stress wave was applied directly to the striker end of the input bar. This accurately replicates the entire SHB experiment. The load was modelled as a sinusoidal stress pulse with a plateau region at its peak. This was presented as a simple method of creating a pulse with no gradient discontinuities and thus minimal dispersion.

Perhaps more applicable to this work is to include a loading pulse derived directly from the incident pulse[8], such as used successfully by Verleysen et al. [49]. The advantage is accuracy in that the exact incident pulse should replicate the experimental loading conditions more closely.

[7] Covered in section 2.3.3.

[8] The incident pulse is that generated by the striker. The SHB process is covered in detail in appendix A.

Specimen Interaction

To model the thread contact, Li and Ramesh[35] used contact pairs defined between the threaded section and the bars. This was implemented successfully by Bowden [38] among others, nevertheless it is a simplification as it ignores possible movement between the threads. The error due to this approximation needs thorough analysis.

Verleysen et al. [49] used glue to attach sheet specimens to the bars. The glue-specimen interaction was defined simply as a tie interaction. This defines the nodes on one surface to follow the same displacements as the mating surface. The end of the specimen were not tied as it was thought unlikely that the glue would withstand the high direct tensile stresses resulting in the region. Although some deformation would occur within the glue zone, this was argued to be minimal. However, the advantage of using a tied connection is that it can easily be replaced by a mode accurate interaction at a later stage[49].

2.6.2 Specimen Material Properties

Verleysen et al. [49] used an elasto-plasticity model that included isotropic hardening to model tensile sheet specimens. The plasticity properties were determined using quasistatic experimental tests and included in tabular format as equivalent stress versus strain. However, as the simulations used dynamic testing, temperature and strain rate need to be included.

A more thorough approach was taken by Bonorchis [54] who compared the simulation specimen stress to that determined experimentally and iteratively changed the material properties until the model corresponded to the experimental results for a wide range of strain rates. This model took into account strain, strain rate and temperature.

A similar iterative process was used by Bao and Wierzbicki [7] to determine the plasticity curve for round and notched tensile specimens. As these were all quasistatic, the rate and temperature effects were not significant and thus the derived stress-strain curve could be input directly.

2.6.3 Specimen Model

Bai and Wierzbicki [17] used $\frac{1}{8}$ symmetry to model quasistatic experiments with grooved flat plates . This technique assumes that the specimen is always in perfect equilibrium and thus is not applicable to the split Hopkinson tests. However, it does minimize the element count for the long running quasistatic tests.

To further decrease the quasistatic run time, Bonorchis [54] among others successfully used mass scaling. This artificially increases element material density, which in turn allows for a lower wave speed and thus greater critical time step, defined as the maximum allowable time increment of an explicit step. Bonorchis found that in modelling mild steel, mass scaling of between 5 and 625 times the initial density was acceptable[9].

In damage simulation, Bai and Wierzbicki [17] found that an axisymmetric mesh with an element size of 0.1mm gave results with an difference of only 0.5% in force-displacement response to that using 0.2mm long elements, indicating convergence. In the final calibrations, the denser mesh of 0.1mm was used. The same density was used by Bai et al. [55] in damage analysis.

To ensure failure occurred in the centre of the gauge zone, Zhang et al. [44] introduced a small imperfection with dimensions of 0.4% specimen width and a notch radius 12 times the thickness to trigger necking. However, the method is not common in the literature. In experimental testing, specimens with small gauge sections fail in the centre due to the restraining influence of the transition radii, from the grip to the gauge section, having the least effect at this point. For larger gauge sections, the influence is low in a large central region and thus necking may occur away from the centre due to a small imperfection. In contrast, a numerical analysis with no imperfections should still predict failure in the centre as the transition radius has the lowest influence at that position.

[9]This is explained fully in the simulation procedure, chapter 4.

Chapter 3

Apparatus Design

3.1 Introduction

This chapter includes all the design and testing work for the experimental tests.

The first section details the design of the tensile split Hopkinson apparatus. The solutions uses a tubular striker with a reversed gas gun to create the incident pulse. Section 2.3 of the literature review found that this technique is favourable as it is requires little modification to the existing compression SHB station.

The second section covers the specimen design. The aim in the design was to create specimens with a wide range of triaxiality and Lode angle. The method of attaching the dynamic specimens to the split Hopkinson bars is also covered.

The final section considers the design of the gluing jig used to prepare specimens to be secured to the TSHB apparatus.

3.2 Tensile Split Hopkinson Bar

The configuration chosen for the tensile rig uses a tubular striker based on that designed by Cloete and Downey [37][10]. This design, shown in figure 3.1, was selected as it can be assembled on the same Hopkinson bar station as a compressive rig. Little modification is required to the conventional compressive SHB apparatus

[10]Considered in detail along with several other configurations in section 2.3.

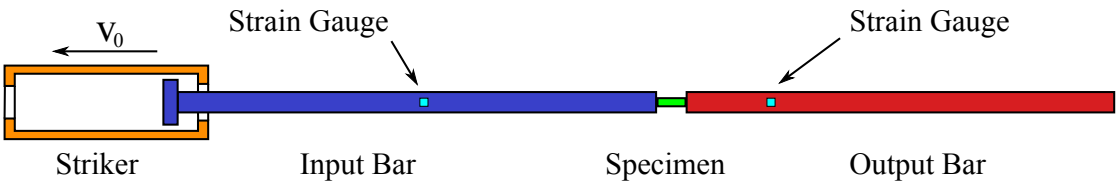

Figure 3.1: Schematic of the tensile split Hopkinson bar using a tubular striker.

as the same gas gun orientation is used and thus changing between compressive and tensile testing can be completed relatively fast. Furthermore, in comparison to many options considered in the literature, the apparatus and specimens are simple to manufacture. This section considers the design process, while detailed drawings are included in appendix C.

The operation, shown in figure 3.2, is as follows:

1. Pressure built up in a gas gun is released through the barrel.
2. The striker is positioned to slide over the barrel and is sealed by a plug on the barrel and a pressure cap at its far end. Thus as air flows through holes in the barrel, pressure builds up behind the pressure cap and moves the striker back towards the gun.
3. After sliding a set distance, the transfer cap on the striker connects with the transfer flange on the input bar.
4. The impact generates a tensile stress wave that travels along the input bar, specimen and output bar.

Strain gauges positioned on the input and output bars record the changes in stress due to the specimen deformation and thus the forces and displacement through the specimen are determined. For a more detailed analysis of the split Hopkinson bar fundamentals see appendix A.

The final design is shown in figure 3.3, with photographs of the bars and striker following in figure 3.4. The striker and bars slide through Teflon bushes and these are contained by clamps, tightened securely to an I-beam. The clamps ensure that the bars do not move out of alignment. The photographs indicate the large scale of the apparatus, which is roughly 9m long in total.

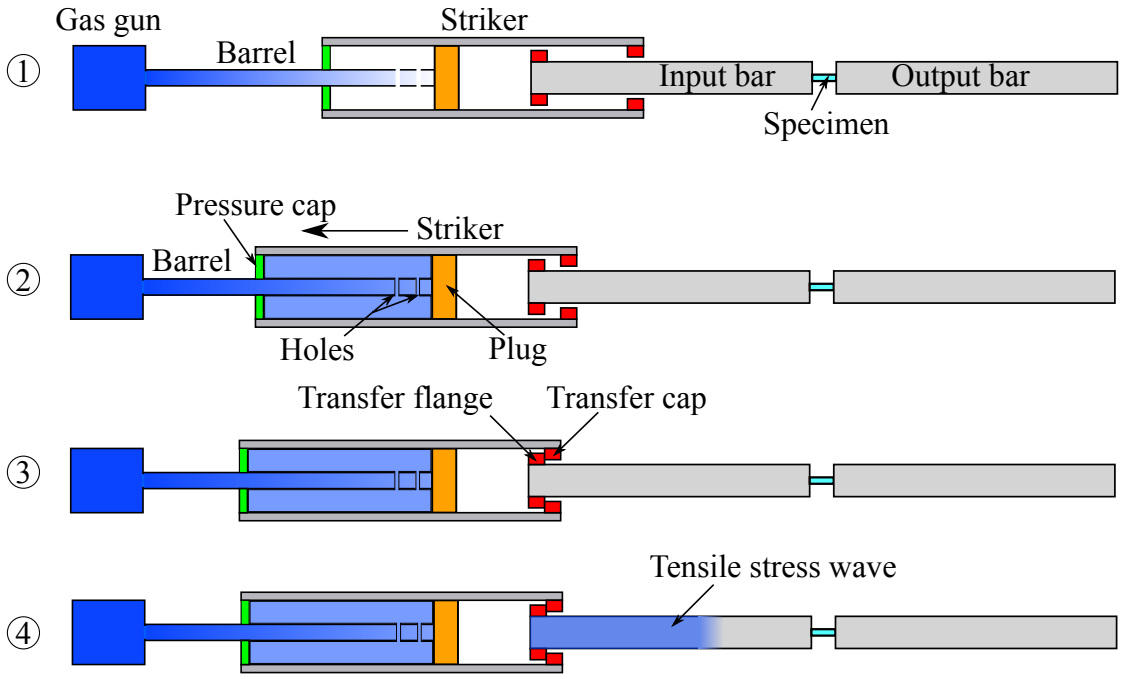

Figure 3.2: Striker interaction with impact bar. The pressure from the gas gun (1) forces the striker to move (2) and impact against the input bar (3). This generates tensile pulse, which travels towards the specimen (4).

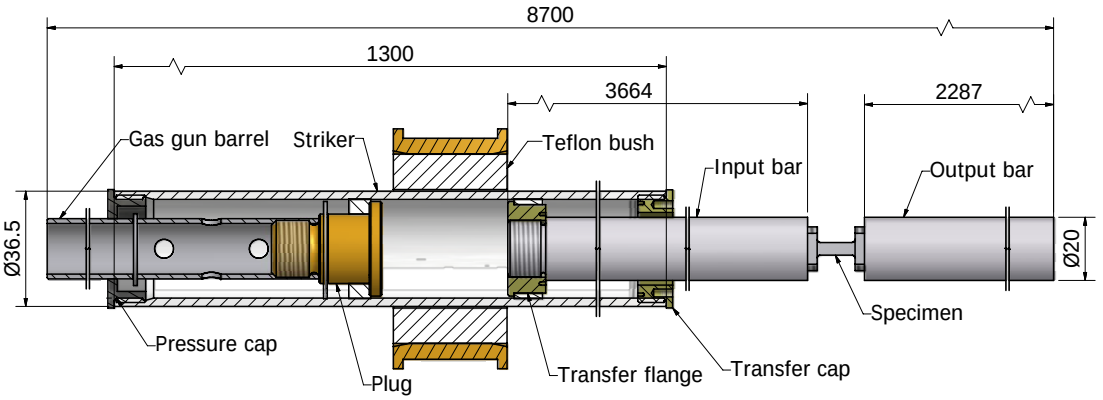

Figure 3.3: Final TSHB design. The total length includes the gas gun (not shown).

(a) Full rig

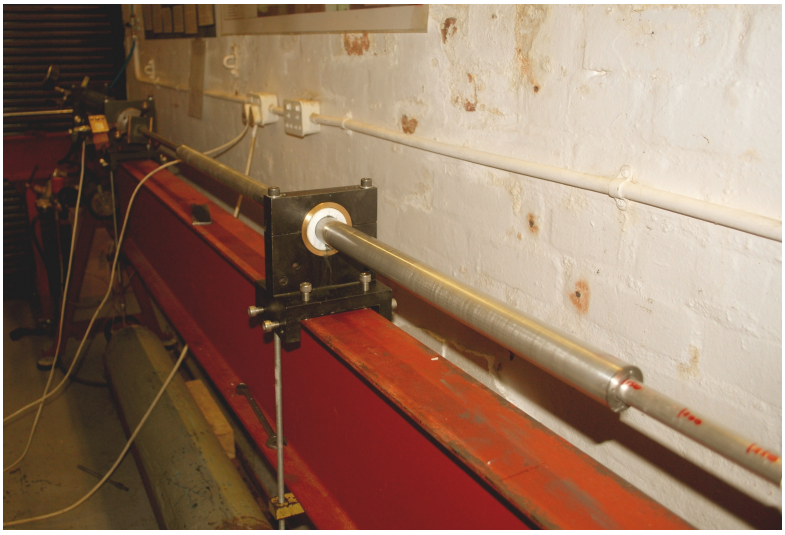

(b) Striker

Figure 3.4: Photographs of the TSHB apparatus.

3.2.1 Striker

Length

The requirement on the tensile rig is to deform specimens to the extent that damage occurs. Thus the rig needs to produce a stress input pulse long enough for specimen damage to occur. Pulse duration, t_P, is directly related to striker length, L_s, through

$$t_P = \frac{2 \cdot L_s}{c} \tag{3.1}$$

where c refers to the wavespeed of the material given by $c = \sqrt{\frac{E}{\rho}}$. Both the striker and input bars are made from aluminium, resulting in a wavespeed of

$$c \approx \sqrt{\frac{70 \times 10^9}{2800}} = 5000\,\mathrm{m.s^{-1}}$$

The striker length is limited by the length of the input bar. To capture the full incident and reflected pulses separately using only one strain gauge, the incident pulse must be fully captured by the time the stress wave reflects back from the specimen and reaches the gauge.

As the input pulse length is nominally twice that of the striker, a strain gauge positioned midway along the input bar should receive both signals separately if the bar length is twice that of the striker, $L_i \geq 2 \cdot L_s$. This is shown schematically in figure 3.5.

The length of the available input bar was $L_i = 3.66\,\mathrm{m}$, resulting in a maximum striker length of $L_s = 1.83\,\mathrm{m}$. However, the generated signal is not perfectly square. To reduce the effects of wave dispersion, a small quantity of putty is placed on the flange. This softens the impact to damp the oscillations visible on the stress pulses, yet adds an estimated combined pulse rise and fall time of $10\,\mu(s)$.

The additional pulse length reduces the gap between pulses by,

$$L = 2 \cdot t \cdot c = 2 \cdot 10 \times 10^{-6} \cdot 5000 = 0.1\,\mathrm{m}$$

Thus to ensure adequate pulse separation, a 1.6m striker tube with a pulse duration of $640\,\mu$s was built.

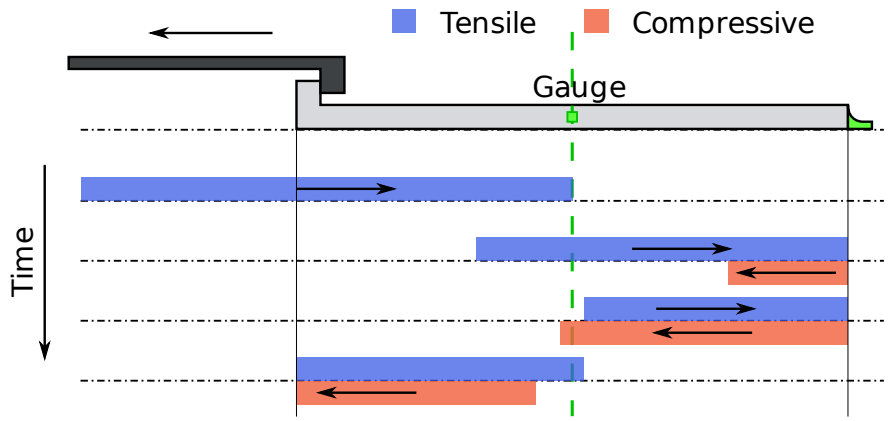

Figure 3.5: Stress wave propagation through the input bar.

In testing, the rise time was greater than expected due to the interaction of the transfer cap with the flange. Ultimately the rise and fall times are approximately 60 μs,which is 50 μs greater than predicted. Thus the length had to be decreased by a minimum of,

$$\Delta L_s = \frac{\Delta t_P \cdot c}{2} = \frac{2 \cdot 50 \times 10^{-6} \cdot 5000}{2} = 0.25m$$

The final striker was conservatively built with a total length of 1.3 m. This proved ideal as it produces an incident wave with a clear separation as shown in figure 3.6.The pulse remains relatively constant at its peak value for roughly 470 μs and, if the rise and fall time is included, the pulse is approximately 590 μs in total.

As a precaution, in case the 1.3 m would not be long enough to fracture all the specimens, a third striker of length 1.45 m was manufactured. Figure 3.6 shows that for this striker, the pulse separation is not perfectly distinct. However, if no pulse smoothing putty is applied, the separation is large enough to conduct TSHB experiments.

A further success of this striker is the smooth incident pulse generated. This is a significant improvement on the previous iteration built by Downey [50] as in that case significant oscillations were evident in the pulse due to the transfer cap, flange and pressure cap. The improvements made to optimize the pulse are included in section 3.2.2.

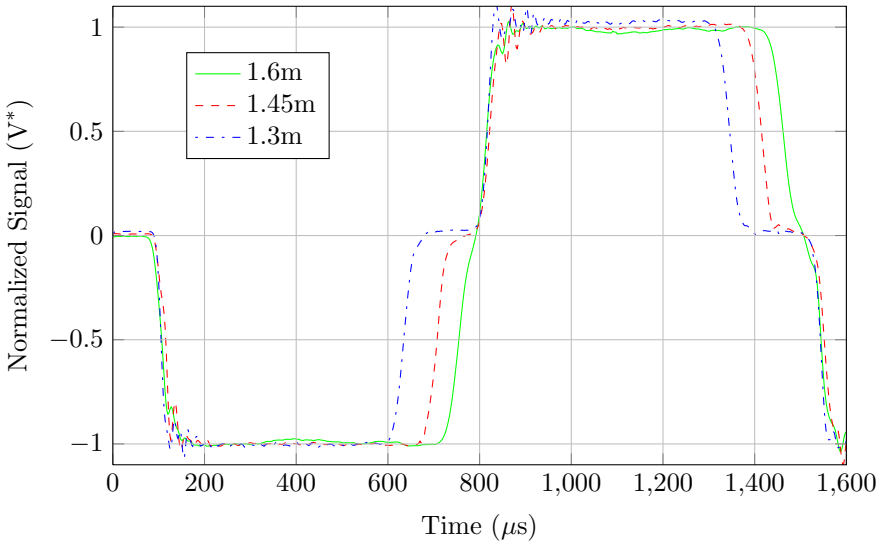

Figure 3.6: Effect of striker length on the incident pulse with no softening. A 1.3m striker was ultimately chosen as the separation between incident and reflected pulse is clear.

Cross-sectional Area

When the striker impacts the incident bar, tensile stress is formed at the contact area. For bars of uniform material properties, the stress at the interface is divided between the striker and input bar relative to the areas of each,[11]

$$\sigma_s = \frac{A_i}{A_i + A_s}\rho c v_s \qquad \sigma_i = \frac{A_s}{A_i + A_s}\rho c v_s \tag{3.2}$$

with σ_s and the σ_i the striker and input bar stress respectively. The variables ρ, c and v_s refer to the density, wavespeed and striker velocity. Thus the greater the area of the striker relative to the input bar, the greater the input bar stress. However, if the striker cross-sectional area is greater than that of the input bar, two or more wave reflections are required before the striker comes to rest[12]. This is undesirable as it results in an input pulse that steps incrementally down to zero, instead of decreasing from the peak to zero in one step.

[11] Derived in section A.3.1.
[12] Explained in detail in section A.3.2.

Clearly the cross-sectional area of the striker must not exceed that of the input bar and ideally to maximize the magnitude of the incident pulse the areas should be equal.

$$\frac{A_s}{A_i} \leq 1 \qquad \therefore \pi \left(D_{outer}^2 - D_{inner}^2\right) \leq d_i^2$$

where D refers to the striker and d to the input bar. As the input bar available is sized as 19.05 mm, a combination of a standard inner diameter of $D_{inner} = 31.75\,mm$ with a machined down outer diameter of 37.0mm results in both the striker and input bar having equal areas. However, as a conservative measure, the outer diameter was ultimately machined to 36.5mm in diameter. This results in an acceptable ratio of $\frac{A_s}{A_i} = 0.9$

Velocity Range

For strikers having the same material as the input bars and an area ratio of 0.9 as shown above, the required collision velocity is derived from equation 3.2 as,

$$\begin{aligned} v_s &= \frac{A_i + A_s}{A_s}\frac{\sigma_i}{\rho c} \\ &= 2.111\frac{\sigma_i}{\rho c} \end{aligned} \tag{3.3}$$

As a rough guide to ensure that the strain gauges do not get damaged this stress should be kept below 200 MPa [50], resulting in a maximum striker velocity of $\approx 30\,\mathrm{m.s^{-1}}$. Using this velocity, the maximum strain rate[13] is found through [25],

$$\dot{\epsilon} \leq \frac{v_s}{l_0} \tag{3.4}$$

where l_0 is the specimen length. Thus a 5mm specimen could attain a maximum strain rate of $6000\mathrm{s^{-1}}$, while a 10mm specimen is capped at $3000\mathrm{s^{-1}}$. Using this potential strain rate, maximum strain is calculated by $\epsilon = \dot{\epsilon} \cdot t_P$. A strain of ≈ 1.6 is achievable for the 10mm specimen. This should be more than adequate to fracture most materials, but can be increased to 3.2 for short specimens of 5mm length.

[13]Strain rate in this sense refers to average strain across the entire gauge length, the critical regions in necked specimens may experience far greater strain rates.

3.2.2 Striker-Input bar Interaction

To form the incident pulse the striker transfer cap collides with a flange screwed onto the input bar. Adding the flange and cap complicates the interaction as the additional inertia has been found to create a signal spike at the start of the signal followed by increased oscillations [38].

The effect is reduced if the cross-sectional area of both pieces is similar. Indeed in tensile tests conducted by Downey [50] using his rig, the spike is evident, but not excessive, even though steel with a much higher density than the aluminium bars was used for the flange and cap.

To minimize the effect both are manufactured out of titanium. This material has the advantage of being relatively lightweight and thus having low inertia. Using cheaper aluminium would have been acceptable from a mass consideration, but connecting two aluminium parts together may result in bonding between the two. As the cap needs to be removed easily to add the pulse smoothing putty for each test, bonding would present a major problem.

The components used to create the tensile pulse are shown in figure 3.7. Note that to remove the stress concentration from the first thread, a circumferential groove is cut into the impact face of both the flange and cap. This same technique was used in [50].

Bowden [38] found similar inertia effects due to the pressure cap at the other end of the striker. However, this piece is only used to trap the gas gun air and is not subjected to the large impact stresses that the transfer cap and flange need to withstand. Thus the cap, shown in figure 3.7, is made out of high density polyethylene (HDPE), with negligible mass.

No seals are required on the plug or pressure cap and free running fits are specified on the interacting parts between striker and barrel as the time required to pressurize the striker is too low for significant leakage. The lack of seals is an advantage as it allows the air to vent and thus prevents repeated impact.

(a) Transfer cap (b) Transfer flange (c) Pressure cap

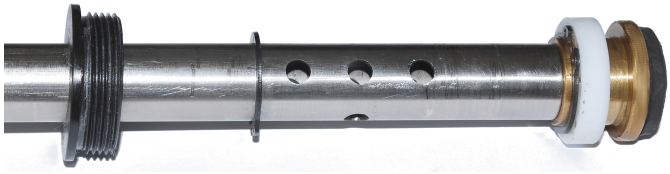

(d) Pressure Cap, barrel and plug

Figure 3.7: Photographs of the striker Components. When the gas gun is fired, pressure builds up between the pressure cap and plug, forcing the transfer cap attached to the striker to impact against the flange on the input bar.

3.2.3 Complications and Adjustments

A Teflon bush on the transfer flange allows the striker to run smoothly over the input bar. In testing this bush caught on the thread at the end of the striker when the striker was removed between experiments. This was easily prevented by adding a low angled taper after the thread.

The long input bar which was significantly bent. This meant that when a laser alignment system was used to correctly align the setup, the bars would not run smoothly in the bushes. Thus the laser alignment system was abandoned and the setup had to be configured manually. This was time consuming, but ultimately successful provided a fair amount of lubrication was applied to the support bushes. One of the two support bushes on the striker was also removed to allow it to align itself more easily relative to the input bar.

3.3 Specimen Design

3.3.1 Specimen Geometries

Ideally, to adequately characterize the Wierzbicki damage model, specimens with a wide range of triaxialities and Lode angles are required. However, the scope of this thesis is limited to uniaxial tensile testing apparatus and hence all lie in the region $0 \leq \eta$ and $0 \leq \bar{\theta} \leq 1$.

The 3 forms of specimen developed are straight sheet, notched sheet and flat grooved plates. The first two are square section adaptations of axisymmetric tensile specimens with $\bar{\theta} \approx 1$, while the latter is similar to the plates tested by Bai and Wierzbicki [17] with $\bar{\theta} \approx 0$ [14].

Section 3.3.2 details the technique used to secure the specimens to the split Hopkinson bars. Concisely, the specimens are glued into slots. This placed two constraints on the specimen design, firstly the maximum cross-sectional area at the gauge section centre was limited to $8mm^2$ to prevent glue failure. Secondly the glue jig, which is used to bond the specimens, required common sized gauge sections between groups of specimens.

Ideally the jig should be able to hold all different specimen types with no modifications. Nevertheless, in practice it was decided to develop *spacers* that would fit in the jig and locate the different specimen geometries precisely[15]. To limit the number of different spacers that needed to be manufactured, the width of the notch and straight specimens was set at 4mm. Secondly the thickness of the notch and groove specimens was set at 2.4mm, just lower than the sheet plate thickness of between 2.7 and 3mm.

[14] The specimens used by Bai and Wierzbicki [17] are included in section 2.5 on page 49.
[15] The jig design is detailed in section 3.4 on page 79

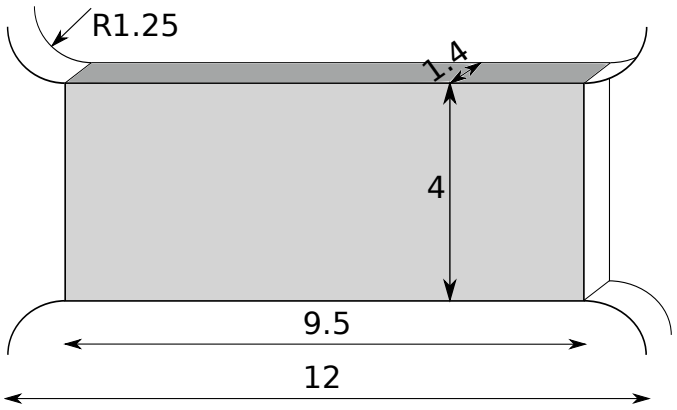

(a) Straight

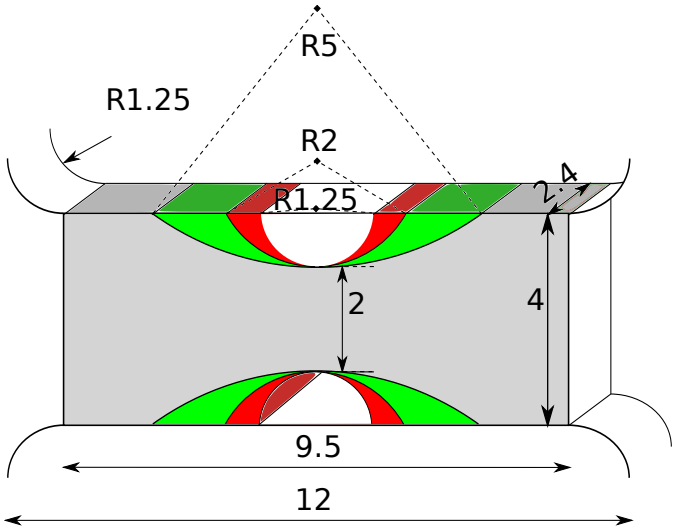

(b) Notch

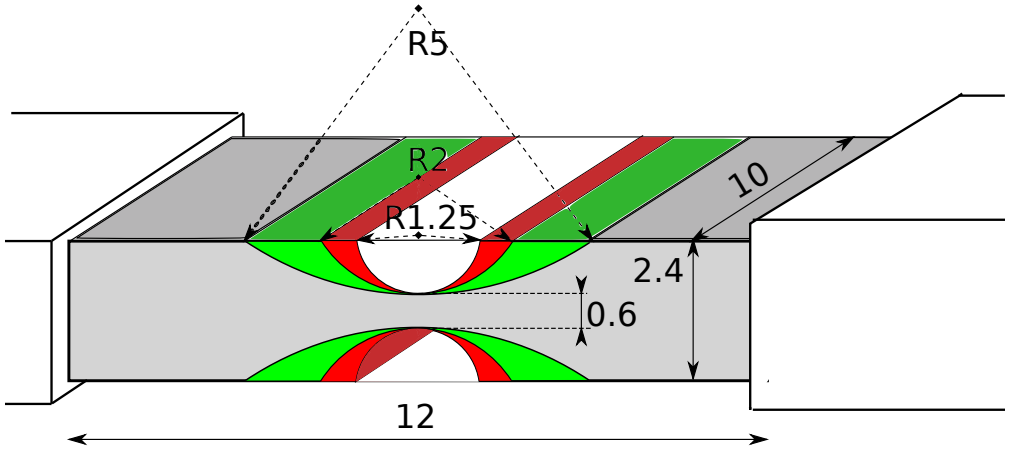

(c) Groove

Figure 3.8: Basic specimen geometries used in both the dynamic and quasistatic tests.

The straight specimens have the lowest triaxiality of the uniaxial tension specimens with $\eta = \frac{1}{3}$ and a high normalized Lode of close to 1. For these specimens a thickness of 1.4mm was set resulting in a cross-sectional area through the gauge zone centre of 5.6mm^2. The specimen, shown in figure 3.8a, was designed with a low transition zone radius of 1mm between the gauge section and glue zone to limit the transition zone deformation. This follows studies found in the literature on transition zone deformation covered in section 2.5.5. Ultimately the radius was increased to $1,25$mm due to machining constraints.

The notched specimens follow the same theory as that used by Bao and Wierzbicki [3] to increase the initial triaxiality by machining 'necks' into the specimens. The triaxiality at yield was approximated by[55]

$$\eta = \frac{1}{3} + \sqrt{2}\ln\left(1 + \frac{a}{2R}\right) \tag{3.5}$$

where a is the minimum radius and R the notch radius. This is a modified version of the Bridgman formula found numerically by Bai, Teng and Wierzbicki for round specimens. In this application square sheet specimens are used and thus as a rough estimation a was set to $\frac{t}{2}$ where t is the minimum thickness through the neck.

Equation 3.5 indicates that the greater the ratio of $\frac{t}{R}$ the higher the triaxiality. Thus to get a broad range of triaxialities, the thickness is kept constant at 2.4mm, while the notch radius increased from 1.25 to 2 to 5mm as shown in figure 3.8b.

The deformation of grooved plate specimens can be approximated by the plastic plain strain condition as the width is great relative to the thickness and hence lie in the region of $\bar{\theta} = 0$. The triaxiality was approximated through [55]

$$\eta = \frac{\sqrt{3}}{3}\left[1 + 2\ln\left(1 + \frac{t}{4R}\right)\right] \tag{3.6}$$

For this case, groove radii of 1.25, 2 and 5mm are again used, but the minimum thickness set at the low 0.6mm to allow the groove to cut significantly into the profile, shown in figure 3.8c.

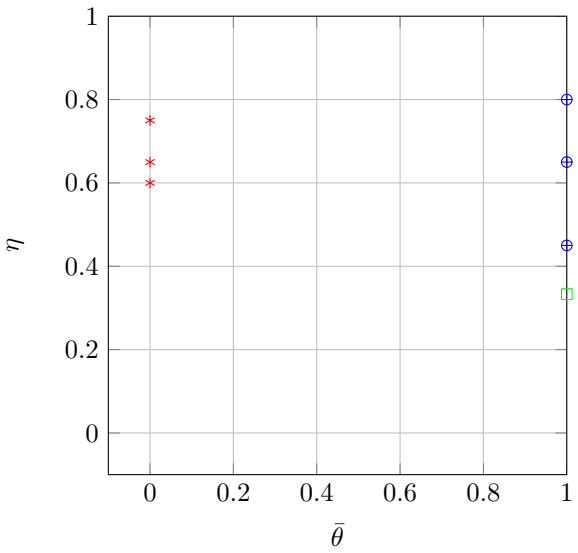

Figure 3.9: Approximate initial specimen states. The grooved specimens have a Lode of $\bar{\theta} \approx 0$, while the straight and notched are higher at $\bar{\theta} \approx 1$.

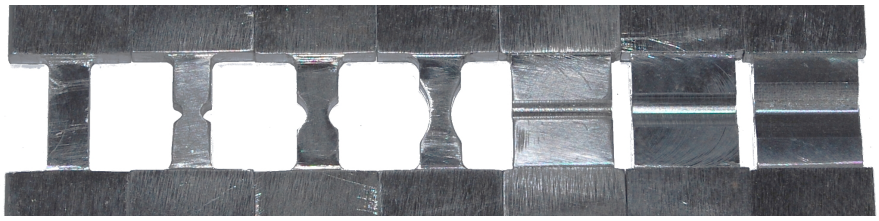

Figure 3.10: Photograph of all the different types of specimen tested. From left to right is an example of a straight specimen followed by 3 notched and finally 3 grooved examples.

The approximate initial specimen states are shown in figure 3.9. The predicted range at $\bar{\theta} = 0$ is narrow, but aimed to contrast the specimens at $\bar{\theta} = 1$. To confirm the approximations, a rough finite element analysis was conducted on each specimen up to yield. This shows similar results, the only major difference being the normalized Lode angle for the notch and straight specimens is lower at $\bar{\theta} \approx 0.8$

The manufactured specimen set is pictured in figure 3.10. Due to the small dimensions, manufacture is difficult and time consuming. Thus the test program is limited to three specimens of every geometry for each of the three strain rates tested. This equates to 63 specimens in total.

Figure 3.11: Sheet specimen glued into two sections of threaded bar.

3.3.2 Securing Specimens to the Split Hopkinson Bars

A complication with tensile testing is the question of how to attach the specimens to the bars. Verleysen et al[36, 48, 49, 52] in work on sheet metal specimens, used glue to secure the specimens directly into slots cut into the Hopkinson bars. In contrast Downey [50], amongst others, tested round specimens by machining a threaded region on either side of the specimen gauge zone and and then screwing the specimens into the bars. This has the advantage of quick specimen setup for testing [16].

In this thesis all specimens were manufactured from one sheet of mild steel, making the task of machining threads onto specimens difficult. The solution is a compromise between both techniques. Slots were cut into short sections of threaded bar that can be screwed into the SHB. The specimens were then glued into the slots with an example shown in figure 3.11. The photograph in figure 3.12 shows a specimen being screwed into the input bar. The next section contains the experimental results used to analyse the glue strength.

3.3.3 Glue Tests

The forces transferred through to the specimen have to be large enough to fracture the material and thus the glue must be able to withstand significant shear forces. With this in mind two types were considered.

The first, *Pratley SP020*, is a quick drying adhesive with a lap shear strength of 29 MPa between two steel parts. The advantage of this option is its fast cure time to handling strength in 5 minutes and full strength in 24 hours.

[16] The literature relating to securing specimens is included in section 2.5.5 on page 54.

Figure 3.12: Photograph of a dynamic specimen being screwed to the TSHB.

The second, *3M Scotch-Weld EPX Adhesive DP490*, requires 6 hours before handling, but 25 hours to full strength, allowing for a heat treat cycle of 1 hour at 80^{o}C. Lap shear tests for steel are unavailable, but that with aluminium using this cure is 28.7 MPa.

To check whether the glue strength in this application matched the lap shear specifications, quasistatic tensile tests were conducted. The tests involved rectangular specimens glued into threaded bar. The bar was then threaded onto attachments connected to the the Zwick tensile testing machine. In these tests the displacement rate was set at 5mm/min.

The first set of specimens was made from mild steel with dimensions shown in table 3.1. As the Hopkinson bars are nominally 20mm in diameter, the threaded bar was set at size M14. This allows for a specimen glue width of 12mm without interfering with the thread. The glue length was set at 30mm as that allowed the specimens to be bonded using an existing jig.

Specimens A through D were made from 2.8mm plate, which was a closely fitted into the 3mm slot cut into the bar. Of these A and B used the Pratleys, while the remainder used the 3M. Specimens E through I were made from 2mm plate, allowing a larger clearance gap of 0.5mm between specimen and bar slot.

The results from Set 1 are shown in figure 3.13. The first observation is that the tests using the 3M product with a close 0.1mm glue gap performed poorly, withstanding a maximum force of 2 kN before failing. This weakness may be due to its thick grease like consistency as when the plate is placed into the clamp slot, most of the epoxy is scraped off.

The Pratleys product performed better with the same glue thickness, exceeding 4 kN. However, it is difficult to work with for two reasons. Firstly it has a water like consistency resulting in a portion of the glue pouring out of the slot before it is fully set and using a larger glue gap would exacerbate this problem. Secondly its rapid cure time to handling strength means that small misalignments when the specimen is first placed into the clamp slot cannot be adjusted.

Interestingly the worst results came from using the 3M product with a cure cycle of 7 days at room temperature. According to its specifications, this should have resulted in the maximum shear strength. Yet in testing it clearly was not properly cured and failed instantly.

Table 3.1: Specimen and threaded bar dimensions used to test glue strength

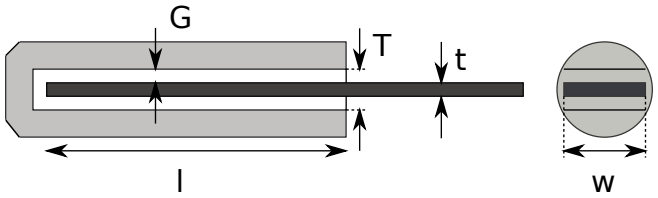

Specimen	w mm	l mm	t mm	T mm	G mm	Glue	Cure	Material
				Set 1				
A-B	12	30	2.8	3	0.1	Pratley	24 hrs	Mild Steel
C-D	12	30	2.8	3	0.1	3M	24 hrs, 1 at 80^{o}C	Mild Steel
E	12	30	2	3	0.5	3M	7 Days	
F-I	12	30	2	3	0.5	3M	24 hrs, 1 at 80^{o}C	Mild Steel
				Set 2				
J-M	12	20	2	3	0.5	3M	24 hrs, 1 at 80^{o}C	Gauge Plate
N-Q	12	20	2	4	1	3M	24 hrs, 1 at 80^{o}C	Gauge Plate

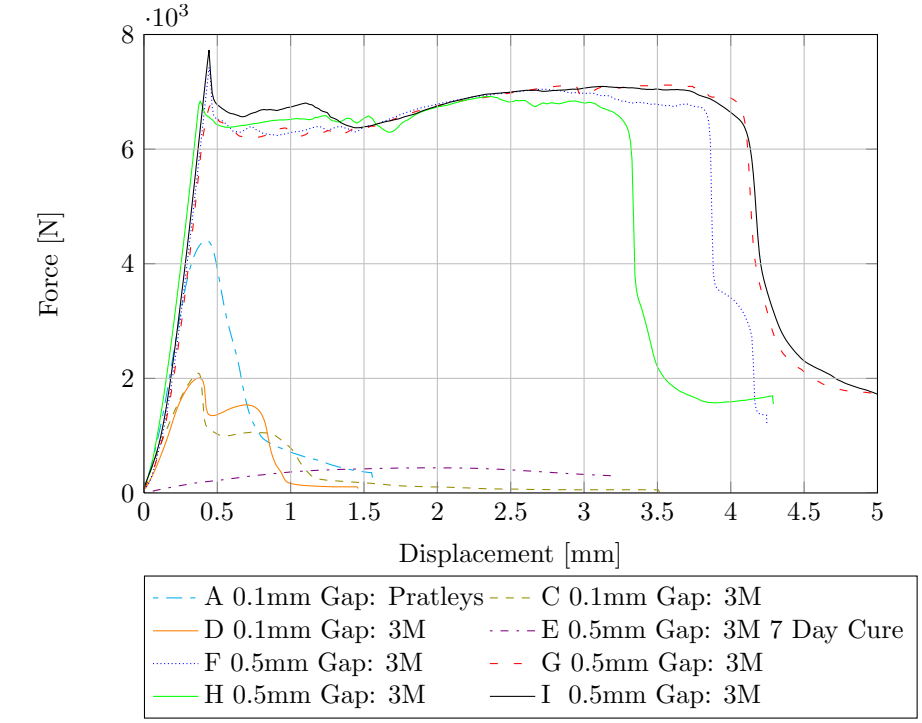

Figure 3.13: Results from Glue Test set 1 showing pulling force versus displacement.

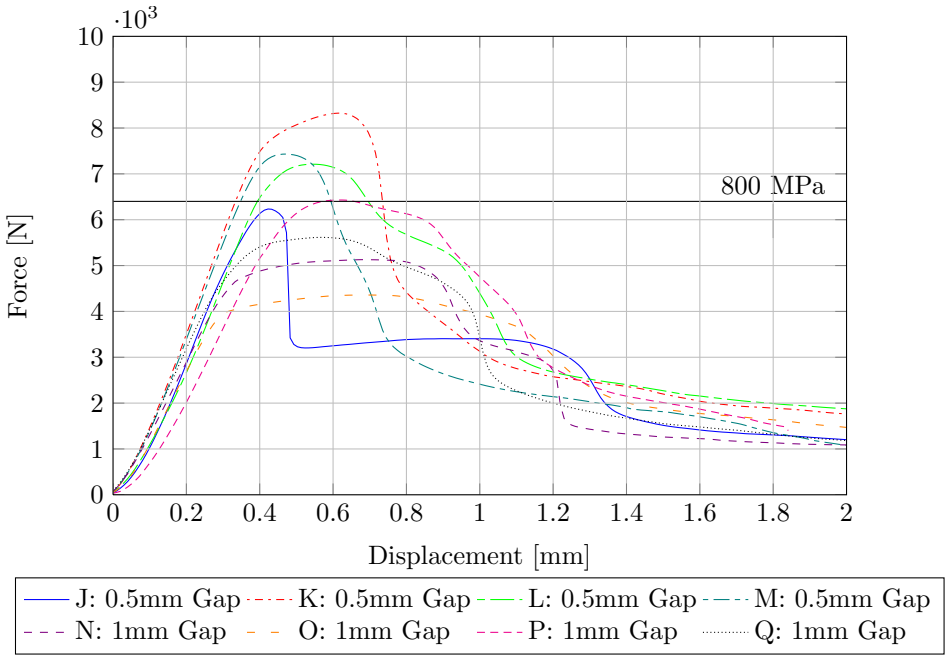

Figure 3.14: Results from Glue Test set 2 showing pulling force versus displacement. The cut-off line indicates the force required to reach a stress of 800MPa in a specimen of gauge section $4 \times 2\,\text{mm}$.

The optimum was the 3M glue with a 0.5mm glue gap, these tests reach a consistent reaction force of 7 kN before failing. However, this force is close to that resulting in plastic yield. These specimens have a constant cross section in the grip zone and gauge section. Thus, if plastic yield did occur, it would yield at the glue interface due to the stress concentration. Plastic yield in the glue region results in instant glue failure, resulting in a sharp drop in reaction force as the epoxy cannot withstand large strains. By measuring the specimen prior and post testing, it is clear that significant plastic deformation exceeding 3mm did occur, and thus a second set of tests, Set 2, were run.

In this group, the specimens were made out of gauge plate steel, which is an annealed high carbon steel far stronger than the mild steel used in Set 1. To ensure that the material did not yield before the glue failed, the glue length was reduced to 20mm. For this set, 3M Scotchweld was used for all the tests and thus the only varying parameter is the clamp slot thickness. This was set at 3mm with a 2mm plate for half the specimens resulting in a glue gap of 0.5mm, while the remainder used a wider slot of 4mm with a glue gap of 1mm.

The results are shown in figure 3.14. This plot cannot be directly compared to those of set 1 due to the lower glue length, thus as a measure of glue strength a cut-off force, corresponding to a stress of 800 MPa for a specimen of cross sectional area $8\,\mathrm{mm}^2$, is considered. The glue performed well with the 0.5mm gap specimens achieving a maximum yield force of 6 to 8 kN. Those with the larger glue gap were not as strong with a yield force of between 4.5 and 6.5 kN.

The large range of results is due to inconsistency in gluing technique. The glue jig used to make the specimens allowed the threaded bar clamps to rotate and change pitch relative to the specimen. This resulted in certain specimens with a large thick glue region on one face, but very little on the other.

If both faces have an equal amount of epoxy, the shear force is divided equally among the two. However, if one face has a far worse bond, the shear force acting on that face would cause it to fail first. Once one face has torn, the shear force acts completely on the remaining face and the bond there fails soon thereafter. The misalignment can be seen when considering the post test pictures (figure 3.15) of test K, which performed well, and J which only reached 6 kN.

(a) Test J showing poor specimen alignment.

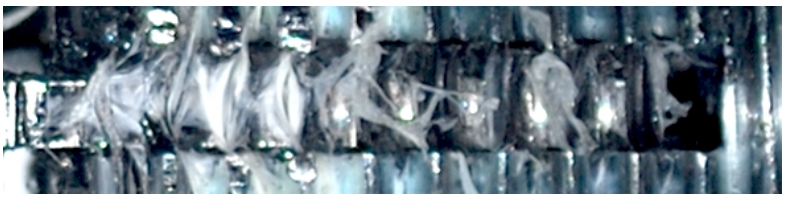

(b) Test K showing better specimen alignment.

Figure 3.15: Post test results of glue test specimens. Specimen J failed at a lower force than K due to the poor alignment between the specimen and slot.

From this test it was concluded that the 3M epoxy could be used for tensile testing. To ensure that the glue did not fail before the specimen gauge section, a larger 30mm glue length is used, while the maximum cross section permitted through the notched region was kept below 8mm^2. This conservative value corresponds to the 800 MPa cut-off line in figure 3.14. To prevent misalignments, the glue jig was optimized to hold the specimens securely during the cure cycle as covered in the following section.

3.4 Gluing Jig

A gluing jig is required to produce large numbers of specimens with the sheet grip sections aligned accurately to the threaded bar slots. The final version is shown in figure 3.16, with detailed drawings in appendix C.

A prototype was developed, loosely based on an already built, but untested, version designed by Govender [56]. It consists of a central removable clamp to hold the specimen, and a base that secures the clamp and threaded bars. The main limitation is that the rotation and pitch of the threaded bar are not fixed. This allows the bar to move relative to the specimen, often resulting in more epoxy being applied to only one of the specimen glue surfaces.

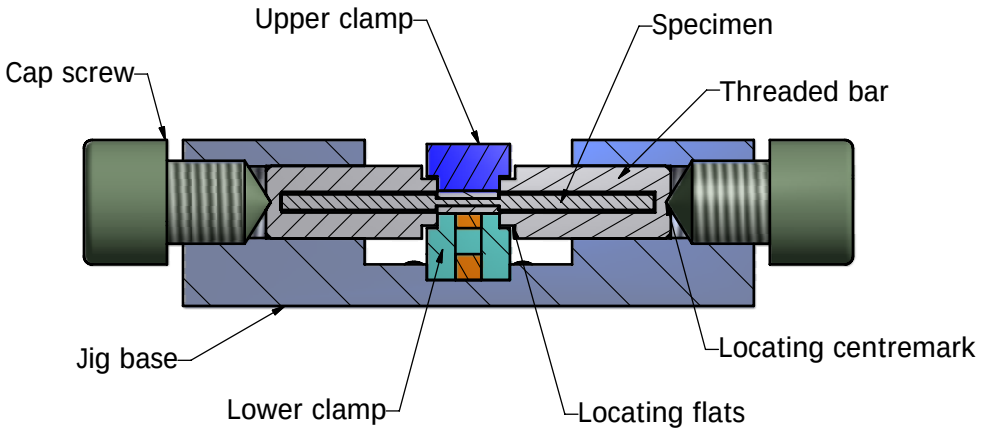

Figure 3.16: Final glue jig design.

Two methods were introduced as improvements. Firstly, to constrain rotation and vertical movement, flats were machined into the end of the threaded bar. Locating sections were then cut into the lower and upper halves of the central clamp to hold the flats firmly. These flats have the added advantage of allowing a spanner to be used in securing and removing the specimens from the Split Hopkinson bars.

To ensure that the pitch remained level, a locating centremark was placed at the other end of the threaded bar. Cap screws were then tapered so that the point at the screw tip would locate the rear end.

The specimens are bonded as follows:

1. First the upper and lower halves of the clamp are screwed together, securing the specimen in between. A spacer is used to correctly position the specimen (figure 3.17).

2. The threaded section is prepared by winding thread tape over the slot (figure 3.18). This prevents glue from spilling onto the thread.

3. Epoxy is then applied to both the specimen gauge section and to the threaded bar slot (figure 3.19).

4. The clamped specimen is the slid into position and screwed down onto the base. Locating screws are placed on either side of the clamp to ensure it is centrally located.

5. The slotted threaded bar sections are slid in through a hole from outside the jig and secured with cap screws (figure 3.20).

6. After curing to handling strength the specimens are removed, this is achieved by removing the upper and lower halves of the clamp separately and removing the cap screws. The specimen is then pushed through either of the holes.

The lower half of the clamp, considered in the first point, was split to allow it to be removed. In the initial prototype the this part was cut into two identical halves with a flat face. However, this allowed for vertical and horizontal motion before the clamp was screwed down. Thus to ensure that both sides are correctly aligned, the mating surfaces had horizontal and vertical sections cut out, shown in figure 3.21. These sections prevent horizontal and vertical motion as well as rotation.

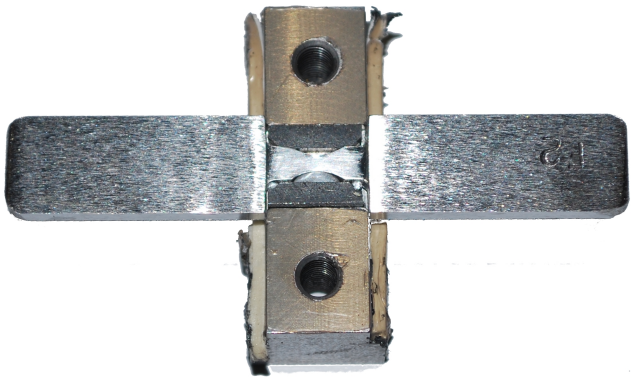

Figure 3.17: Photograph of the specimen positioned in the lower clamp by a spacer. Several spacers were made to locate the different specimen geometries.

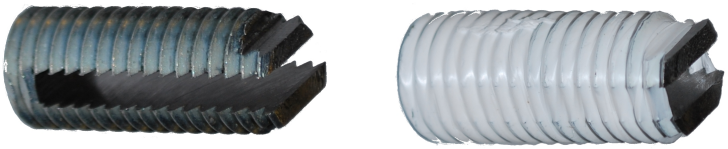

(a) Original (b) Taped

Figure 3.18: Slotted threaded bar showing thread tape covering the glue slot. The tape prevents epoxy from spilling onto the thread during the curing process. Note the flat machined at the front of the bar, this is used to align the slot as well as grip the specimen when it is screwed into the bars.

Figure 3.19: Clamped specimen and threaded bars with epoxy applied. The clamp was covered in tape before gluing to prevent the epoxy from bonding the lower and upper clamp sections together.

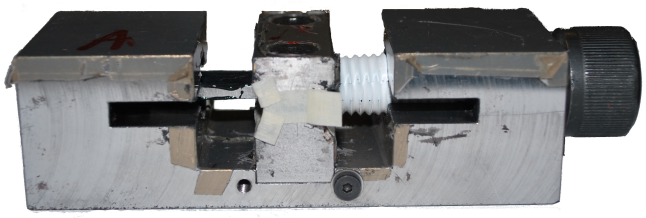

Figure 3.20: Bar bonding to specimen in the jig. The cap screw aligns the rear of the bar and compresses it against the clamp.

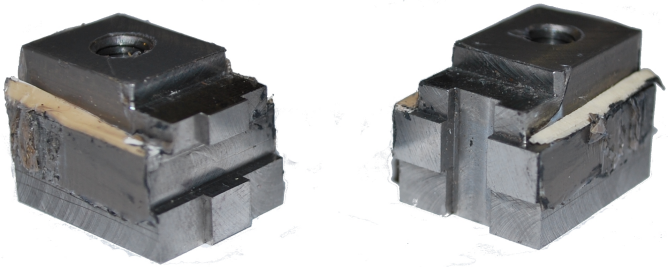

Figure 3.21: Photograph of the lower glue jig clamp. The piece is comprised of two halves which key together to ensure accurate vertical and horizontal alignment.

Chapter 4

Simulation Procedure

4.1 Introduction

This chapter contains the theory and techniques used to develop the material models and simulate the experiments.

The first two sections deal with the development of the plasticity and damage failure model written as a user defined material model (VUMAT) in Fortran. Plasticity is described by the Zhao model [57], which is valid across a wide range of strain rates, while a simplified symmetric Bai-Wierzbicki failure locus [17] is included to track damage propagation.

The latter sections cover techniques used to model the geometry and loading conditions. First the dynamic model is considered, followed by the quasistatic.

4.2 Plasticity Model

Plastic deformation refers to that in which strains are not totally recoverable [58] and thus permanent deformation remains once the load is removed. This analysis considers the Mises flow rule to determine whether plastic deformation occurs. The von Mises, or 'distortion energy', criteria assumes that plastic deformation is caused only by the shear strain, or 'deviatoric', energy components and thus deformation related to volume change has no influence [58].

The plasticity model begins by assuming the increment is strain is purely elastic. With this assumption a trial stress is determined and compared to that predicted by the yield function. If the trial is lower than yield the step is elastic and the trial stresses are taken as the final stresses, while if the trial is greater than yield the change in plastic strain needs to be solved.

In this analysis, scalar quantities are written as lower case letters, tensor quantities as upper case with components i and j. The subscript *old* refers to the state of the previous time step, while *new* indicates the current.

The repeated index summation convention is used.

4.2.1 Trial stress

The trial stress is determined using Hooke's law,

$$\Delta T_{ij}^{trial} = 2G\Delta E_{ij} + \lambda E_{kk}\delta_{ij} \tag{4.1}$$

where G is the shear modulus and λ is the first lamé parameter. T_{ij} refers to the Cauchy stress tensor and E to the strain tensor. The final trial stress is simply,

$$T_{ij}^{trial} = T_{ij}^{old} + \Delta T_{ij}^{trial} \tag{4.2}$$

The equivalent von Mises stress is derived from the deviatoric components, S_{ij}, thus the hydrostatic pressure, p, needs to be removed.

$$p = -\frac{1}{3}T_{ii}^{trial} \tag{4.3}$$

$$S_{ij}^{trial} = T_{ij}^{trial} + p\delta_{ij} \tag{4.4}$$

Thus the equivalent trial stress is given by,

$$\therefore \sigma^{trial} = \sqrt{\frac{3}{2}S_{ij}S_{ji}} \tag{4.5}$$

Check for yield

The step involves plastic deformation if the trial stress is greater than the yield function, f.

$$f(\epsilon^{pl}, \dot{\epsilon}^{pl}, T) - \sigma^{trial} \leq 0 \tag{4.6}$$

If not met, the strain step is purely elastic. The final stress is equal to the trial stress and all state variables are set to the previous values.

$$T_{ij} = T_{ij}^{trial} \tag{4.7}$$

4.2.2 Plastic Strain

Large deformation results in a large trial stress. This is mostly irrecoverable and thus the plastic portion must be determined. In this scenario, both the new plastic strain and equivalent stress need to be found. Two solutions were attempted, the first used a nonlinear solver, while the second implemented a linear predictor return algorithm.

In this section subscript *pl* refers to plastic variables and *el* to elastic.

Method I: Nonlinear Solver

The nonlinear solver method determines the change in strain using the previous elastic strain and the current strain increment. Newton's method is used to iterate towards the exact solution. The basic theory is given in the Abaqus documentation [59], but is limited. Thus a full derivation is included here for the sake of completeness.

Firstly, the old elastic strain is found using the old deviatoric stress. The pressure can be determined directly from the old stress state as plastic deformation is assumed to be independent of hydrostatic pressure, p.

$$p = -\frac{1}{3}T_{ij}^{old} \tag{4.8}$$

$$S_{ij}^{old} = T_{ij}^{old} + p\delta_{ij} \tag{4.9}$$

$$\therefore E_{ij}^{el}|^{old} = \frac{S_{ij}^{old}}{2G} \tag{4.10}$$

The equation for the final deviatoric stress is separated into knowns and unknowns,

$$\begin{aligned}
S_{ij} &= 2GE_{ij}^{el} \\
&= 2G\left(E_{ij}^{el}|^{old} + \Delta E_{ij}^{el}\right) \\
&= 2G\left(E_{ij}^{el}|^{old} + \Delta E_{ij} - \Delta E_{ij}^{pl}\right) \\
&= 2G\left(E_{ij}^{el}|^{old} + \Delta E_{ij} - \Delta\epsilon^{pl}N_{ij}\right) \\
&= 2G\left(E_{ij}^{el}|^{old} + \Delta E_{ij} - \Delta\epsilon^{pl}\frac{3}{2}\frac{S_{ij}}{\sigma_v}\right) \qquad \text{as } N_{ij} = \frac{3}{2}\frac{S_{ij}}{\sigma_v}
\end{aligned}$$

$$\therefore S_{ij}\left(1 + \frac{3G}{\sigma}\Delta\epsilon^{pl}\right) = 2G\underbrace{\left(E_{ij}^{el}|^{old} + \Delta E_{ij}\right)}_{\hat{E}_{ij}} = 2G\hat{E}_{ij} \tag{4.11}$$

This is reduced to scalar form by taking the inner product of both sides with themselves and taking the square root of the solution.

$$\begin{aligned}
\sqrt{S_{ij}S_{ji}\left(1 + \frac{3G}{\sigma}\Delta\epsilon^{pl}\right)^2} &= \sqrt{(2G)^2\hat{E}_{ij}\hat{E}_{ji}} \\
\therefore \frac{\sigma}{\sqrt{3/2}}\left(1 + \frac{3G}{\sigma}\Delta\epsilon^{pl}\right) &= 2G\sqrt{\hat{E}_{ij}\hat{E}_{ji}} \qquad \text{from equation 4.5} \\
\sigma + 3G\Delta\epsilon^{pl} &= 3G\underbrace{\sqrt{\frac{2}{3}\hat{E}_{ij}\hat{E}_{ji}}}_{\tilde{\epsilon}} = 3G\tilde{\epsilon}
\end{aligned} \tag{4.12}$$

This forms a description of the yield surface, s.

$$s = 3G\left(\tilde{\epsilon} - \Delta\epsilon^{pl}\right) - \sigma = 0 \tag{4.13}$$

The function is in the correct form to be solved using Newton's method, which is described by,

$$c = x_n - x_{n+1} = \frac{s\left(x_n\right)}{s'\left(x_n\right)}$$

where c is the residual. The solution is regarded to have converged when this value is within a specified tolerance[17]. Thus applied to equation 4.13

$$c^{pl} = \frac{3G\left(\tilde{\epsilon} - \Delta\epsilon^{pl}\right) - \sigma}{3G + H} \tag{4.14}$$

where H is the derivative of the equivalent stress term, $\dfrac{d\sigma}{d\epsilon^{pl}}$

After each iteration ,n, the plastic strain is updated through

$$\Delta\epsilon_n^{pl} = \Delta\epsilon_{n-1}^{pl} + c^{pl}$$

and the equivalent stress, σ, is recalculated until c^{pl} is within the tolerance. Note that for this implementation, the strain rate and temperature is kept constant during the iterations to minimize the computation. This will lead to marginal errors, but as the time increment is very small these should be insignificant. At the end of the iteration the strain rate and temperature are updated.

Once the final equivalent plastic strain and stress are known, the deviatoric stress components are found using equation 4.11 rearranged as,

$$S_{ij} = \frac{2G}{1 + \frac{3G}{\sigma_v}\Delta\epsilon^{pl}}\hat{E}_{ij} \tag{4.15}$$

[17]The tolerance used is discussed in section 4.2.4 on page 94.

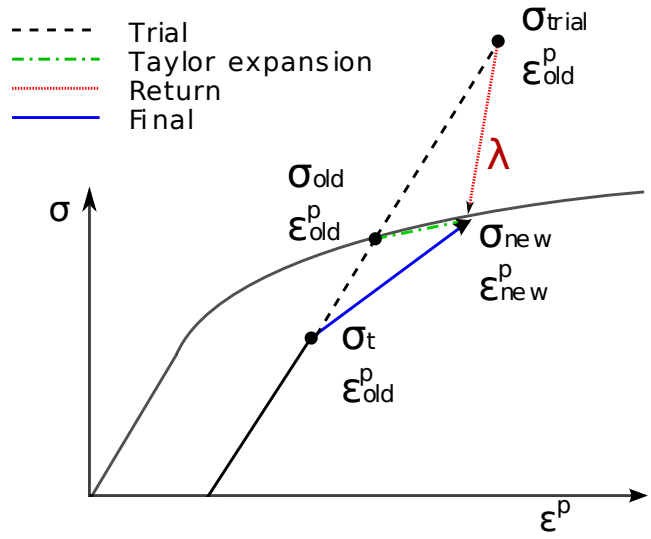

Figure 4.1: Predictor return algorithm used to determine the new position on the yield surface. The step is first assumed to be elastic from which a trial stress is found, this is then scaled using a factor λ and combined with a Taylor expansion of the flow rule to find the final plastic strain.

Method II: Predictor Return Algorithm

The predictor return method[18] was attempted due to instabilities in the implementation of Method I. In this case the new position on the yield surface is predicted by scaling the magnitude of the trial stress by a factor λ and by using a Taylor expansion from the previous point on the surface [54]. This is shown graphically in figure 4.1.

The scaling factor is given by [60] as,

$$\lambda = \frac{\sigma^{new}}{\sigma^{trial}} = 1 - \frac{3G\Delta\epsilon^{pl}}{\sigma^{trial}} \tag{4.16}$$

The trial stress here is the same equivalent von Mises stress found in equation 4.5, while σ^{new} refers to the final position on the yield surface that needs to be found.

By rearranging to solve for the change in equivalent strain, $\Delta\epsilon^{pl}$ is shown to be directly related to the trial stress.

$$\Delta\epsilon^{pl} = (1-\lambda)\frac{\sigma^{trial}}{3G} \tag{4.17}$$

[18]Derived and implemented successfully by Bonorchis [54]

Two equations are needed for the two unknowns, ϵ^{pl}_{new} and σ_{new}, the second is derived from the Taylor expansion of the flow rule as follows,

$$\begin{aligned}\sigma^{new} &= \sigma^{old} + \left(\frac{\delta\sigma}{\delta\epsilon^{pl}}\right)^{old}\Delta\epsilon^{pl} + \left(\frac{\delta\sigma}{\delta\dot{\epsilon}^{pl}}\right)^{old}\Delta\dot{\epsilon}^{pl} + \dots \\ &\approx \sigma^{old} + \left(\frac{\delta\sigma}{\delta\epsilon^{pl}}\right)^{old}\Delta\epsilon^{pl} + \left(\frac{\delta\sigma}{\delta\dot{\epsilon}^{pl}}\right)^{old}\left(\frac{\Delta\epsilon^{pl}}{\Delta t} - \dot{\epsilon}^{pl}_{old}\right)\end{aligned} \tag{4.18}$$

where σ^{old} is the yield stress determined from the yield function, f, and is related to the plastic strain, strain rate and temperature from the previous plastic step.

Thus from equations 4.17 and 4.18 the scale factor can be found,

$$\lambda = \frac{\sigma^{old} + A - B}{\sigma^{trial} + A} \tag{4.19}$$

where,

$$A = \frac{\sigma^{trial}}{3G}\left[\left(\frac{\delta\sigma}{\delta\bar{\epsilon}^{pl}}\right)^{old} + \left(\frac{\delta\sigma}{\delta\dot{\epsilon}^{pl}}\right)^{old}\frac{1}{\Delta t}\right]$$

and,

$$B = \left(\frac{\delta\sigma}{\delta\dot{\epsilon}^{pl}}\right)^{old}\dot{\epsilon}^{pl}_{old}$$

Finally the change in plastic strain is found through equation 4.17 and the deviatoric stress components are solved simply through,

$$S^{new}_{ij} = \lambda S^{trial}_{ij} \tag{4.20}$$

The method is more efficient and stable computationally than using Newton's method as no iterations are required. The approximation of the flow rule does introduce a degree of error, but in an explicit analysis the time step increments are so small that this error is insignificant.

Stress

Once the new deviatoric stress is known the total stress can be found. Plastic deformation is assumed by the von Mises criteria to be independent of hydrostatic stress [58], thus the p used is that calculated from the trial pressure.

$$T_{ij} = S_{ij} - p\delta_{ij} \tag{4.21}$$

Plastic Strain Rate

Newton's method requires the current strain rate, this is approximated through the deviatoric equivalent strain, before the iterations begin.

$$\Delta E^D_{ij} = \Delta E_{ij} - \frac{1}{3}\Delta E_{kk} \tag{4.22}$$

$$\Delta \epsilon^D = \sqrt{\frac{2}{3}\Delta E^D_{ij}\Delta E^D_{ji}} \tag{4.23}$$

$$\dot{\epsilon}^{pl} \approx \frac{\Delta \epsilon^D}{\Delta t} \tag{4.24}$$

In contrast, the predictor return algorithm only requires the strain rate from the previous plastic increment, this is found simply from the change in plastic strain and stored.

$$\dot{\epsilon}^{pl} = \frac{\Delta \epsilon^{pl}}{\Delta t} \tag{4.25}$$

Temperature

Temperature is a function of plastic strain and is thus updated after every plastic step. Firstly, the heat flux, q, per unit volume, V, for a time step is defined in [59] as,

$$\frac{q}{V} = \hat{\eta} T_{ij} \Delta E^{pl}_{ji} \tag{4.26}$$

where $\hat{\eta}$ is the percentage of plastic work that is converted into heat [19].

[19] Note that this ratio is generally referred to as η (see for example [54, 59]), but is referred to in this work as $\hat{\eta}$ to distinguish it from triaxiality.

Heat flux is defined as,

$$\begin{aligned} q &= mC_p\Delta T \\ &= \rho V C_p \Delta T \end{aligned} \tag{4.27}$$

where C is the specific heat. Thus from equations 4.26 and 4.27 the change in temperature can be found.

$$\begin{aligned} \rho C_p \Delta T &= \hat{\eta} T_{ij} \Delta E^{pl}_{ji} \\ \therefore \Delta T &= \frac{\hat{\eta}}{\rho C_p} T_{ij} \Delta E^{pl}_{ji} \end{aligned} \tag{4.28}$$

In the solver routine, the plastic strain is found as an equivalent strain. Thus it is convenient to transform the strain and stress terms into equivalent scalar forms,

$$\begin{aligned} T_{ij}\Delta E^{pl}_{ji} &= \sigma N_{ij} \Delta\epsilon^{pl} N_{ji} \\ &= \sigma \Delta\epsilon^{pl} N_{ij} N_{ji} \\ &= \sigma \Delta\epsilon^{pl} \end{aligned} \tag{4.29}$$

Thus the form implemented is,

$$\Delta T = \frac{\hat{\eta}\sigma\Delta\epsilon^{pl}}{\rho C_p} \tag{4.30}$$

Internal and Dissipated Energy

The final state variables that need to be updated are the specific internal energy and the dissipated inelastic specific energy[59].

The former is found by calculating the integral of average stress and strain during the increment.

$$\Delta P = \frac{1}{2}\left(T^{new}_{ij} + T^{old}_{ij}\right) E_{ij} \tag{4.31}$$

The internal energy is then given by,

$$\text{Energy}^{new}_{intern} = \text{Energy}^{old}_{intern} + \frac{\Delta P}{\rho} \tag{4.32}$$

While the dissipated energy is the product of the plastic strain increment and equivalent stress, or plastic work, per unit mass.

$$\Delta W = \sigma \cdot \Delta \epsilon^{pl} \tag{4.33}$$

$$\text{Energy}_{diss}^{new} = \text{Energy}_{diss}^{old} + \frac{\Delta W}{\rho} \tag{4.34}$$

4.2.3 Yield Function

Johnson-Cook

The first model considered was that by Johnson and Cook given below. Note that in this analysis, the equivalent strain always refers to the plastic strain, ϵ^{pl}, thus the superscript is dropped for convenience.

$$f = \sigma = [A + B\epsilon^n] \left[1 + C \ln \left(\frac{\dot{\epsilon}}{\dot{\epsilon}_0}\right)\right] [1 - T^{*m}] \tag{4.35}$$

The first term is a affected by plastic strain and gives the function an exponential shape defined by the constants a, B and n. The second is related to the strain rate with the constant C and the reference strain rate $\dot{\epsilon}_0$ predicting an increase in yield with rate. Finally the last term, using the constant m, decreases yield with an increase in temperature.

The temperature term is defined by,

$$T^* = \frac{T - T_{trans}}{T_{melt} - T_{trans}} \tag{4.36}$$

This introduces two additional constants: T_{trans}, which is the transition, or room, temperature and T_{melt}, the melting temperature. T^* is set to 0 if the temperature is below the transition and set to 1 if the melting temperature is reached.

On a scale of the log of strain rate versus stress, Johnson-Cook predicts a linear relationship. This has since been shown to be a fair approximation only in two distinct regions, low strain rates of less than $1\,\text{s}^{-1}$ and high rates above $100\,\text{s}^{-1}$ [57]. In this thesis a single model is required to cover both regions and thus a change is required.

As an alternative solution, the strain rate adjustment term can be replaced by that used by Cowper-Symonds as given in[61]. This was shown in chapter 6 to give a closer approximation to the material properties.

$$\frac{\sigma}{\sigma_0} = 1 + \left(\frac{\dot{\epsilon}}{\dot{\epsilon}_0}\right)^{1/k} \tag{4.37}$$

Zhao

A more refined model was developed by Zhao [57]. This is a major improvement as it was designed to be valid across a wide race of strain rates. However, nine constants need to be calibrated.

$$\sigma = \left(A + B\epsilon^n + [C - D\epsilon^m] \log\left[\frac{\dot{\epsilon}}{\dot{\epsilon}_0}\right] + E\dot{\epsilon}^k\right) f(T) \tag{4.38}$$

The advantage is that at low strains, the model is tailored by changing the constants C, D and m which relate to the log term, while high strain rate behaviour is influenced mainly by the exponential term constants E and k. This relation was used to calibrate the model in chapter 6.

The temperature term was taken as that used by Johnson-Cook

4.2.4 Evaluation

To evaluate the plasticity model a series of tests were conducted, first on single elements $5 \times 5 \times 5\,\mathrm{mm}^3$ subjected to tension, then on a $5 \times 5 \times 5$ block of elements under the same loading conditions and finally on a simulated experiment.

Using Newton's Method

The first set considered the basic Johnson-Cook model using Newton's method. The properties were set at that for 1006 steel given by Johnson and Cook [15] with temperature and strain rate effects included. Johnson-Cook is useful as a convenient first attempt as there is a built-in model in Abaqus to compare it against.

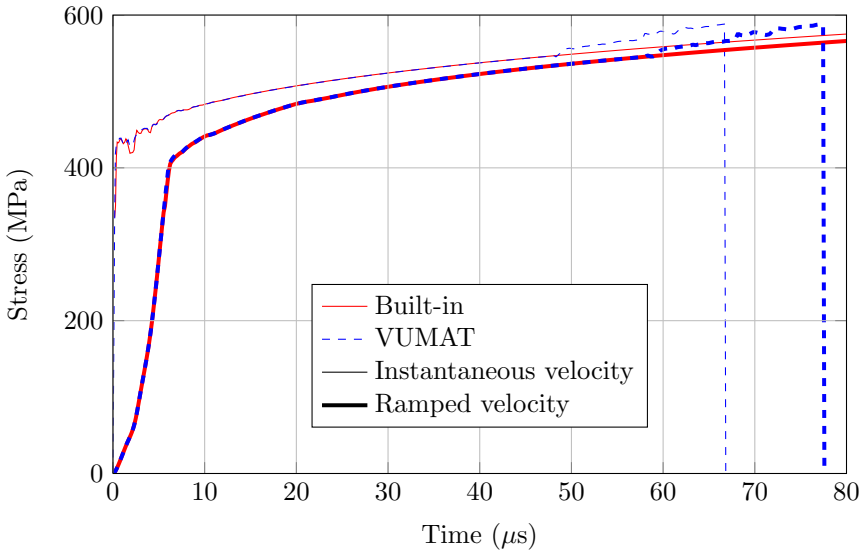

Figure 4.2: Equivalent stress resulting from using the built-in and VUMAT Johnson-Cook models on a 5×5 block of elements subjected to a $10\,\mathrm{m.s^{-1}}$ tensile boundary condition

Two sets of velocity boundary conditions were tested, the first was set at $10\,\mathrm{m.s^{-1}}$ with a strain rate expected in the region of $\dot{\epsilon} \approx \frac{v}{L} = 2000$. The model performed perfectly as shown in figure 4.2. For the 5 by 5 element block oscillations occurred both in the VUMAT and built-in models, but this was easily stabilized by ramping the velocity over $20\,\mu$s. In the actual high speed experiments the velocity is ramped during the rise time of the input pulse thus this is not a problem. Note that the increased stress followed by a sudden drop around $70\,\mu$s is due to the damage model removing the elements.

However, at the low velocity of $0.005\,\mathrm{m.s^{-1}}$ equivalent to a strain rate $\dot{\epsilon} \approx \frac{v}{L} = 1$ significant oscillations were evident as shown in figure 4.3.

Some understanding of the instability is gained by considering the change in plastic strain in figure 4.4. The strain follows that of the built-in model almost exactly, but a closer view reveals that elastic steps (indicated by the horizontal regions in the curve) occur in between the plastic steps.

Even though the average of the sharp plastic strain increments followed by the elastic regions results in the correct total plastic strain, the sharp increases in strain result in significantly oscillations to the strain rate. This in turn results in the oscillations evident in figure 4.3.

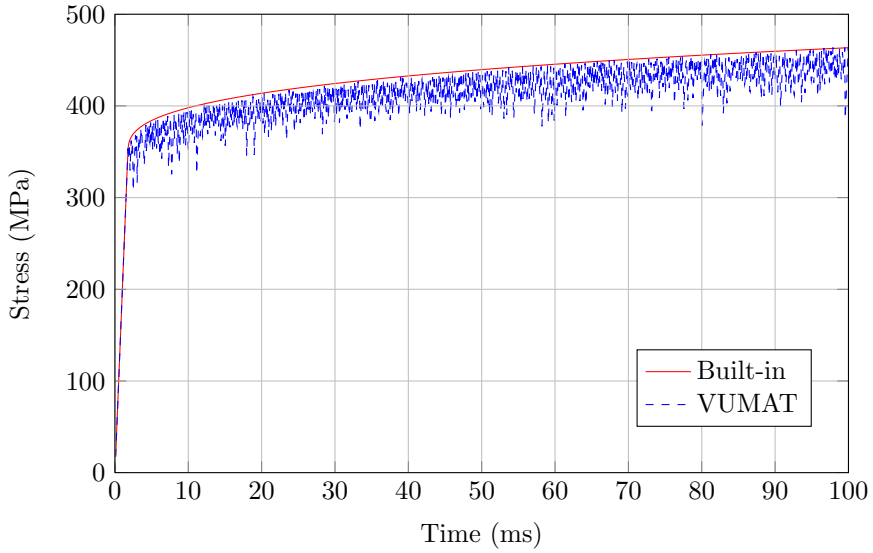

Figure 4.3: Equivalent stress resulting from using the built-in and VUMAT Johnson-Cook models on a single element subjected to a $0.005\,\mathrm{m.s^{-1}}$ tensile boundary condition

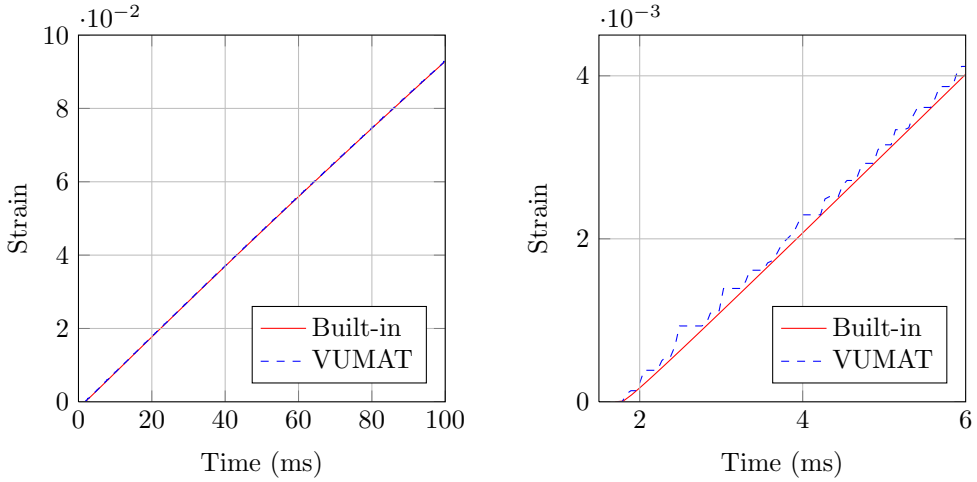

(a) Full (b) Detailed

Figure 4.4: Plastic strain versus time for the model at a low strain rate using the Johnson-Cook model. Instabilities arise due to the elastic steps which follow plastic deformation as shown in the detailed view.

The stepped form of the plastic curve is due to errors with the Newton solver, but decreasing the tolerance required to complete the Newton steps does not help. The problem is that at low strain rates, the strain during a single time step is so small that the algorithm does not predict the strain precisely. Setting the strain rate at a constant value completely removes the instability. This is not an ideal solution, but as the strain rate has only a minor influence at low strains it is viable.

For these simulation the Newton's Method tolerance initially taken as $|c^{pl}| \leq 1 \times 10^{-9}$, which is 10 times lower than that used in developing a Newton's method dynamic material model by Bonorchis [62]. Decreasing the tolerance to $|c^{pl}| \leq 1 \times 10^{-16}$ resulted in no improvement. In addition, changes were implemented to update the strain rate and temperature during each iteration. This increases the computation steps required, but should increase the accuracy of the solution. However, this adjustment did not correct the problem.

Despite these complications, tests were run on a simulated SHB experiment. At first these seemed to perform correctly until the strain rate itself was considered. Increasing the strain rate term, C, from 0.022 to the high 0.085 resulted in significant oscillations within the strain rate as shown in figure 4.5. In this case the elements were significantly smaller than those used in the single element tests and measured roughly $0.1 \times 0.1 \times 0.1\,\text{mm}$. Thus despite the high strain rate the stable time increment was very small. In this case the same problem occurred to that of the single element tests at slow rates, sharp plastic steps resulting in significant strain rate oscillations followed by elastic steps to correct the overestimation.

An attempt was made to correct the oscillations by setting the strain used in the solver to be a weighted average of the current and previous strain with the form,

$$\dot{\epsilon}_{avg} = \frac{\dot{\epsilon} + N.\dot{\epsilon}_{old}}{N+1} \tag{4.39}$$

where N is the weighting factor.

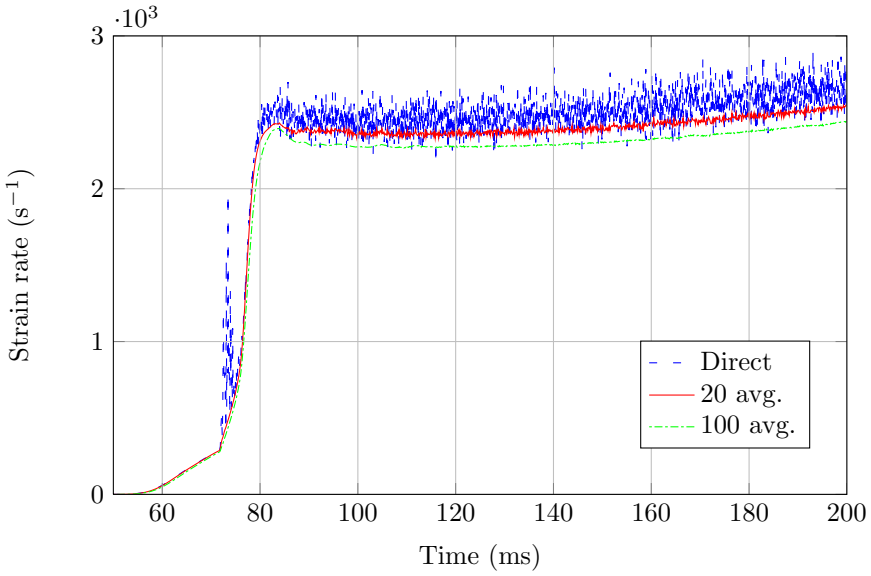

Figure 4.5: Strain rate resulting from using the Newton's Method solver to simulate a SHB experiment. A weighted average is used to reduce oscillations.

Two weighting options are included in figure 4.5. With $N = 100$, the strain rate is stable and with $N = 20$ the oscillations should not affect the yield surface significantly. Yet both predictably result in a decrease in strain rate. Several attempts were made at improving this, the most promising was to use Lagrange extrapolation to better predict the new strain rate instead of simply the weighted average, but no improvement resulted. Attempts were also made using the Cowper-Symonds and Zhao models with similar negative effects.

Interestingly, Abaqus [59] reports using Newton's Method in solving isotropic plasticity models, which include Johnson-Cook. In the Abaqus implementation, the solution is stable and thus improving the method to achieve stable results is possible. However, Abaqus does not detail how a stable solution is achieved and this may be proprietary.

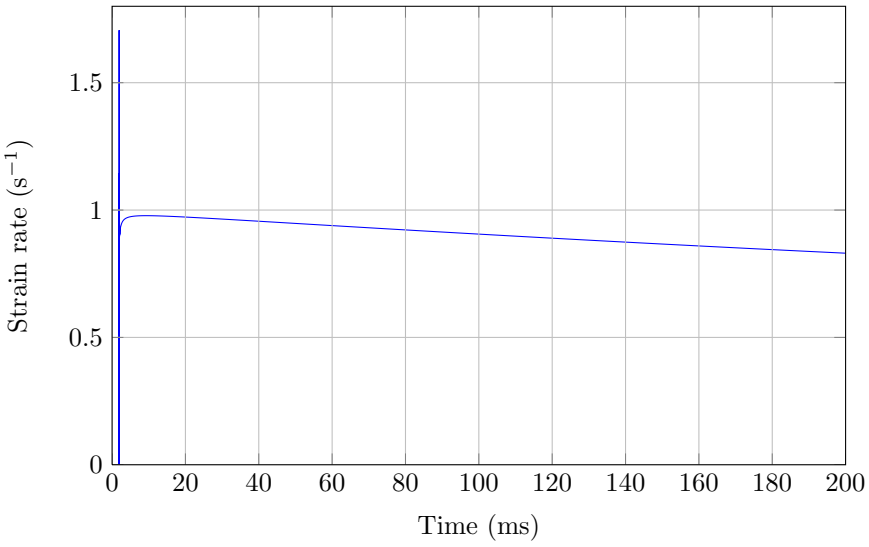

Figure 4.6: Strain rate of a single element test using a Predictor Return algorithm for the Johnson Cook model

Using the Predictor Return Method

The predictor return algorithm was attempted as an alternative to using Newton's method due to the instabilities in strain rate. In this case the Johnson-Cook model resulted in a stable strain rate result, even in the case of the low velocity of $0.005\,\mathrm{m.s^{-1}}$ as shown in figure 4.6. The only problem was the spike at the beginning of the pulse which occurred for both the low and high strain rate cases.

The Zhao model was then implemented due to its validity across a large range of stain rates. When applied to the high strain rate model the results were perfect, with no oscillations at all. However when applied to a low rate as shown in figure 4.7 significant instability occurs until suddenly at around $90\,\mu$s when it becomes perfectly stable. This is presumably the same problem as seen using the Newton's Method algorithm as some elastic steps are evident, but not in the same quantity as that using Newton's Method. This was easily corrected by using the average of the previous and current strain rate.

At lower strain rates a higher degree of weighted averaging was required. In this case at a strain rate of 0.2, a averaging weight of $N = 2$ was required before convergence was reached, shown in figure 4.8. This was predictable as a lower strain rate would have more elastic steps following a plastic step.

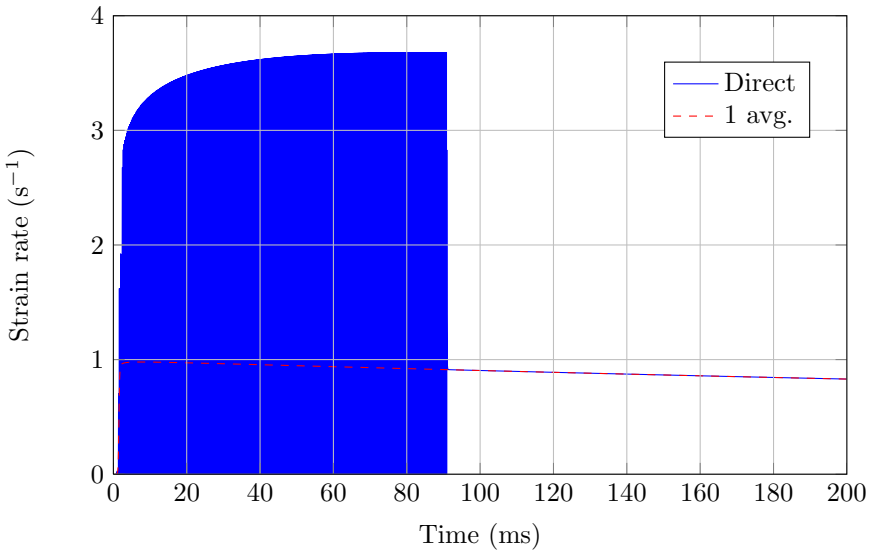

Figure 4.7: Strain rate of a single element test using a Predictor Return algorithm for the Zhao model at $\dot{\epsilon} \approx 1$. Using an average strain rate averaged over the previous and current step results in stability.

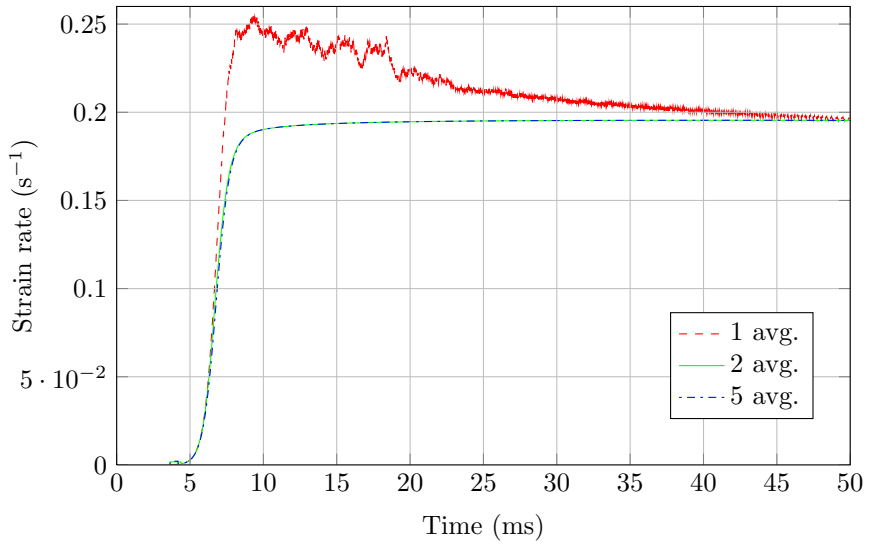

Figure 4.8: Strain rate of a single element test using a Predictor Return algorithm for the Zhao model at a slow strain rate of 0.2. In this case a weighted average of $N = 2$ is required for stability

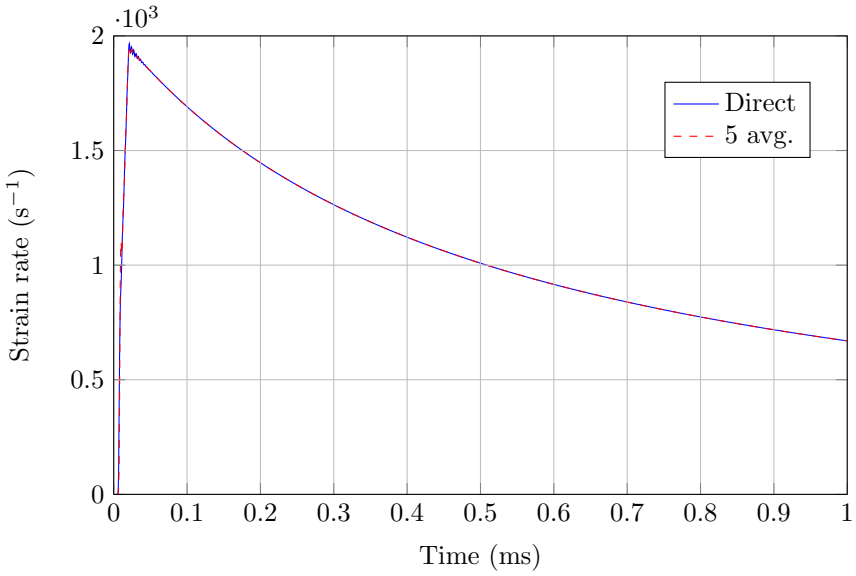

Figure 4.9: Strain rate of a single element test using a Predictor Return algorithm for the Zhao model at dynamic rates. The effect of using an average strain rate is negligible.

The dynamic tests at a strain rate of between 500 and 2000 required no averaging, but to ensure that the correct strain rate was still obtained an averaging method of weight $N = 5$ was compared to that using no averaging in figure 4.9. The difference is insignificant and thus it is acceptable to use a small degree of strain rate averaging in the simulations across all strain rates.

Thus the Zhao locus using the Predictor Return algorithm was chosen to run all the models. To ensure the quasistatic tests ran smoothly an average weighting of $N = 5$ was used across the simulations.

4.3 Damage Model

Of all the damage models reviewed in section 2.2, the fracture locus developed by Bai and Wierzbicki [17] was selected. Bai and Wierzbicki argued that the model is accurate across a wide range of loading conditions and thus is ideal for the work conducted by BISRU. The full form is asymmetric about the normalized lode of 0, yet as all the experiments had normalized Lode angles in the range $0 \leq \bar{\theta} \leq 1$, the reduced symmetric form of the model was implemented.

$$\epsilon_f\left(\eta, \bar{\theta}\right) = \left[D_1 e^{-D_2\eta} - D_3 e^{-D_4\eta}\right] \bar{\theta}^2 + D_3 e^{-D_4\eta} \tag{4.40}$$

This involves 4 constants to be calibrated, as opposed to 6 in the full model.

The terms η and $\bar{\theta}$ refer to the average quantities of triaxiality and normalized Lode defined as,

$$\eta_{avg} = \frac{1}{\epsilon^{pl}} \int_0^{\epsilon^{pl}} \eta(\epsilon^{pl}) \mathrm{d}\epsilon^{pl} \qquad \bar{\theta}_{avg} = \frac{1}{\epsilon^{pl}} \int_0^{\epsilon^{pl}} \bar{\theta}(\epsilon^{pl}) \mathrm{d}\epsilon^{pl} \tag{4.41}$$

The model is calibrated using the method described in [17] and summarized here:

1. The FEA element at which failure occurs first is located, for the specimens tested here this is in the centre of the specimen.
2. At the time of fracture, ϵ^{pl}, η and $\bar{\theta}$ are recorded for the element.
3. The result for each specimen is then included in a Matlab curve fitting algorithm which uses a least-squares approach to find the constants that fit the experimental data optimally.

In implementation failure occurs once the element strain is greater than the failure strain.

$$\epsilon_f(\bar{\theta}, \eta) - \epsilon^{pl} \leq 0 \tag{4.42}$$

At this point the element is deleted from the mesh and does not function in the stiffness matrix for the remainder of the simulation.

4.4 SHB Simulations

A limitation to modelling Split Hopkinson Bar experiments is the length of the two bars relative to the specimen. For example, the input bar is 3.664m long, *i.e.* over 300 times the length of a 12mm specimen.

The problem is twofold, firstly the total test duration is far longer than that required to deform the specimen as the stress wave has to travel the complete length of the input bar and through to the output gauge. The second is that the element count due to the bars is substantial. These elements do not need to be as small as through the specimen, yet the stability time increment, t_{crit}, is determined by the smallest element size and is constant for all elements. Thus the additional computation is substantial.

Three techniques were attempted to reduce computation time. The first involved replacing the $\frac{1}{4}$ symmetry elements through the bar with beam elements. The second removed the bars completely, placing velocity boundary conditions on either side of the specimen based on the experimental results. Finally part of the bars were replaced with infinite elements, which allow the stress wave to pass through without reflecting back.

4.4.1 Beam Elements

Using beam elements does not reduce the physical time duration as the stress wave still needs to travel the length of the bars. However, it does reduce the element count substantially.

The model to determine the validity of the technique is shown in figure 4.10.In the model, a tensile stress pulse is applied at the far end of the solid bar. This stress pulse travels the length of the bar before reaching the beam elements and travelling through these. The interaction is defined by constraining the 3D nodes to move with the same displacement as the beam elements.

The results are compared by considering the stress at a point along the 3D bar, close to the interface. These are shown in figure 4.11, where beam elements with a round cross section and diameters 5, 6 and 10mm are connected to $\frac{1}{4}$ symmetry 20mm diameter bar.

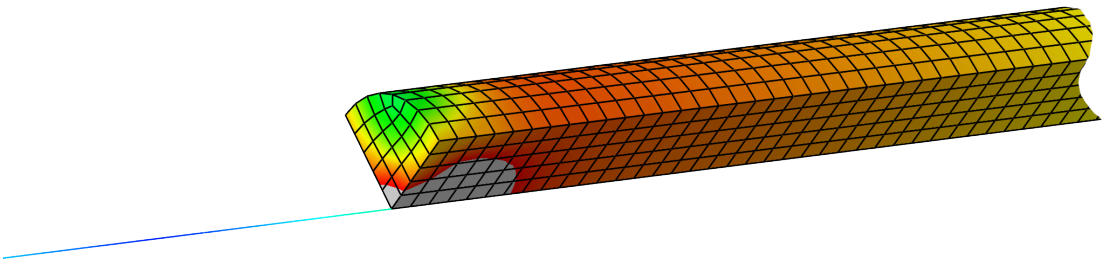

Figure 4.10: Model used to study the effect of replacing the input bar with beam elements. At the interaction surface, the 3D nodes are constrained to move with the same displacement as the beam node.

The ϕ 10 mm beam was chosen initially as it had the same cross sectional area as the 3D section. For this case a significant reflection of over 50 MPa is evident. Interestingly, the reflection of the wave is also tensile, indicating that the interface is acting in a similar manner to a fixed boundary. Thus the solution improved when the beam diameter was decreased, yet could not be perfected as the ϕ 5 mm and smaller beams did not result in improvement from the ϕ 6 mm. However, in repeating the simulation using a full circular solid section with cylindrical beam elements of the same diameter, the stress wave passed completely through the interface with no reflection.

The failure of the beam elements implemented together with the quarter symmetry bar may be to do with the position of the beam axis. For these tests the axis was placed on the edge of the beam (see figure 4.10) and thus the beam cross section is effectively offset from that of the the bar. Abaqus implements the Timoshenko beam theory which, unlike conventional Euler-Bernoulli beam elements, allow for transverse shear strain [59]. Thus the cross section of the beam element may rotate away from being orthogonal to the beam axis. This appears likely to occur in this case due to the beams cross-section being offset from the bar.

The full circular beam test proves that the beam elements could work. It is assumed that these can also be applied successfully to a quarter symmetry bar if the beam axis is selected such that the cross-section of the beam lines up with that of the bar. However, the benefit is limited as the job still needs to be run for the full duration of the Hopkinson experiment. Due to the effectiveness of the infinite element implementation, this investigation was not pursued further.

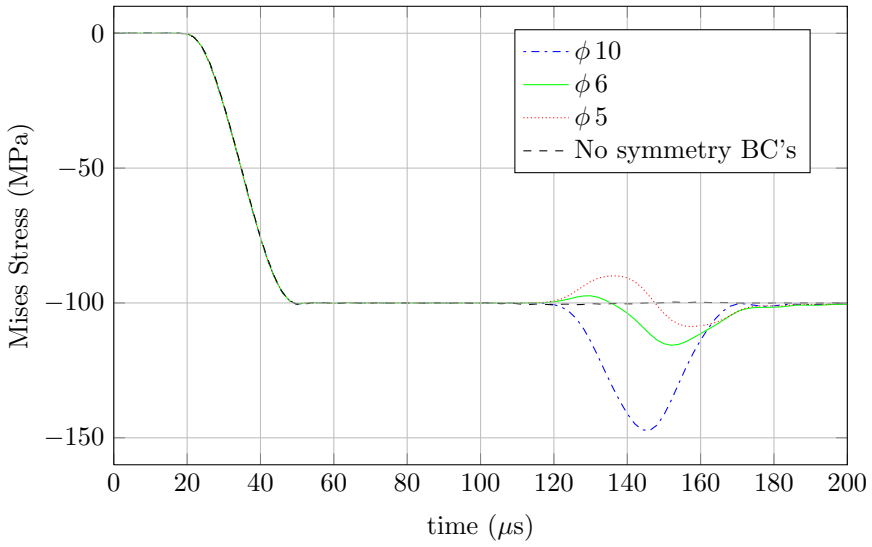

Figure 4.11: Effect of using circular beam elements with dimensions $\phi 10$, $\phi 6$ and $\phi 5$mm with a $\phi 20$, $\frac{1}{4}$ symmetry bar.$\phi 10$mm corresponds to the same cross-sectional area as the bar. Also shown is the result from using a full 3D bar, with no symmetry boundary conditions, together with beam elements of the same dimensions.

4.4.2 Displacement Boundary Condition

An ideal option would be to model the specimen, but remove the bars. This technique was used by Rodríguez et al. [51] to analyse tensile specimens and no errors relating to the loading conditions were reported [20]. The advantage is twofold, firstly the element count is minimized and secondly the simulation is only required to run for the duration deformation occurs.

The aim in this case was to determine whether applying displacement boundary conditions derived from the SHB experiments directly on either side of the specimen would result in accurate simulations. An axisymmetric model was used to test the option. The first simulation included both bars specimen and was used to determine the displacements on either side of the specimen resulting from a stress pulse being applied as in a physical test. The built-in Johnson-Cook plasticity model was used for the specimen with properties $A = 350\,\text{MPa}$, B=275 MPa, C=0.022, $\eta = 0.36$, $\dot{\epsilon} = 1$, a melting temperature of 1811K and room temperature of 300K.

[20] See section 2.6.1.

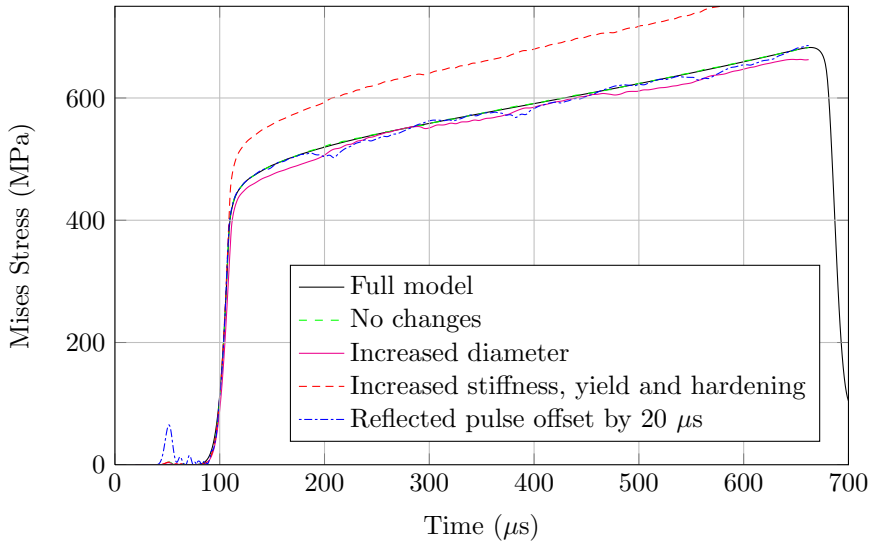

Figure 4.12: Specimen stress versus strain curves resulting from using velocity boundary conditions. The full model is compared to that using the velocity BC's with the same specimen properties. The properties are then changed resulting in poor correlation.

The first comparison, shown in figure 4.12, modelled only the specimen using the derived displacements, but keeping all material specimen properties constant. This gave an identical result to the complete setup. However, in finite element simulations, the calibrated material properties are only a good approximation to the true properties.

Furthermore, small errors may occur in measuring specimens. To determine whether these minor errors could result in poor simulations, the specimen properties and dimensions were altered. Thus in the second comparison, the specimen diameter was increased from 5 to 6mm resulting in some oscillations and a slight decrease in magnitude.

Keeping the dimensions the same as the original, but increasing the Elastic modulus from 200 GPa to 210 GPa, and the yield constants A and B to 400 MPa and 325 MPa respectively predictably resulted in a stronger specimen. However, additional oscillations within the signal are evident.

The situation is even worse when the reflected pulse is incorrectly offset by 20 μs. This results in the correct magnitude, but significant oscillations.

The first issue of magnitude is not related to displacement conditions, but rather to material properties. For example a higher yield leads to greater elastic strain and thus higher stresses within the plastic regime.

The second issue of oscillations within the signal can be explained by spurious reflections within the specimen. Using a specimen with identical properties to the actual works correctly as the stress waves generated by the displacement boundary conditions create displacements on the specimen-bar interface identical to the imposed boundary. However, changing the properties creates a mismatch between the imposed displacements and those generated from the stress waves. For example a larger specimen diameter results in lower deformation through this region and at the output boundary.

Thus stress wave reflections occur at the boundary creating oscillations and loading the specimen differently to that in tests. Determining exact specimen properties to eliminate these is unlikely. The method is workable if specimen geometries and properties are extremely close to the actual properties, but is not ideal.

4.4.3 Infinite Elements

A more natural solution is to use *infinite elements* to replace the bars. In explicit analysis, Abaqus includes an implementation of infinite elements based on that by Lysmer and Kuhlemeyer [63]. These are designed to damp the boundary such that no stress wave reflection is returned.

The method is simple, the infinite elements result in damping on the boundary of the form,

$$T_{11} = -d_p \dot{u}_1 \qquad T_{12} = -d_s \dot{u}_2 \qquad T_{13} = -d_s \dot{u}_3 \tag{4.43}$$

where T_{ij} represents the Cauchy stress components, d_p and d_s the damping constants under normal stress and shear, and $\dot{u}_j$ the velocity components.

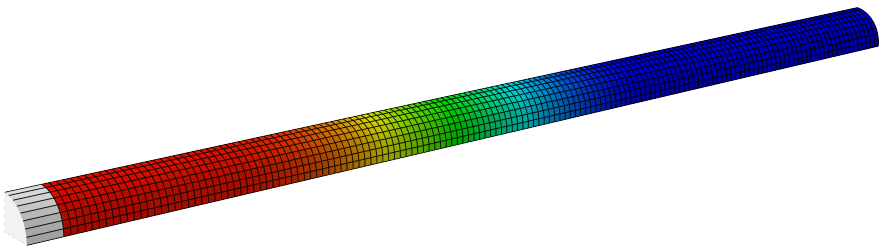

Figure 4.13: Model used to study the effect of placing infinite elements in place of the input bar. The infinite elements are in the foreground.

The damping constants are calibrated to prevent stress reflections at the boundary by setting the value to,

$$d = \rho c \tag{4.44}$$

Thus the constant is related to the density and wave speed, which itself is given by $c = \sqrt{\frac{E}{\rho}}$.

Using Infinite Elements as a Boundary

The configuration for testing the effectiveness of the infinite elements is shown in figure 4.13 and consists of a quarter symmetry bar with infinite elements placed on the one end. A stress pulse is applied to the free end and an element sampled midway along the bar, to record spurious reflections. The properties of the bar were modelled as aluminium with $E = 70\text{GPa}$ and $\rho = 2800\text{m.s}^{-1}$

Figure 4.14 shows the incident pulse followed by the reflection against the infinite boundary. Interestingly a reflection of roughly 5% did occur. A small error is not completely unexpected as the Abaqus documentation [59] describes the infinite boundaries as “quiet” as opposed to “silent”. The reflection is of the same nature (tensile) as the incident wave and thus the infinite elements were over-damping the boundary.

By iteratively decreasing the elastic modulus of the infinite elements by roughly 25% to 53.5 GPa, or a decrease in damping coefficient of 12.5%, the reflection is minimized. With reduced damping, infinite elements seem ideal to simulate the SHB bars as the reflection is negligible.

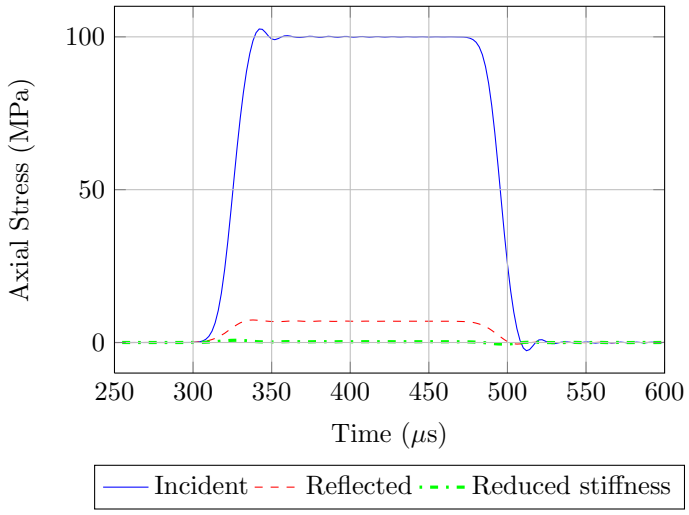

Figure 4.14: Incident pulse reflected against a boundary of 'infinite elements'.

Applying the load

If infinite elements are used, a load needs to be placed in the centre of the bar, between the infinite and continuum elements. The load can be either a displacement or a stress and, in the case of a split Hopkinson test, it is convenient to use a stress as this is taken directly from the strain gauge reading.

To test the system, an incident stress pulse of 70 MPa was aimed for at a point along the bar. The load cannot be placed at the end of the infinite elements, as these would absorb the stress pulse, and thus must be placed between the infinite and continuum elements. In this case the load is applied to one surface (the continuum elements), but acts on two (the infinite elements and the continuum elements). Thus the magnitude of the applied load should be twice that required.

The results for the test are included in figure 4.15 and show that if infinite elements with no reduced damping are used, the input stress needs to be increased from 140 to around 150 MPa. In contrast, the reduced damping infinite elements required very little change to the input pulse magnitude. Indeed in calibrating the infinite elements to damp the actual bars, no magnitude modification was required.

A technicality when using the Abaqus software for the FEA analysis is that the load must be applied as part of a user defined load, or *VDLOAD*. If not, Abaqus does not recognise loads applied internally in the bars.

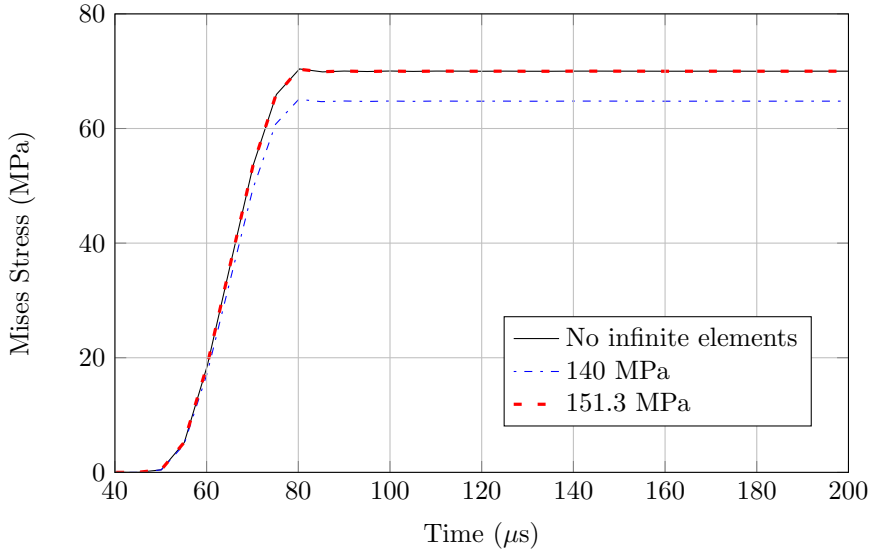

(a) Using infinite elements with properties identical to that of the bar

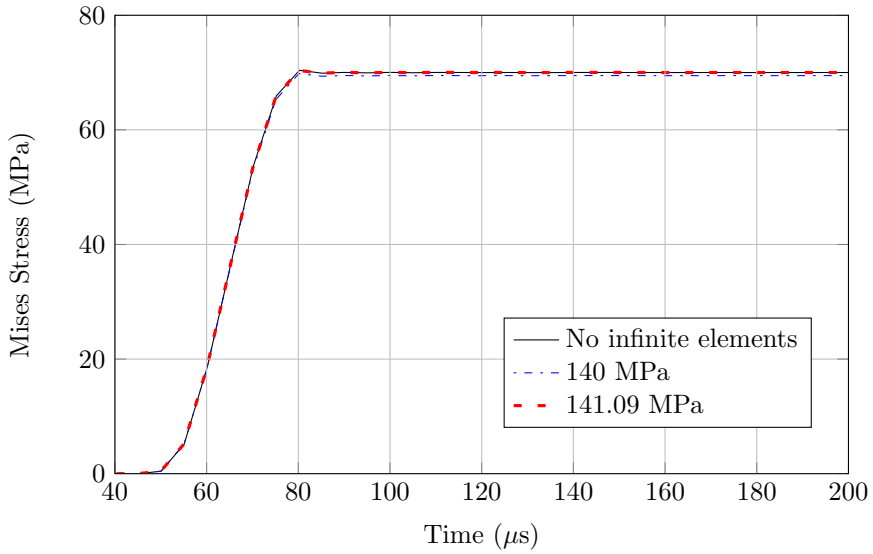

(b) Using infinite elements with modified properties to minimize reflections

Figure 4.15: Stress obtained in the bar by applying a pressure load at the boundary between the infinite and regular elements.

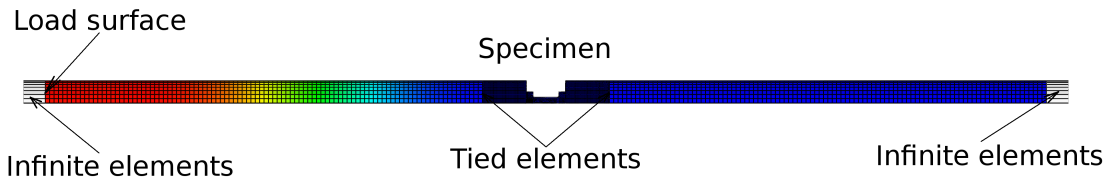

Figure 4.16: Final model for simulation split Hopkinson bar experiments.The model consists of input and output bars with infinite elements and a densely meshed specimen and bar region.

Application to TSHB Test

The final setup for the SHB simulations is shown in figure 4.16. This consists of an input bar with infinite elements at the end where the load is applied, a densely meshed region including the specimen and finally the output bar with infinite elements at its far end. Note that the infinite elements are placed 200mm from the specimen as it is recommended to position the elements away from the main area of interest[59].

The specimen is densely meshed and thus the simplest way to connect the coarse bars to the specimen is to set a nodal tie which constrains the displacement of the nodes at the interface to move in the same manner. To ensure that this interface does not have any effect on the specimen itself, a small region of bar of length 20mm is meshed on either side of the specimen and this is tied to the outer bars.

As a final validation, a series of parallel tests were run comparing the setup shown in figure 4.16 including infinite elements to a full model with the bars. A built-in Johnson-Cook plasticity model with both temperature and strain rate effects was used. Both stress in the centre of the specimen as well as the bar displacements on either side of the specimen were compared.

The first test considered using infinite elements with no reduced damping, but with an increased input stress to compensate for the small reflection at the infinite boundary as considered in section 4.4.3. Figure 4.17 shows that while the stress profile is correct, the displacements on both bars is underestimated. This must be due to the tensile reflections reducing the displacement through the bars. However, the resulting specimen extension is correct.

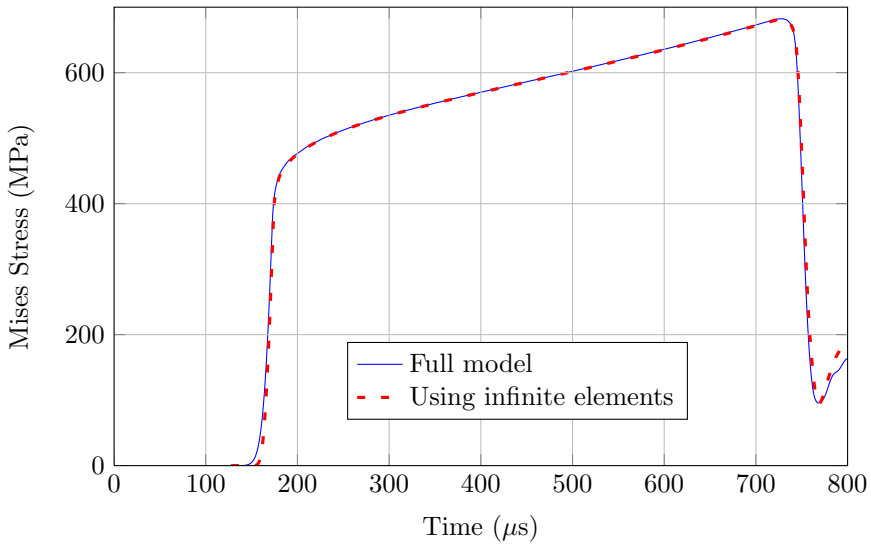

(a) Equivalent stress at the specimen centre.

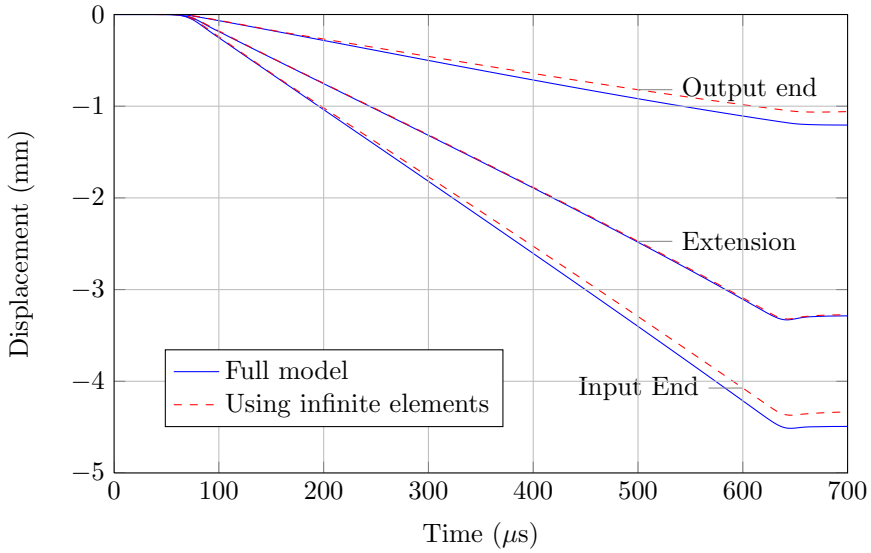

(b) Displacement at either side of the specimen.

Figure 4.17: Specimen deformation resulting from using infinite elements with properties identical to the bars and iteratively increasing the load magnitude until the input stress is equal to that in the full model.

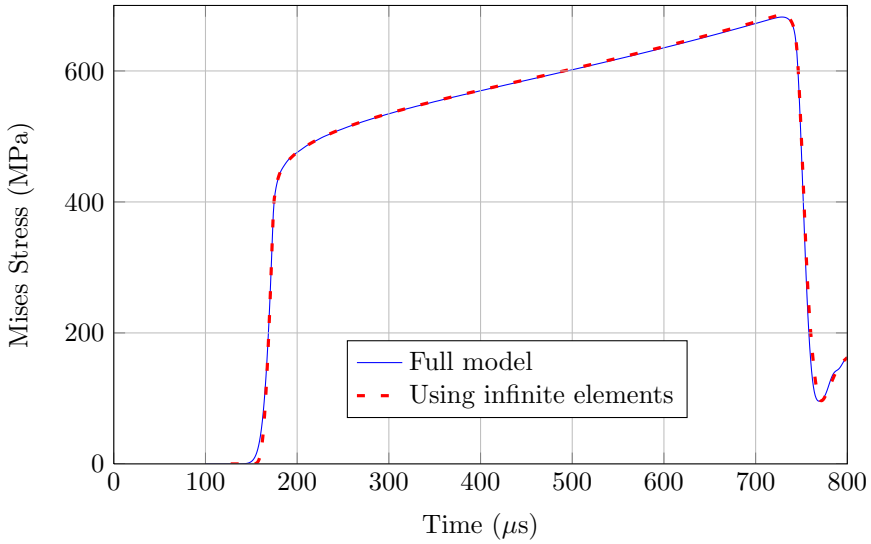

(a) Equivalent stress at the specimen centre.

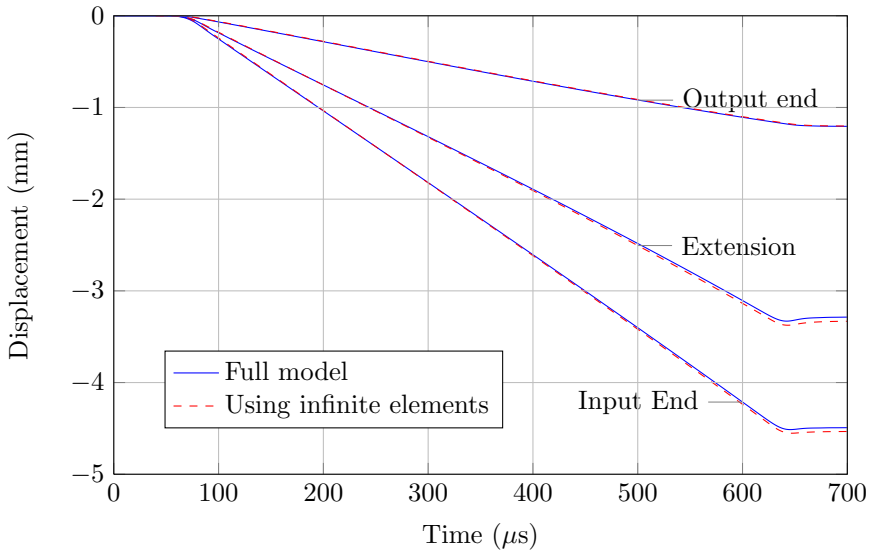

(b) Displacement at either side of the specimen.

Figure 4.18: Specimen deformation resulting from using infinite elements with material properties optimized to prevent reflections.

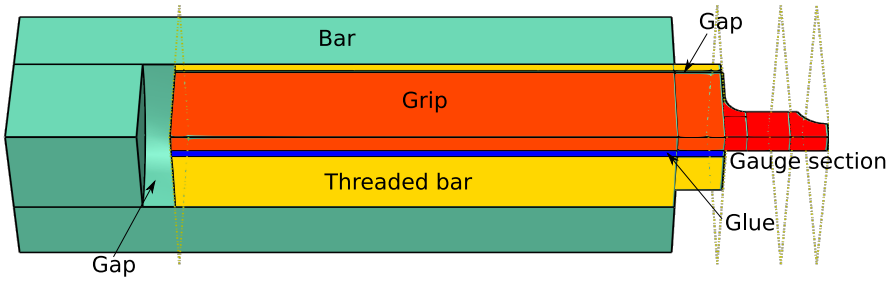

Figure 4.19: Dynamic model specimen geometry.

A better solution is obtained with reduced damping infinite elements, shown in figure 4.18. In this case both the specimen stress profile and bar displacements correlate almost perfectly. This method was chosen to run the simulations as the specimen iteration is almost identical to that modelling the complete apparatus. Although a simple addition, a benchmarking test on a coarsely meshed TSHB setup showed that using infinite elements cut down runtime from 12.3 to 1.2 min., a reduction over 90%. Thus the time saved running densely meshed simulations is significant.

4.4.4 Modelling the Specimen

Figure 4.19 shows a typical dynamic model of a specimen attached to a short section of bar. Note that the only geometry simplification is the threaded connection, which is this case is modelled simply as a solid part with section cut out of it representing the threaded bar.

Plasticity is expected to occur within the gauge section and thus the damage VUMAT is applied. The specimen grip section is glued onto the threaded bar. It is assumed that the deformation through the region is very low and limited to the elastic region and thus the material was modelled as elastic.

Fixing the specimen to the threaded bar is a 0.5mm thick layer simulating the epoxy. This was approximated as elastic with a density of 1200 $\mathrm{kg.m^{-3}}$, Poisson's ratio of 0.4 and elastic modulus of 1.8 GPa. The stiffness was taken as that used by Djilal [64] with the same epoxy as used here.

The threaded bar was given generic properties for mild steel of $E = 20\,\text{GPa}$, $\nu = 0.3$ and $\rho = 7800\,\text{kg.m}^{-3}$. At the end of the thread a small gap was set as the threaded bar is only fixed at its surface. Finally the bar sections were given the same properties as the input or output bar depending upon which each was tied to.

4.5 Quasistatic Tests

4.5.1 Mass Scaling

Normally when modelling a quasistatic tensile test an implicit finite element scheme is used as these are not constrained by the critical time constant, t_{crit}, that is required for stability in explicit analyses. However, writing an equivalent user model for an implicit analysis ($UMAT$) is beyond the scope of this thesis and thus an explicit finite element method was used for both the quasistatic and dynamic simulations.

The critical time constant poses a major problem for an explicit analysis that is required to run over several seconds as it is so small relative to the total duration. In a typical case $t_{crit} \approx 5 \times 10^{-9}\,s$ or lower with a total test time of 3s resulting in 600 million time steps. This is unrealistic even with extensive computing power.

An option is to introduce mass scaling. This technique artificially increases the density of critical elements. Thus the wave speed, $c = \sqrt{\frac{E}{\rho}}$, decreases leading to an increase in the critical time constant, approximated by

$$t_{crit} \approx \frac{L_{min}}{c} \tag{4.45}$$

where L_{min} is the smallest critical dimension of an element.

Thus increasing ρ by f^2 reduces the number of increments, n, to $\frac{n}{f}$[59]. However, if the density is increased too much, the inertia of these elements becomes significant, degrading the accuracy of the solution.

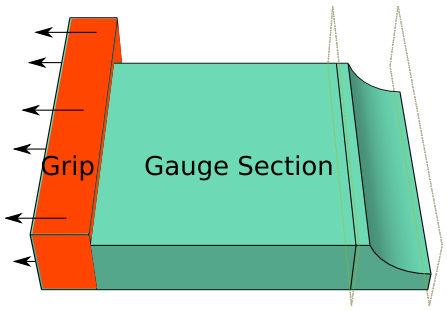

Figure 4.20: Quasistatic model specimen geometry.

In characterising steel for blast simulations, Bonorchis [54], successfully used mass scaling to simulate quasistatic tensile tests. Mass scaling between between 5 and 625 times was implemented with little ill effects. Thus in this analysis the mass scaling was kept within this range. The negative effect of the technique used in these limits seems negligible as mass scaling of 350 resulted in identical readings to that using only 8.

In implementation, a minimum stable time step, typically 3×10^{-7} s, was set and the mass of elements resulting in lower critical times increased to meet this limit. Thus a significant number of time steps were still required, but most jobs were able to run in under 20 hours using 6 processors.

4.5.2 Specimen

The model for the quasistatic specimen is simple and consists of a gauge region with the same properties as the VUMAT and a small grip section with only the elastic properties. $\frac{1}{8}$ symmetry was used to minimize the element count, while a set velocity boundary condition was applied to the grip section, shown in figure 4.20. It was found that simplifying the model further and applying the boundary condition directly onto the end of the gauge region resulted in marginally different deformation. The change is presumably due to the transition from the grip to the gauge zone influencing the loading distribution, yet only a small grip section was required to correct this.

The results for all the final simulations, which model the specimens, are covered in chapter 6.

Chapter 5

Experimental Tests

5.1 Introduction

This chapter presents the experimental results of deforming tensile specimens at dynamic and quasistatic strain rates. The specimens, designed together with the apparatus in chapter 3, have differing geometry to create a range of loading conditions characterized by triaxiality and Lode angle. These results are used in the simulations of chapter 6 to study rate effects and the effectiveness of the Bai-Wierzbicki damage locus, covered in section 2.2.

The first two sections cover the the techniques used to analyse the readings. For the dynamic experiments this includes calibration techniques as well as a brief study on the influence of threaded connections used to secure the specimens. The quasistatic section deals with removing machine compliance and specimen slip effects.

The final three sections contain both the quasistatic and dynamic results for the straight specimens followed by the notched and finally the grooved specimens.

Due to the complicated geometry it is not trivial to determine the true stress throughout the specimen. For this reason an engineering stress is used to express the results. This is defined as,

$$\sigma = \frac{F}{A_0} \tag{5.1}$$

where F is the force through the specimen and A_0 the initial area through the notch cross-section. In certain cases the data collection failed and these have been excluded. Note that where strain gauge stress readings are shown, tensile stress is taken as negative.

5.2 Dynamic Test Procedures

5.2.1 Calibration

To analyse the split Hopkinson bar results, the bar material properties of elastic modulus E, density ρ and wavespeed c are required. Secondly the calibration factor, K, which is the ratio between the measured strain gauge reading and stress in the bar must be determined.

Bar Properties

Wavespeed can be determined by timing the movement of a stress pulse through the bar and comparing it to the distance travelled. In implementation, a short striker with excess putty is used to create an approximately sinusoidal pulse with almost no dispersion. The sinusoidal pulse is formed as the excess putty dampens the impact, removing high frequency wave components and thus minimizing dispersion[21].

The stress wave is recorded as it passes the strain gauge and again after it reflects against the end of the bar and returns. The reflected wave is processed by shifting it in time until it is aligned with the original signal and this offset is taken as the delay, Δt. The distance is twice that from the gauge to the end of the bar.

$$c = \frac{d}{\Delta t} \tag{5.2}$$

[21] Dispersion is covered in section 2.3.3 on page 44.

A degree of error exists as the reflected signal is offset manually. However, the bars are long and thus the magnitude of the offset is large compared to possible error.

The density is determined from the volume and mass and thus finally, knowing the wavespeed, the elastic modulus is determined simply by [5],

$$E = c^2 \rho \tag{5.3}$$

Gauge Factor

The gauge factor is used to convert the strain gauge output, in volts, to axial stress that can be used to analyse specimen deformation. This factor is estimated using strain gauge theory (*theoretical calibration factor*), but human error dictates that the strain gauges are not perfectly aligned and thus a degree of error exists. Thus a more accurate measure is experimental testing. In this work two methods are considered, the first determines the change in momentum of the striker (*momentum balance calibration factor*) when it hits the bar as this is equal to the momentum transferred as the incident pulse. The second method uses the impact of uniform bars theory to relate the maximum stress in the bar to the striker velocity (*maximum stress calibration factor*).

Theoretical Calibration Factor

The gauge output signal based on strain gauge theory is given by [65],

$$V_{out} = \frac{1}{4} K_{gf} N \epsilon V_{in}$$

where K_{gf} is the strain gauge factor, N is the number of arms in the Wheatstone bridge and V_{in} the bridge voltage. Noting that,

$$\epsilon = \frac{\sigma}{E} \quad \text{and} \quad V_{out} = \frac{V_{read}}{G_{amp}}$$

with V_{read} the amplified output and G_{amp} the gain, and that the calibration factor is defined by,

$$K = \frac{\sigma}{V_{read}}$$

The factor can be written as,

$$K_{theory} = \frac{4E}{G_{amp} K_{gf} N V_{in}} \tag{5.4}$$

For TSHB setup at BISRU $K_{gf} = 2.16$, $N = 4$ and a gain of 1000 is used resulting in,

$$K_{theory} = \frac{E}{2160 V_{in}} \tag{5.5}$$

Momentum Balance Calibration Factor

The momentum calibration is given by [54],

$$K_{mom} = \frac{I}{A_b \int_0^T V_{read} dt} \tag{5.6}$$

where the impulse can be determined from the striker velocity,

$$I = m_s \Delta v$$

The initial velocity is measured using a light sensor on the barrel, while the final velocity can be obtained using equation A.20, which is based on the elastic impact of bars with uniform material properties.

$$v_f = \frac{v_i \left(\frac{A_s}{A_b} - 1 \right)}{\left(1 + \frac{A_s}{A_b} \right)}$$

Using this calibration factor, pulse smoothing should not be used as the putty absorbs part of the energy due to the striker impact and thus the momentum transferred to the bar is reduced.

Table 5.1: TSHB properties.

	E (GPa)	ρ (kg.m^{-3})	c (m.s^{-1})	K_{theory} (MPa/V)	K_{mom} (MPa/V)	K_{stress} (MPa/V)
Input bar	73.7	2762	5165	13.767	12.40	13.17
Output bar	73.5	2769	5150	13.63	12.75	12.98

Maximum Stress Calibration Factor

A second method is simply to determine the maximum stress in the bar and compare that to the readings.

$$K_{stress} = \frac{\sigma^{max}}{V^{max}} \tag{5.7}$$

with the maximum stress estimated from equation A.18,

$$\sigma^{max} = \frac{A_s}{A_s + A_b} c\rho v_i$$

For this technique pulse smoothing should be used to minimize the oscillations due to dispersion throughout the region of maximum stress.

Implementation

For accurate calibration, the impact area should be the same as that through the remainder of the bar. However, the TSHB provided complications as the output bar could not be directly calibrated due to the thread hole drilled into the specimen end. Thus the calibration factor for the input bar was determined first. The output bar could then be calibrated by securing it with a threaded bar to the input bar and comparing the signals in each.

The properties for both bars are given in table 5.1. Three tests were run for each calibration and the average taken. Ultimately the stress calibration factor was used as this has been found to give the most accurate results[22]. A typical calibration curve using the maximum stress calibration technique is included in figure 5.1.

[22]Private conversation with R. Govender

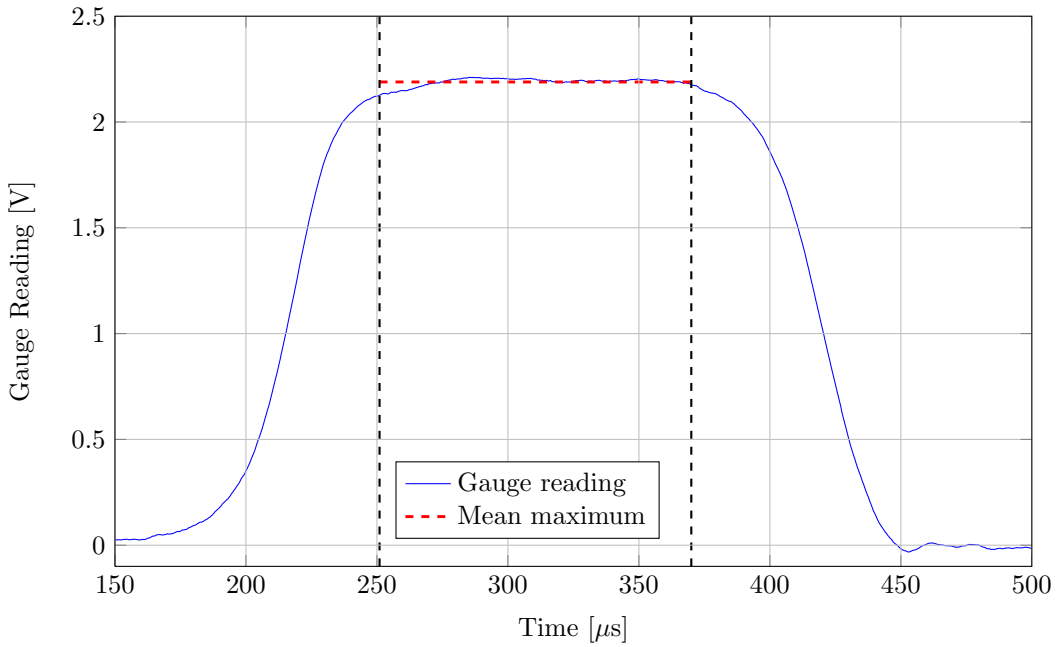

Figure 5.1: Maximum stress calibration factor curve. The peak stress is taken as the mean in the centre of the pulse, between the rise and fall.

5.2.2 Thread effect

The two major uncertainties with the specimen attachment technique are the thread connection together with the effectiveness and stiffness of the glue. The former was investigated by connecting the input and output bars directly together with a length of threaded bar. By using the striker to create a tensile pulse in the input bar, the change in pulse through the thread interface can be found.

The result, shown in figure 5.2, indicates that the thread interaction has only a minor effect. Some discrepancies are evident at the start of the pulse, but nothing significant later on. Note that for this comparison the output pulse needs to be scaled by a factor $\left(\frac{d_o}{d_i}\right)^2$, with d_o and d_i the output and input bar diameters respectively, due to the different areas of each bar.

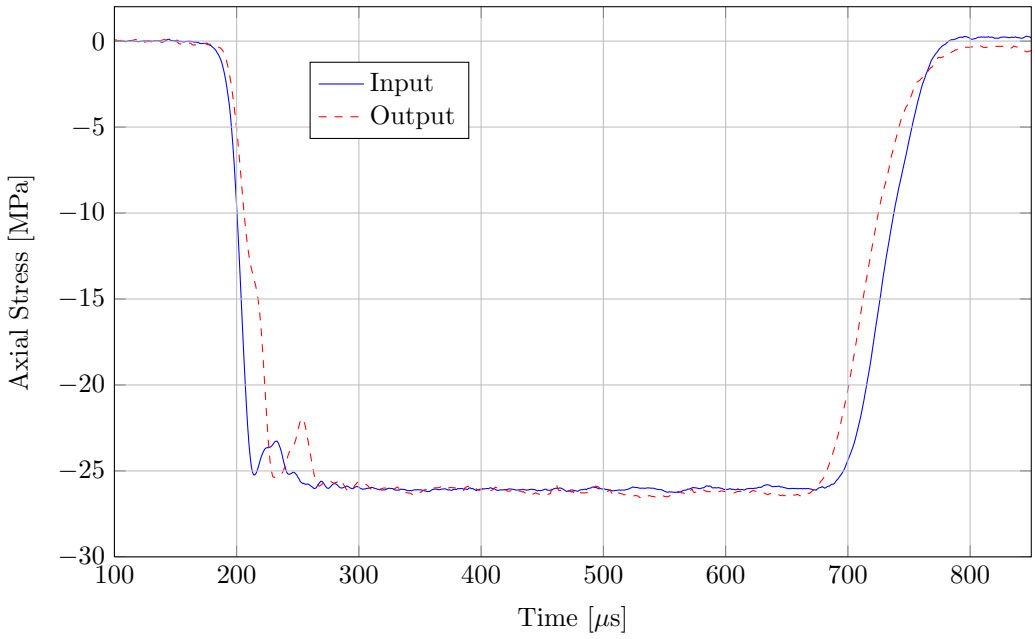

Figure 5.2: Effect of the threaded connection on the stress pulse. Measurements were taken at the input gauge before the thread interaction and at the output gauge after. Note that tensile stress is taken as negative.

For certain SHB experiments, the thread interaction may have had a greater effect, one example is the 1.25mm radius grooved specimen 4. This did not fracture, instead figure 5.3 indicates that a large velocity occurs in a region of zero stress. On analysing high speed camera footage of the experiment (recorded at 5×10^4 frames per second), the thread can be seen to shift slightly back and forwards as the stress wave passed through. This is shown in figure 5.4.

Although the specimen is an extreme case, analysis of the other tests shows that minor displacements within the threads does occur, with the severity possibly depending on how tightly the specimens are screwed into the bars. This would result in the initial specimen velocity result being too high and thus an overestimation of displacement, being the integral of velocity.

A second case was specimen 2 shown in figure 5.5 with a large displacement of 0.2mm before the peak was reached. This case may be due to shifting in the thread as the stress remains low before peaking sharply. However, the effect on the majority of specimens is noticeably lower. Furthermore, the relative influence is much smaller for the notched and straight specimens due to the greater displacement at failure.

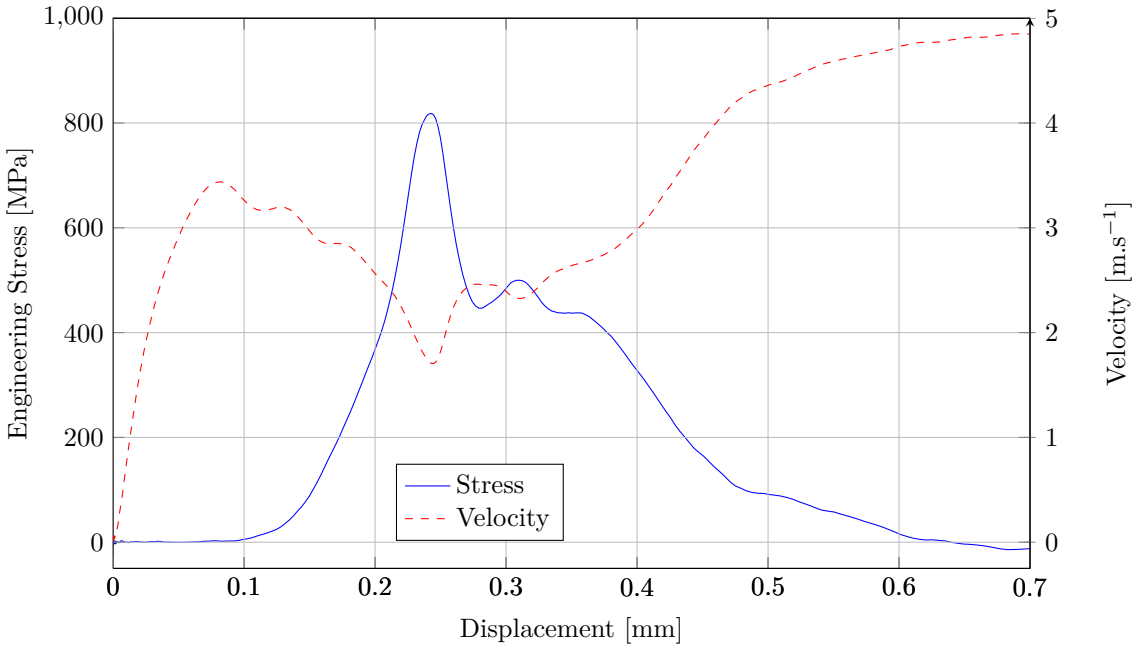

Figure 5.3: TSHB results for the 1.25mm radius grooved specimen 4. This specimen did not fracture during testing.

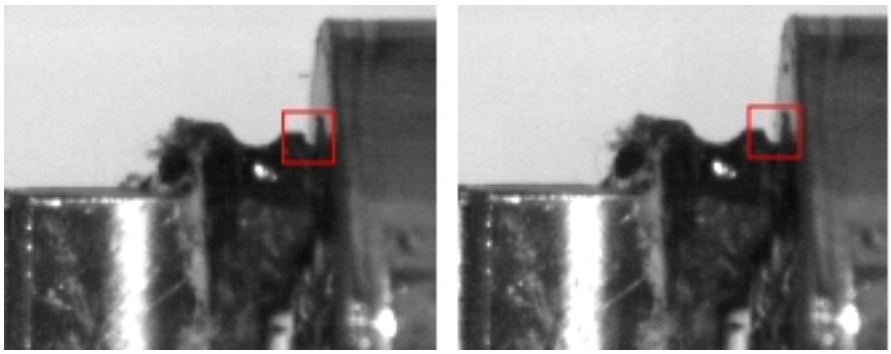

Figure 5.4: High speed camera images showing the threaded bar move within the output bar. The displacement can be seen by considering the tip of a thread as highlighted.

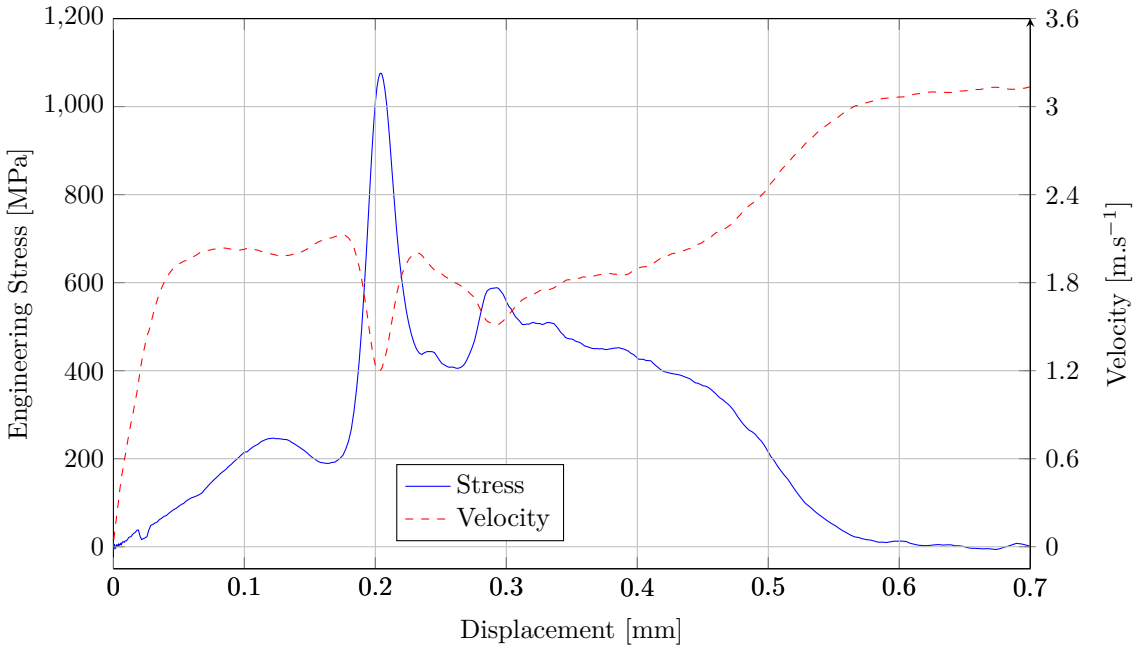

Figure 5.5: TSHB results for the 2mm radius grooved specimen 2.

5.3 Quasistatic Test Procedures

The quasistatic tests are conducted on a Zwick 1484 testing machine with the specimens held on either side with self locking wedge grips. These provide a gripping force proportional to the tensile axial force through the machine. A typical result is shown in figure 5.6, note that significant slip occurs initially before the tensile force is great enough to grip the specimen correctly. This is not a major obstacle as no visible slip occurred at greater stresses.

There is inherent machine compliance due mainly to the wedge grips, the apparatus needed to secure these to the Zwick and the crosshead beam deflection. As the specimens are small, the compliance has a major influence over the results and if not removed the specimen deformation is significantly overestimated.

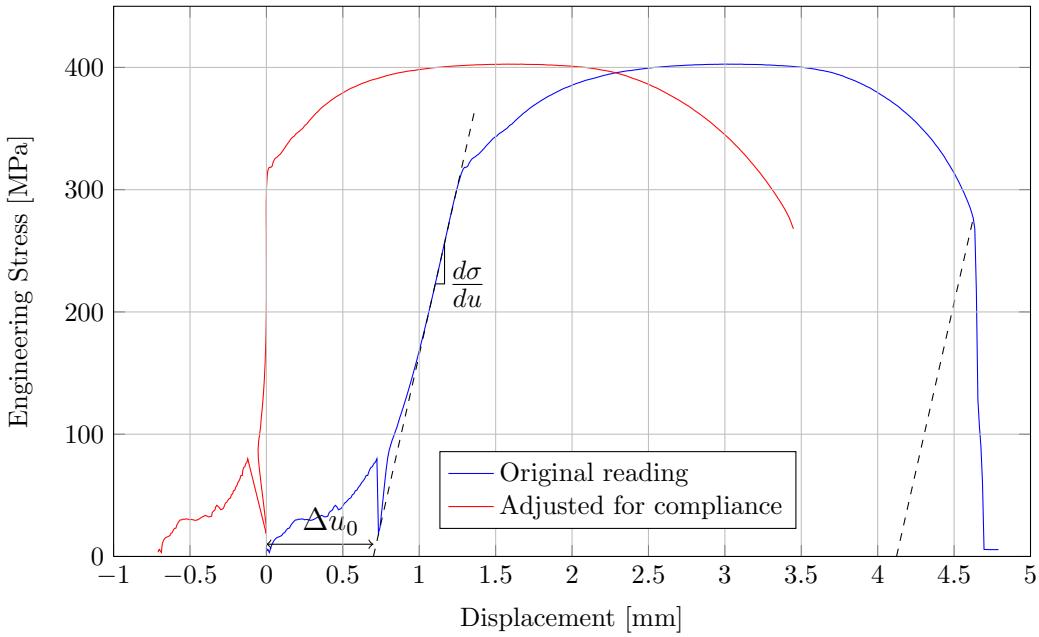

Figure 5.6: Original quasistatic reading and that with machine compliance and slip removed.

For these experiments the compliance effect is accounted for by determining the ratio of engineering stress σ, proportional to the reaction force through the load cell, and displacement, u.

$$m = \frac{\delta\sigma}{\delta u} \tag{5.8}$$

The reading was taken through the region with the highest gradient as shown in figure 5.6.

The displacement due to the compliance, u_c is taken as proportional to the magnitude of the engineering stress,

$$u_c = \frac{\sigma}{m} \tag{5.9}$$

Once the gradient is known, the initial slip can be determined by considering intercept displacement of a line with this gradient passing through the point of maximum gradient, (u^*, σ^*) and the zero stress axis.

$$\begin{aligned} \sigma &= mu + c \\ \therefore c &= \sigma^* - mu^* \\ \text{and } u_0 &= -c/m \end{aligned}$$

The correct displacement, u_f can now be determined by removing that due to compliance and slip,

$$u_f = u - u_c - \Delta u_0 \tag{5.10}$$

A measure of accuracy is given by table 5.2. This compares the measured displacement at failure for the 5mm radius notched specimens to that calculated using the force displacement history, taking into account compliance and slip. The results compare very closely and are generally within the tolerance of the vernier calliper (0.02mm) used to measure the specimens. Thus the technique is a valid method for determining specimen deformation.

Table 5.2: Final calculated and measured specimen displacement for the 5mm radius notch specimens.

No.	Calculated (mm)	Measured (mm)	Difference (%)
1	1.83	1.8	1.64
2	1.83	1.82	0.55
3	1.71	1.7	0.58
4	1.74	1.76	1.09
5	1.73	1.7	1.73
6	1.83	1.82	0.55

Table 5.3: Measured dimensions of the straight specimens.

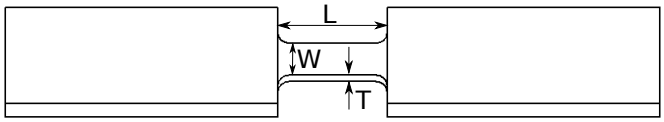

No.	L (mm)	W (mm)	T (mm)
SHB specimens			
1	11.9	4.15	1.31
2	11.9	4.11	1.34
3	11.9	4.11	1.38
4	11.98	4.03	1.39
5	11.98	4.025	1.41
6	11.98	4.00	1.37
Zwick specimens			
1	12	4.05	1.44
2	11.98	4	1.23
3	11.98	4.02	1.39
4	12.14	4.015	1.385
5	12.1	4.03	1.34
6	11.98	3.98	1.26

5.4 Straight Specimens

The measured dimensions for the straight specimens are included in table 5.3, with an example of specimen deformation in figure 5.7. For this design the length and width are consistent to within 4.5%. However, as the thickness varied between 1.23 and 1.44mm, a discrepancy of roughly 15%, direct comparisons between the specimen results can be misleading.

The quasistatic results with compliance and slip removed are shown in figure 5.8. Two displacement rates were used, the first 0.6mm/min or 0.01mm/s corresponds to a low initial strain rate of $\approx 1 \times 10^{-3}\text{s}^{-1}$. The second was 100 times faster with a strain rate of roughly 0.1s^{-1}. These are referred as the *slow* and *fast* quasistatic rates.

To compare the strain rate effect on final displacement, it is convenient to group the specimens with those of similar thickness. These are 1 & 4; 2 & 6; 3,4 & 5. In each case the specimens broken at the fast rate fail at a slightly greater displacement than those at the slow rate.

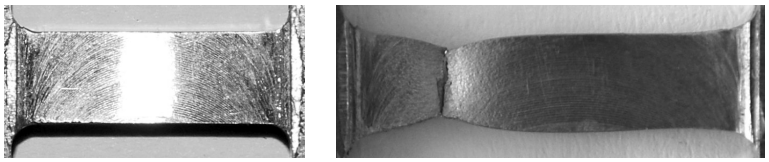

(a) Quasistatic 4

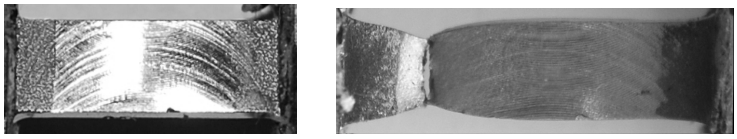

(b) Dynamic 6

Figure 5.7: Straight specimen photographs showing a quasistatic and dynamic example taken before and after deformation.

Having to group the specimens raises the question of repeatability. The specimen geometry inconsistencies indicate that either machining accuracy needs to be improved, or more specimens should be tested at each strain rate to ensure that several have almost identical dimensions. However, due to the manufacturing time required this was not possible. Positively, the results for the notched and grooved specimens are more consistent.

In contrast to the trend at low strain rates, the dynamic specimens fail at noticeably lower displacements than the quasistatic specimens. These results are shown in figure 5.9 and show the specimens failing at displacements between 2.3mm and 2.8mm in comparison to the quasistatic results between 3.2mm and 3.8mm. This is clear from analysing the specimens post failure with the two specimens shown in figure 5.7 having similar widths, but the quasistatic deforming significantly more. All the dynamic specimens failed away from the gauge centre, while the quasistatic specimens failed both in the centre and to the side.

The considerable difference in final displacement is at least partly due to the relative strain hardening gradient through the specimen. In calibrating plasticity models Zhao [57] among others found that specimens deformed at quasistatic rates yield far earlier, but undergo greater hardening with strain than those tested dynamically.

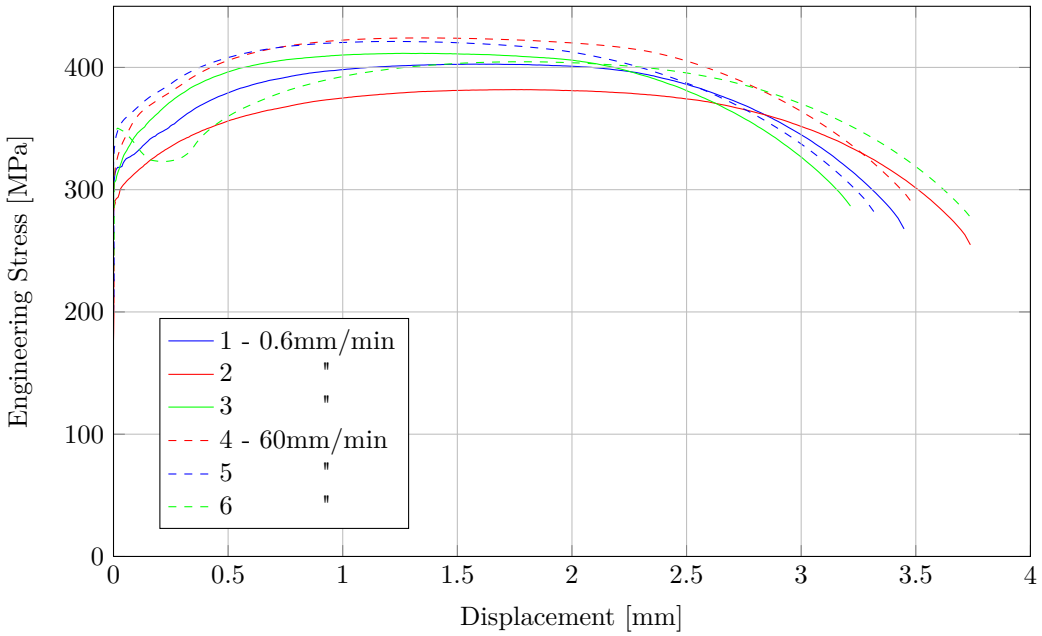

Figure 5.8: Quasistatic results for the straight specimens.

In addition, the Considère criterion [43] states that necking occurs when the true hardening rate equals the true stress,[23]

$$\frac{d\sigma}{d\epsilon} = \sigma \tag{5.11}$$

Thus a material with a higher hardening gradient should neck later than one with a lower gradient. This is evident for the straight specimens considered here as the dynamic specimens neck at a considerably lower displacement than the quasistatic equivalents. Necking is an unstable deformation resulting in localized strain and ultimately ductile failure and hence specimens that neck early can be expected to fail at a lower displacement. Note however, the effect of strain rate on ductile fracture itself cannot be separated from this phenomenon without parallel simulations to determine the strain in the neck centre.

[23] Detailed in section 2.4 on page 45.

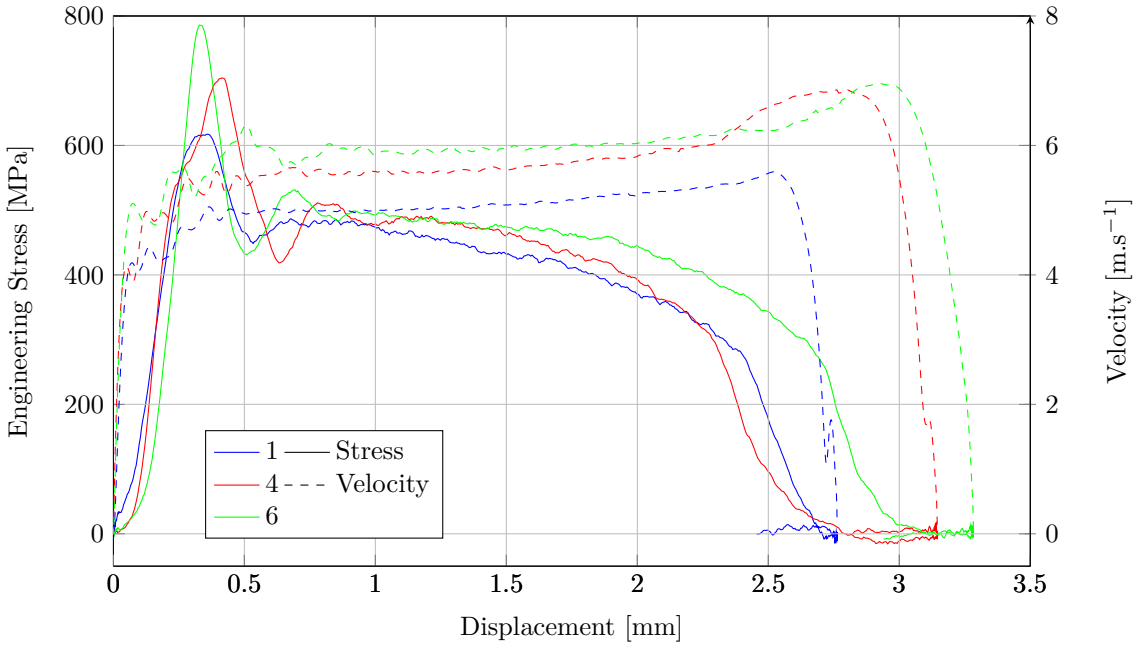

Figure 5.9: The deformation velocity is measured as the difference between the bar velocities on either side of the specimen.

The deformed specimen photograph (figure 5.7) highlights the main problem with testing these straight specimens. Failure is expected to occur in the specimen centre as the influence of the transition zone on either side of the gauge section is lowest [24]. However, generally failure does not occur in the centre of the gauge section. For example, the specimens shown in the figure failed very close to the transition zone, presumably due to a small notch (imperfection) at the location that resulted in the neck being formed away from the centre.

The failure location poses a complication for the simulations as a rough analysis showed that these predict failure in the specimen centre. As the specimens fail close to the transition zone, it is unlikely that the non-axial stress distribution, which affects triaxiality, is the same as in the centre. Thus for an accurate analysis imperfections would need to be placed in the model to initiate necking in the correct location.

[24] Covered in the literature review section 2.5.5 on page 53.

The dynamic results show the success of this version of the tensile split hopkinson bar method. Apart from a stress spike at low displacements, the resulting engineering stress is relatively free of oscillations. The stress spike is not evident in the incident pulse, shown in figure 5.10, and may be due to the interaction of the glue and thread securing the specimen to the bars. Similarly, the velocity profile is relatively constant up until fracture at which point it increases as the load is removed.

The success of the tubular striker method is seen in figure 5.10 by the form of the incident wave which has a constant magnitude with low oscillations. Further the change between the transmitted stress wave and the difference between the incident and reflected is small indicating that the specimen is in quasi-equilibrium for a significant duration of the test.

Note that as the output bar (ϕ20.05 mm) has a larger area than the input (ϕ19.1 mm), the transmitted stress is expected to be lower than that measured from the input bar. A clearer comparison is shown in figure 5.11 in which the transmitted pulse is scaled by the the bar area ratio of $\left(\frac{d_i}{d_o}\right)$ where d_i and d_o refer to the input and output bar diameters respectively. The scaled stress is still lower than the difference between the incident and reflected waves, indicating that the specimens are not in perfect equilibrium. This may be explained by the additional inertia of the threaded bars securing the specimen, but needs further investigation to confirm. However, the two differ by only 1 MPa and thus a state of quasi-equilibrium occurs.

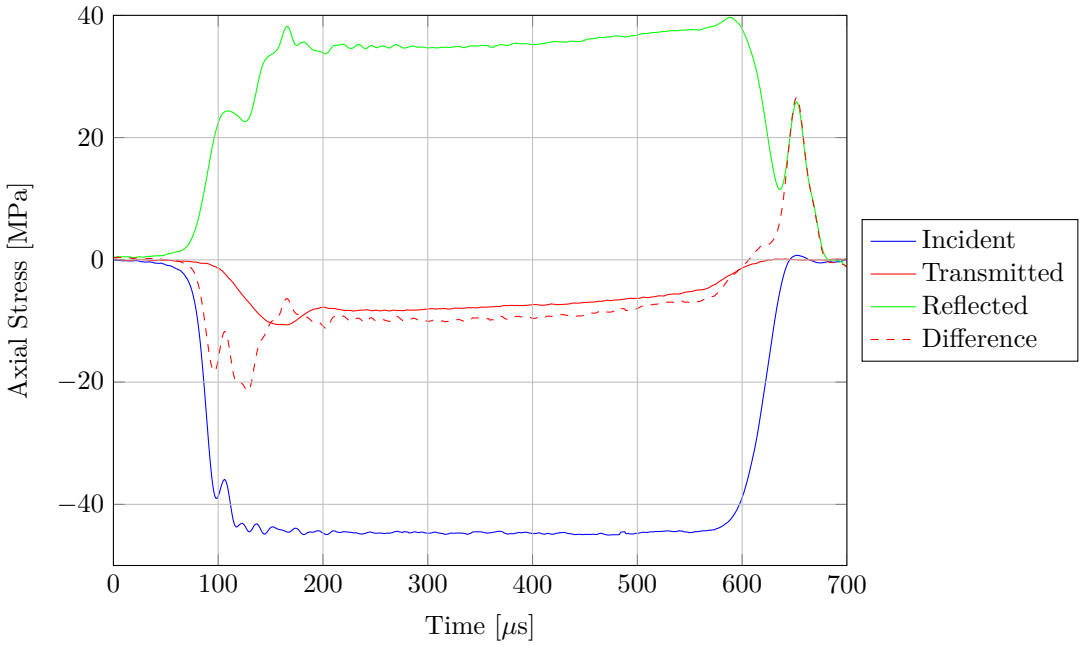

Figure 5.10: Strain gauge readings for specimen 'Straight 1'. The incident, transmitted and reflected waves are shown, together with the difference between the incident and reflected wave.

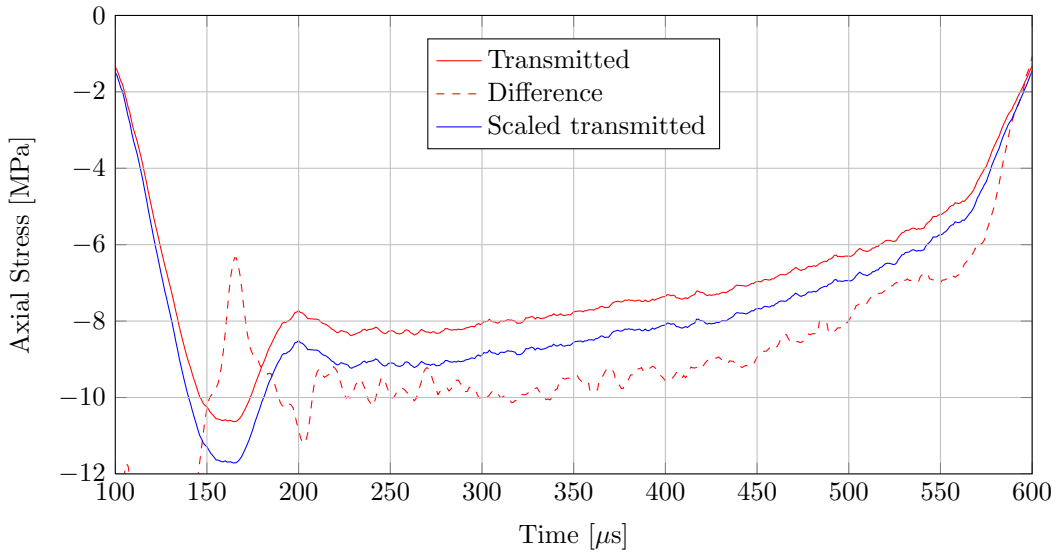

Figure 5.11: Transmitted gauge reading for specimen 'Straight 1'.

5.5 Notched Specimens

The notch results fail in the centre of the gauge section due to the low cross sectional area in the region. Generally the fast quasistatic specimens fail at higher displacements to the slow, while the dynamic specimens fail before either. This result is consistent with that found for the straight specimens.

5.5.1 1.25mm Radius Notch

The 1.25mm radius notch specimen geometry is included in table 5.4 with photographs of example specimens in figure 5.12. There are similar geometric inconsistencies to the straight specimens, most notably the size of the gap between the notches.

The quasistatic results, included in figure 5.5.1, show a similar strain rate displacement to failure trend to the straight specimens. Those deformed at 0.2mm/min break at about 1.3mm, while those at 20mm/min fracture at just below 1.5mm. Specimen 2 is the only anomaly, breaking later than 1 and 3, but this had a significantly greater initial gap thickness of $G = 2.14$mm compared to 1.8mm for the other two.

A second quasistatic specimen trend that was not noticeable for the straight specimens is the stress magnitude. For an equivalent displacement, the stress is higher for the specimens strained at the faster rate. However, as mild steel has rate dependent plasticity behaviour, with strength increasing with strain rate, this observation is not unexpected. Interestingly, the different material properties at the two rates does not appear to have a significant influence over the initiation of necking as specimens at both rates neck after a displacement of roughly 0.35mm.

The dynamic results in figure 5.15 are relatively consistent, generally failing around 1.2mm, noticeably below the range of 1.3 to 1.8mm for the quasistatic specimens. Specimens 5 and 6 fail early, but then these specimens have a gap width 15% lower than the remainder.

Table 5.4: Measured dimensions of the 1.25mm radius notch specimens.

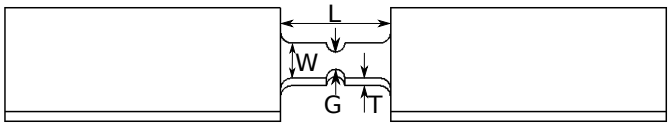

No.	L (mm)	W (mm)	T (mm)	G (mm)
SHB specimens				
1	11.98	3.89	2.275	2.19
2	11.98	3.98	2.24	2.19
3	12	3.88	2.29	2.18
4	11.98	3.87	2.21	2.19
5	11.98	3.8	2.29	1.89
6	12	3.76	2.29	1.85
7	11.96	4.02	2.38	2.11
Zwick specimens				
1	12	3.75	2.24	1.81
2	12	4.02	2.23	2.14
3	11.98	3.72	2.27	1.82
4	11.98	3.74	2.5	1.79
5	11.98	3.77	2.49	1.91
6	11.98	3.75	2.255	1.83
7	12.05	3.99	2.4	2.1

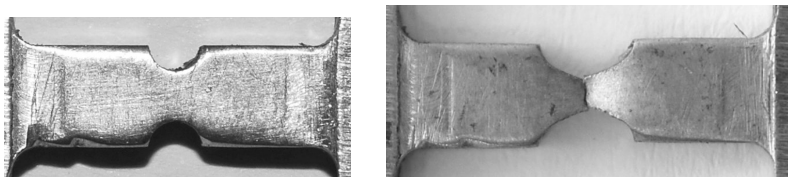

(a) Quasistatic 4

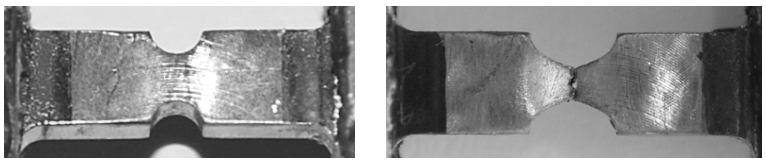

(b) Dynamic 6

Figure 5.12: Photographs of the 1mm radius notched specimens.

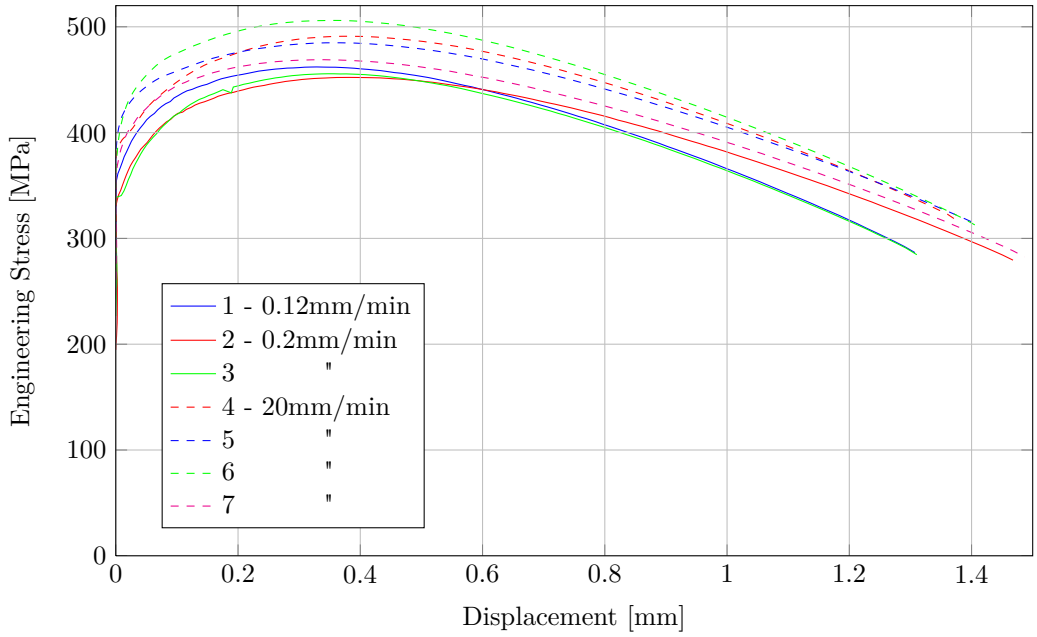

Figure 5.13: Quasistatic results for the 1.25mm radius notched specimens.

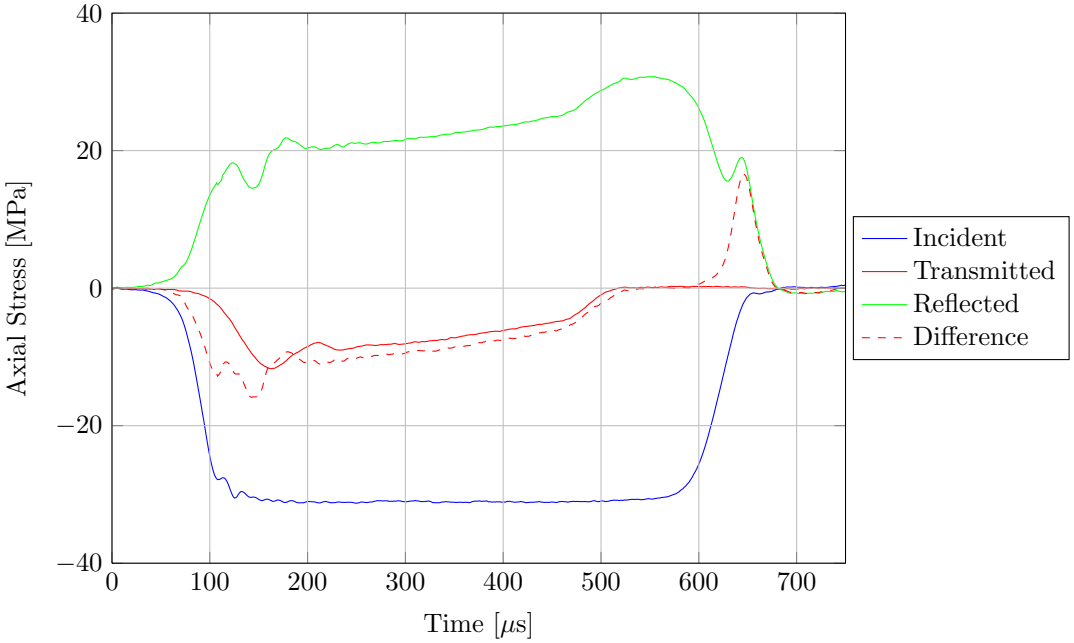

Figure 5.14: Strain gauge readings for 1.25mm radius notched specimen 4.

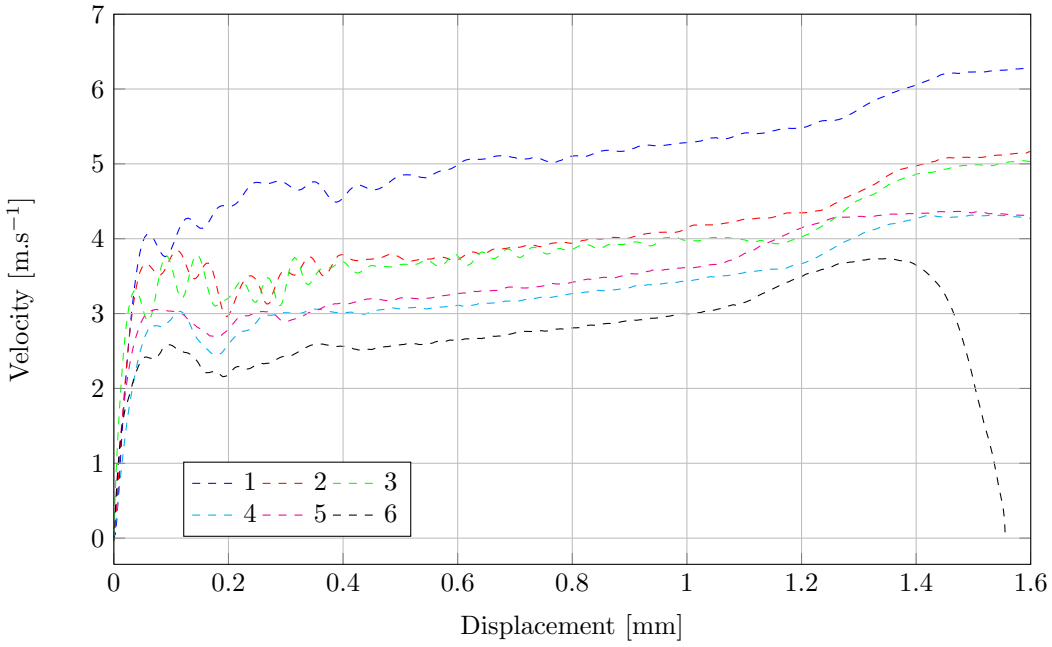

(a) Velocity

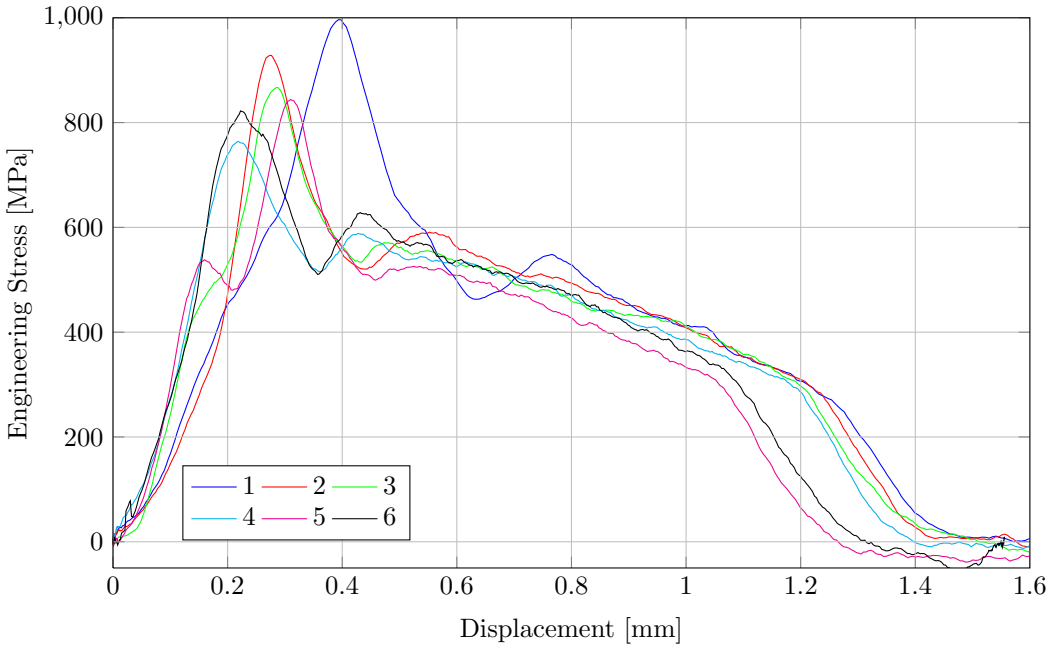

(b) Engineering Stress

Figure 5.15: TSHB results for the 1.25mm radius notched specimens.

As the specimens fail at significantly lower displacements than the straight specimens, the initial load peak dominates the first half of the stress-displacement curve. This spike is larger than expected and may be due to the combination of thread and glue interactions. A similar spike is evident in the literature for tensile bars which use threaded specimens (see for example [50], [29]). However, the magnitude of the spike for these specimens is larger. This may be due to the small specimen size resulting in the peak being large relative to the load required for deformation and or the glue influence. A thorough investigation is required to confirm this hypothesis and ideally reduce the peak. Positively, for this analysis the oscillations are minimal at the point of fracture. A 1.25mm notch gauge reading set is included in figure 5.14.

5.5.2 2mm Radius Notch

The 2mm radius notch specimens result in very consistent results. The quasistatic tests, shown in figure 5.17, show two distinct failure regions of 1.45mm for the slow rate and 1.65mm for the faster rate. However, this difference may be exaggerated due to the gap width of the slower specimens being roughly 10% lower than the remainder (table 5.5). The change in gap width may also account for the fast rate specimens necking at a larger displacement than the slow rate specimens, which is not as evident for the 1.25mm and 5mm radius notched specimens.

The dynamic results in figures 5.18 and 5.19 all fail around 1.3mm, again significantly lower than the quasistatic specimens. This is clearly evident in considering the deformed specimens of figure 5.16, chosen as examples as both had a similar gap width. Clearly the final notch of the quasistatic is significantly wider than the dynamic.

The trend in dynamic specimens failing before the quasistatic is in contrast to that found by Johnson and Cook [14] who used the final cross-sectional area at failure to determine the fracture strain. A similar comparison given in figure 5.20, which shows a scaled cross-section of grooved specimens at failure for both a quasistatic and dynamic specimen. In this case the final cross-section of the quasistatic specimen is smaller, indicating a greater failure strain.

Table 5.5: Measured dimensions of the 2mm radius notch specimens.

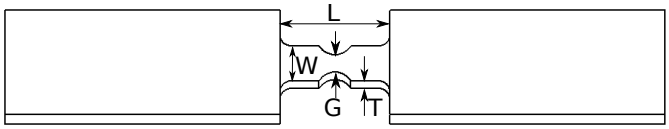

No.	L (mm)	W (mm)	T (mm)	G (mm)
SHB specimens				
1	12	4.07	2.275	2.09
2	12	4.07	2.27	2.12
3	12	3.78	2.265	1.75
Zwick specimens				
1	12	3.81	2.27	1.9
2	11.98	3.84	2.27	1.91
3	11.98	3.83	2.28	1.92
4	11.98	4.06	2.24	2.07
5	12	4.04	2.27	2.07
6	12	4.06	2.31	2.09

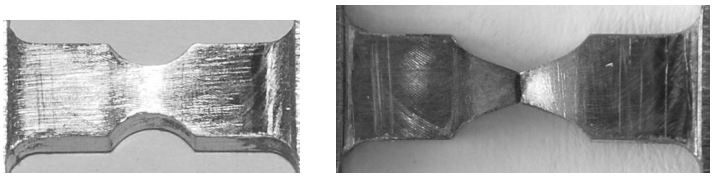

(a) Quasistatic 5

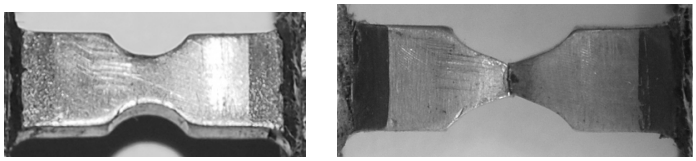

(b) Dynamic 1

Figure 5.16: Photographs of the 2mm radius notched specimens.

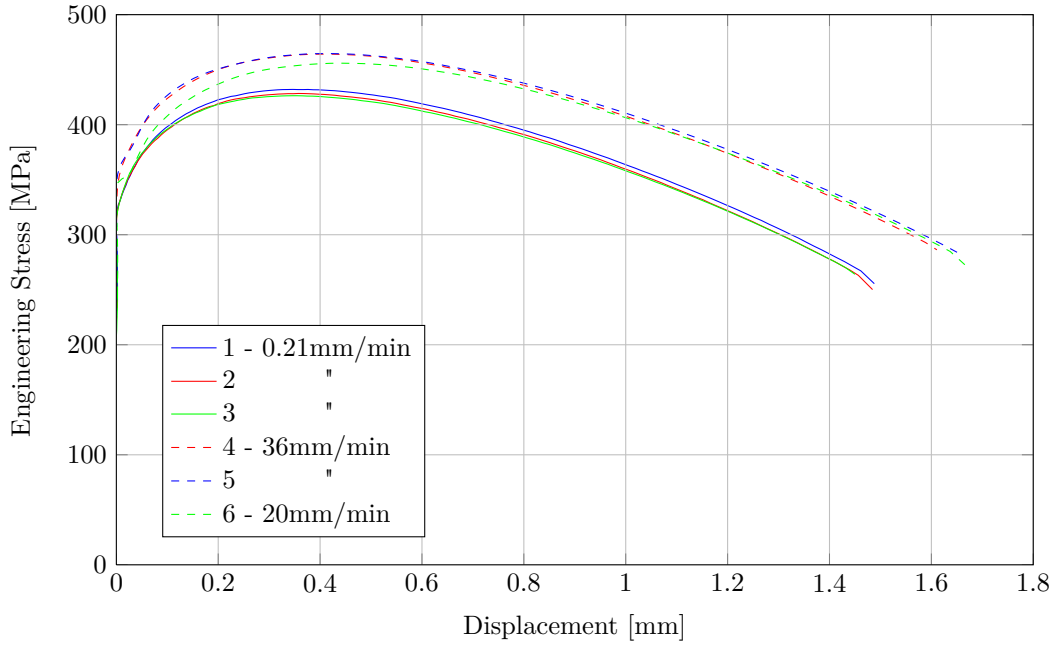

Figure 5.17: Quasistatic results for the 2mm radius notched specimens.

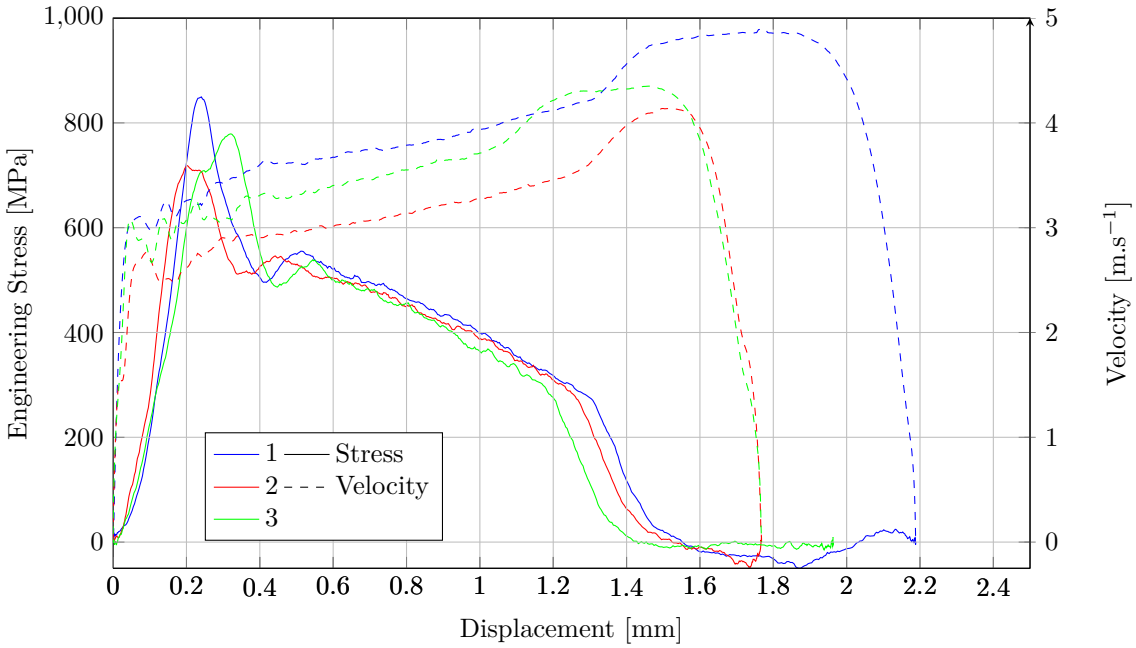

Figure 5.18: TSHB results for the 2mm radius notched specimens.

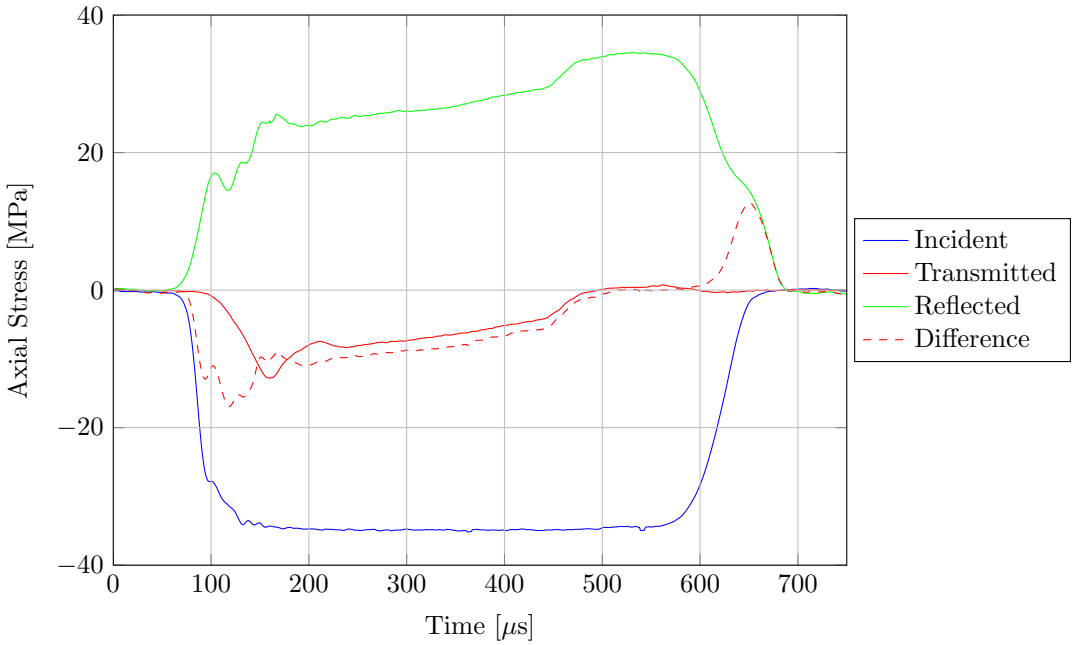

Figure 5.19: Strain gauge readings for 2mm radius notched specimen 1.

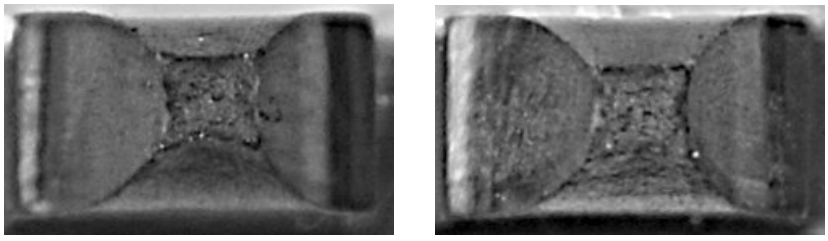

(a) Quasistatic specimen 5

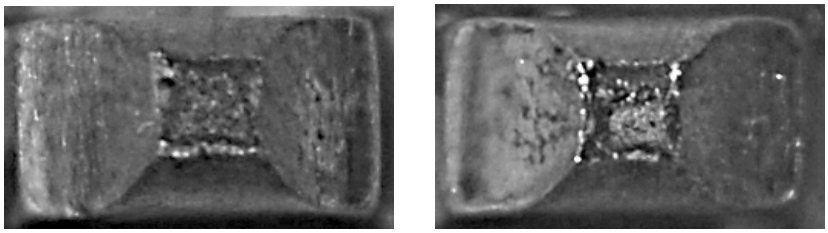

(b) Dynamic specimen 1

Figure 5.20: Fracture surface of the 2mm radius notched specimens. The cross sectional area of the quasistatic specimen is visually smaller than that of the dynamic.

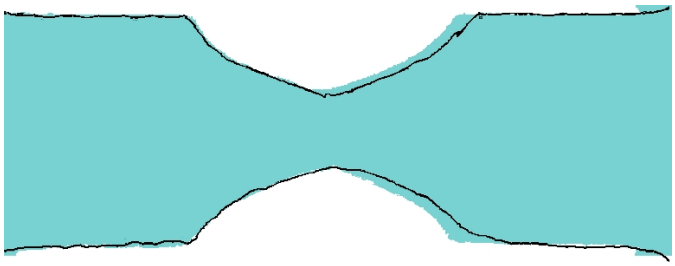

Figure 5.21: Profile of the 2mm radius notched specimens at failure. The dynamic specimen 1 is shaded while the quasistatic specimen 5 is shown as an outline.

The difference between the quasistatic and dynamic specimen deformation is also evident in figure 5.21, which compares the profile of the dynamic and quasistatic specimens at failure. At the point of fracture, the quasistatic specimen has a grooved region which is both longer and thinner in the centre than the dynamic equivalent.

5.5.3 5mm Radius Notch

Finally, the 5mm notch specimen results are included in figures 5.23 to 5.25. The quasistatic results seem to go against the trend of the faster rate specimens breaking at greater displacements. However, as before this again can be explained by inconsistencies in the geometry, shown in table 5.6. Specimens 1 and 2 both have noticeably thick notch gaps and predictably fail at high displacements. In comparing specimens 3 at a slow rate and 4 to 6 at the faster rate, the latter all fail later, even though all the specimens yield at a displacement of around 0.5mm. Note that even specimen 5 with a very low gap size and thickness failed after specimen 3.

The dynamic results are excellent both in terms of consistency and the shape of the stress displacement curve. For these, the initial stress peak plays only a minor role in the initial 25% of the stress-displacement result. Past this point the result is very smooth. Failure occurs after 1.5mm of travel compared to 1.8mm for the quasistatic tests.

Table 5.6: Measured dimensions of the 5mm radius notch specimens.

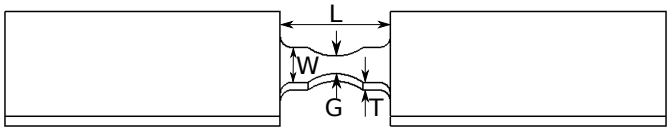

No.	L (mm)	W (mm)	T (mm)	G (mm)
SHB specimens				
1	12	4.08	2.27	2.13
2	11.98	4.08	2.285	2.16
3	12	4.08	2.22	2.11
Zwick specimens				
1	12	4.06	2.3	2.13
2	11.98	4.075	2.305	2.14
3	12	3.8	2.25	1.83
4	12	3.69	2.26	1.78
5	12	3.65	2.205	1.66
6	11.98	3.85	2.3	1.96

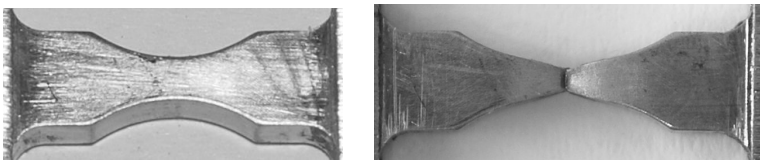

(a) Quasistatic 4

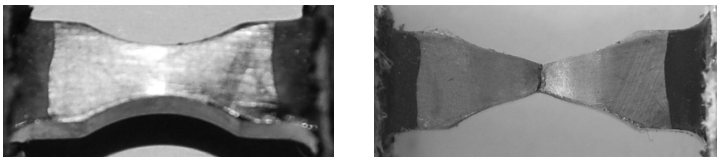

(b) Dynamic 2

Figure 5.22: Photographs of the 5mm radius notched specimens.

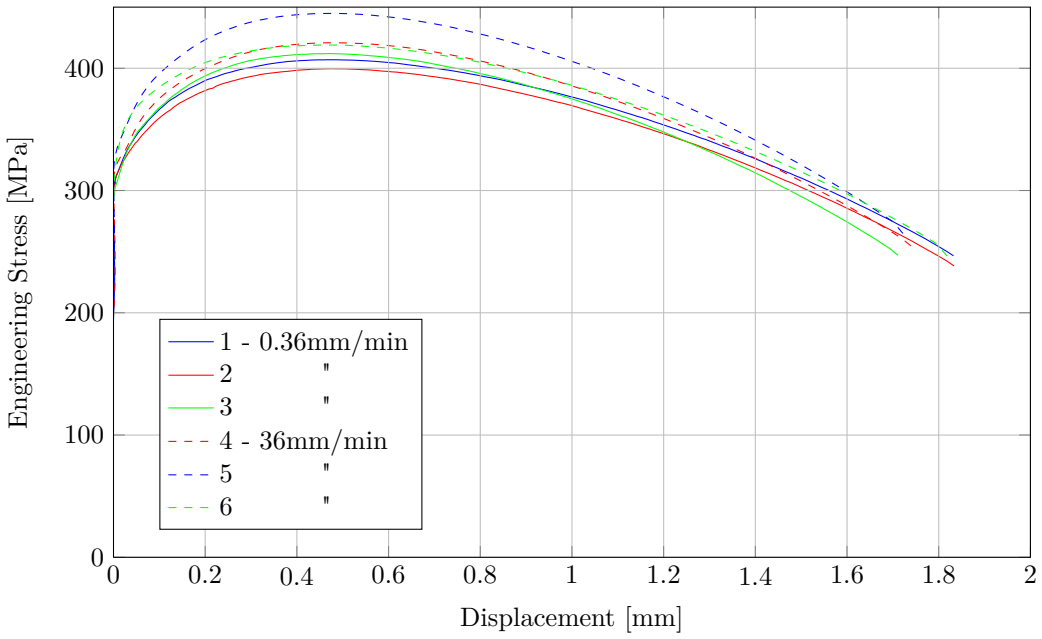

Figure 5.23: Quasistatic results for the 5mm radius notched specimens.

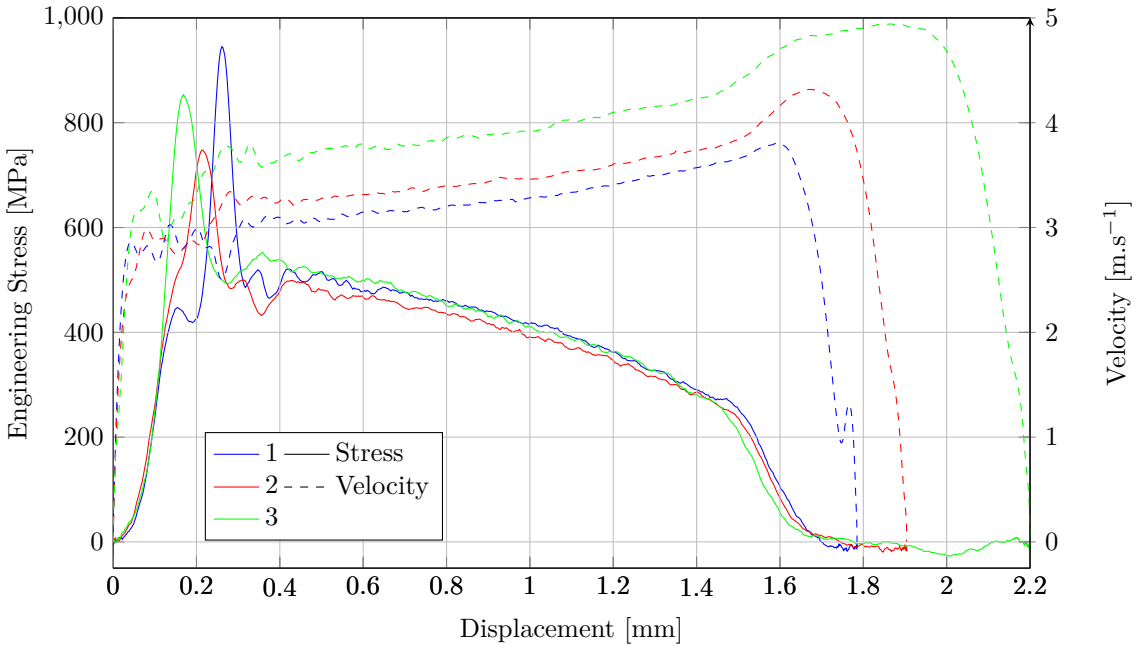

Figure 5.24: TSHB results for the 5mm radius notched specimens.

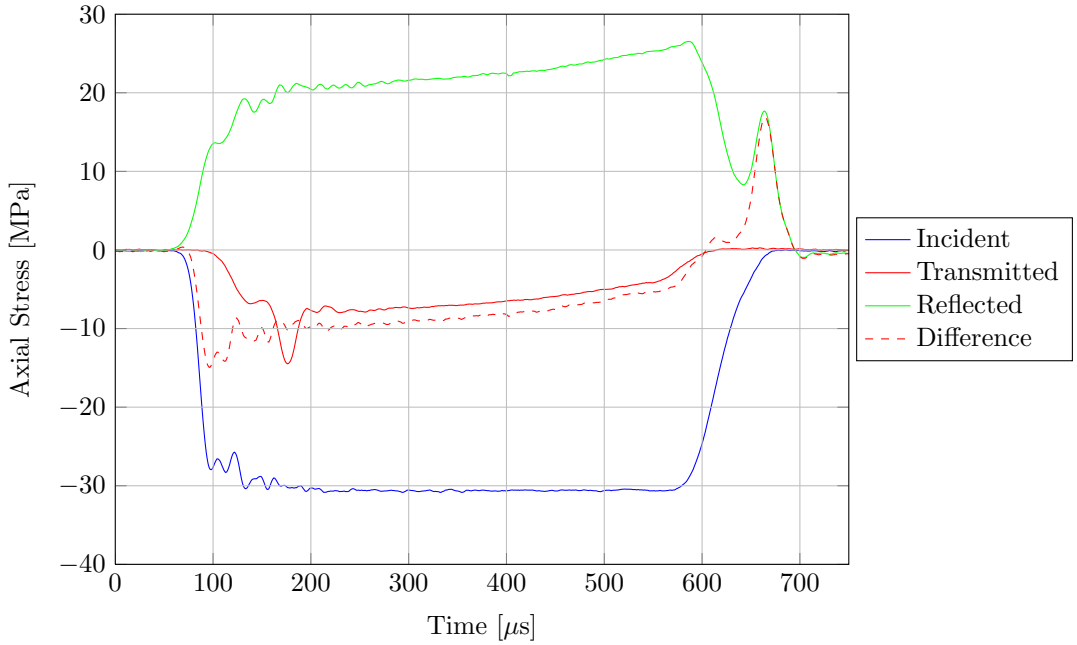

Figure 5.25: Strain gauge readings for 5mm radius notched specimen 1.

5.6 Grooved Specimens

The grooved specimens fail at significantly lower displacements than the notched and straight tests with final displacements generally less than 0.5mm. Due to the early fracture, analysing strain rate trends is more problematic as the differences in fracture displacement are small.

5.6.1 1.25mm Radius Groove

The 1.25mm radius results show the problem clearly as very little distinction can be made between the failure displacements of the fast and slow quasistatic specimens, despite each set showing good consistency.

The groove specimens are heavily affected by the problems inherent in manufacturing small specimens. The groove gap for example was specified as 0.6mm, but the manufactured (table 5.7) varied between 0.73 and 1.06. This is a difference of 45% and the latter is over 75% above that selected.

Table 5.7: Measured dimensions of the 1.25mm radius groove specimens.

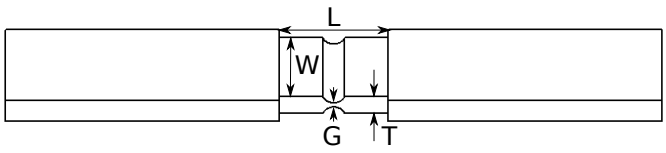

No.	L (mm)	W (mm)	T (mm)	G (mm)
SHB specimens				
1	11.9	9.97	2.44	0.78
2	11.9	10.08	2.5	0.73
3	11.9	10.05	2.52	0.78
4	11.98	9.875	2.45	1.06
5	11.98	9.8	2.455	0.915
6	11.98	9.81	2.45	0.91
Zwick specimens				
1	12	9.77	2.37	0.9
2	11.98	9.75	2.44	0.89
3	12	9.75	2.46	0.9
4	11.98	9.73	2.475	0.905
5	11.98	9.77	2.5	0.95
6	12	9.68	2.45	0.89

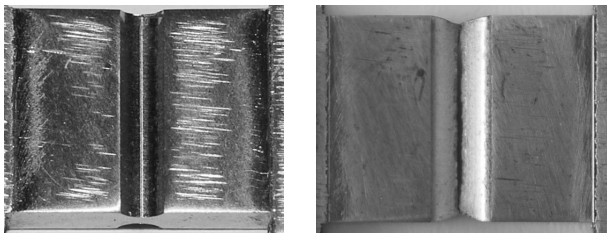

(a) Quasistatic 6

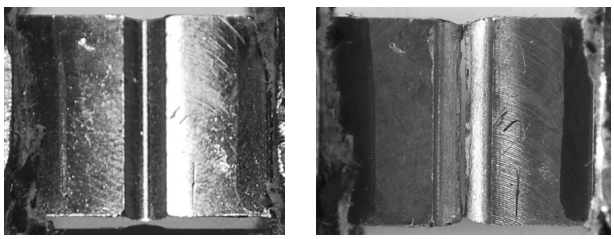

(b) Dynamic 5

Figure 5.26: Photographs of the 1mm radius grooved specimens.

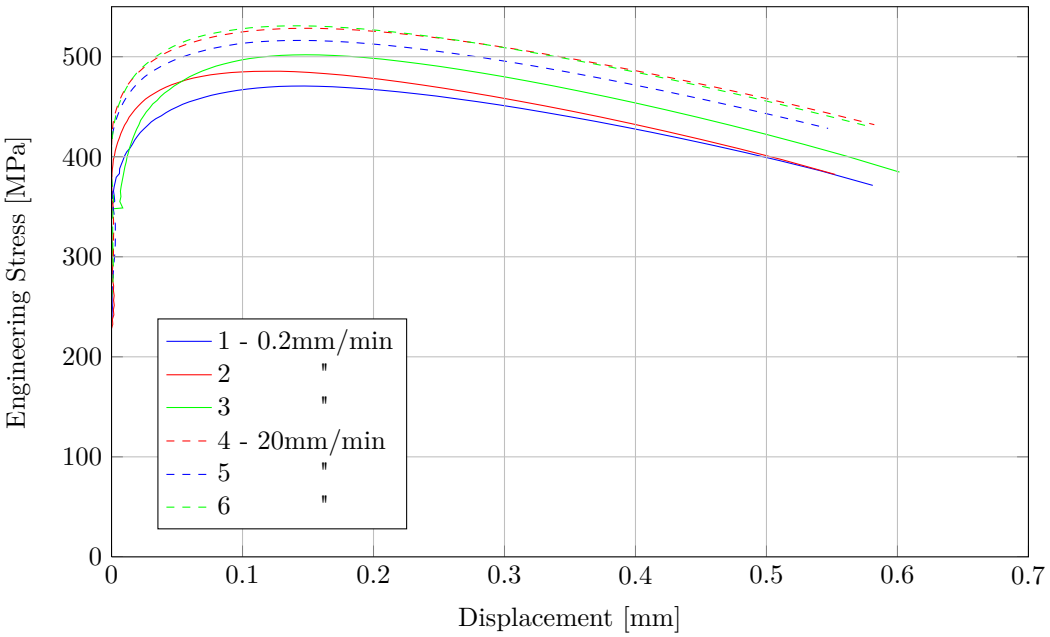

Figure 5.27: Quasistatic results for the 1.25mm radius grooved specimens.

The difference between the dynamic (figure 5.28) and quasistatic (figure 5.27) results is less distinct than the notch specimens, but the latter again fracture marginally after the dynamic with a displacement of 0.6mm compared to less than 0.5mm.

It is difficult to obtain the optimal striker velocity for the groove specimens. Too low a velocity and the specimen fails to break, while higher magnitudes result in a short deformation recording time as shown in the strain gauge reading of figure 5.29. A further difficulty is the relatively large stress spike at the start pulse, which for these small specimens is noticeable. For example in figure 5.28 the stress peak ends after 0.22mm, affecting the load over almost 45% of the total displacement. Interestingly, specimen 5, which has the lowest velocity and specimen 1, with the highest, have almost no stress peaks. The reason for this is unclear, but may indicate that, if optimized, using glue and threaded bar to secure the specimens should not affect the loading significantly.

The specimens shown in figure 5.26 include a case where the gauge section was affected by the sanding process on the grip section, but care was taken to ensure that the grooved section itself had no visible imperfections. The remaining groove specimens were protected with tape to prevent this occurring.

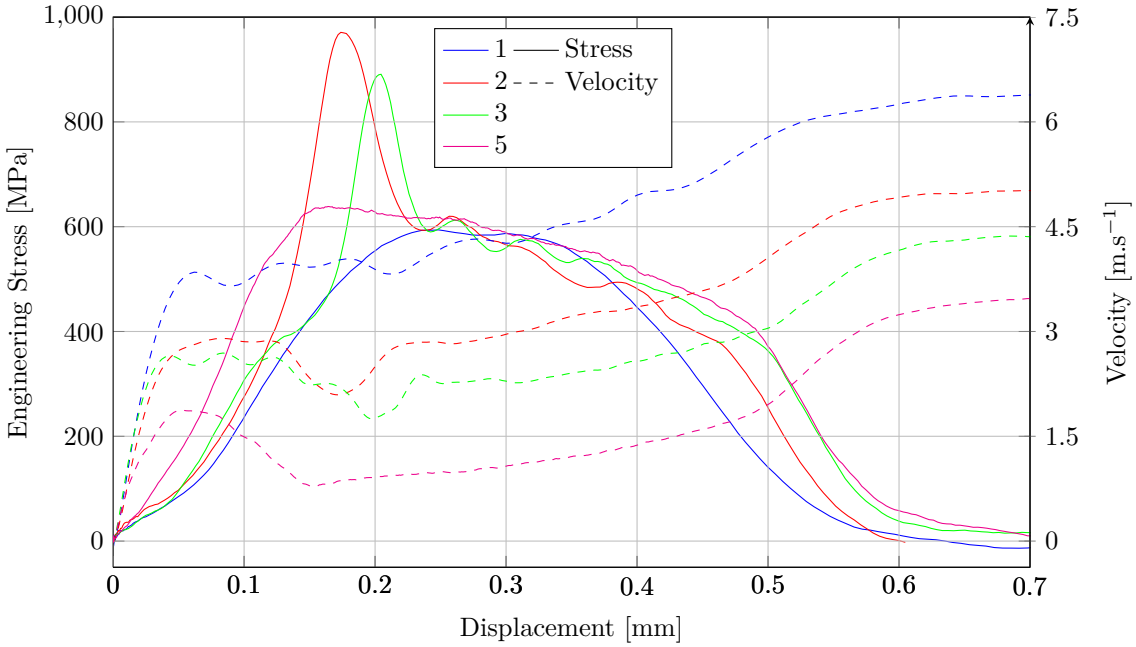

Figure 5.28: TSHB results for the 1.25mm radius grooved specimens.

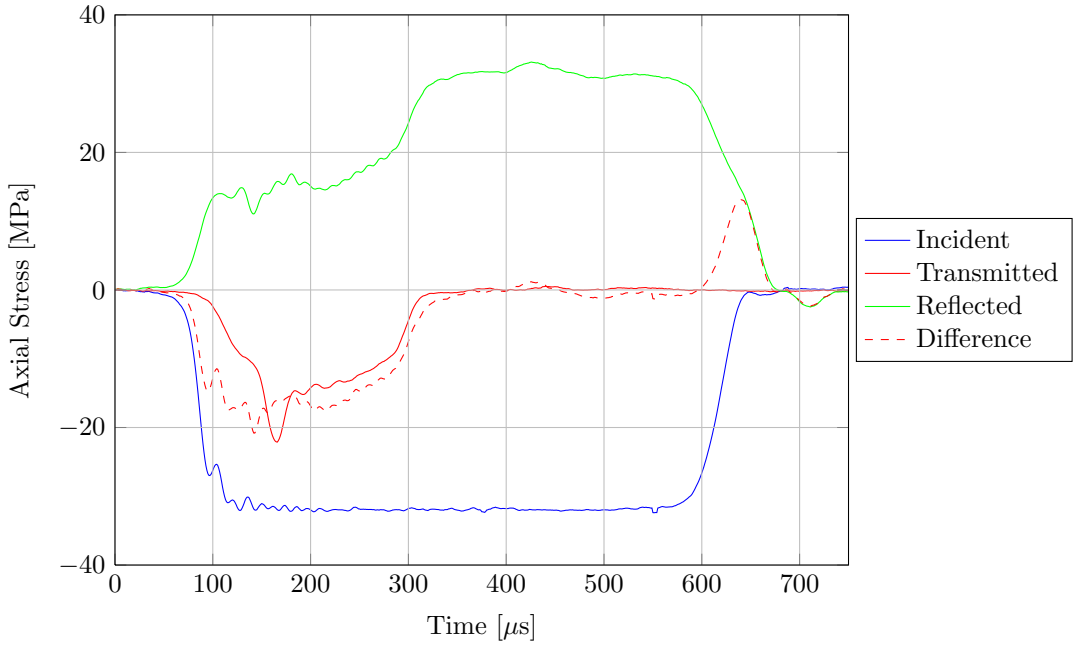

Figure 5.29: Strain gauge readings for 1.25mm radius grooved specimen 3.

Table 5.8: Measured dimensions of the 2mm radius groove specimens.

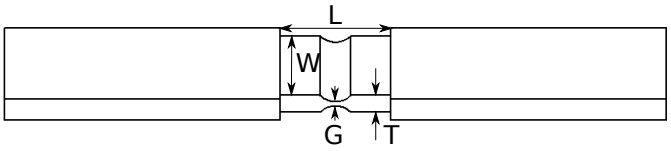

No.	L (mm)	W (mm)	T (mm)	G (mm)
SHB specimens				
1	12	10.14	2.47	0.57
2	11.98	10.15	2.38	0.58
3	12	10.16	2.48	0.54
Zwick specimens				
1	12	10.15	2.46	0.575
2	12	10.2	2.47	0.565
3	11.98	10.26	2.5	0.59
4	12	10.17	2.49	0.58
5	11.98	10.12	2.48	0.555
6	11.98	10.225	2.47	0.56

5.6.2 2mm Radius Groove

The 2mm radius specimens produced similar results with the quasistatic specimens all failing at approximately 0.45mm and the dynamic at the marginally lower 0.36 and 0.4mm. Good consistency is evident in the quasistatic results (figure 5.31). However, the dynamic again showed the difficulty in testing this type of specimen.

In the two dynamic tests considered, specimen 1 took longer to peak than 3 and resulted in a larger displacement prior to fracture. This may be due to specimen 3 being glued poorly. Although specimen 3, with strain gauge reading shown in figure 5.33 is an acceptable result, the poor consistency indicates that the derived properties should be used with caution.

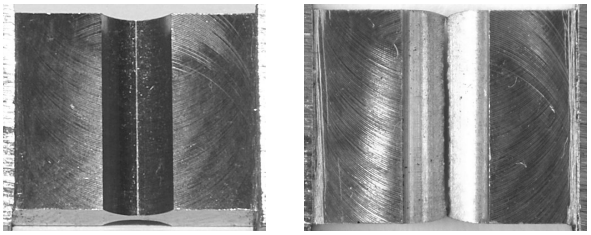

(a) Quasistatic 3

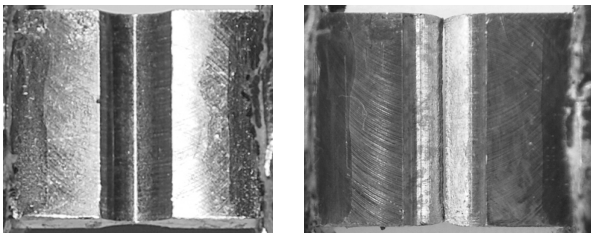

(b) Dynamic 3

Figure 5.30: Photographs of the 2mm radius grooved specimens.

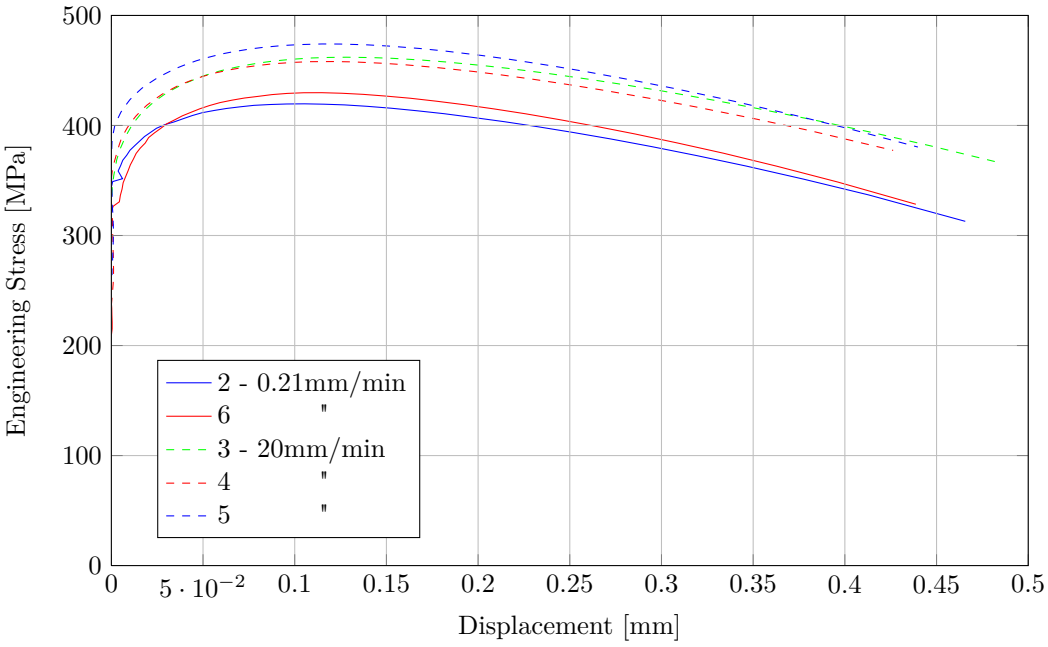

Figure 5.31: Quasistatic results for the 2mm radius grooved specimens.

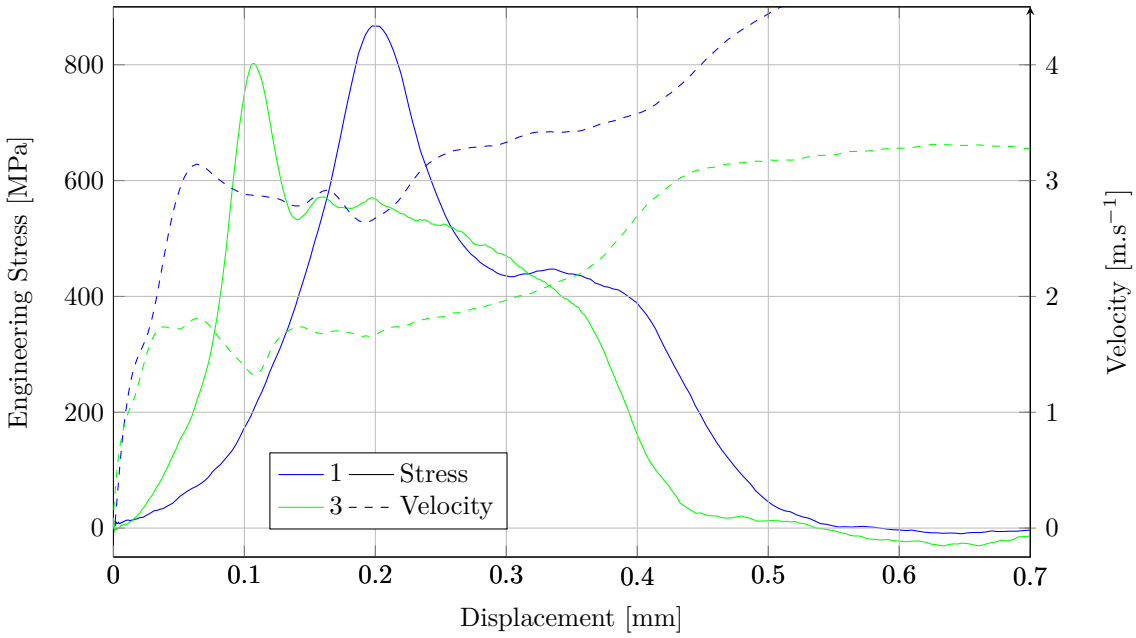

Figure 5.32: TSHB results for the 2mm radius grooved specimens.

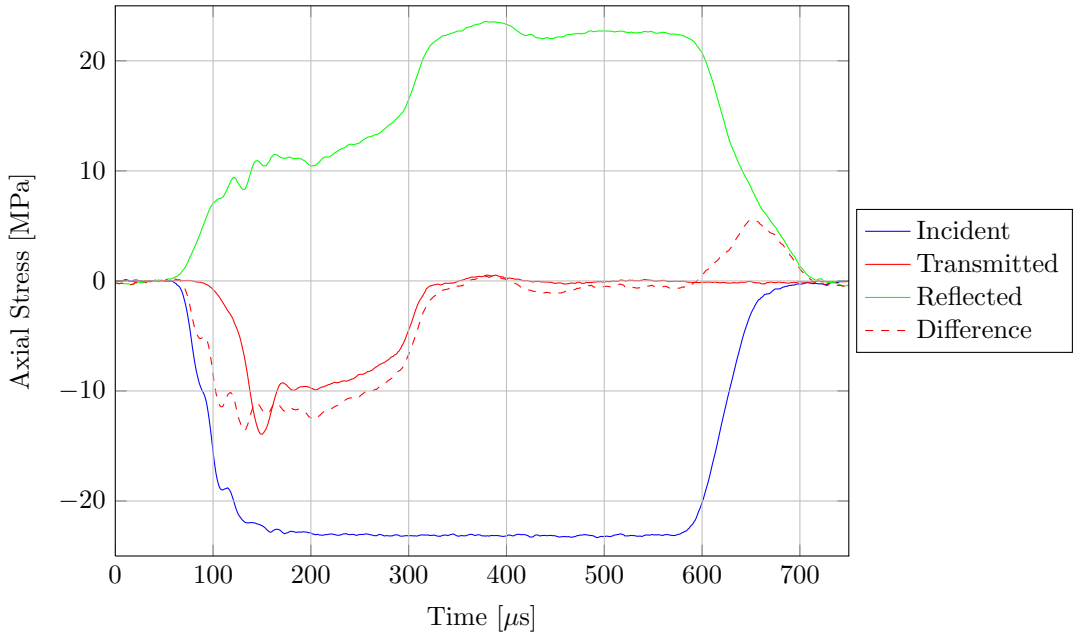

Figure 5.33: Strain gauge readings for 2mm radius grooved specimen 3.

5.6.3 5mm Radius Groove

Better results are obtained from the 5mm radius groove experiments. In this case, the quasistatic results shown in figure 5.36 show a similar trend to the straight and notch specimens with those deformed at the slow strain rate fracturing after 0.55mm and those at the higher rate at roughly 0.6mm. However, whether a difference of 0.05mm is significant is debatable. Specimen 3 is an anomaly as it has the lowest groove gap, but a significantly higher strength.

The dynamic results are encouraging, with all three specimens failing. Interestingly fracture in this case occurs between 0.5mm and 0.57mm, which is only marginally lower than the range for the quasistatic tests. This is evident both in figure 5.34, which compares the deformation of a quasistatic and dynamic specimen and in analysing the damage cross-section in figure 5.35. The only difference is that the fracture surface of the dynamic specimen is rough compared to the quasistatic, possibly due to slight misalignment while gluing .However, it may simply be due to the material properties at the two strain rates affecting neck formation differently.

Figure 5.38, shows that for the 5mm groove specimens a lower incident pulse than the smaller radius groove tests was produced. A lower input pulse decreases the strain rate and thus increases the duration through which deformation is recorded. This improves the quality of the result as the stress peak has a much smaller influence. Thus minimizing the input pulse magnitude may improve the reading for the smaller groove specimens. The procedure needs careful refinement as the difference in striker velocity resulting in no fracture compared to that which creates a large stress peak is small.

Table 5.9: Measured dimensions of the 5mm radius groove specimens.

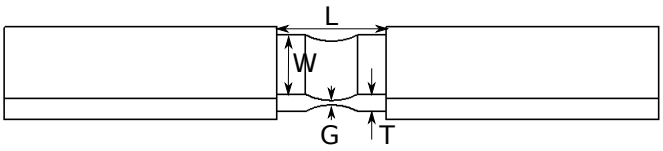

No.	L (mm)	W (mm)	T (mm)	G (mm)
SHB specimens				
1	12	10.16	2.38	0.66
2	11.98	10.08	2.35	0.66
3	11.98	10.16	2.315	0.62
Zwick specimens				
1	11.98	10.2	2.95	0.61
2	11.98	10.14	2.335	0.65
3	12	10.19	2.33	0.57
4	12	10.155	2.36	0.65
5	11.98	10.145	2.51	0.64
6	11.98	10.16	2.32	0.62

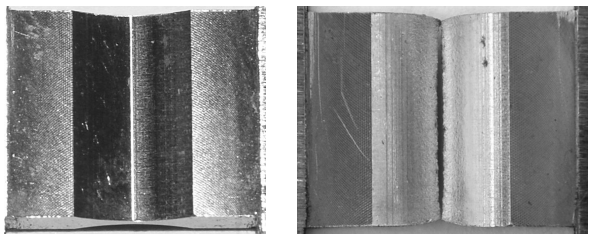

(a) Quasistatic 6

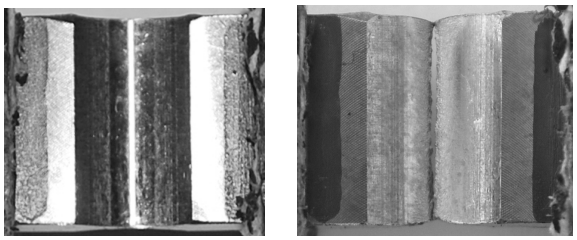

(b) Dynamic 3

Figure 5.34: Photographs of the 5mm radius grooved specimens.

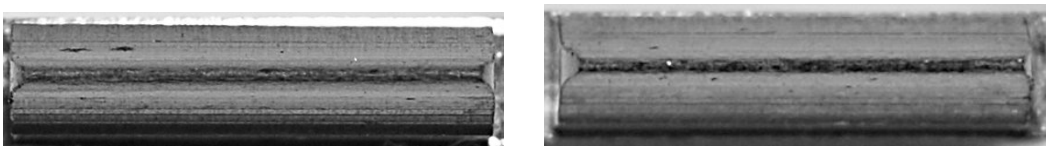

(a) Quasistatic specimen 6

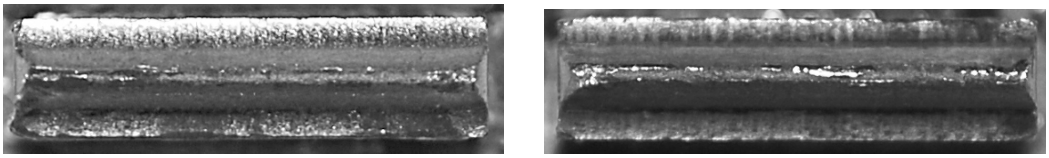

(b) Dynamic specimen 3

Figure 5.35: Fracture surface of the 5mm radius grooved specimens. Unlike the notched specimens a trend in cross-sectional area is not obvious. The only visible difference is the rough break on the dynamic specimen relative to the quasistatic.

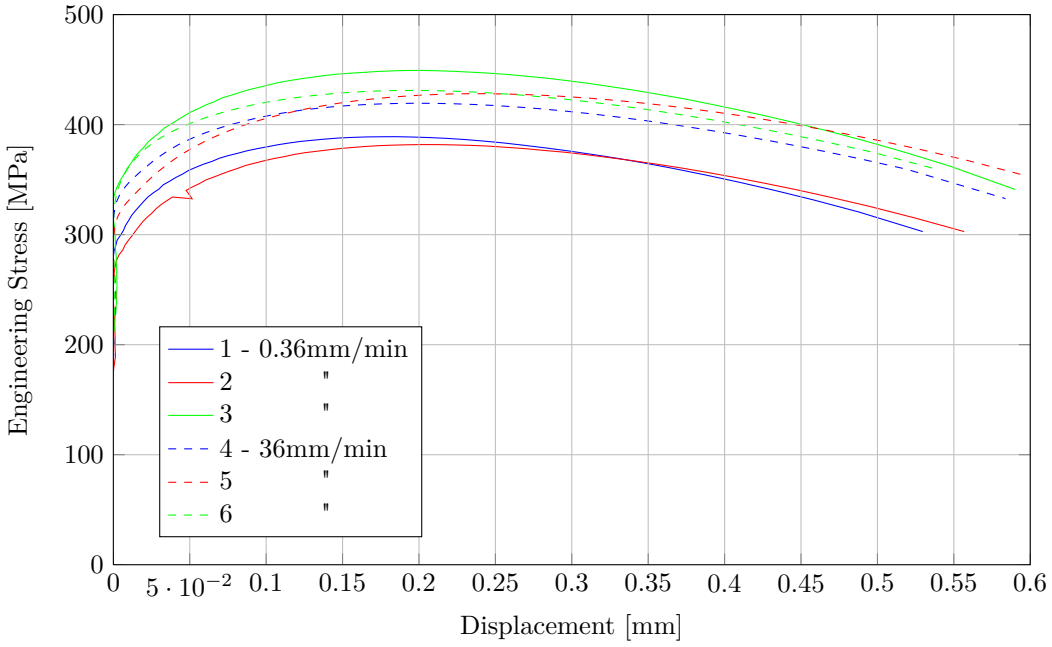

Figure 5.36: Quasistatic results for the 5mm radius grooved specimens.

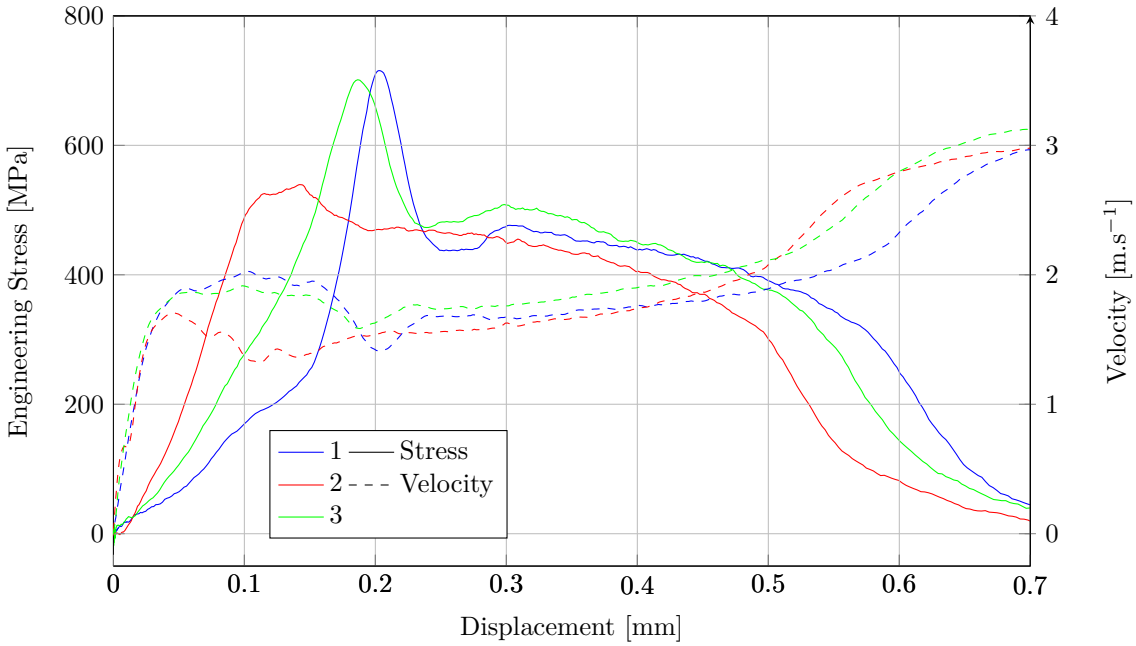

Figure 5.37: TSHB results for the 5mm radius grooved specimens.

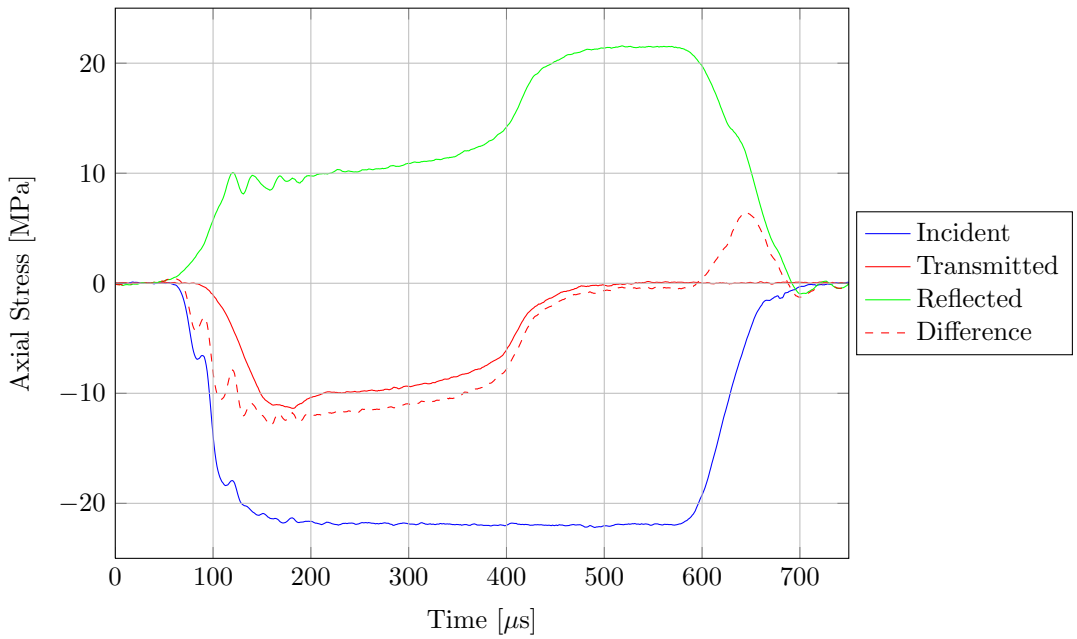

Figure 5.38: Strain gauge readings for 5mm radius grooved specimen 2.

Chapter 6

Numerical Simulation

6.1 Introduction

This chapter considers the finite element simulations used to analyse the damage properties of the mild steel specimens damaged experimentally in chapter 5.

The first section details the meshing techniques as well as the methods to determine the reaction force, velocity and parameters required for the damage analysis. The next contains the calibration of the plasticity model, this was achieved by iteratively changing the Zhao [57] model constants until the numerical work corresponded closely to the experimental.

The latter sections relate to fracture analysis. The third section uses the calibrated models to determine the relationships between triaxiality, Lode angle, strain rate and failure strain. The final section implements a simplified version of the Bai-Wierzbicki failure locus[17] to a specimen test.

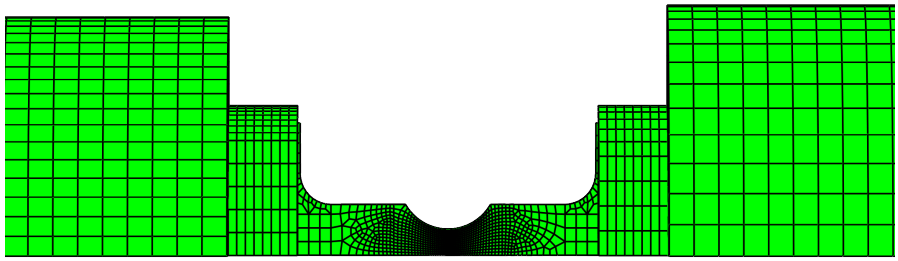

(a) Wide view

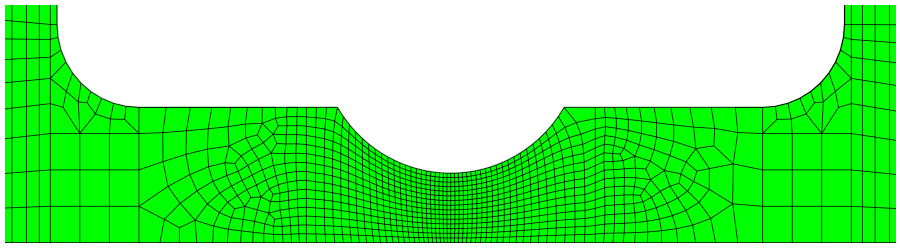

(b) Close view

Figure 6.1: Dynamic 2mm radius notched specimen mesh.

6.2 Mesh and Readings

In simulating damage, Bai and Wierzbicki [17], found that a mesh density of element size 0.2mm was sufficient for a converged solution. The study used similar specimens to those used here, although the straight and notched specimens were round, not sheet specimens as used in this thesis. The specimens were also larger with a minimum radius through the round notched specimens 8mm and the minimum thickness through the grooved specimen 1.6mm.

As the specimens tested in this thesis are smaller, the specimen length in the axial direction was limited to a maximum of 0.05mm at the specimen centre. The density through the notch or groove was also kept high with the element length increasing to 0.2mm at the notch edge.

Outside of the notch, no plastic deformation occurs and thus the density can be increased significantly to limit the total number of elements. This is especially important for the dynamic model in which the thread, glue and part of the bars are modelled as the same part as the specimen[25]. An example of the mesh used for a dynamic simulation is shown in figure 6.1.

[25]See chapter 4.

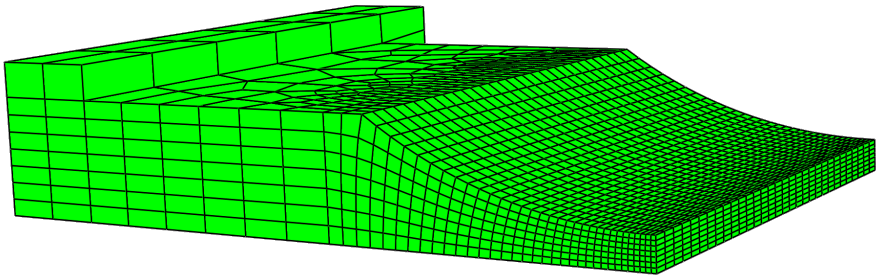

Figure 6.2: Quasistatic 5mm radius grooved specimen mesh.

The quasistatic model is smaller and kept to a minimum size as these take considerable time to run. In this case only a small grip section was included with the displacement boundary conditions applied to it. Figure 6.2 shows a grooved quasistatic specimen.

For the dynamic tests three sets of readings were taken, the first used an element on the output bar 120mm from the edge to output the axial stress as a strain gauge would do in an experiment. Generally, the output strain gauge is placed at approximately 10 bar diameters (200mm for the built TSHB apparatus) from the specimen interface as at this distance 1D wave propagation can be applied [5]. However, simulation showed that the signal at a distance of 120mm was the same as that at 200mm and thus this length was selected. From the output bar element, the reaction force at the specimen-bar interface can be determined.

The second reading measured the bar interface velocity on either side of the specimen to infer the specimen velocity, in this case several nodes were selected on each bar and the average taken. In future testing this is not necessary as each reading is so similar that one node at any point on the interface is sufficient. Finally for the damage analysis, an element was selected in the centre of the gauge section to record the Lode angle, triaxiality and equivalent strain.

Note that as the stress wave takes a finite amount of time to reach the output 'gauge', the resulting stress pulse needed to be shifted in time to the specimen interface, as in a SHB experiment.

In the case of the quasistatic specimens the $\frac{1}{8}$ symmetry was taken advantage of to record the reaction force at each node along the symmetry boundary in the centre of the groove or notch. These were then summed to determine the total reaction force as recorded by the Zwick tensile testing machine. The damage analysis was accomplished in a similar manner by selecting the central element.

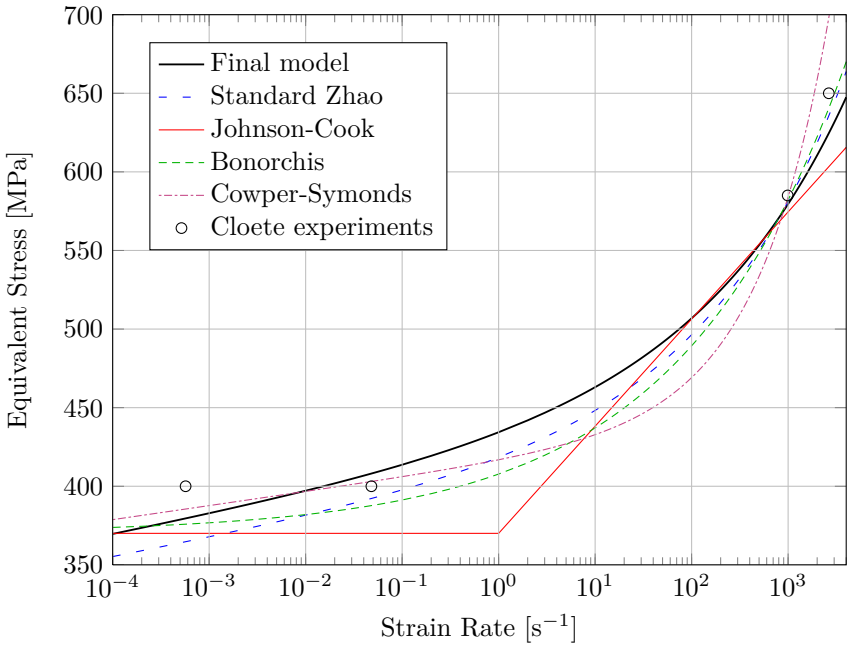

Figure 6.3: Comparison of the final calibrated Zhao flow stress model to those in the literature at a strain of 0.1. Also shown is experimental data conducted by Cloete [66] on specimens manufactured from same sheet as used in this work.

6.3 Calibrating the Plasticity Model

6.3.1 Model Comparison

Thorough quasistatic tensile and dynamic compressive tests were conducted by Cloete [66] on the same mild steel sheet as tested in this work. Several standard material models applied to the data result in close correlation. These are shown together with the experimental data and final model in figure 6.3.

The most basic model is that by Johnson-Cook model, calibrated by Tanimura et al. [67]. The locus is reasonably accurate at strain rates of between 10 and 1000 s^{-1}, but due to its simplistic linear form on a log scale the approximation is poor elsewhere [61]. An improved solution uses the Johnson-Cook strain and temperature terms, but replaces the strain rate dependence with that proposed by Cowper-Symonds[61]. In this example, the constants are taken from [66].

The standard Zhoa[57] mild steel model also shows good correlation as does that by Bonorchis [54], which uses a simplified form of the Zhao strain rate dependence, but with more detailed strain dependence.

The challenge was to calibrate a plasticity model with approximately the same strain rate dependence as the models outlined above, but that also simulated the experimental results closely. This work used an iterative process to calibrate the constants from the Zhao model[26] by simulating the experiments from chapter 5 until the simulated results corresponded well to the experimental. The Zhao damage locus is described by,

$$\sigma = \left(A + B\epsilon^n + [C - D\epsilon^m] \log \left[\frac{\dot{\epsilon}}{\dot{\epsilon}_0} \right] + E\dot{\epsilon}^k \right) f(T) \tag{6.1}$$

with the temperature term taken as that used by Johnson-Cook,

$$f(T) = 1 - T^{*m} \qquad T^* = \frac{T - T_{trans}}{T_{melt} - T_{trans}} \tag{6.2}$$

The optimal solution is shown compared to the other models and the experimental data by Cloete [66] in figure 6.3. The greatest discrepancy to the standard Zhao [57] mild steel model is at low strain rates where the model underestimates the material strength. This change was implemented by increasing the constants A to D by 4%. Finally, to prevent this increase on influencing the high strain rate values, the exponent k, which has a large influence on high strain rate strength, was reduced from 0.3 to 0.28. The chosen material properties are included in table 6.1.

The temperature dependent data was taken directly from Bonorchis [54], with only the transition temperature being changed marginally from 300 to 293K. Although this data is also from testing mild steel, the temperature term does have a significant influence and may need further calibration. This data is detailed in table 6.2.

[26]The Zhao model is dealt with in detail in section 4.2.3 on page 93.

Table 6.1: Constants used for the standard Zhao [57] and the final chosen plasticity models.

	A (MPa)	B (MPa)	C (MPa)	D (MPa)	E (MPa)	k	n	m
Standard	145	550	35	47	18.5	0.3	0.42	0.3
Final	150.8	572	36.4	48.88	18.5	0.28	0.42	0.3

Table 6.2: Temperature constants used in the final model. $\hat{\eta}$ is the proportion of plastic work that is dissipated as heat.

m	T_{trans} (K)	T_{melt} (K)	C_p (J/kgK)	$\hat{\eta}$
0.669	293	1811	452	1

6.3.2 Specimen Calibration Tests

Ideally, a general model for each design using the specified geometries should be modelled and compared to all the experimental data for that design. However, due to the inconsistencies in the specimen dimensions, this method was not feasible. Instead, a representative example of each was selected and modelled. These chosen specimens are labelled in table 6.3.

Note that the straight specimens were not considered here as these generally failed away from the centre due to imperfections[27]. Failure in these locations complicates the simulation process as the stress distribution at the failure location is different to that in the centre, where the numerical simulations predict failure. Not simulating the straight specimens is ultimately a limiting factor to the applicable range of the damage model as the triaxiality of these is lower than both the notch and groove examples.

A further limitation is the explicit finite element scheme used. As detailed briefly is section 4.5.1, an explicit analysis is limited by the critical time step. Using mass scaling allows the fast quasistatic tests to be run. However, the slow tests have durations often exceeding 500s compared to roughly 5s for the faster rate.

[27] See section 5.4 on page 129.

Table 6.3: Specimens analysed in the simulations.

	Quasistatic:	Dynamic:
R1.25mm notched specimen	4	3
R2mm notched specimen	5	1
R5mm notched specimen	4	2
R1.25mm grooved specimen	6	2
R2mm grooved specimen	3	3
R5mm grooved specimen	6	3

To simulate the slow tests in under 24 hours using the computing power available would require excessive mass scaling rates that would be detrimental to the results. A solution would be to write a material model for an implicit analysis in Abaqus (UMAT), but this is beyond the scope of this thesis. Thus only the fast quasistatic specimens are simulated and the effect of strain rate in the low regime must be inferred from the experimental results.

The accuracy of the plasticity simulation can be seen in figures 6.4 to 6.10. These compare the simulations to the experimental results by considering the 'engineering stress' defined previously as $\sigma = \frac{F}{A_0}$, where F is the reaction force and A_0 the minimum original cross sectional area. In the dynamic results the change in velocity between the two bar ends can also be compared, whereas in the quasistatic tests this value is nominally constant.

Figure 6.4 considers the 1.25mm radius notch specimen. For this model, and the notched models in general, the simulation closely predicts the experiment. The major discrepancy in this and indeed all the SHB simulations is the stress peak evident at the start of the dynamic experiment deformation, but absent from the numerical. When compared to the numerical simulation, the experimental result appears similar to a mass-spring-damper system (figure 6.5) with the response lagging behind the expected load followed by an overshoot and subsequent damping. The lag may be due to the glue straining elastically, while the glue may also damp the signal by decreasing the magnitude of the oscillations. However, although the epoxy was simulated in the model, this response is not captured and thus the simulation procedure clearly needs further analysis.

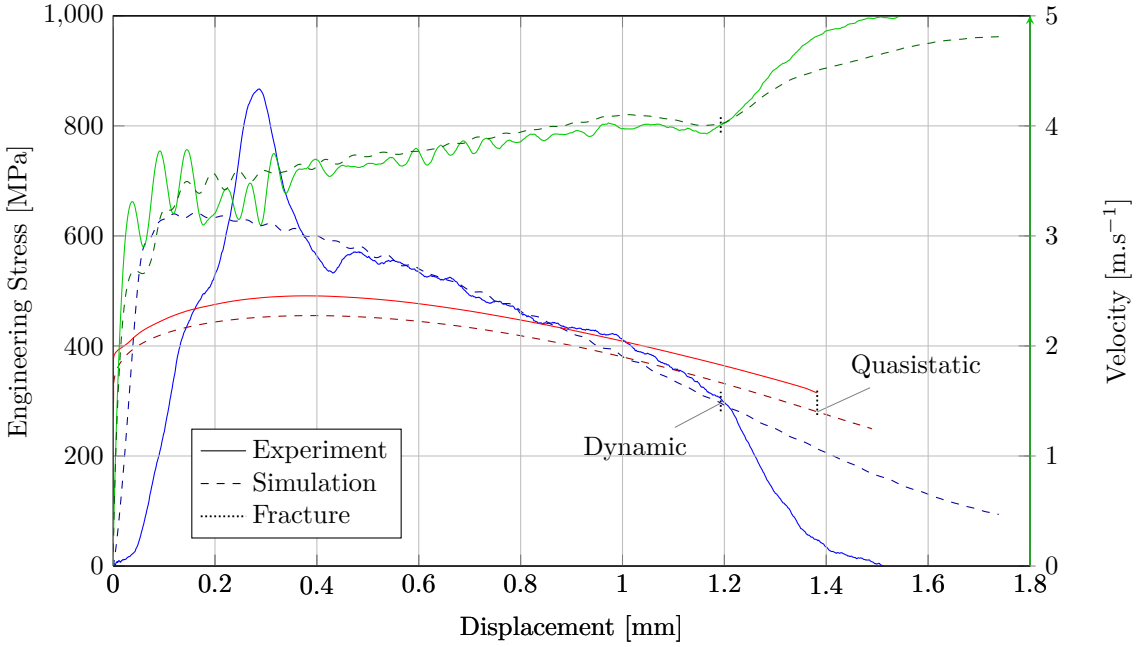

Figure 6.4: Simulation of the 1.25mm radius notched specimen compared to the experimental result. Both the quasistatic and dynamic tests are shown with the latter comparing both engineering stress and velocity. Also shown is the displacement where fracture was taken to occur.

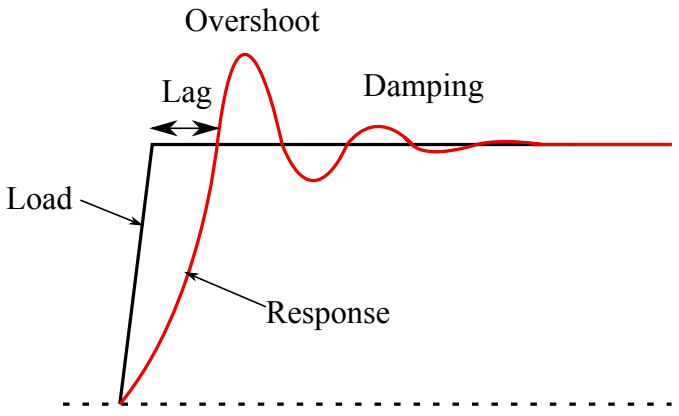

Figure 6.5: Mass-spring-damper system load response.

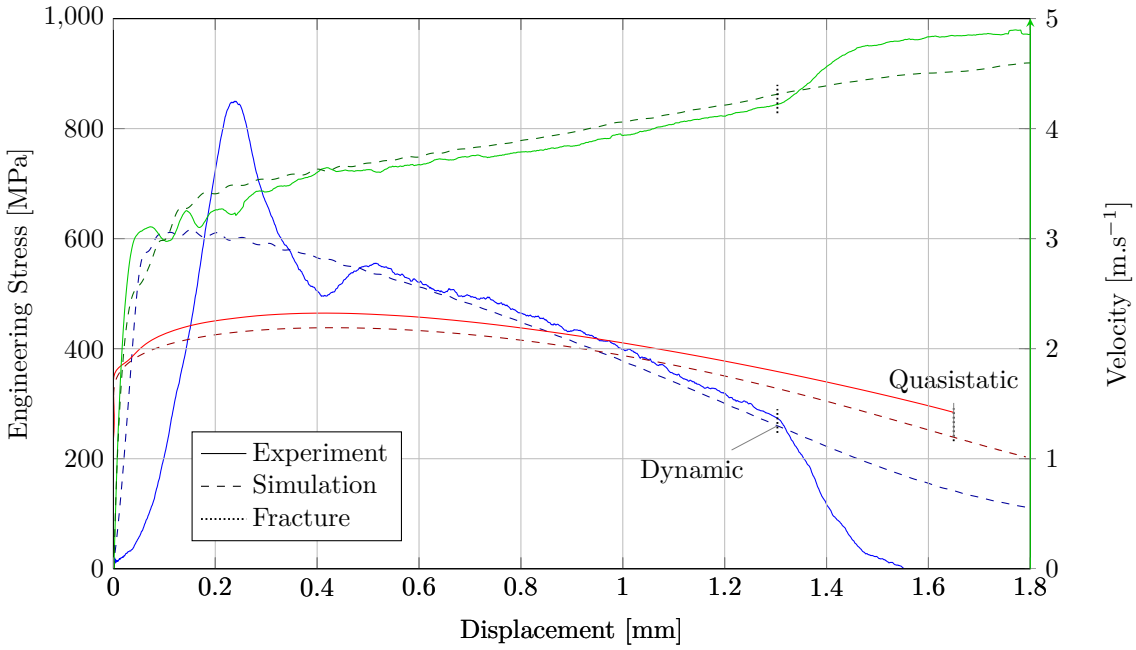

Figure 6.6: Simulation of the 2mm radius notched specimen compared to the experimental result.

Positively, the time period through which the peak occurs is far from the point of damage and the effect on the average triaxiality and Lode angle at failure should be minimal. Further, the velocity from the simulations closely tracks the experimental. This is especially pleasing as the Bai-Wierzbicki model is primarily related to deformation, not stress magnitude.

Figure 6.4 also shows is the position at which fracture is taken to occur. This failure displacement is found from the experimental result and used to determine the simulation state for the same travel. The position is evident as a distinct gradient change, both in the stress and velocity plot.

Figures 6.6 and 6.7 show the 2mm and 5mm radius notched specimens with similarly good correlation.

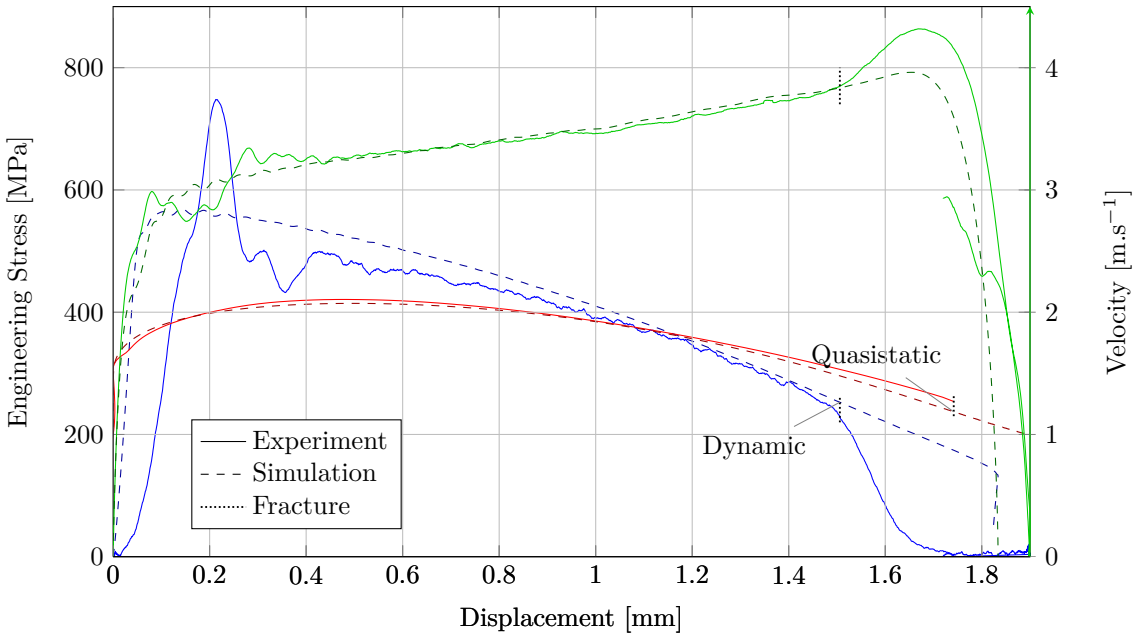

Figure 6.7: Simulation of the 5mm radius notched specimen compared to the experimental result.

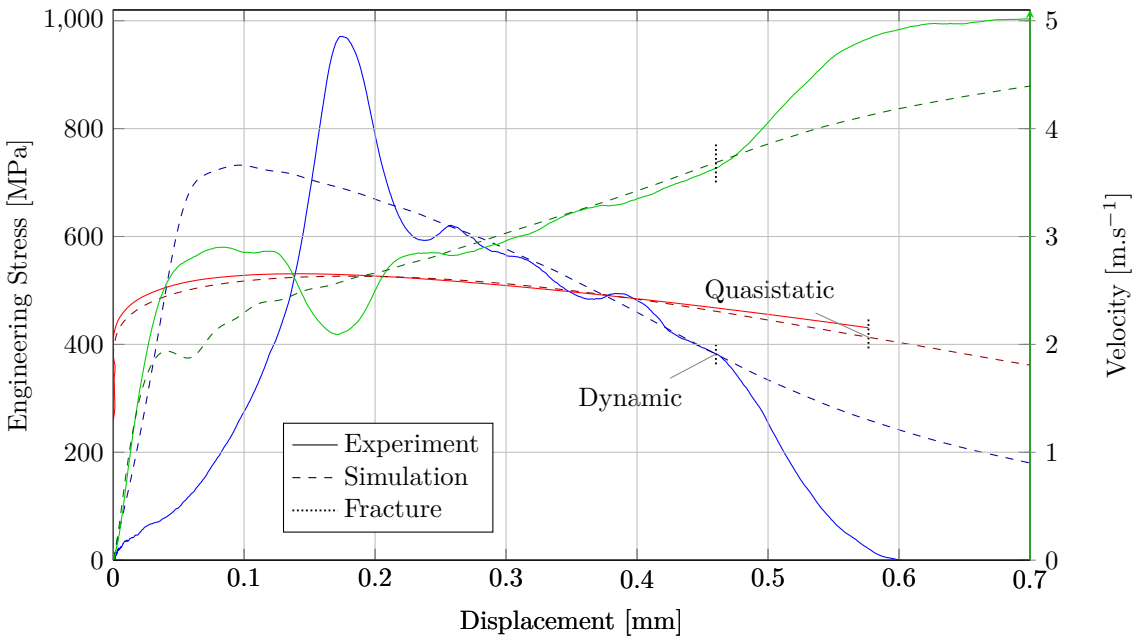

Figure 6.8: Simulation of the 1.25mm radius grooved specimen compared to the experimental result.

The grooved specimens in figures 6.8 to 6.10 are more difficult to analyse, but the simulations proved to be reasonably accurate. In the dynamic results the stress peak has a more pronounced effect, but this is due to fracture occurring much earlier than in the notched specimens. Of interest is the velocity plot, as the experimental result shows the velocity increasing rapidly before dropping suddenly at the time the stress peaks. The simulation follows a similar pattern, but on a much smaller scale. For the 1.25mm radius specimens, the experimental velocity drops after a displacement of 0.18mm, while the numerical after only 0.07mm. It seems likely that this trend is related to the glue. When the glue stiffness is reduced, the magnitude of the first velocity peak increases.

The influence of the peak is small over the notch specimens, but in the case of the grooved specimens the displacement to fracture is so small that the effect may be negatively influencing the results. In this case, if the epoxy has a lower elastic modulus than considered here, the dynamic strain would be overestimated.

After the peak, the 1.25mm grooved specimen shows good correlation. The simulation of the 2mm specimen overestimates the stress magnitude slightly, but follows the velocity profile closely. Finally, the 5mm specimen simulation overestimates the stress, while underestimating the velocity. This discrepancy may be explained by the findings of Bai and Wierzbicki [17] who found that simulations of similar grooved specimens correlated far better the the experimental results if the Lode angle was accounted for in the plasticity model. This reduced the error between experimental and the simulations from 19% to less than 2%. This approach is beyond the scope of this thesis and requires further study.

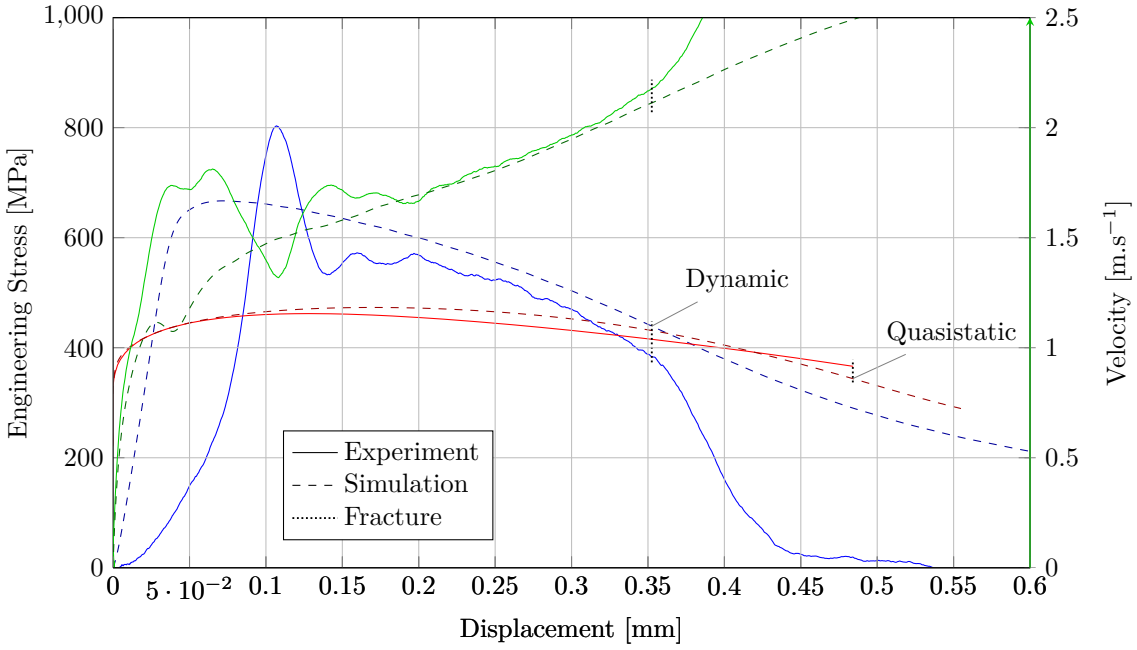

Figure 6.9: Simulation of the 2mm radius grooved specimen compared to the experimental result.

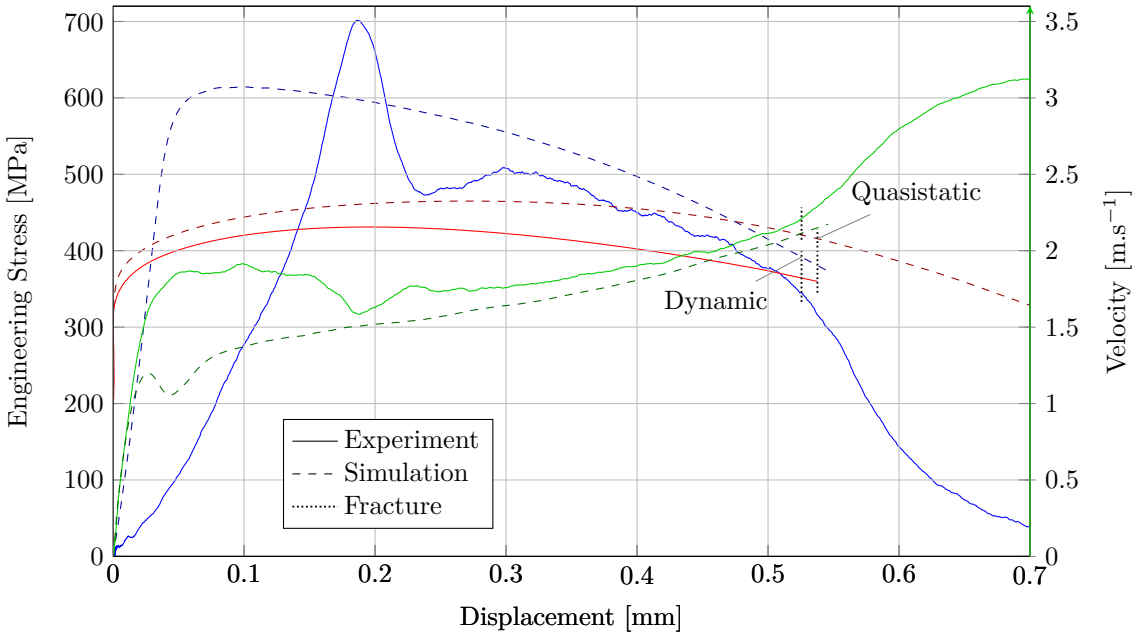

Figure 6.10: Simulation of the 5mm radius grooved specimen compared to the experimental result.

6.4 Damage Analysis

6.4.1 Applicable Loading Range

The Bai-Wierzbicki damage model is a locus generated in average triaxiality, η_{avg}, and average normalized Lode angle, $\bar{\theta}_{avg}$, space. Thus ideally tests should result in a wide range of these invariants at failure. As covered in section 3.3.1, the scope for this analysis is limited to $\eta, \bar{\theta} \geq 0$. However, figure 6.11 shows that the final coordinates in this space are in a relatively narrow range.

The Lode angle, as expected, is close to 0 for the grooved specimens, while the notched specimens are generally around 0.7. As round specimens in tension have $\bar{\theta} \approx 1$, this value of 0.7 seems reasonable. For these specimens the notch is only cut into one plane. Thus the specimen thickness retards strain in that direction and hence decreases the Lode angle.

The range in triaxiality is lower than expected for the notched specimens. In the design phase the specimens were estimated to have an initial triaxiality varying between 0.45 and 0.8, whereas the simulation range at failure is a much smaller 0.67 to 0.8 for the quasistatic and 0.73 to 0.88 for the dynamic. The triaxiality underestimation is probably also due to the square cross section used in the experiments versus the round used to approximate the initial values. Triaxiality increases with non-axial stress and thus a small notch with a narrow notch gap has a high value. In the case of round specimens, this notch acts all around the axis. However, the notched specimens used in this work had a section cut out of only one plane, with the thickness through the plane kept constant. Thus prior to necking, the non-axial stresses normal to the plane are minimal, moderating the influence of the neck.

The initial and final strain rates for the element in the centre of each specimen are shown in figure 6.12. Plastic deformation strain rate dependence is generally compared on a log scale (see for example [57]) and thus the strain rates are plotted in this format. Encouragingly, the final set of strain rates for all the quasistatic specimens lie within in a narrow range and the final dynamic specimen strain rates are close. Thus it is valid to compare all the specimens in each set together.

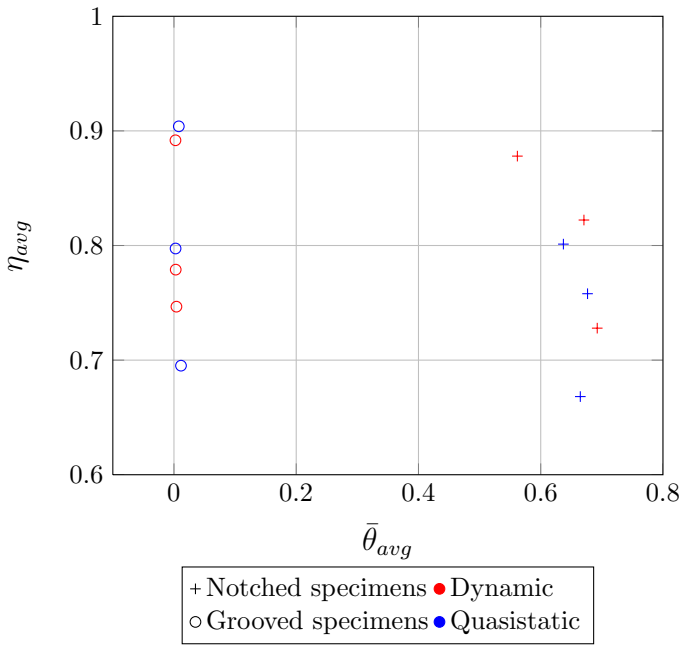

Figure 6.11: Final average normalized Lode angle, $\bar{\theta}_{avg}$, and triaxiality, η_{avg}.

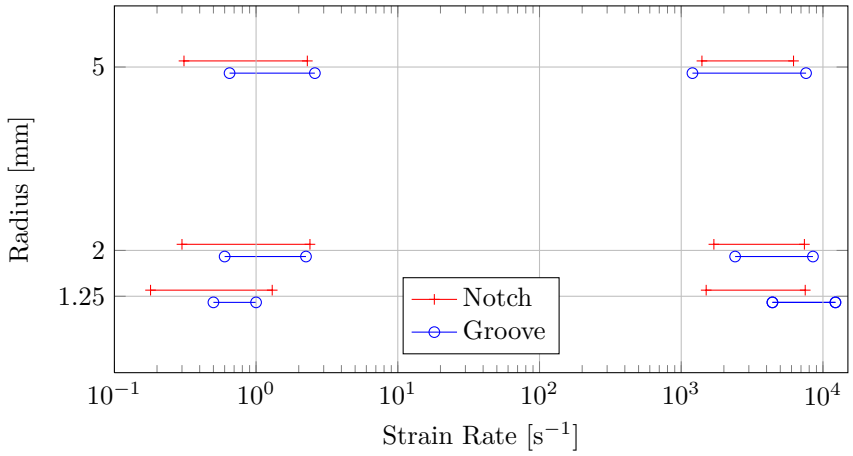

Figure 6.12: Initial and final strain rate of the element in the centre of the specimen. The final strain rate is similar across all the different specimens for both those deformed dynamically and at quasistatic rates.

6.4.2 Triaxiality Evolution

Figure 6.13 shows the evolution of triaxiality with equivalent strain. In the first plot the change in instantaneous triaxiality is shown. Predictably the triaxiality is greatest for the specimens with smaller notches and increases with strain as necking further deepens the notches. Interestingly, the triaxiality for the dynamic results start similarly to the quasistatic, but then become noticeably higher than the quasistatic equivalents. This is due to the greater hardening gradient at low strain rates retarding localization within the neck. The phenomenon ties into the experimental finding that quasistatic specimens fail significantly later, partly due to delayed localization.

Figure 6.13a reveals a mesh density issue that arises at high strains. As detailed in section 6.2, the element length is kept at under 0.05mm in the centre of the notched region. However, at high strains even these small elements become significantly distorted. This results in irregularities in the triaxiality, especially evident for the 1.25mm radius notch specimen.

Figures 6.14 and 6.15, respectively, consider a 1mm radius groove specimen under dynamic loading conditions and a 2mm radius grooved specimen deformed quasistatically. In both cases the central elements are distorted, especially the groove example in which only 7 elements are included through the minimum thickness. If more elements are included in this direction the density needs to be increased considerably else each element would have an even larger length to thickness ratio. This issue has not been pursued further due to constraints on time and server space, but possible inaccuracies due to distorted elements need to be kept in mind during the failure analysis.

For the damage model itself, Wierzbicki et al [7, 3, 68, 17] used the average triaxiality and Lode angle, arguing that damage is history dependent and thus some measure of the previous values are required. It could be argued that the stress state when voids begin to form just prior to fracture is far more important than that just after yield, but this has not been investigated here. Using an average measure of triaxiality does remove the irregularities as evident in figure 6.13b.

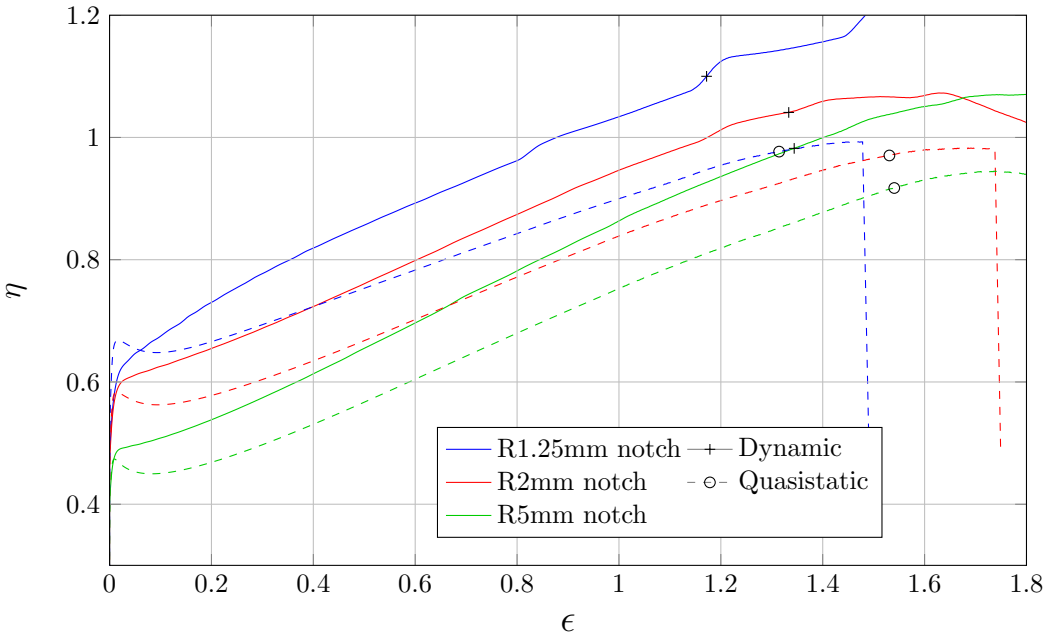

(a) Instantaneous

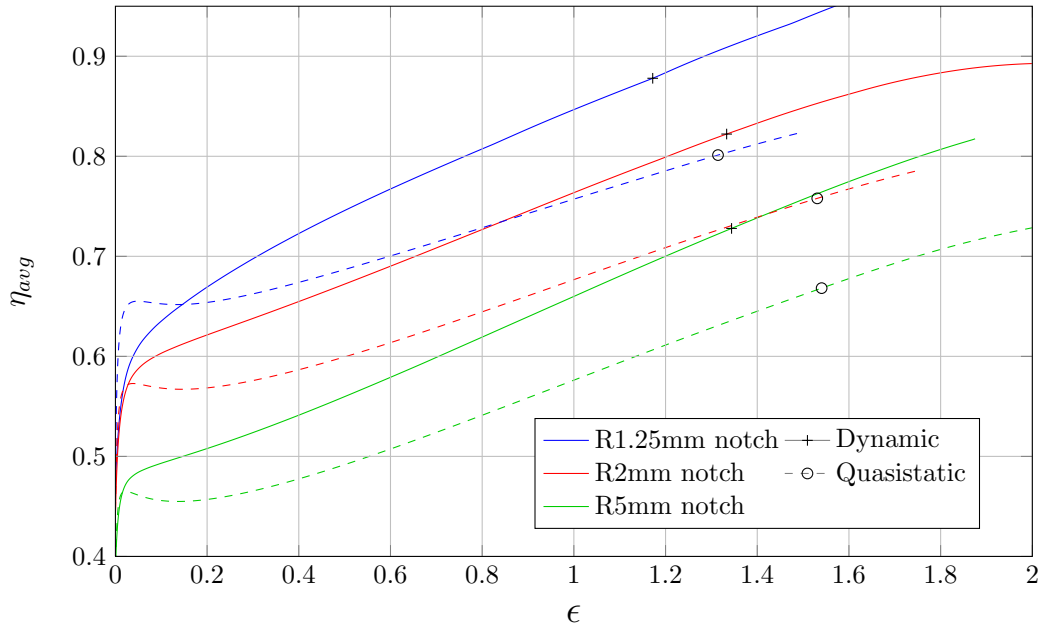

(b) Average

Figure 6.13: Change in triaxiality with equivalent strain for the notched specimens. Both the instantaneous and the average triaxiality, which is used in the Bai-Wierzbicki damage model, are considered. The symbols indicate the strain at which fracture occurs.

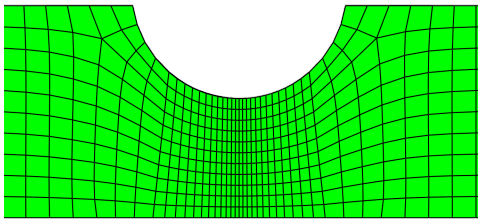

(a) No deformation

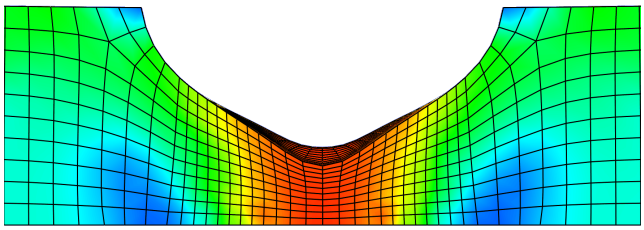

(b) At point of fracture

Figure 6.14: Dynamic model of the 1.25mm notched specimen shown before deformation and at the point of fracture. The relative magnitude of von Mises stress is included.

Despite these complications, the expected trend of failure stain decreasing with an increase in triaxiality is evident[28]. Furthermore, the strain rate does appear to have an influence over the failure strain for a given triaxiality.

In contrast, it is difficult to decipher a failure pattern for the grooved specimen triaxiality evolution, shown in figure 6.16. This may indicate that strain rate and triaxiality has only a minor influence for specimens with a low Lode angle around zero. However, the grooved specimens should be considered with caution as mesh density may play a greater role than for the notched specimens as fewer elements are placed across the thickness.

Note that a discrepancy appears with the 1.25mm radius grooved specimen having a greater triaxiality in the quasistatic case, in contrast to the remaining two grooved specimens and all the notch specimens. However, this is due to the variation in the machined dimensions. The groove gap for the quasistatic specimen is over 20% larger than that of the dynamic resulting in an inflated initial triaxiality. At higher strains the dynamic specimen increases in triaxiality at a greater rate than the quasistatic, in line with the other results.

[28]Found in several fracture models reviewed in chapter 2.

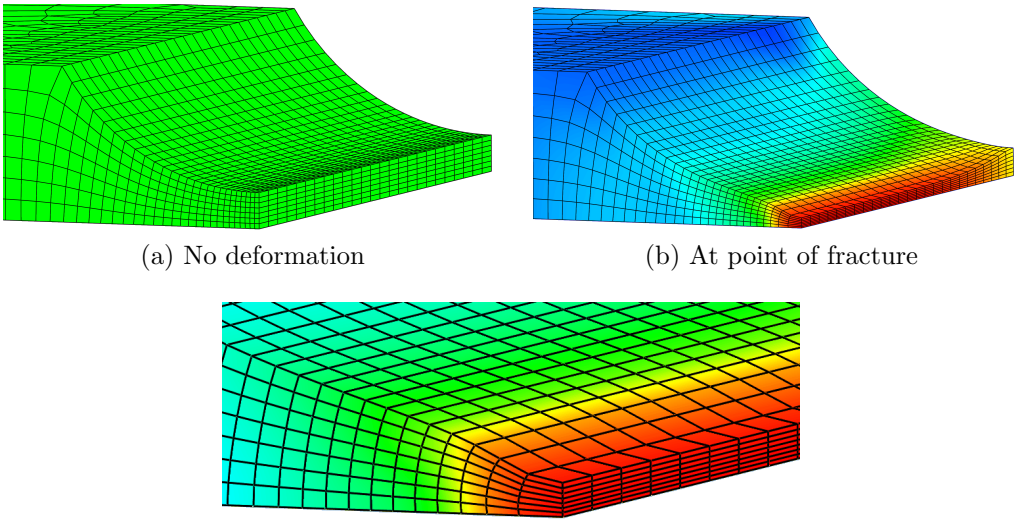

(a) No deformation

(b) At point of fracture

(c) Close view at fracture

Figure 6.15: Quasistatic model of the 2mm grooved specimen shown before deformation and at the point of fracture.

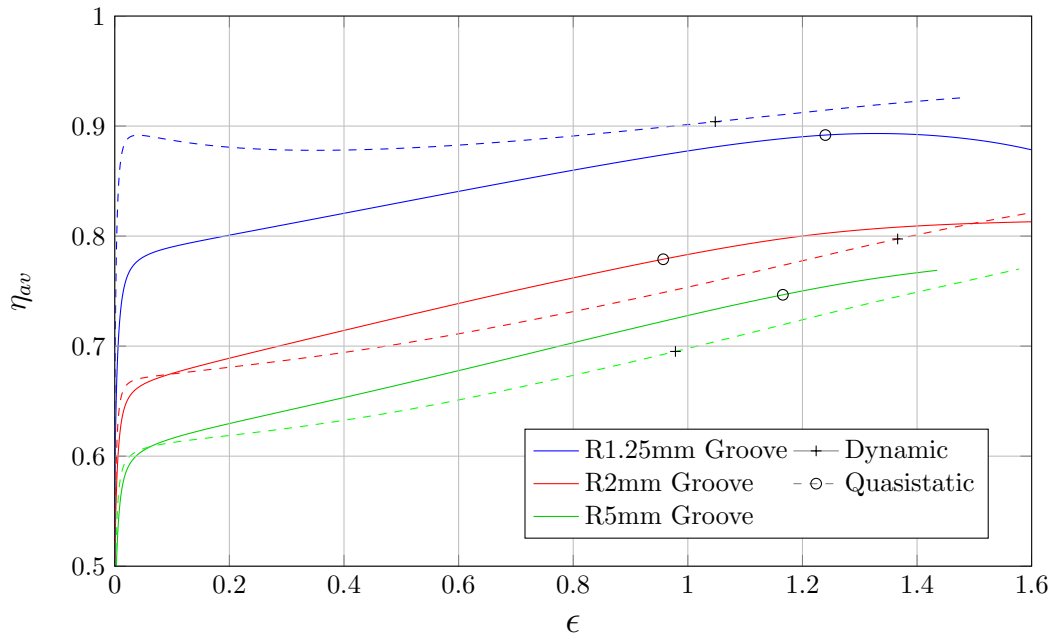

Figure 6.16: Change in average triaxiality with equivalent strain for the grooved specimens.

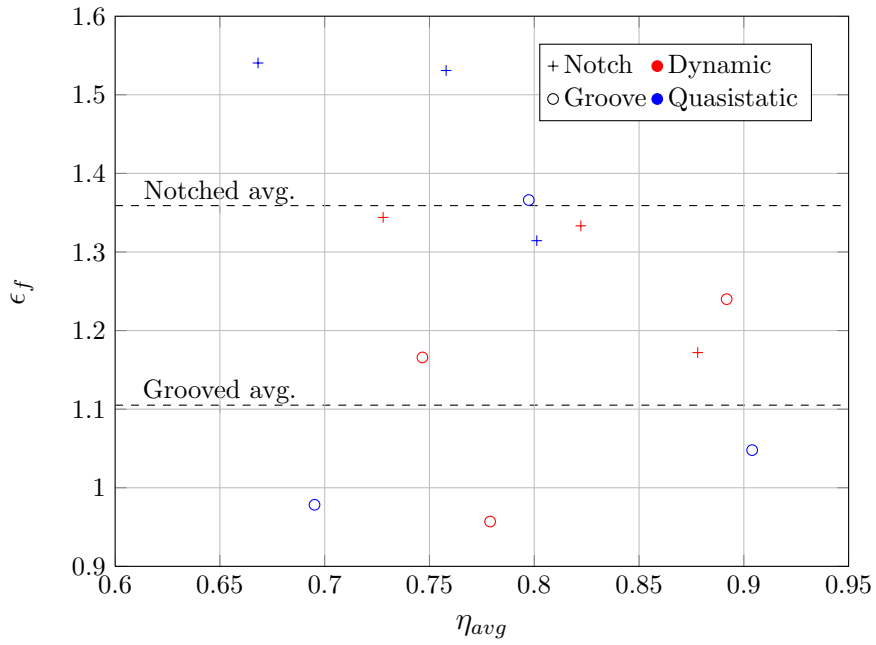

Figure 6.17: Fracture strain for all types of specimen. In general the dynamic specimens fail at a lower strain than the quasistatic.

6.4.3 Effect of Strain Rate and the Invariants

The final fracture strain is plotted against average triaxiality for all the specimen geometries in figure 6.17. The most simple observation is that the grooved specimens, with a low Lode angle of 0, generally fail at lower strains than the notched specimens, with a much higher Lode. This ties in with the findings of Wierzbicki et al. [68, 55] that a measure of the third deviatoric stress invariant is required to correctly predict fracture.

A second trend is the slight, but distinct effect of strain rate on fracture. In general, the quasistatic specimens fail at a higher strain than the dynamic equivalents. This is especially evident among the notch results, which appear to be the most consistent. The trend is less clear for the grooved specimens and thus strain rate may play less of a role for these specimens.

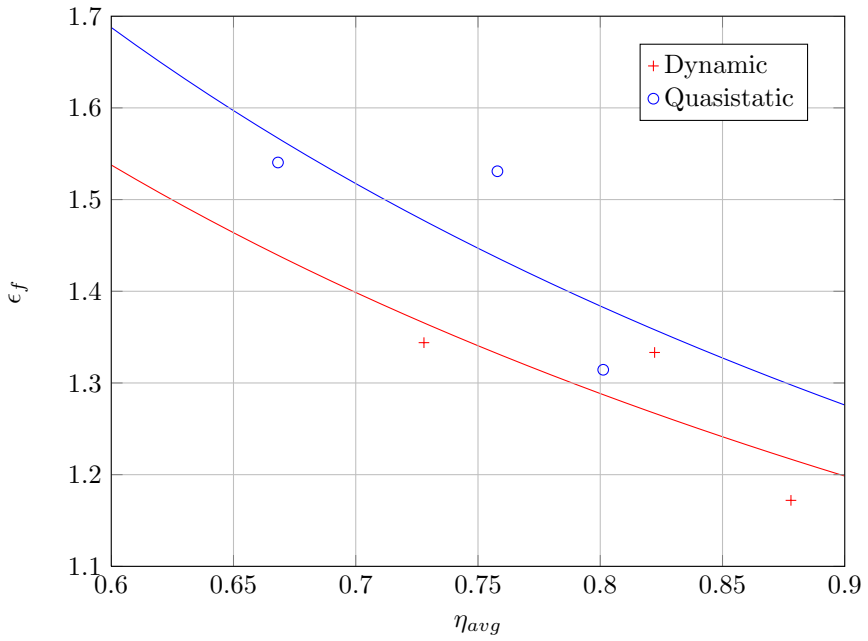

Figure 6.18: Failure strain versus average triaxiality for the notched specimens. Exponential curve-fits indicate the dynamic specimens failing before the quasistatic.

A closer view of the notch results is given in figure 6.18, which again compares average triaxiality to failure strain. In addition an exponential curve fit of the form,

$$\epsilon_f = A\eta_{avg}^K$$

was applied to both sets of data with interesting results. This type of curve fit was used by Bao and Wierzbicki [3] in the high triaxiality region. The fitted curve for the quasistatic specimens is clearly above that for the dynamic, especially at low triaxialities. There is a danger in implying too much from trend-lines made up of only three data points each. However, the strain rate appears to have a distinct effect.

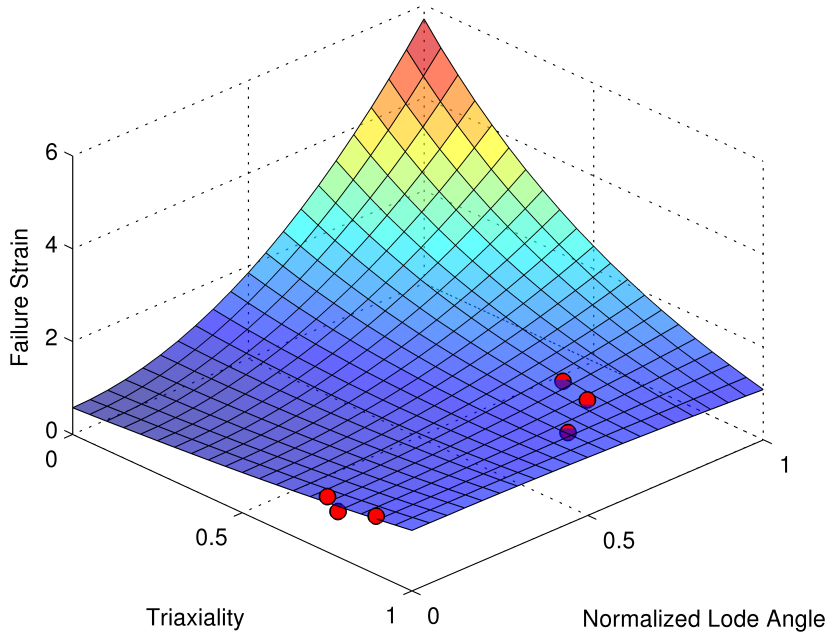

Figure 6.19: Fracture locus generated using the dynamic results.

6.5 Implementation

The experimental results reported here are located within a narrow band of triaxiality and thus the derived Wierzbicki damage surface is not assumed to be applicable for a wider range of geometries. However, to determine the success of the damage model implemented in the VUMAT, a symmetric damage curve similar to that used by Xue and Wierzbicki [68] was developed.

To derive the constants a Matlab script was written that uses the least squares method to determine which constants result in the closest correlation. The final solution, shown in figure 6.19, is different to that expected as the minimum is set at $\bar{\theta}, \eta = 0$, whereas an increase in triaxiality should result in a lower failure strain. The discrepancy is due to the influence of the grooved specimens, which predict a slight increase in failure strain with triaxiality. This result is in contrast to that in the literature (see for example [17]) and indicates that more tests in this loading region are required. This complication shows clearly the importance of conducting shear and compression tests to cover a larger region of the locus.

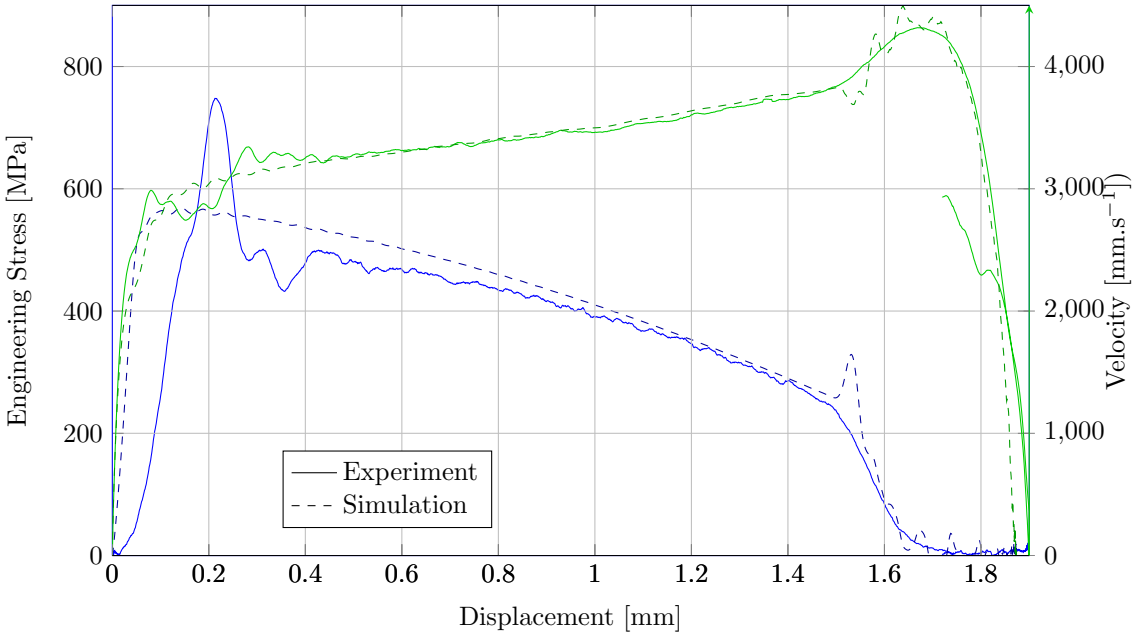

Figure 6.20: 5mm notched specimen damage simulation compared to the experiment. A sudden stress peak occurs at the point of fracture due to the elements being removed instantly from the mesh with no prior softening.

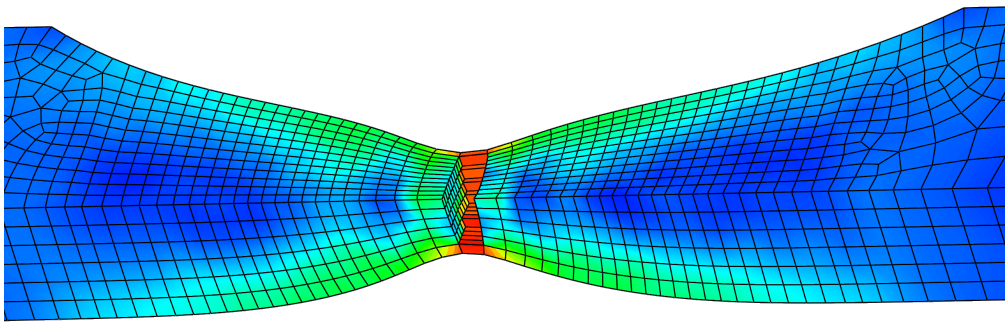

Figure 6.21: Simulated 5mm radius notched specimen during fracture. At this stage the central elements have failed and been removed, while the outer elements remain in the mesh.

Nevertheless the average error between the calibration strains and fracture surface is only 4.4% and thus a dynamic model of the 5mm radius notched specimen was tested. The result is included in figure 6.20 with fracture occurring at the correct central location, shown in figure 6.21. Interestingly, a stress spike occurs at the point of failure. In the current implementation an element is immediately removed from the stiffness matrix once the failure criterion is reached. This action could result in an instability within the solver as the remaining elements are subjected to a velocity determined during the previous step, before damage occurs. A possible solution would be to introduce progressive element weakening as the fracture locus approached, decreasing the element stiffness such that when the element is finally removed the change to the total stiffness matrix is minimal.

Chapter 7

Discussion

7.1 Introduction

In this chapter an analysis is conducted of both the apparatus and techniques developed and the central experimental results. The first section considers the design of the tensile split Hopkinson pressure bar and specimens developed in chapter 3. The TSHB design is a significant success and is clearly an excellent method in conducting tensile dynamic experiments. The simulation procedures of chapter 4 are assessed in the next section, which primarily considers the infinite element technique and the implementation of the user model.

The final sections are related to the experimental and numerical results. Section 7.4 considers the specimen deformation and the influence of the small specimen geometry. This is followed by an analysis of the influence strain rate has over damage by reviewing the results from chapters 5 and 6. Significantly, the results indicate that at quasistatic to intermediate strain rates, an increase in rate increases strain to failure, while at higher dynamic rates, failure strain decreases with strain rate. Finally the damage model itself is reviewed.

7.2 TSHB Effectiveness

One of the major successes of this project is the development of the tensile SHB. Central to the design is the tubular striker that, although simple compared to other options in the literature, produces a clear square pulse with minimal oscillations.

The striker was significantly improved from the previous iteration by Downey [50] by replacing the steel transfer cap and flange with titanium pieces and the pressure cap material with HDPE. This drastically decreases the inertia of the attachments and hence reduces the stress spikes and oscillations seen in some of Downey's results. Clearly minimizing the mass of the end pieces is essential to producing a clear incident pulse.

A further improvement was to use aluminium as the output bar to increase the magnitude of the transmitted signal. Small specimens are deformed with a relatively low reaction force and thus the stress signal through the output bar can be minimal. However, aluminium has an elastic modulus of around 70 GPa compared to 200 GPa for steel and thus the equivalent stress results in a much larger strain being read by the strain gauge. The success of the aluminium bars indicates that more materials are worth investigating to increase the strain gauge reading even further. Magnesium may be a good option as the elastic modulus is only 45 GPa, while it has a very similar impedance to both aluminium and steel with a wavespeed of $c \approx 5000\,\mathrm{ms}^{-1}$.

Finally the large scale of the bar allows for testing flexibility. The striker length was carefully calibrated to generate a long pulse with an adequate delay between pulses to ensure that each is read independently. If softening putty is used, the 1.3m striker is ideal as it produces an incident pulse of $590\,\mu$s. Significantly, the peak stress is maintained for $470\,\mu$s . The pulse length can be extended even further if the 1.45m striker is used without putty. However, softening is not possible with this striker as the additional rise time results in inadequate separation between the incident and reflected waves. The advantage of such a long signal is that specimens can be deformed at a lower strain rate and still reach the point of fracture in the initial loading.

The novel specimen attachment technique succeeds in allowing the specimens to fracture without permanent deformation within the glue or thread zones. Furthermore, by securing the specimens firstly to lengths of threaded bar, the same split Hopkinson bars can be used for characterizing both round and sheet metal specimens. However, clearly some elastic deformation will occur within the glue zone. This strain has a greater relative effect over the grooved specimens as these fail after a very small displacement. If simulations are to be conducted on every specimen this is not a major issue if the epoxy material properties can be accurately determined. However, in practice many tests will be run without parallel simulations. In these cases a possible solution may be to use a compliance factor, similar to that used in the quasistatic experiments, to isolate and remove the displacement due to deformation within the glue zone.

The gluing jig is a useful tool to glue the specimens and keep these correctly aligned within the threaded bar slots. However, the gluing process itself is time consuming as the 3M Scotchweld cure time to handling strength is 6 hours. In practical terms this results in only two specimens being glued every six hours, one in each of the two jigs. Thus, although this glueing technique is effective, further attachment methods should be investigated.

7.3 Modelling

Using infinite elements to model the TSHB is an elegant solution. This technique cuts down simulation time significantly as the stress pulse need not travel the complete length of both bars. Implementing these elements is the optimal method for this experimental setup.

It seems odd that the scheme has not been more generally applied in the literature. Only an oblique reference was found by Kammerer and Neme [53] who used infinite elements to model the split Hopkinson bars in the study of composites. However, little mention was given to the details of the implementation, or success.

This work found that using the Abaqus implementation of infinite elements with the same properties as the bars results in spurious reflections. It appears that the unmodified elements over-damp the boundary. However, by simply reducing the elastic modulus of the infinite elements iteratively this reflection is made negligible.

An important success is the development and implementation of the user material model, or VUMAT. This is presented in sections 4.2 to 4.3, while the complete code is included in appendix B. In its final form the solver uses a predictor return algorithm to determine plastic strain as this is stable for both quasistatic and dynamic strain rates.

Using the iterative Newton's method resulted in instabilities when applied at quasistatic rates to a single element and to the full model in the dynamic case. This is due to small errors in approximating the plastic strain as the increment is overestimated resulting in a strain rate spike and followed by elastic steps to to correct the initial mistake. The Abaqus implementation uses the iterative Newton's method [59] with stable results and thus, although not successful here, optimising the Newton's method implementation of the VUMAT must be possible.

The final, implemented model is stable through the entire range of strain rates tested here. Furthermore, as it is designed to be easily adaptable to different plasticity and damage functions, the model is a useful tool for the BISRU researchers to use.

7.4 Specimen Deformation

The specimens were kept small firstly to ensure that fracture occurred before the glue failed. In addition the grip width had to fit into the groove cut out of the M14 threaded bar. The major limiting factor was the glue and specimens were kept to a maximum cross-sectional area of $8\,\mathrm{mm}^2$ in the centre of the gauge length.

The small geometry proved to be a problem as several specimens were machined with dimensions quite different to that specified. The dimensions resulted in minor machining error having a significant influence as, for example, a groove gap of 0.8mm when 0.6mm was specified.

Imperfections result from the machining process, especially the removal of burrs. These may have a greater influence on damage initiation than similar sized defects on larger specimens. With this in mind the specimens were prepared post manufacture and generally fail in the centre of the gauge section as required.

The specimens that were deformed at similar strain rates fall within the same band, indicating that the defects did not have a major influence. However, ideally, the specimens should be polished to completely remove this risk.

The success of the glue indicates that the cross-sectional area can be increased. The glue tests in section 3.3.3, showed that if the material had a yield strength of 800 MPa and a glue length of 20mm, the glue would be between 15 and 30% stronger than required by a specimen with a cross-sectional area of $8\,\mathrm{mm}^2$. Thus conservatively, the area can be increased by a factor of 1.15. Furthermore, the final glue length was 30mm. Assuming the glue strength is directly related to the glue length, this results in a potential area increase of

$$1.15 \times \frac{30}{20} = 1.725\,\text{times}$$

Finally, as the mild steel yielded at around 600 MPa, which increases the maximum area by a combined

$$1.725 \times \frac{800}{600} = 2.3\,\text{times}$$

Thus an acceptable cross-sectional area of $18.4\,\mathrm{mm}^2$ can be approximated. This is a significant increase and specimens with this geometry could still have a grip that fits into the threaded bar slot.

A separate, but interesting observation is that the specimens deformed at around the fast quasistatic rate were noticeably stronger than those at the low rate, which were deformed approximately 100 times slower. Thus rate dependency for plastic deformation is clearly evident even at quasistatic rates. Predictably, the material is far stronger in the case of the dynamic specimens.

7.5 Strain Rate Effect on Ductile Fracture

The experimental results in chapter 5 show that at quasistatic strain rates, the specimens deformed at the faster rate fracture consistently at a greater displacement. The higher rate specimens had a nominal strain rate in the centre of roughly $0.5\,\mathrm{s}^{-1}$ at yield and $2\,\mathrm{s}^{-1}$ at fracture. While the slow rate specimens were deformed at a velocity nominally 100 times less and thus the strain rate should be approximately $0.02\,\mathrm{s}^{-1}$ at fracture.

The lower rate specimens could not be modelled using an explicit analysis due to the impractical computation time required[29]. Thus a conclusive indication of the strain rate influence at these low rates cannot be taken directly from the simulations. Instead, trends must be inferred from the experimental results. These show that the specimens at both rates neck at roughly the same displacement, but the fast specimens fracture at noticeably larger displacements. Thus it appears likely that at quasistatic strain rates, fracture strain increases with strain rate.

In contrast, the specimens deformed dynamically at strain rates in excess of $1000\,\mathrm{s}^{-1}$ fail significantly earlier than those at the quasistatic rates. This trend is partly due to the material plasticity behaviour at different strain rates. The quasistatic specimens yield early, but have a high hardening gradient subsequently and this delays the onset of necking. However, dynamic specimens, although having a greater yield stress, have a low hardening gradient post yield and thus neck before the quasistatic specimens. This is confirmed by the experimental result, which clearly show the dynamic specimens necking consistently before the quasistatic equivalents. The early onset of necking results in stress localizing in the dynamic before the quasistatic specimens and this reduces the displacement to failure.

However, by simulating the experiments a deeper understanding can be gained. The simulation results in chapter 6 show that the notch specimens deformed at the dynamic rate fail at a lower strain than the quasistatic. The trend is not as clear for the grooved specimens, which fail at far lower displacements and thus are difficult to assess. The lack of trend may be due to mesh density problems as the specimens were very thin at the groove. However, the difference may be explained by the Lode angle parameter. The notched specimens have a high normalized Lode angle of approximately 0.7, while the grooved specimens have a low Lode angle of zero. Thus it is speculated that strain rate has a greater influence at high Lode angles.

[29] Covered in section 6.3.2 on page 163

The major difference between the quasistatic tests and the dynamic is temperature, with the latter being approximated as adiabatic due to the experiment time scale being so short. In contrast, specimens deformed at slow rates dissipate heat while plastic deformation occurs and thus undergo an isothermal process. However, without completing tests at different initial temperatures it is difficult to isolate the influence of strain rate and that of temperature.

Johnson and Cook [14] tested notched, round specimens quasistatically and dynamically to study damage. To determine the temperature effect, dynamic specimens were heated to differing degrees prior to testing. The authors concluded that both strain rate and temperature result in increased strain before failure, in contrast to the results found in this thesis.

Johnson and Cook used the cross-sectional area through the neck at failure to approximate the final strain. It was found that the dynamic specimens and those at higher temperatures had a smaller final area than the quasistatic and inferred that the failure strain was greater. However, the opposite is found here. Instead, the lower cross-sectional area for the quasistatic specimens in this thesis[30] supports the finite element analysis, which shows a slight trend for the slow rate specimens to fail at a greater strain for equivalent triaxialities. In the Johnson and Cook analysis, round specimens were tested in comparison to the square cross-sections considered in this work, but this should not have a significant influence over the strain rate effect.

Little work has been published on strain rate or temperature effect since that by Johnson and Cook. Indeed when Teng and Wierzbicki [13] used the Wierzbicki-Xue model to simulate high velocity perforation, material data was obtained from quasistatic tests and used directly with no strain rate or temperature modification.

This study has shown that the combination of strain rate and temperature does have an effect on the failure strain. The following trends appear likely for this material:

1. In the quasistatic range, fracture strain increases slightly with strain rate.
2. From high quasistatic to dynamic rates, fracture strain decreases with strain rate.

[30] See for example figure 5.20 on page 142.

For mild steel the strain variation is small and thus if only an approximate damage analysis is required, using quasistatic data to generate a damage model implemented in the dynamic regime should be acceptable. However, these must be used with caution as the quasistatic specimens fail at a greater strain and thus using the data would lead to an overestimation of fracture strain.

7.6 Damage Model

The Bai-Wierzbicki model [55] appears promising as it takes into account decreased fracture strain at low Lode angles. The grooved specimens with a low Lode angle of zero fail earlier than the notched examples with higher Lode parameters, thus clearly some measure of the deviatoric stress invariant is required.

The model comes at the cost of extensive calibration as at least six tests are required across the range of Lode angle and triaxiality. In this analysis the Bai-Wierzbicki locus was simplified into a symmetric form about a Lode of 0 as all the experiments have positive Lode angles. This version requires only four experiments, but tests should include as wide a range of triaxialities as possible, else the form of the locus may be incorrect. This occurred here as despite attempts to create specimens with a wide range of triaxialities, the final band was narrow.

Implementing the damage model in the method used by Teng and Wierzbicki [4] requires further analysis. The method involved removing elements from the stiffness matrix when the failure criteria were met. However, a dynamic simulation showed that this immediate change creates an instability which results in a reaction force spike. Increasing the mesh density may improve this, but a more promising solution would be to progressively weaken the elements when the failure is approached such that when the element is finally removed, the change to the stiffness matrix is minor.

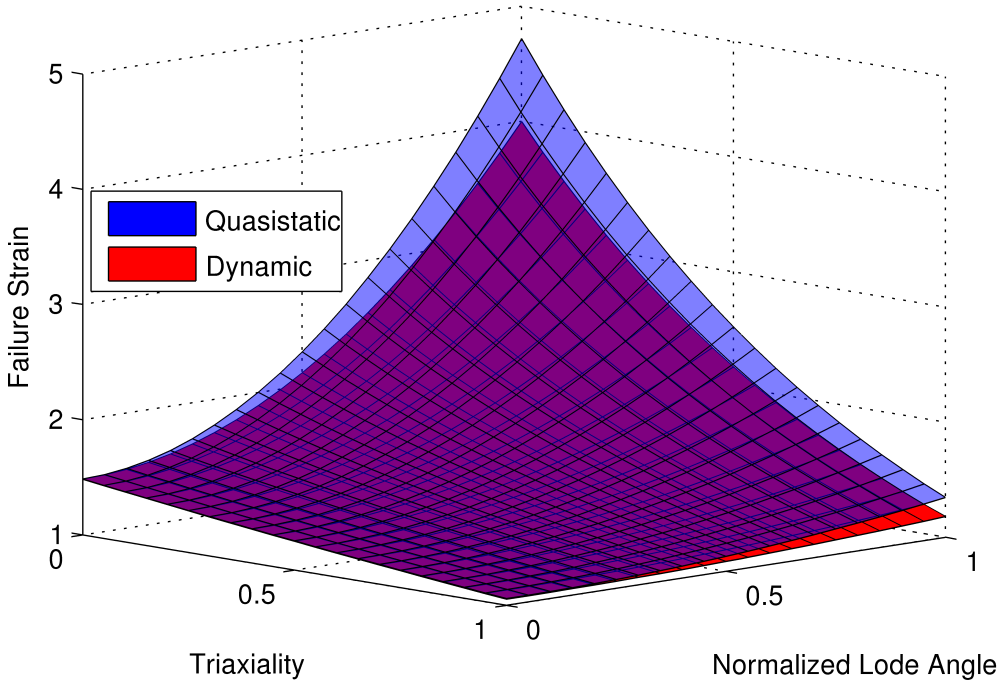

Figure 7.1: Predicted strain rate effect to the Bai-Wierzbicki damage mode. A decrease in fracture strain is predicted at high Lode angles for dynamic experiments.

The strain rate analysis indicated that strain rate does have an effect on fracture strain. It is speculated that the effect is greatest at high Lode angles and minimal at a Lode angle of zero. A possible form is shown in figure 7.1. This uses the data from the simulations in chapter 6, but adds a data point at the location $\bar{\theta}, \eta = 0$ to prevent this location from becoming a local minimum. Thus to confirm the locus, shear experiments need to be conducted as these have low Lode angles and triaxiality.

Chapter 8

Conclusions

8.1 Introduction

The main goals of this thesis were to develop a testing procedure aimed at determining the influence of strain rate to ductile failure and to make an initial attempt at establishing these properties. Although further research is needed, the first goal was met. Of the latter, strain rate does have an influence over ductile failure and further testing is required to quantify the effect.

8.2 Testing Procedure

The design of the tensile split Hopkinson bar rig is a significant success. Using a tubular striker is an uncomplicated method of producing a tensile pulse, but when optimized results in little noise. Furthermore, the scale of the rig allows a large degree of flexibility for future testing as significant specimen deformation can be achieved using a wide range of strain rates.

A further success is the adaptation using the combined system of threaded bar and glue to secure the sheet specimens to the bars, as for every test the specimen failed before the epoxy. However, some elastic deformation will occur within the glue zone and thus this effect must be quantified.

An advantage of the specimens configured here is that identical designs can be used for both dynamic and quasistatic testing. This aids the manufacturing as it reduces the number of jig changes required and hence decreases machining time. The only disadvantage is that some slip occurs during quasistatic tests, but this is limited to the elastic range and can easily be accounted for.

In modelling two methods were implemented for the different strain rate regimes. The most significant is the use and refinement of infinite elements to replace the split Hopkinson bars, which significantly reduce the dynamic experiment computation time. Secondly, using mass scaling of up to 600 times reduces the computation time for the quasistatic specimens, with no ill effects. Regrettably the duration of the slow rate quasistatic tests at $0.001\,\mathrm{s}^{-1}$ was too long to simulate using an explicit algorithm, even with mass scaling, and thus this will be the subject of future work.

The damage and plasticity model was programmed as a user defined VUMAT in Fortran. This implementation is stable for both low and high strain rates and takes into account temperature, strain rate as well as the damage parameters Lode angle and triaxiality. A further advantage is that it is easily adaptable to different types of plasticity and damage loci.

The testing procedure to determine damage properties can be summarised as follows:

1. Conduct quasistatic and dynamic tests for each specimen. Record the reaction force, displacement and velocity.

2. Perform parallel numerical simulations, calibrating the plasticity constants to allow good correspondence to the experimental data.

3. Determine the point of failure in the experimental results using point at which the force gradient reduces significantly.

4. Use the position with equivalent displacement on the numerical result to determine Lode angle, triaxiality and fracture strain.

5. Apply the surface fitting technique in Matlab to determine the Bai-Wierzbicki damage model constants.

8.3 Strain Rate Effect to Ductile Damage

At quasistatic strain rates, the specimens strained at the slow rate ($\approx 0.02\,\mathrm{s}^{-1}$ at fracture) fail at a lower displacement than those at the fast rate ($\approx 2\,\mathrm{s}^{-1}$ at fracture). This trend is not due to neck initiation as both appear to neck after similar displacements and thus strain rate is predicted to increase failure strain in this regime.

In contrast, the dynamic specimens fail at significantly lower displacements than those at the quasistatic strain rates. This can partly be explained by the low hardening gradient experienced by the material at high rates leading to necking at low strain. However, the simulations show that dynamic specimens generally fail at a lower plastic strain within the neck than the quasistatic for equivalent Lode angles and triaxialities. This trend is distinct for the specimens at high Lode angles of 0.7, but less so for those at Lode angles of zero. Thus it is speculated that, for tensile specimens, strain rate has a greater influence in loading cases where the triaxiality is high.

The results confirm the need to take into account a measure of the deviatoric stress for the damage model. The simulations showed that the grooved specimens, with a normalized Lode angle of zero, fail at a lower strain than the notched specimens with a greater Lode of around 0.7. Thus models such as the Bai-Wierzbicki[17] damage locus, which consider this effect, look promising for accurate damage analysis.

A simplified symmetric version of this model was implemented in Abaqus. The fracture locus generated has a different form to that reported by Bai and Wierzbicki [17] for A710 steel due to the final triaxialities of the specimens being located in too narrow a band. This raises an important point, to correctly formulate the model tests should be completed through a wider range of triaxiality and Lode angle than occur within the intended application. The model correctly predicts the point of failure, but results in a stress peak at the point of damage. The spike is due to a mesh instability caused by instantaneously removing the damaged element from the mesh.

Chapter 9

Recommendations

9.1 Introduction

This chapter considers the steps required to further improve both the testing procedure and damage analysis. The First section deals with small changes that would make using the tensile split Hopkinson pressure bar apparatus an easier and more efficient process. It also contains possible options to improve the sheet specimen attachment method. Section 2 details the specimen design. Problems with the specimens stem chiefly from the small dimensions, but these can be increased. The final section recommends procedures to increase the accuracy of the numerical simulations, such that the strain rate effect can be quantified.

9.2 TSHB

The built tensile rig is a significant success. However, due to the extreme length of the bars, alignment is time consuming. This could be improved in two ways, firstly by investigating methods to straighten the bars and secondly by improving the laser alignment system as currently the light is severely diffracted when it reaches the far end of the bar.

In the current apparatus, calibration is completed using a compressive striker as the striker velocity can be determined using a light sensor developed for compressive testing. The procedure is time consuming as the tensile barrel and striker both need to be replaced by the compression equivalents. Ideally a short tensile striker could be used instead, with a light sensor adapted for the apparatus. Developing this useful adaptation should be is a simple task, but it is one that will increase testing efficiency considerably.

Prior to each experiment, the transfer cap must be removed from the striker to allow putty to be placed on the transfer flange attached to the input bar. An alternative would be to replace the putty with a fixed material, for example a thin rubber gasket, that would soften the impact, but not need regular replacement. An added advantage would be the increased consistency in the degree of softening.

An additional practical adaptation would be to use left and right handed threaded bar on either side of the specimen, thus allowing the specimen to be screwed in while the bars are fixed in place. With the current system the specimen can be screwed into one bar, but the second bar must then be rotated while the specimen is fixed. This is inconvenient due to the strain gauge wires that must be protected. Ideally a basic tool needs to be developed to clamp onto both sides of the specimen and thus prevent the gauge section from being damaged during the screwing process.

The greatest unknown with the current attachment system is the degree of deformation within the glue. In the simulations, the epoxy was approximated as an elastic material with properties found in the literature[64]. However, thorough investigation is required to characterize this material correctly. One method would be to glue a solid rectangular specimen into the two sections of threaded bar such that the two halves completely cover the specimen. The resulting transmitted stress signal could then be compared to a similar experiment using only a solid section of threaded bar to replace the specimen. This test could be repeated on the Zwick quasistatic tensile machine by screwing the threaded bar into the same end fixtures used in the glue strength tests in this work.

An alternative attachment system is to use a clamping system. A potential design would be to manufacture a tapered bar with thread machined onto its outer surface. This would then be split and the specimen placed in between such that when the clamp sub-assembly is screwed into the bars it tightens over the specimen. A major advantage with a clamping system is the much lower preparation time as no epoxy is required.

A final long term goal should be to develop an image processing capacity so that deformation through the specimen can be compared more closely to the FEA models.

9.3 Specimen design

The tests in this thesis are in too narrow a triaxiality band to correctly calibrate the Bai-Wierzbicki damage model and thus the test range needs expansion. As the work in BISRU revolves mainly around the blast loading of plates the most important regions are those dominated by tension and shear and thus concentrating on the triaxiality and Lode range of $0 \leq \bar{\theta}, \eta$ should be sufficient.

The notched and groove specimens cover the high triaxiality regions and redoing the straight specimen tests should result in a mid triaxiality of around $\frac{1}{3}$. However, notably absent is a test with Lode and triaxiality close to zero, this region is equivalent to a state of pure shear and is a key area to research as the damage mechanism is no longer failure due to void growth. Ideally pure shear needs to be tested as well as that with superimposed tension and compression to fully populate the region.

To improve consistency of the experimental results the specimens need optimization. The problems with the current versions revolve around the following:

- Manufacture. The small specimens are difficult to manufacture accurately. The process could be improved by designing a jig specifically to hold tensile specimens securely in the CNC milling machine.
- Specimen preparation. Imperfections caused by burrs may result in necking, and indeed failure, occurring earlier than predicted in the numerical work. These imperfections have a larger influence the smaller the specimen size.

- Measurement. Small errors in measurements result in relatively large errors in the numerical work.
- Handling. The thin straight and groove specimens had to be handled with caution as these were easily bent.

Ultimately, the inconsistencies only had a detrimental influence on the groove specimens. These have a specified thickness of only 0.6mm to allow for a relatively deep groove, yet increasing this dimension to 1mm will allow an acceptable groove depth of 1mm. As the epoxy held firm for all tests, larger specimens can be developed and a cross-sectional area of 18 mm^2 should be acceptable. In addition, focus needs to be placed on accurate machining and specimen preparation to minimize imperfections.

For ease in manufacture, the quasistatic specimens are exactly the same design as the dynamic. Yet this results in significant slip during early elastic deformation of the quasistatic experiments. Ideally the quasistatic grip surface width should be increased, especially if larger specimens are to be tested.

A measurement that was not taken prior to testing was the notch and groove radii. This was assumed to be correct due to the correct milling bit used. Yet in light of the inconsistencies it would be best in future to develop a system to accurately measure radii as these have a major influence on triaxiality and hence damage initiation.

9.4 Modelling

The current simulations are useful to identify trends in the failure pattern, yet for a more quantitative analysis these need revision. At present there are several unknowns, chief among these is the effect the threaded connection and glue have on the readings. The glue stiffness requires physical testing, yet the thread should be modelled to see whether the initial stress peak found in the experiments can be repeated. However, this should not have a significant influence on the damage analysis as the thread effects are only evident during early deformation.

Another influence is mesh density. The simulations were developed using element sizes from the literature[17, 55] as a guide. However, the element size does seem to have an effect as those in the specimen centre are distorted at high strains. This leads to minor errors in determining the status at the point of failure and could explain the lack of clear trends within the grooved specimens. Due to numerical time constraints using the explicit scheme, a deeper analysis with much greater mesh densities was not completed and needs consideration.

For accurate quasistatic analysis, the VUMAT, which is only valid for an explicit analysis, should to be rewritten as a UMAT to allow an implicit finite element solver to be used. This in turn would allow much higher mesh densities through the quasistatic specimens with no reliance on a mass scaling factor. Furthermore, the slow quasistatic experiments could be simulated easily. As an increase in strain rate seems to increase fracture strain in the low rate regime, this analysis would aid understanding rate sensitivity considerably.

Although, implementing infinite elements is a significant success, the element properties of these elements needed to be altered. In the final model, the infinite element elastic modulus was reduced as the elements appeared to be over-damping the boundary. However, this modification is not suggested by either the Abaqus documentation [59] or the work by Kammerer and Neme [53] and thus requires investigation.

For several models, the simulated engineering stress differed from the experiments. In developing the plasticity model, Bai and Wierzbicki [17] found that by introducing a hydrostatic and Lode angle effect to the model, tensile specimen deformation could be simulated more accurately. The change was most noticeable for the grooved specimens at a low Lode angle, which is where the correlations for this work are the weakest and is thus worth attempting.

Finally, to improve the implementation of failure, a progressive damage model needs to be attempted. The theory behind this is that by weakening the elements prior to removal, the final change to the stiffness matrix at element failure will be minor. Thus if the instability at failure is due to the sudden change of removing the elements instantaneously, as believed, it could be corrected.

References

[1] T. Wierzbicki, Y. Bao, Y. Lee, and Y. Bai. Calibration and evaluation of seven fracture models. *International Journal of Mechanical Sciences*, 47(4-5): 719 – 743, 2005. A Special Issue in Honour of Professor Stephen R. Reid's 60th Birthday.

[2] F.A. McClintock. A criterion for ductile fracture by the growth of holes. *Journal of Applied Mathematics*, 35:363–371, 1968.

[3] Y. Bao and T. Wierzbicki. On fracture locus in the equivalent strain and stress triaxiality space. *International Journal of Mechanical Sciences*, 46(1): 81 – 98, 2004.

[4] X. Teng and T. Wierzbicki. Numerical study on crack propagation in high velocity perforation. *Computers & Structures*, 83(12-13):989 – 1004, 2005.

[5] G. T. Gray III. Classic split-hopkinson pressure bar technique. *ASM International*, 8:1–36, 1999.

[6] P.W. Bridgman. The stress distribution at the neck of a tension specimen. In *Transactions of American Soceity for Metals*, volume 32, pages 553–572, 1944.

[7] Y. Bao and T. Wierzbicki. A comparative study on various ductile crack formation criteria. *Journal of Engineering Materials and Technology*, 126(3): 314–324, 2004.

[8] *Macroscopic Aspects of Fracture.* Key to Metals, http://steel.keytometals.com/Articles/Art154.htm. Accessed 20/08/2009.

[9] J. R. Rice and D. M. Tracey. On the ductile enlargement of voids in triaxial stress fields. *Journal of the Mechanics and Physics of Solids*, 17(3):201 – 217, 1969.

[10] A.L. Gurson. Continuum theory of ductile rupture by void nucleation and growth: part i - yield criteria and flow rules for porous ductile media. *Journal of Engineering Material Technology*, 99:2–15, 1977.

[11] A. Needleman and V. Tvergaard. An analysis of ductile rupture in notched bars. *Journal of the Mechanics and Physics of Solids*, 32(6):461 – 490, 1984.

[12] M.G. Cockcroft and D.J. Latham. Ductility and the workability of metals. *Journal of the institute of metals*, 96:33–39, 1968.

[13] X. Teng and T. Wierzbicki. Evaluation of six fracture models in high velocity perforation. *Engineering Fracture Mechanics*, 73(12):1653 – 1678, 2006.

[14] G.R. Johnson and W.H. Cook. Fracture characteristics of three metals subjected to various strains, strain rates, temperatures and pressures. *Engineering Fracture Mechanics*, 21(1):31 – 48, 1985.

[15] G. R. Johnson and W. H. Cook. A constitutive model and data for metals subjected to large strains, high strain rates and high temperatures. *Proceedings of the 7th International Symposium on Ballistics*, the Hague, Netherlands:541–547, 1983.

[16] M. L. Wilkins, R. D. Streit, and J. E. Reaugh. Cumulative-strain-damage model of ductile fracture: simulation and prediction of engineering fracture tests. Technical report, Lawrence Livermore Labroratory, University of California, 1980.

[17] Y. Bai and T. Wierzbicki. A new model of metal plasticity and fracture with pressure and lode dependence. *International Journal of Plasticity*, 24(6):1071 – 1096, 2008.

[18] Y. Bao and T. Wierzbicki. On the cut-off value of negative triaxiality for fracture. *Engineering Fracture Mechanics*, 72(7):1049 – 1069, 2005.

[19] P.W. Bridgman. *Studies in large plastic flow and fracture, with special emphasis on the effects of hydrostatic pressure*. Harvard University Press, 1964.

[20] T. Wierzbicki and L. Xue. On the effect of the third invariant of the stress deviator on ductile fracture. Technical report, Massachusetts Institute of Technology, 2005.

[21] L. Xue. Damage accumulation and fracture initiation in uncracked ductile solids subject to triaxial loading. *International Journal of Solids and Structures*, 44(16):5163 – 5181, 2007.

[22] G.R. Johnson and T.J. Holmquist. Test data and computational strength and fracture model constants for 23 materials subjected to large strain, high strain rates, and high temperature. Technical report, Los Alamos National Labroratory, 1989.

[23] T. Børvik, M. Langseth, O. S. Hopperstad, and K. A. Malo. Perforation of 12mm thick steel plates by 20mm diameter projectiles with flat, hemispherical and conical noses: Part i: Experimental study. *International Journal of Impact Engineering*, 27(1):19 – 35, 2002.

[24] T. Børvik, O. S. Hopperstad, T. Berstad, and M. Langseth. Perforation of 12mm thick steel plates by 20mm diameter projectiles with flat, hemispherical and conical noses: Part ii: numerical simulations. *International Journal of Impact Engineering*, 27(1):37 – 64, 2002.

[25] M. M. Al-Mousawi, S. R. Reid, and W. F. Deans. The use of split hopkinson pressure bar techniques in high strain rate materials testing. *Journal of Mechanical Engineering Science*, 221:273–292, 1997.

[26] B. Hopkinson. A method of measuring the pressure produced in the detonation of high explosives or by the impact of bullets. *Philosophical Transactions of the Royal Society of London. Series A, Containing Papers of a Mathematical or Physical Character*, 213:437–456, 1914.

[27] R. M. Davies. A critical study of the hopkinson pressure bar. *Philosophical transaction of the Royal Society of London. Series A, Mathematical and Physical Sciences*, 240(821):375–457, 1948.

[28] H. Kolsky. An investigation of the mechanical properties of materials at very high rates of loading. *Proceedings of the Physical Society B*, 62:76–700, 1949.

[29] J. Harding, E.O. Wood, and J.D. Campbell. A direct-tension split hopkinson bar for simultaneous torsion and compression. *Journal of Mechanical Engineering Science*, 2:88–96, 1960.

[30] H. Huh, W. J. Kang, and S. S. Han. A tension split hopkinson bar for investigating the dynamic behavior of sheet metals. *Experimental Mechanics*, 42(1):8–17, 2002.

[31] U.S. Lindholm and L.M. Yeakley. High strain-rate testing:tension and compression. *Experimental Mechanics*, 8(1):1–9, 1968.

[32] T. Nicholas. Tensile testing of materials at high rates of strain. *Experimental Mechanics*, 21(5):177–185, 1981.

[33] S. Ellwood, L.J. Griffiths, and D.J. Parry. A tensile technique for materials testing at high strain rates. *Journal of Physics E Scientific Instruments*, 15: 1169–1172, 1982.

[34] G.H. Staab and A. Gilat. A direct-tension split hopkinson bar for high strain-rate testing. *Experimental Mechanics*, 31:232–235, 1991.

[35] Y. Li and K.T. Ramesh. An optical technique for measurement of material properties in the tension kolsky bar. *International Journal of Impact Engineering*, 34:784–798, 2007.

[36] P. Verleysen and J. Degrieck. Measurement of the evolution of the axial strain distribution in hopkinson specimens. *Journal de Physique IV France*, 110:501–506, 2003.

[37] T.J. Cloete and M. Downey. Reversed gas gun tensile split hopkinson pressure bar apparatus. Private conversation, 2007.

[38] A.S. Bowden. Numerical investigation of the tensile split hopkinson bar. Honours thesis, Blast Impact and Survivability Research Centre, UCT, 2007.

[39] R. A. Govender, T. J. Cloete, and G. N. Nurick. A numerical investigation of dispersion in hopkinson pressure bar experiments. *Journal de Physique IV France*, 134:521–526, 2006.

[40] L. Pochammer. On the propagation velocitie of small oscillations in an unlimited isotropic circular cylinder. *Journal for Pure and Applied Mathematics (Crelle)*, 81:324–326, 1876.

[41] C. Chree. The equations of an isotropic elastic solid in polar and cylindrical coordinates, thier solutions and applications. *Transactions of the Cambridge Philosophical Society*, 14:250–369, 1889.

[42] A. Tyas and A. J. Watson. An investigation of frequency domain dispersion correction of pressure bar signals. *International Journal of Impact Engineering*, 25:87–101, 2001.

[43] A. Considére. Memoire sur lemploi du fer et de lacier dans les constructions: ii. *Annales des Ponts et Chausses*, 9(6):574–605, 1885.

[44] Z. L. Zhang, M. Hauge, J. Ødegård, and C. Thaulow. Determining material true stress-strain curve from tensile specimens with rectangular cross-section. *International Journal of Solids and Structures*, 36(23):3497 – 3516, 1999.

[45] G. Le Roy, J.D. Embury, G. Edwards, and M.F. Ashby. A model of ductile fracture based on the nucleation and growth of voids. *Acta Metallurgica*, 29 (8):1509 – 1522, 1981.

[46] H. E. Davis, G. E. Troxell, and C. T. Wiskocil. *The Testing and Inspection of Engineering Materials*. The McGraw-Hill Book Company, 1941.

[47] P. Matic, G. C. Kirby III, and M. I. Jolles. The relation of tensile specimen size and geometry effects to unique constitutive parameters for ductile materials. *Proceedings of the Royal Society of London*, 417(1853):309–333, 1988.

[48] P. Verleysen, J. Degrieck, J. van Slycken, B. De Cooman, and L. Samek. Experimental investigation of the influence of the specimen geometry on hopkinson tensile test results. *Structures Under Shock and Impact*, 8:497–505, 2004.

[49] P. Verleysen, B. Verhegge, J. Degrieck, and B.C. De Cooman. Numerical study of the influence of the specimen geometry on split hopkinson tensile test results. *WIT Transactions on Engineering Sciences*, 49:549–562, 2005.

[50] M. Downey. Design, build and test a tensile split hopkinson bar. Honours thesis, Blast Impact and Survivability Research Centre, UCT, 2007.

[51] J. Rodríguez, C. Navarro, and V. Sánchez-Gálvez. Numerical assessment of the dynamic tension test using the split hopkinson bar. *Journal of Testing and Evaluation*, 22(4):335–342, 1994.

[52] P. Verleysen and J. Degrieck. Experimental and numerical study of the response of steel sheet hopkinson specimens. *Journal de Physique IV France*, 134:541–546, 2006.

[53] C. Kammerer and A. Neme. Plane behaviour at high strain rates of a quasi-unidirectional e-glass/polyester composite : Impact application. *J. Phys. IV France*, 07(C3):C3 693–C3 698, August 1997.

[54] D. Bonorchis. *Analysis and Simulation of Welded Plates Subjected to Blast Loading.* PhD thesis, Blast Impact and Survivability Research Centre, University of Cape Town, December 2007.

[55] Y. Bai, X. Teng, and T. Wierzbicki. On the application of stress triaxiality formula for plane strain fracture testing. *Journal of Engineering Materials and Technology*, 131:1–10, 2009.

[56] R.A. Govender. Specimen gluing jig. Unpublished drawings, August 2005.

[57] H. Zhao. A constitutive model for metals over a large range of strain rates. identification for mild-steel and aluminiun sheets. *Materials Science and Engineering Fracture Mechanics*, A230:95–99, 1997.

[58] E. Hearn. *Mechanics of Materials.* Butterworth-Heinemann, 1997.

[59] *Abaqus Theory.* Dassault Systemes Simulia Corp, Providence, RI, USA, 6.8 edition, 2008.

[60] O.Y. Vorobiev. Improved numerical integration of elastic-viscoplastic models with hardening and rate-dependence in autodyn. Technical report, Century Dynamics Inc.

[61] N. Jones. *Structural Impact.* Cambridge University Press, 1989.

[62] D. Bonorchis. Implementation of material models for high strain rate applications as user-subroutines in abaqus/explicit. Master's thesis, Blast Impact and Survivability Research Centre, University of Cape Town, 2003.

[63] J. Lysmer and R.L. Kuhlemeyer. Finite dynamic model for infinite media. *Journal of the Engineering Mechanics Division of the ASCE*, 95:859–887, 1969.

[64] T. Djilal. *Development of a Gluing solution for the assemblies working at high and low temperature: the Joint Multi-adhesives. Implementation of the technological solution and prediction of its behavior in service.* PhD thesis, Laboratory of Engineering of Production of the National School of Engineers TARBES, 2007.

[65] A.L. Window and G.S. Holister. *Strain Gauge Technology.* Applied Science Publishers Ltd., Barking Essex England, 1982.

[66] T.J. Cloete. Rate effect. Experimental data for mild steel from same sheet as tested here.

[67] S. Tanimura, K. Mimura, and T. Umeda. New testing techniques to obtain tensile stress-strain curves for a wide range of strain rates. *J. Phys. IV France*, 110:385–390, sep 2003.

[68] L. Xue and T. Wierzbicki. Ductile fracture initiation and propagation modeling using damage plasticity theory. *Engineering Fracture Mechanics*, 75(11):3276 – 3293, 2008. Local Approach to Fracture (1986-2006): Selected papers from the 9th European Mechanics of Materials Conference.

[69] R.A. Serway and J.W. Jewett. *Physics for Scientists and Engineers.* Thomson Brooks/Cole, 6 edition, 2004.

Appendices

Appendix A

Split Hopkinson bar theory

Contents

Figures

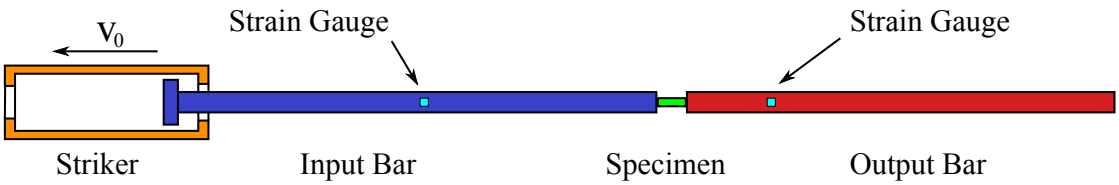

Figure A.1: Tensile split Hopkinson bar.

A.1 Introduction

The classic split Hopkinson bar theory, used to determine the stress and strain of the specimen, is based on one-dimensional elastic wave propagation through the pressure bars[5]. This chapter uses the concept to explain the basic principles behind deriving stress and displacements from the experimental results. One-dimensional wave theory is also used to analyse the interaction between the striker and input bar during the striker collision.

A.2 Basic Principles

To review, the basic split Hopkinson pressure bar consists of two long bars, namely the input and output bar, with a test specimen in between. A simplified setup of a tensile TSHB is shown in figure A.1. The gas gun is used to fire a striker at the input bar. This generates a stress wave (*incident wave*) that travels through the bar. At the input bar - specimen interface, part of the wave travels through the specimen (*transmitted wave*), while the remainder is reflected back (*reflected wave*). This reflected pulse is of opposite nature to the incident, that is if the incident wave is tensile, the reflected will be compressive.

Strain gauges, situated on the outer surface of both bars, are used to record the wave as it passes. As the bars remain elastic, the stress is proportional to the recorded strain as defined by the one-dimensional Hooke's law,

$$\sigma = E \cdot \epsilon \tag{A.1}$$

with σ, ϵ and E the stress, strain and elastic modulus respectively.

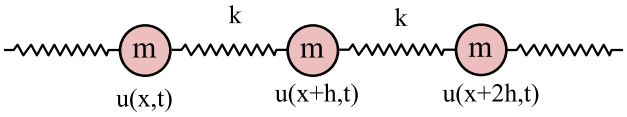

Figure A.2: Developing the one dimensional wave equation.

In practise the strain, as a volt reading, is converted directly to a stress through the gauge calibration factor. By analysing the three captured waves (incident, reflected and transmitted) the force and velocity at either side of the specimen can be determined [5].

The pressure bars need to remain elastic during the experiment and hence the bar yield strength limits the maximum stress that the specimen can be subjected to [25]. Generally high strength metals, such as maraging steel, are used as these allow for high specimen stress. However, materials with lower stiffness are ideal to test low strength materials [5] and these reduce dispersion [31].

A.2.1 Wave equation in One Direction

The wave equation is used to describe wave propagation and is used in this case to describe propagation through the pressure bars.

The one dimensional wave equation can be derived from Newton's second law and Hooke's law and thus assumes that the bars are formed from a linear elastic material [69]. From figure A.2, forces due to both laws can be written as,

$$\begin{aligned} F_{Newton} &= ma \\ &= m \cdot \frac{\partial^2}{\partial t^2} u(x+h,t) \qquad \text{(A.2)} \\ F_{Hooke} &= F_{x+2h} + F_x \\ &= k[u(x+2h,t) - u(x+h,t)] + k[u(x,t) - u(x+h,t)] \qquad \text{(A.3)} \end{aligned}$$

where m is the element mass, a accelleration, k the material stiffness, h the distance between successive elements and finally u the displacement.

[31] Dispersion is covered in the literature review section 2.3.3 on page 44.

A value N is defined such that the masses are spread over a length $L = Nh$, with the total mass $M = Nm$. Thus by noting that the total stiffness is given by $E = \frac{k}{N}$, the motion can be described by,

$$\frac{\partial^2 u(x+h,t)}{\partial t^2} = \frac{EL^2}{M} \cdot \frac{u(x+2h,t) - 2u(x+h,t) + ku(x,t)}{h^2} \tag{A.4}$$

The wavespeed, c, in a material is given by [25],

$$c = \sqrt{\frac{E}{\rho}} \tag{A.5}$$

Over length L, this is equal to,

$$c = \sqrt{\frac{EL^2}{M}}$$

Thus finally, if the limits are taken as $N \to \infty$ and $h \to 0$ for equation A.4, the wave equation for one dimensional propagation is given by [69],

$$\frac{\partial^2 u}{\partial x^2} = \frac{1}{c^2}\frac{\partial^2 u}{\partial t^2} \tag{A.6}$$

The general form of this equation can be written in the following form [5],

$$u = f(x - ct) + g(x + ct) \tag{A.7}$$

where f and g are functions that describe the wave set. For a single wave moving in the positive x direction, the wave displacement as a function of time is,

$$u = f(x - ct)$$

From this basic equation, the velocity and strain are found simply by differentiating displacement with respect to time, t, and position, x, respectively,

$$v = \frac{\partial u}{\partial t} = -cf' \tag{A.8}$$

$$\epsilon = \frac{\partial u}{\partial x} = f' \tag{A.9}$$

Combining equations A.8 and A.9 leads to the relation,

$$v = -c\epsilon \tag{A.10}$$

By noting that stress is related to strain through equation A.1, and the wavespeed is related to the elastic modulus through equation A.5, the velocity can be written in the form,

$$\begin{aligned} v &= -c \cdot \frac{\sigma}{E} \\ &= -\frac{\sigma}{\rho c} \end{aligned} \tag{A.11}$$

Compressive stress is conventionally taken as positive in bar wave theory [25] resulting in the common form that is used through this analysis,

$$\Delta\sigma = \rho c \Delta v \tag{A.12}$$

A.3 Striker interaction

The striker is set at an initial velocity by the gas gun, causing it to strike the input bar. This interaction creates a square incident stress wave that travels towards the specimen. One dimensional wave propagation theory can be used to explain the interaction and the effects that bar size and material material have on the pulse.

In this analysis, the striker is denoted as bar *1*, with the incident bar as *2*. The basic form of the derivation is similar to that followed by Bonorchis [54].

A.3.1 Impact of uniform cylindrical bars

The impact of the SHB striker colliding with a bar produces stress waves that move in opposite directions along both bars. This stress change has been shown in section A.2.1 to be related to the change in particle velocity. A split Hopkinson pressure bar experiment exploits this phenomenon to produce a relatively square wave in the input bar. The stress magnitude that results is related to the cross-sectional area, density and Young's modulus of both bars and to the striker velocity.

From equation A.12, at impact the particle velocities in both bars are given as,

$$v_1 = \frac{\sigma_1}{c_1\rho_1} \qquad v_2 = \frac{\sigma_2}{c_2\rho_2} \tag{A.13}$$

The combined velocity at the interface, v_0, is simply the sum of the two bar velocities. This is also equivalent to the initial striker velocity.

$$\begin{aligned} v_0 &= v_1 + v_2 \\ &= \frac{\sigma_1}{c_1\rho_1} + \frac{\sigma_2}{c_2\rho_2} \end{aligned} \tag{A.14}$$

Due to force equilibrium at the contact zone, the stress in the striker and bar is related by the respective cross-sectional areas,

$$\begin{aligned} \sigma_1 A_1 &= \sigma_2 A_2 \\ \therefore \sigma_1 &= \left(\frac{A_2}{A_1}\right)\sigma_2 \end{aligned} \tag{A.15}$$

Thus solving for σ_2 from equations A.14 and A.15 yields,

$$\begin{aligned} \sigma_2 &= v_0 / \left[\frac{A_2}{A_1}\cdot\frac{1}{c_1\rho_1} + \frac{1}{c_2\rho_2}\right] \\ &= v_0 \left[\frac{A_1(c_1\rho_1)(c_2\rho_2)}{A_1c_1\rho_1 + A_2c_2\rho_2}\right] \end{aligned} \tag{A.16}$$

This relationship can be simplified if the materials chosen for both bars have the same properties, resulting in,

$$\sigma_2 = \frac{A_1}{A_1 + A_2} c\rho v_0 \tag{A.17}$$

and similarly the stress in the striker is given by,

$$\sigma_1 = \frac{A_2}{A_1 + A_2} c\rho v_0 \tag{A.18}$$

In the case of the split Hopkinson bar, the striker is bar 1, while the input bar 2. Clearly to maximise the stress in the input bar, the material should be dense, but stiff, with a high Young's modulus compared to its density as $c = \sqrt{E/\rho}$.

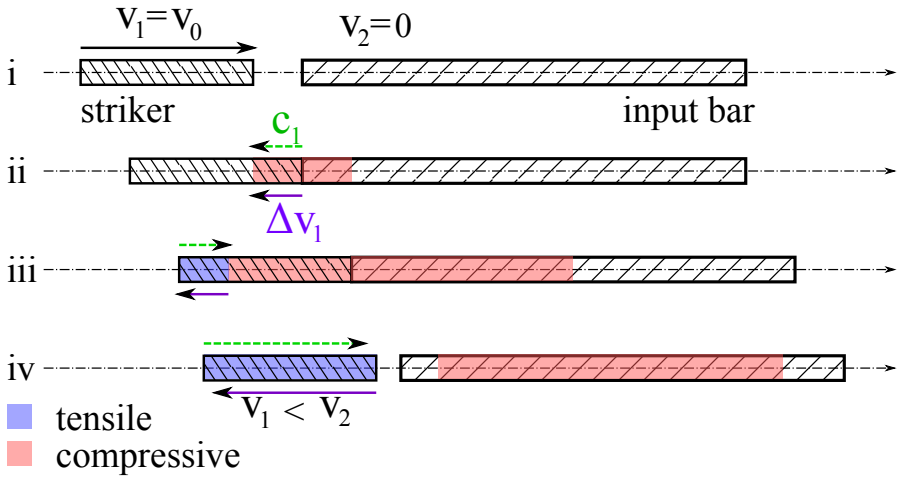

Figure A.3: Impact of the striker and incident bars. c_1 indicates the direction of the wave, while Δv_1 considers the change in particle velocity through the striker.

However, as the signal to noise ratio is greater for materials with high stiffness [5], a compromise between stress attained and acceptable noise levels is often used. Simply increasing the initial striker velocity, v_0, will also increase the stress attained.

Equations A.17 and A.18 show that, if the size of the incident bar is kept constant, an increase in striker cross-sectional area increases the stress within the the incident bar, while reducing that in the striker itself.

A.3.2 Pulse length

If a striker with an acceptable cross sectional area is selected, the length of the resulting incident pulse will be nominally twice that of the striker. This is due to the stress wave within the striker needing to perform one reflection before the striker velocity drops below that of the incident bar. This section considers the phenomenon in detail.

In this explanation compressive stress is defined as positive and the positive axial direction runs from the striker through the bar as shown in figure A.3. A compressive collision is considered, although the principles apply equally to the tensile situation.

As shown in figure A.3, initially (stage i) there is no stress in either bar, while bar 1 has an initial velocity. This changes after contact (stage ii) in which a compressive stress is formed in both bars. Initially the change in velocity is in the negative direction through the striker, reducing the particle speed as the stress is compressive.

$$\Delta v = \frac{\overbrace{\Delta\sigma}^{>0}}{\rho \underbrace{c}_{<0}} < 0$$

The wave then reflects against the end of the striker (stage iii), becoming a tensile pulse. The change in particle velocity remains negative as, the wave is moving in the positive direction, but the stress is negative.

$$\Delta v = \frac{\overbrace{\Delta\sigma}^{<0}}{\rho \underbrace{c}_{>0}} < 0$$

Using equation A.18, the change in velocity is related to the bar area by,

$$\Delta v = \frac{\sigma_1}{\rho c} = \frac{A_2}{A_1 + A_2} v_0 \tag{A.19}$$

For bars of equal area, the velocity change is,

$$\Delta v = \frac{A}{2A} v_0 = \frac{1}{2} v_0$$

Thus for a particle on the bar to come to rest ($\Delta v = v_0$), the stress wave needs to pass the point twice. This will occur once as the impact stress passes the particle and again as the reflection passes. In practical terms this results in the length of the striker being nominally twice that of the striker if the wave velocity, c through each is the same.

However, if the area of the striker is greater than that of the incident bar, the relative stress through the striker will be reduced. This results in a lower change in velocity.

$$\Delta v < \frac{1}{2} v_0$$

Thus the stress wave must pass the particle three (or more) times before the striker comes to rest. In practise, this results in the stress pulse through the input bar decreasing after one striker reflection, but only returning to zero after two (or more). This should be avoided as ideally the input pulse should have constant amplitude through the duration.

Clearly the cross-sectional area of the striker must not exceed that of the input bar and ideally, to maximize the magnitude of the stress in the input bar, the areas should be equal.

A.3.3 Final Striker Velocity

From the change in velocity during each reflection, the final striker velocity can be determined and used in calibrating the strain gauges. Assuming only one wave reflection within the striker is required, the final velocity is given by,

$$\begin{aligned} v_f &= v_0 - 2\Delta v \\ &= v_0 - 2v_0\frac{A_1}{A_1 + A_2} \qquad \text{from equation A.19} \\ &= v_0\frac{A_1 - A_2}{A_1 + A_2} \end{aligned} \tag{A.20}$$

A.4 Specimen Deformation

A.4.1 Specimen engineering stress

The stress through the specimen is found by calculating the force acting at the specimen interfaces, at the end of both the incident and transmitted bars. This derivation combines elements presented by both Al-Mousawi et al. [25] and Gray III [5].

Three distinct stress waves act on the specimen during deformation, namely the incident σ_i, reflected σ_r and transmitted σ_t. These are shown in figure A.4 together with the resultant velocities and loads. Bar *1* refers to the input, while the output bar is labelled *2*.

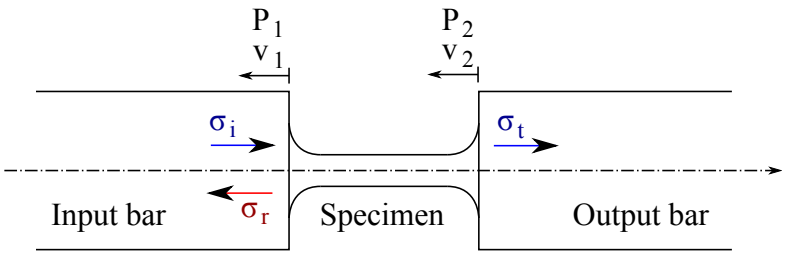

Figure A.4: Velocity and loads acting on the specimen-bar interface.

Equation A.12 states that the change in particle velocity through the bar is directly related to the change in stress. The input bar 1 has a tensile incident pulse moving in the positive axial direction interacting with a compressive reflected pulse acting in the opposite direction. Thus the velocity, v_1, is given by,

$$\begin{aligned} v_1 &= v_i + v_r \\ &= \frac{\sigma_i}{\rho_1 c_1} + \frac{\sigma_r}{\rho_1(-c_1)} \\ &= \frac{\sigma_i - \sigma_r}{\rho_1 c_1} \end{aligned} \tag{A.21}$$

where v_i and v_r are the ahange in velocity due to the incident and reflective waves respectively.

At the transmitted bar interface, only the transmitted tensile wave, travelling in the positive axial direction is present and thus the velocity at the end of the bar, v_2 is simply,

$$v_2 = v_t = \frac{\sigma_t}{\rho_2 c_2} \tag{A.22}$$

Similarly, as the cross-sectional area of both the incident bar, A_1, and transmitted bar, A_2, are known, the loads acting on the specimen due to the stresses in each bar can be calculated as,

$$P_1 = (\sigma_i + \sigma_r) \cdot A_1 \qquad P_2 = \sigma_t \cdot A_2 \tag{A.23}$$

Using these two forces the engineering stress in the specimen is found as,

$$\sigma = \frac{P}{A_0} = \frac{P_1 + P_2}{2A_0} \tag{A.24}$$

where P is the average force acting on the specimen and A_0 the initial specimen area.

Assuming force equilibrium between the bars, $P_1 \cong P_2$ and thus the stress calculation requires data only from the transmitted signal.

$$\sigma = \frac{P_1}{A_0} = \sigma_t \left(\frac{A_1}{A_0}\right) \tag{A.25}$$

A.4.2 Specimen travel

Similarly to the stress derivation that calculated the forces acting on both bars, the displacement can be determined by considering the velocity at the bar ends.

By integrating the bar interface velocity over time, the displacements, u_1 and u_2 are found simply as,

$$u_1 = \int_0^t v_1 dt \qquad u_2 = \int_0^t v_2 dt \tag{A.26}$$

The specimen displacement is simply the difference, $\Delta u = u_1 - u_2$.

For specimens with uniform gauge sections, the average strain is calculated based on the displacement. The specimen gauge length at any moment in time can be described by the original length and the extension,

$$l = l_0 + |\Delta u| \tag{A.27}$$

True strain is found by taking the natural log of the instantaneous length over the original,

$$\epsilon = \ln\left(\frac{l}{l_0}\right) \tag{A.28}$$

The strain rate is can be determined directly from the bar velocities,

$$\dot{\epsilon} = \frac{|\Delta v|}{l_0} \tag{A.29}$$

If a constant strain rate is applied, the maximum strain attained in the specimen is simply the strain rate multiplied by the time over which it acts. Thus by noting that the length of the stress pulse is double that of the striker[32], a simple relation can be derived.

$$\begin{aligned} \epsilon_{max} &= \dot{\epsilon} \cdot t_{pulse} \\ &= \dot{\epsilon} \cdot \frac{2L_s}{c_s} \end{aligned} \tag{A.30}$$

with t_{pulse} the wave duration and L_s and c_s the length and wave propagation speed of the striker.

[32]see section A.3.2

Appendix B

Abaqus User Files

Contents

B.1 Plasticity and Damage Model VUMAT

B.1.1 Predictor Return Algorithm

This is the final VUMAT used to study damage. Both the full and symmetric Bai-Wierzbicki damage models can be selected.

```
C ////////////////////////////////////////////////////////////
C VUMAT for 3D model

C Johnson-Cook plasticity model
C Bai-Wierzbicki damage model
C Strain rate & temperature plasticity dependence

C Andrew Bowden - 23/09/2009
C ------------------------------------------------------------
```

```
C SYNTAX:
C s : stress              e : strain
C d : deviatoric  i : increment
C E : elastic             P : plastic
C 0 : old component       Eq: equivalent
C ////////////////////////////////////////////////////////////////
      subroutine vumat(
C ---------------- Variables to be used ----------------------------
C Read only -
     1  nblock, ndir, nshr, nstatev, nfieldv, nprops, lanneal,
     2  stepTime, totalTime, dt, cmname, coordMp, charLength,
     3  props, density, strainInc, relSpinInc,
     4  tempOld, stretchOld, defgradOld, fieldOld,
     3  stressOld, stateOld, enerInternOld, enerInelasOld,
C Write only -
     6  tempNew, stretchNew, defgradNew, fieldNew,
     5  stressNew, stateNew, enerInternNew, enerInelasNew )

C ---------------------- Required file ----------------------------
      include 'vaba_param.inc'
C ---------------------- State Variables ----------------------------
C The state variables are stored as:
C       STATE(*,1) = total equivalent plastic strain
C       STATE(*,2) = strain rate calculated after previous step
C       STATE(*,3) = strain rate used in previous step
C       STATE(*,4) = LodeInt
C       STATE(*,5) = TriaxInt
C       STATE(*,6) = DAMAGE
C ---------------------- Array Dimensions ----------------------------
C All arrays dimensioned by (*) are not used in this algorithm
      dimension props(nprops), density(nblock),
     1  coordMp(nblock,*),
     2  charLength(*), strainInc(nblock,ndir+nshr),
     3  relSpinInc(*), tempOld(nblock),
     4  stretchOld(*), defgradOld(*),
     5  fieldOld(*), stressOld(nblock,ndir+nshr),
     6  stateOld(nblock,nstatev), enerInternOld(nblock),
     7  enerInelasOld(nblock), tempNew(nblock),
     8  stretchNew(*), defgradNew(*), fieldNew(*),
     9  stressNew(nblock,ndir+nshr), stateNew(nblock,nstatev),
     1  enerInternNew(nblock), enerInelasNew(nblock)
```

```
C Max length of material name
      character*80 cmname
C ------------------------- Define Parameters ------------------------
      real E, nu,
     1 A, B, C, D, E1, k, n, m, SR0, Tm, Ttrans, Tmelt, Cp, eta,
     1 D1, D2, D3, D4, D5, D6
      double precision G, twoG, lamda,
     1 s1, s2, s3, s4, s5, s6, sEq, p,
     1 ds1, ds2, ds3, ds4, ds5, ds6, dsmag,
     1 T, Tstar,
     1 strainTerm, strainRateTerm, tempTerm, yield,
     1 deriv1, deriv2, termA, termB, scaleFactor,
     1 ePEq, iePeq, ieVol, ide1, ide2, ide3, ideEq,
     1 ideEqDot, ideEqDotLog,
     1 rCubed, xi, Lode, LodeAve, Triax, TriaxAve, failstrain,
     1 factor, stressPower, plasticWorkInc
      integer count

      parameter( zero = 0., one = 1., two = 2., three = 3.,
     1   third = one/three, half = .5, twoThirds = two/three,
     2   threeHalfs = 1.5d0, nineHalfs = 4.5,
     3   pi = 3.141592654, lg10 = 2.302585093  )

C ------------------- Retrieve Material Properties -------------------
C      Elastic
       E        = props(1)
       nu       = props(2)
C      PLastic
       A        = props(3)
       B        = props(4)
       C        = props(5)
       D        = props(6)
       E1       = props(7)
       k        = props(8)
       n        = props(9)
       m        = props(10)
       SR0      = props(11)
       Tm       = props(12)
       Ttrans   = props(13)
       Tmelt    = props(14)
       Cp       = props(15)
       eta      = props(16)
```

```
C       Damage
        D1      = props(17)
        D2      = props(18)
        D3      = props(19)
        D4      = props(20)
        D5      = props(21)
        D6      = props(22)

C---------------------- Calculate Lame Parameters ---------------------
        G  = E / ( two * (one + nu) )        ! Shear Modulus
        twoG = two*G
        lamda = twoG * nu / (one - two*nu)   ! 1st Lame parameter

C ////////////////////////////////////////////////////////////////

C Begin Calc Stress at each integration point
        do 80 i = 1,nblock

C ------------------- Trial stress (Hooke's Law) --------------------
          ieVol  = strainInc(i,1) + strainInc(i,2) + strainInc(i,3)

          s1 = stressOld(i,1) + twoG*strainInc(i,1) + lamda*ieVol
          s2 = stressOld(i,2) + twoG*strainInc(i,2) + lamda*ieVol
          s3 = stressOld(i,3) + twoG*strainInc(i,3) + lamda*ieVol
          s4 = stressOld(i,4) + twoG*strainInc(i,4)
          s5 = stressOld(i,5) + twoG*strainInc(i,5)
          s6 = stressOld(i,6) + twoG*strainInc(i,6)

C Deviatoric part of trial stress [S]
          p = - third * ( s1 + s2 + s3 )
          ds1  = s1 + p
          ds2  = s2 + p
          ds3  = s3 + p

C Magnitude of the deviatoric trial stress difference  [sqrt(S:S)]
          dsmag = sqrt( ds1**2 + ds2**2 + ds3**2
     1                + 2.*s4**2 +2.*s5**2 +2.*s6**2 )

C ------- Get equivalent plastic strain from previous step --------
          ePEq = stateOld(i,1)
```

```
C------------------------ Calculate Tstar ------------------------
      T = tempOld(i)
      if (T .lt. Ttrans) then
            Tstar = zero
      elseif (T .ge. Ttrans .and. T .le. Tmelt) then
            Tstar = (T - Ttrans) / (Tmelt - Ttrans)
      else
            stateNew(i,6) = 0
            Tstar = zero
      end if

C---------------------- Determine strain rate ----------------------
      ideEqDot = ( 5*stateOld(i,3) + stateOld(i,2))/6
      stateNew(i,3) = ideEqDot

      if (ideEqDot .gt. zero) then
            ideEqDotLog = log10(ideEqDot/SR0)
      else
            ideEqDotLog = zero
      end if
C ---------------------- Calculate yield stress ----------------------
        tempTerm    = one - Tstar**Tm
      yield = (   A + B*ePEq**n + (C - D*ePEq**m)*ideEqDotLog
     1            + E1*ideEqDot**k   )*tempTerm
      sEq = sqrt(threeHalfs)*dsmag

      if( (sEq .le. abs(yield))
     1  .or. (stepTime + totalTime .eq. zero) ) then
C     ////////////////////// ELASTIC \\\\\\\\\\\\\\\\\\\\\\
            stressNew(i,1) = s1
            stressNew(i,2) = s2
            stressNew(i,3) = s3
            stressNew(i,4) = s4
            stressNew(i,5) = s5
            stressNew(i,6) = s6

            stateNew(i,1) = stateOld(i,1)
            stateNew(i,2) = stateOld(i,2)
            stateNew(i,3) = stateOld(i,3)
            stateNew(i,4) = stateOld(i,4)
            stateNew(i,5) = stateOld(i,5)
            stateNew(i,6) = stateOld(i,6)
```

```
      else
C     ////////////////////// PLASTIC \\\\\\\\\\\\\\\\\\\\\\
C     ---------- Solve for change in eq plastic strain ----------
C     ---------------------- Predictor Return ----------------------
            if ( ePEq .lt. 1.0d-8 ) ePEq = 1.0d-8
            deriv1 = ( n*B*ePEq**(n-one)
     1                 - m*D*ePEq**(m-one)*ideEqDotLog ) * tempTerm

            if ( ideEqDot .lt. 1.0d-7 ) ideEqDot = 1.0d-7
            deriv2 = ( (C - D*ePEq**m) * SR0/(lg10*ideEqDot)
     1                  + E1*k*ideEqDot**(k-1) ) * tempTerm

            termA = sEq/(three*G) * (deriv1 + deriv2/dt)
            termB = deriv2 * ideEqDot
            scaleFactor = (yield + termA - termB)/(sEq + termA)

            iePEq = (one-scaleFactor)*sEq/(three*G)
            ePEq = ePEq + iePEq
            ideEqDot = iePEq/dt
            sEq = (A + B * ePEq**n + (C-D*ePEq**m)*ideEqDotLog
     1              + E1*ideEqDot**k)*tempTerm
C     -------- Calc deviatoric stress components [Snew] --------
            ds1 =  scaleFactor * ds1
            ds2 =  scaleFactor * ds2
            ds3 =  scaleFactor * ds3
            ds4 =  scaleFactor * s4
            ds5 =  scaleFactor * s5
            ds6 =  scaleFactor * s6
C     ---------------------- Set new stress ----------------------
            stressNew(i,1) = ds1 - p
            stressNew(i,2) = ds2 - p
            stressNew(i,3) = ds3 - p
            stressNew(i,4) = ds4
            stressNew(i,5) = ds5
            stressNew(i,6) = ds6
C     ------------------ Calculate temperature ------------------
            tempNew(i) = tempOld(i)
     1                   + eta*iePEq / (density(i) * Cp) * sEq
C     ------------------ Update state variables ------------------

            stateNew(i,1) = ePEq     !Eq plastic strain
            stateNew(i,2) = ideEqDot !Eq plastic strain rate
```

```
C     ////////////////// Check for damage \\\\\\\\\\\\\\\\\\\\

C     ---------------------- Stress Invariants -------------------
            dsXds1 = ds1**2 + ds4**2 + ds6**2
            dsXds2 = ds4**2 + ds2**2 + ds5**2
            dsXds3 = ds6**2 + ds5**2 + ds3**2
            dsXds4 = ds1*ds4 + ds4*ds2 + ds6*ds5
            dsXds5 = ds4*ds6 + ds2*ds5 + ds5*ds3
            dsXds6 = ds1*ds6 + ds4*ds5 + ds6*ds3

            rCubed = nineHalfs*(dsXds1*ds1 + dsXds2*ds2 + dsXds3*ds3
     1                  + 2.*dsXds4*ds4 + 2.*dsXds5*ds5 + 2.*dsXds6*ds6)
            xi = rCubed / (sEq**three)

            if(abs(xi) .gt. one)xi = one
            Lode = 1 - 2/pi * acos(xi)

            Triax = -p/sEq

C     ----------------- Find Ave Lode & Triax -------------------
            stateNew(i,4) = stateOld(i,4) + Lode * iePEq
            LodeAve = stateNew(i,4) / ePEq

            stateNew(i,5) = stateOld(i,5) + Triax * iePEq
            TriaxAve = stateNew(i,5) / ePEq

C     ----------------- Find Strain To Failure -------------------
C
C                         FULL MODEL
C
C           failStrain = (half*( D1*exp(-D2*TriaxAve)
C     1                     + D5*exp(-D6*TriaxAve) )
C     1                     - D3*exp(-D4*TriaxAve) )*LodeAve**2
C     1                      + half*( D1*exp(-D2*TriaxAve)
C     1                      - D5*exp(-D6*TriaxAve) ) * LodeAve
C     1                      + D3*exp(-D4*TriaxAve)

C                         SYMMETRIC MODEL
C
            failStrain = ( D1*exp(-D2*TriaxAve)
     1                      - D3*exp(-D4*TriaxAve) )*LodeAve**2
     1                      + D3*exp(-D4*TriaxAve)
```

```
C     ------------------- Remove Damaged Elements -------------------
            if ( (ePeq .ge. failStrain)
     1           .and. (failStrain .gt. zero) ) then
                  stateNew(i,6) = 0
                  print*,"FAILED ELEMENT :",i
                  print*,"Time       ",stepTime + totalTime
                  print*,"LodeAve    ",LodeAve
                  print*,"TriaxAve   ",TriaxAve
                  print*,"failStrain",failStrain
                  print*,"ePEq       ", ePEq
                  print*,"-----------------------------------"
            else
                  stateNew(i,6) = 1
            end if
      end if

C/////////////////////////////////////////////////////////////////

C Update the specific internal energy
      stressPower = half * (
     1          ( stressOld(i,1)+stressNew(i,1) )*strainInc(i,1)
     1    +     ( stressOld(i,2)+stressNew(i,2) )*strainInc(i,2)
     1    +     ( stressOld(i,3)+stressNew(i,3) )*strainInc(i,3)
     1    + two*( stressOld(i,4)+stressNew(i,4) )*strainInc(i,4)
     1        + two*( stressOld(i,5)+stressNew(i,5) )*strainInc(i,5)
     1    + two*( stressOld(i,6)+stressNew(i,6) )*strainInc(i,6) )

        enerInternNew(i) = enerInternOld(i) + stressPower / density(i)

C Update the dissipated inelastic specific energy -
      plasticWorkInc = iePEq * sEq
      enerInelasNew(i) = enerInelasOld(i) + plasticWorkInc / density(i)

   80 continue
C
      return
      end
```

B.1.2 Nonlinear Solver

This is less stable than the Predictor Return algorithm, but is included here for completeness. Only the plasticity code is shown. To implement, copy this section and paste it in the full code above, replacing from the section "Calc strain rate" up until "Set new stress".

```
C---------------------- Calculate strain rate ------------------------
      ideEqDot = ideEq/dt
      stateNew(i,5) = ideEqDot

      if (ideEqDot .gt. zero) then
            ideEqDotLog = log10(ideEqDot/SR0)
      else
            ideEqDotLog = zero
      end if
C ---------------------- Calculate yield stress ----------------------
      yieldConst = A + C*ideEqDotLog + E1*ideEqDot**k
c     tempConst   = one - Tstar**Tm
      yield = yieldConst + B*ePEq**n - D*ideEqDotLog*ePEq**m
C ------------------------ Check for yield --------------------------
      dsEq = sqrt(threeHalfs)*dsmag
      if( (dsEq .le. abs(yield))
     1     .or. (stepTime + totalTime .eq. zero) ) then
C     ////////////////////// ELASTIC \\\\\\\\\\\\\\\\\\\\\\
C           if (i .eq. 1) print*, "Elastic", dsEq, Yield
            iePEq = zero
            stressNew(i,1) = s1
            stressNew(i,2) = s2
            stressNew(i,3) = s3
            stressNew(i,4) = s4
            stressNew(i,5) = s5
            stressNew(i,6) = s6
            stateNew(i,1) = stateOld(i,1)
            stateNew(i,2) = stateOld(i,2)
            stateNew(i,3) = stateOld(i,3)
            stateNew(i,4) = 1
C           stateNew(i,5) = zero
      else
C     ////////////////////// PLASTIC \\\\\\\\\\\\\\\\\\\\\\
            if (i .eq. 1) print*, "Plastic", dsEq, Yield
```

```
C     ------------------ old deviatoric stresses ------------------
            p0 = -third * ( stressOld(i,1)
     1           + stressOld(i,2) + stressOld(i,3) )
            ds01 = stressOld(i,1) + p0
            ds02 = stressOld(i,2) + p0
            ds03 = stressOld(i,3) + p0
C     ------------ Find equivalent deviatoric strains ------------
            eC1 = ds01            / (twoG) + ide1
            eC2 = ds02            / (twoG) + ide2
            eC3 = ds03            / (twoG) + ide3
            eC4 = stressOld(i,4) / (twoG) + strainInc(i,4)
            eC5 = stressOld(i,5) / (twoG) + strainInc(i,5)
            eC6 = stressOld(i,6) / (twoG) + strainInc(i,6)
C     ---------- Calculate eT = sqrt(2/3 * eC:eC) ----------
          eCmag = sqrt(eC1**2 + eC2**2 + eC3**2
     1                    + 2.*eC4**2 + 2.*eC5**2 + 2.*eC6**2)
          eT = sqrt(twoThirds) * eCmag
C     ---------- Solve for change in eq plastic strain ----------
C     ---------------------- NEWTONS METHOD ----------------------
          err = one
          R = one
          count = 0
c         iePEq = 0
              iePEq = ideEq
          newtonTol = 1.0d-9
          reduction  = 5
          do while ( (err .ge. newtonTol) .and. (count .le. 15) )
              count = count + 1
              R0 = R
              ePEq = stateOld(i,1) + iePEq
              sEq = yieldConst  + B*ePEq**n - D*ideEqDotLog*ePEq**m
              H = B*n*ePEq**(n-1) - D*ideEqDotLog*m*ePEq**(m-1)
              R = (three*G * (eT - iePEq) - sEq) / (three*G + H)
              iePEq = iePEq + R
              do while ( stateOld(i,1) + iePEq .le. zero )
                  iePEq = iePEq/reduction
                  if ( stateOld(i,1) .eq. zero ) iePEq = abs(iePEq)
              end do
              err = abs(R)
          end do
              if (count .gt. 15) print*,
     1        "WARNING - Newton iterations exceeded"
```

```
C     ------ Calculate deviatoric stress components [Snew] ------
      factor = two*G / ( one + three*G/sEq * iePEq )
      ds1 =  factor * eC1
      ds2 =  factor * eC2
      ds3 =  factor * eC3
      ds4 =  factor * eC4
      ds5 =  factor * eC5
      ds6 =  factor * eC6
```

B.2 Load Application VDLOAD

This is required to apply the incident stress pulse to the input bar. The basic code sets the value to the amplitude stored in the input deck mutiplied by the maximum incident stress value.

```
C ////////////////////////////////////////////////////////////////
C VDLOAD to apply load to infinite elment boundary
C
C Value should be twice that required for the incident wave magnitude
C Amplitude must be included in input deck
C
C Andrew Bowden - 10/08/2009
C ---------------------------------------------------------------------
      subroutine vdload(nblock,ndim,stepTime,totalTime,amplitude,
     1 curCoords,velocity,dirCos,jltyp,sname,value)
      include 'vaba_param.inc'

      dimension curCoords(nblock,ndim),velocity(nblock,ndim),
     1 dirCos(nblock,ndim,ndim),value(nblock)
      character*80 sname

C ---------------------- Set wave magnitude ---------------------------
      do km=1,nblock
            value(km) = -amplitude*7.003254e+07
      end do

      return
      end
```

Appendix C

Drawings

Contents

C.1 Tensile Split Hopkinson Pressure Bar

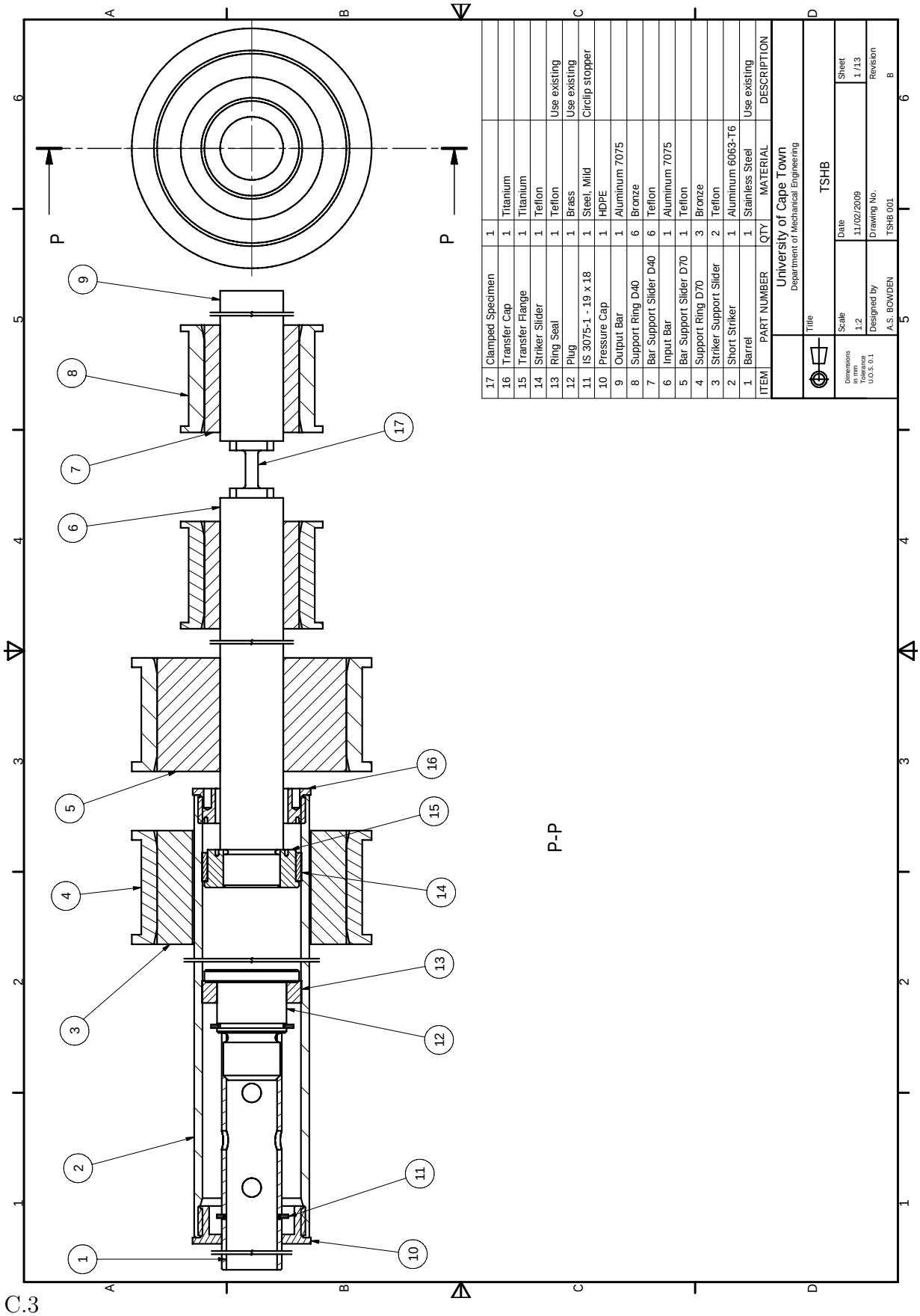
P
P
P-P
17 Clamped Specimen 1
16 Transfer Cap 1 Titanium
15 Transfer Flange 1 Titanium
14 Striker Slider 1 Teflon
13 Ring Seal 1 Teflon Use existing
12 Plug 1 Brass Use existing
11 IS 3075-1 - 19 x 18 1 Steel, Mild Circlip stopper
10 Pressure Cap 1 HDPE
9 Output Bar 1 Aluminum 7075
8 Support Ring D40 6 Bronze
7 Bar Support Slider D40 6 Teflon
6 Input Bar 1 Aluminum 7075
5 Bar Support Slider D70 1 Teflon
4 Support Ring D70 3 Bronze
3 Striker Support Slider 2 Teflon
2 Short Striker 1 Aluminum 6063-T6
1 Barrel 1 Stainless Steel Use existing
ITEM PART NUMBER QTY MATERIAL DESCRIPTION
University of Cape Town
Department of Mechanical Engineering
Title
TSHB
Scale 1:2
Date 11/02/2009
Sheet 1 / 13
Designed by A.S. BOWDEN
Drawing No. TSHB 001
Revision B
Dimensions in mm
Tolerance U.O.S. 0.1

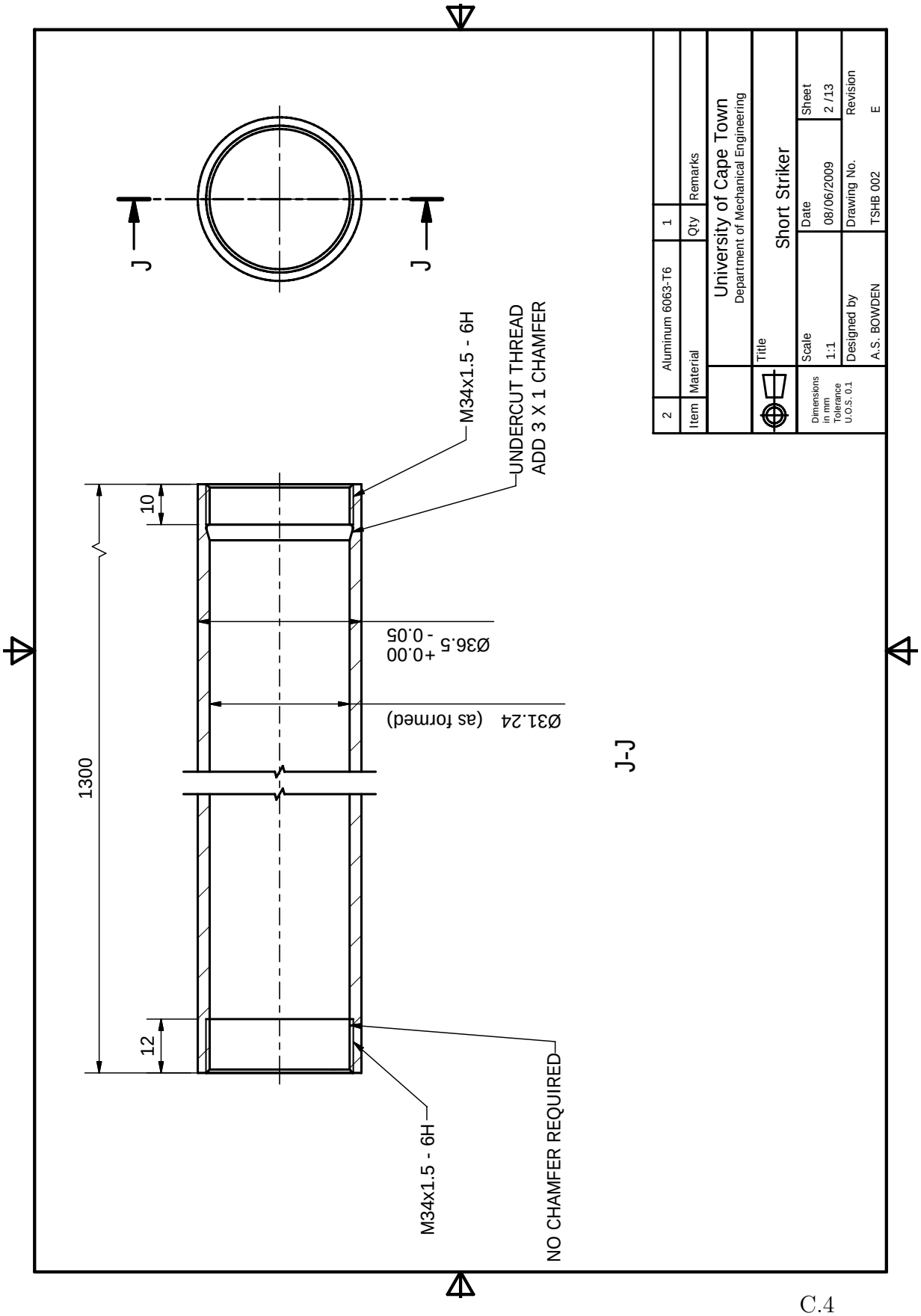
J
J
M34x1.5 - 6H
UNDERCUT THREAD
ADD 3 X 1 CHAMFER
10
1300
12
Ø36.5 +0.00 - 0.05
Ø31.24 (as formed)
J-J
M34x1.5 - 6H
NO CHAMFER REQUIRED
2 Aluminum 6063-T6 1
Item Material Qty Remarks
University of Cape Town
Department of Mechanical Engineering
Title
Short Striker
Scale 1:1
Date 08/06/2009
Sheet 2 /13
Dimensions in mm Tolerance U.O.S. 0.1
Designed by A.S. BOWDEN
Drawing No. TSHB 002
Revision E

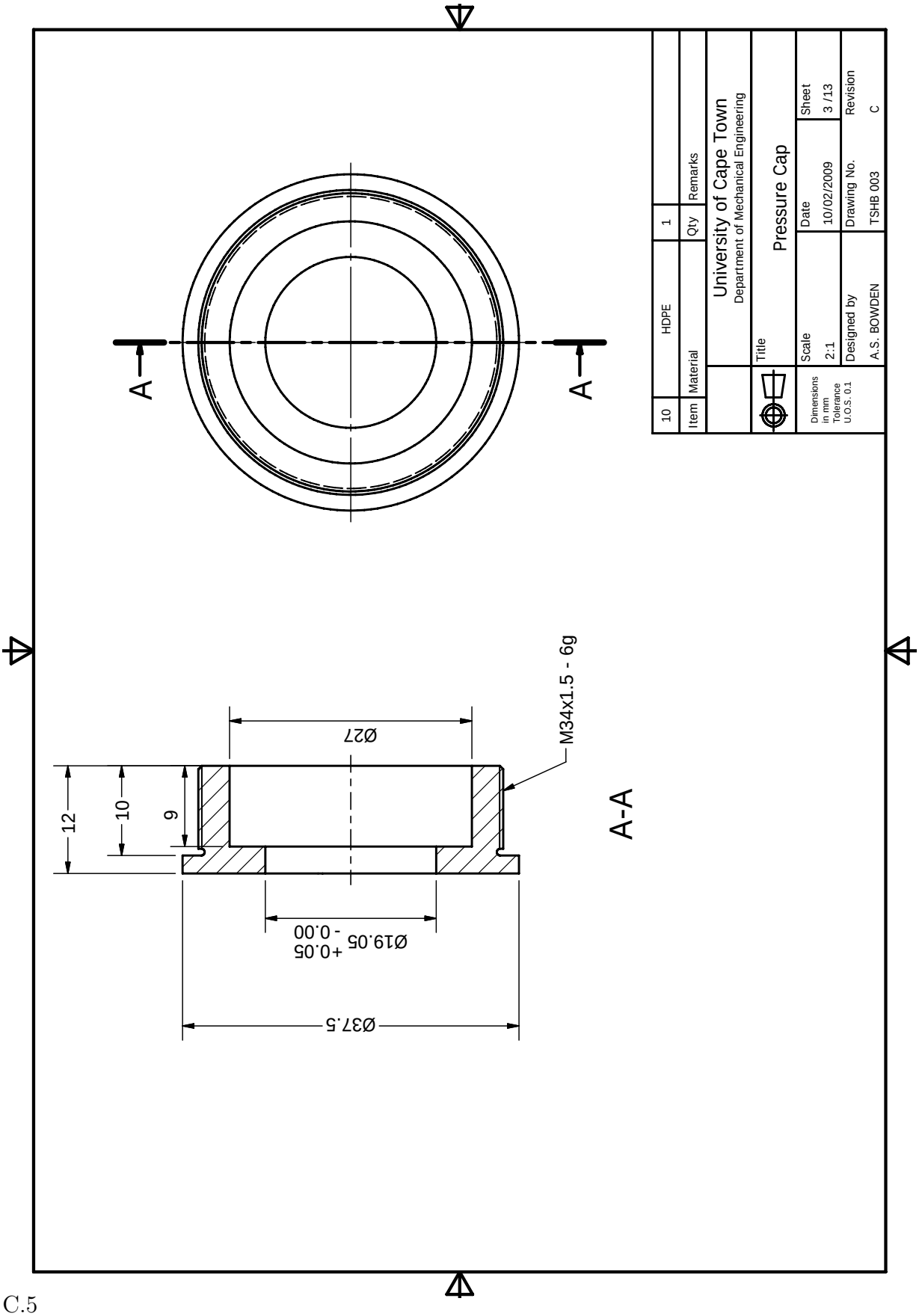
A
A
A-A
M34x1.5 - 6g
Ø27
12
10
9
Ø19.05 +0.05 -0.00
Ø37.5
10
HDPE
1
Item
Material
Qty
Remarks
University of Cape Town
Department of Mechanical Engineering
Title
Pressure Cap
Scale
2:1
Date
10/02/2009
Sheet
3 /13
Dimensions in mm
Tolerance U.O.S. 0.1
Designed by
A.S. BOWDEN
Drawing No.
TSHB 003
Revision
C

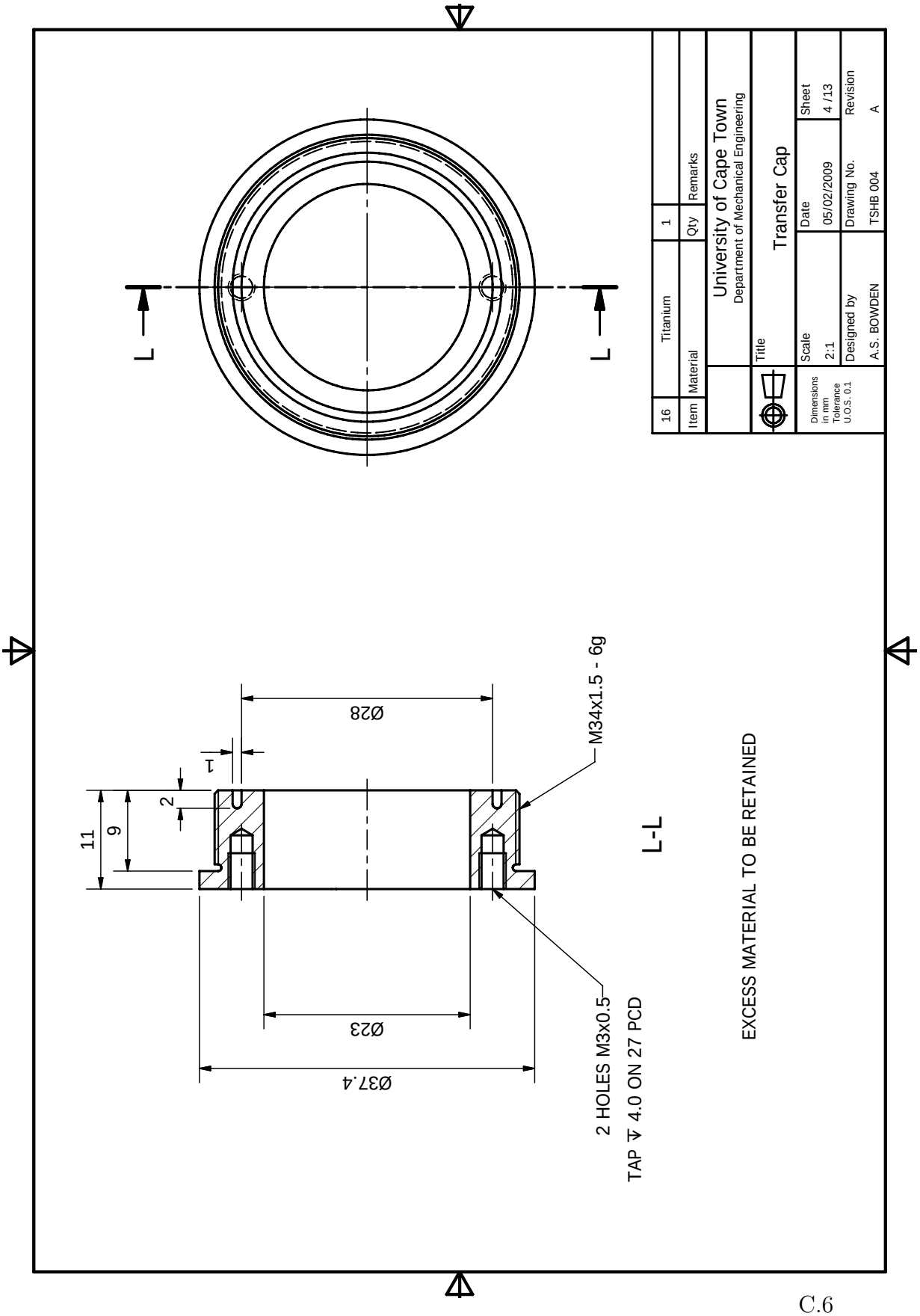
L
L
16
Item
Titanium
Material
1
Qty
Remarks
University of Cape Town
Department of Mechanical Engineering
Title
Transfer Cap
Scale
2:1
Date
05/02/2009
Sheet
4 /13
Designed by
A.S. BOWDEN
Drawing No.
TSHB 004
Revision
A
Dimensions in mm
Tolerance
U.O.S. 0.1
Ø28
M34x1.5 - 6g
1
2
6
9
11
Ø23
Ø37.4
2 HOLES M3x0.5
TAP ↧ 4.0 ON 27 PCD
L-L
EXCESS MATERIAL TO BE RETAINED

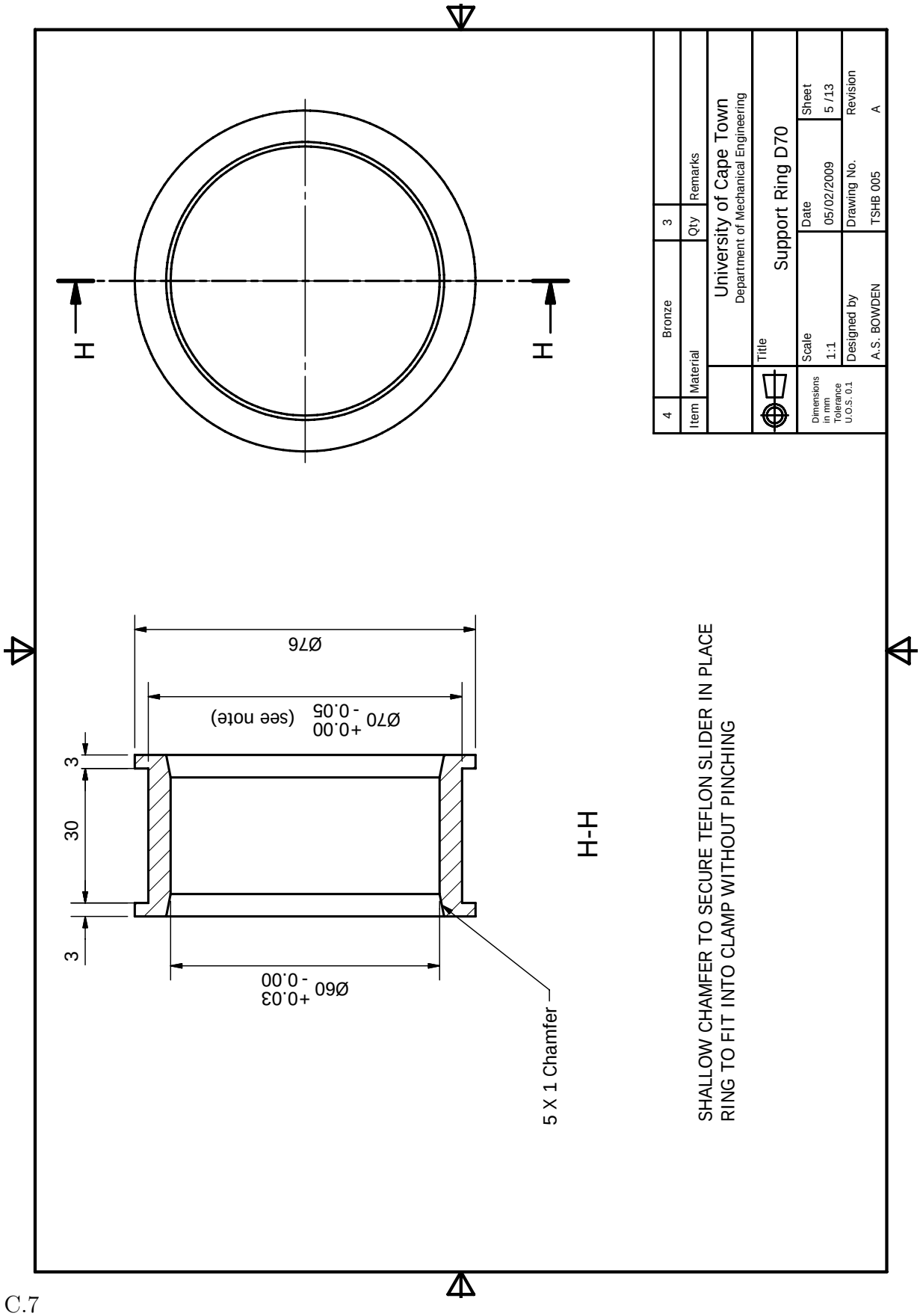
H
H
Ø76
Ø70 +0.00 -0.05 (see note)
3
30
3
Ø60 +0.03 -0.00
5 X 1 Chamfer
H-H
SHALLOW CHAMFER TO SECURE TEFLON SLIDER IN PLACE
RING TO FIT INTO CLAMP WITHOUT PINCHING
4 Item
Bronze Material
3 Qty
Remarks
University of Cape Town
Department of Mechanical Engineering
Title
Support Ring D70
Scale 1:1
Date 05/02/2009
Sheet 5 /13
Designed by A.S. BOWDEN
Drawing No. TSHB 005
Revision A
Dimensions in mm
Tolerance U.O.S. 0.1

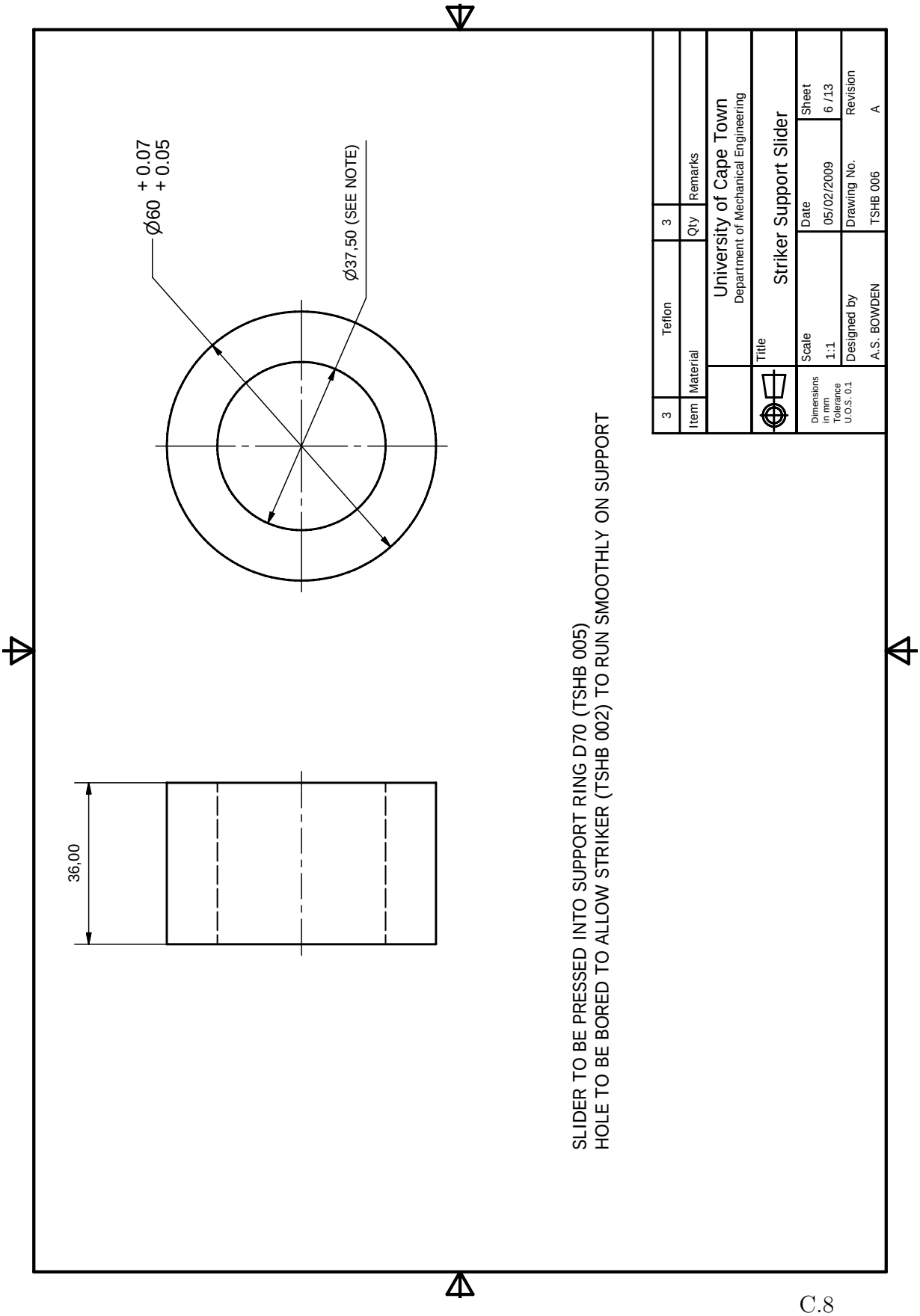
Ø60 + 0.07 + 0.05
Ø37,50 (SEE NOTE)
36,00
SLIDER TO BE PRESSED INTO SUPPORT RING D70 (TSHB 005)
HOLE TO BE BORED TO ALLOW STRIKER (TSHB 002) TO RUN SMOOTHLY ON SUPPORT
3 Teflon 3
Item Material Qty Remarks
University of Cape Town
Department of Mechanical Engineering
Title
Striker Support Slider
Scale 1:1
Date 05/02/2009
Sheet 6 /13
Designed by A.S. BOWDEN
Drawing No. TSHB 006
Revision A
Dimensions in mm
Tolerance U.O.S. 0.1

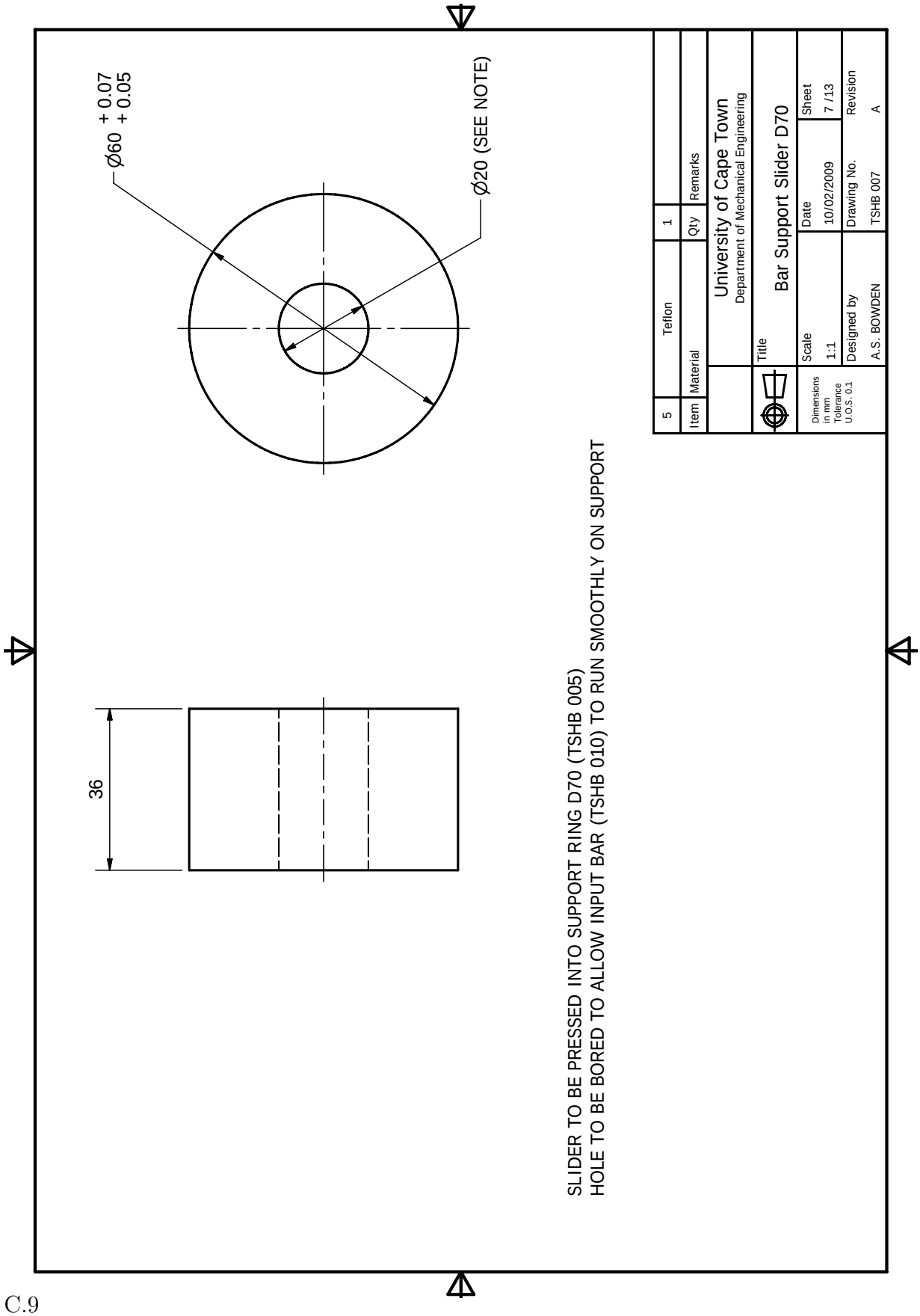
Ø60 + 0.07 + 0.05
Ø20 (SEE NOTE)
36
SLIDER TO BE PRESSED INTO SUPPORT RING D70 (TSHB 005)
HOLE TO BE BORED TO ALLOW INPUT BAR (TSHB 010) TO RUN SMOOTHLY ON SUPPORT
5 Teflon 1
Item Material Qty Remarks
University of Cape Town
Department of Mechanical Engineering
Title
Bar Support Slider D70
Scale 1:1
Date 10/02/2009
Sheet 7 /13
Dimensions in mm
Tolerance U.O.S. 0.1
Designed by A.S. BOWDEN
Drawing No. TSHB 007
Revision A

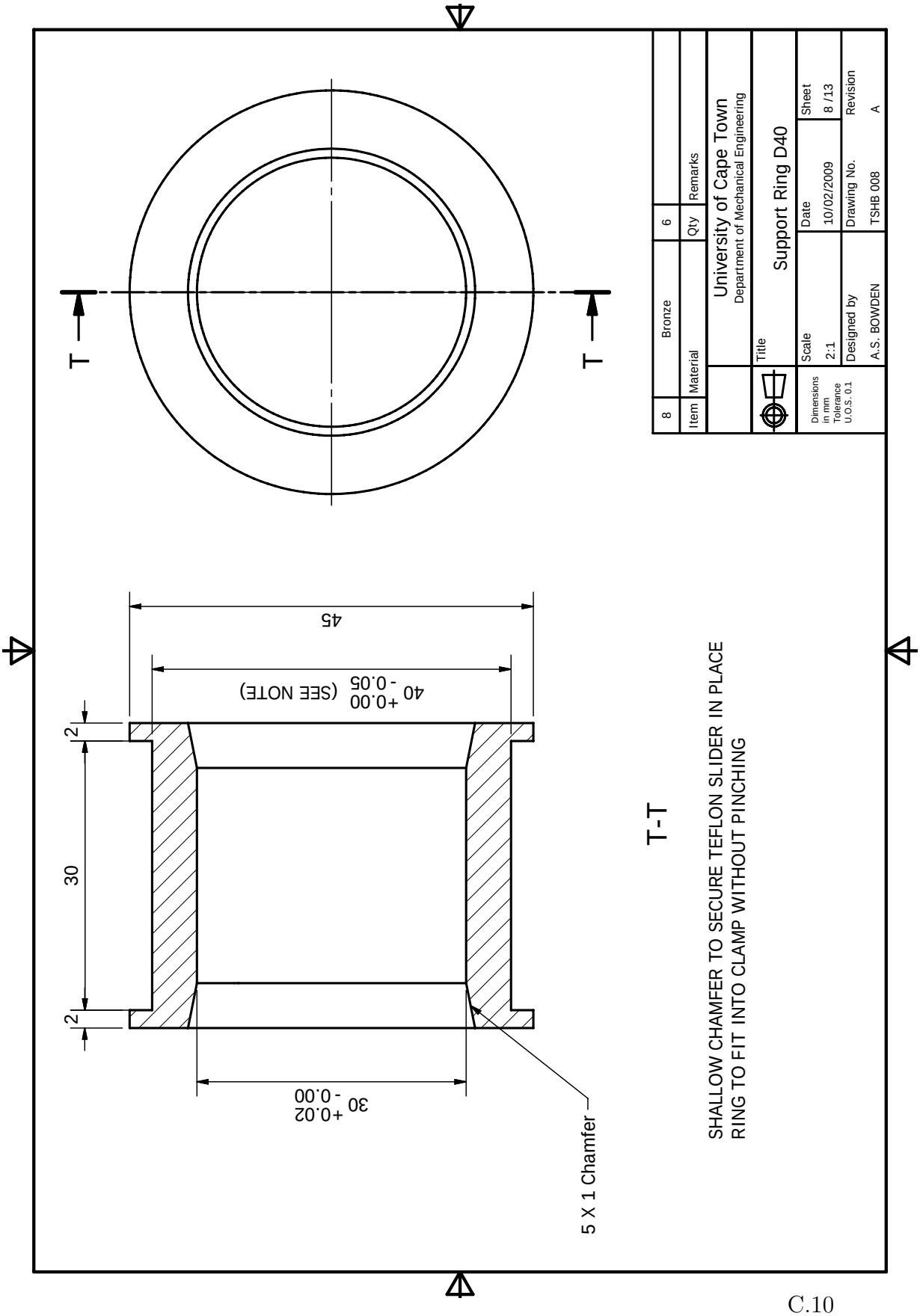
T
T
45
40 +0.00 -0.05 (SEE NOTE)
2
30
2
30 +0.02 -0.00
5 X 1 Chamfer
T-T
SHALLOW CHAMFER TO SECURE TEFLON SLIDER IN PLACE
RING TO FIT INTO CLAMP WITHOUT PINCHING
8
Item
Material
Bronze
6
Qty
Remarks
University of Cape Town
Department of Mechanical Engineering
Title
Support Ring D40
Scale
2:1
Date
10/02/2009
Sheet
8 /13
Designed by
A.S. BOWDEN
Drawing No.
TSHB 008
Revision
A
Dimensions in mm
Tolerance U.O.S. 0.1

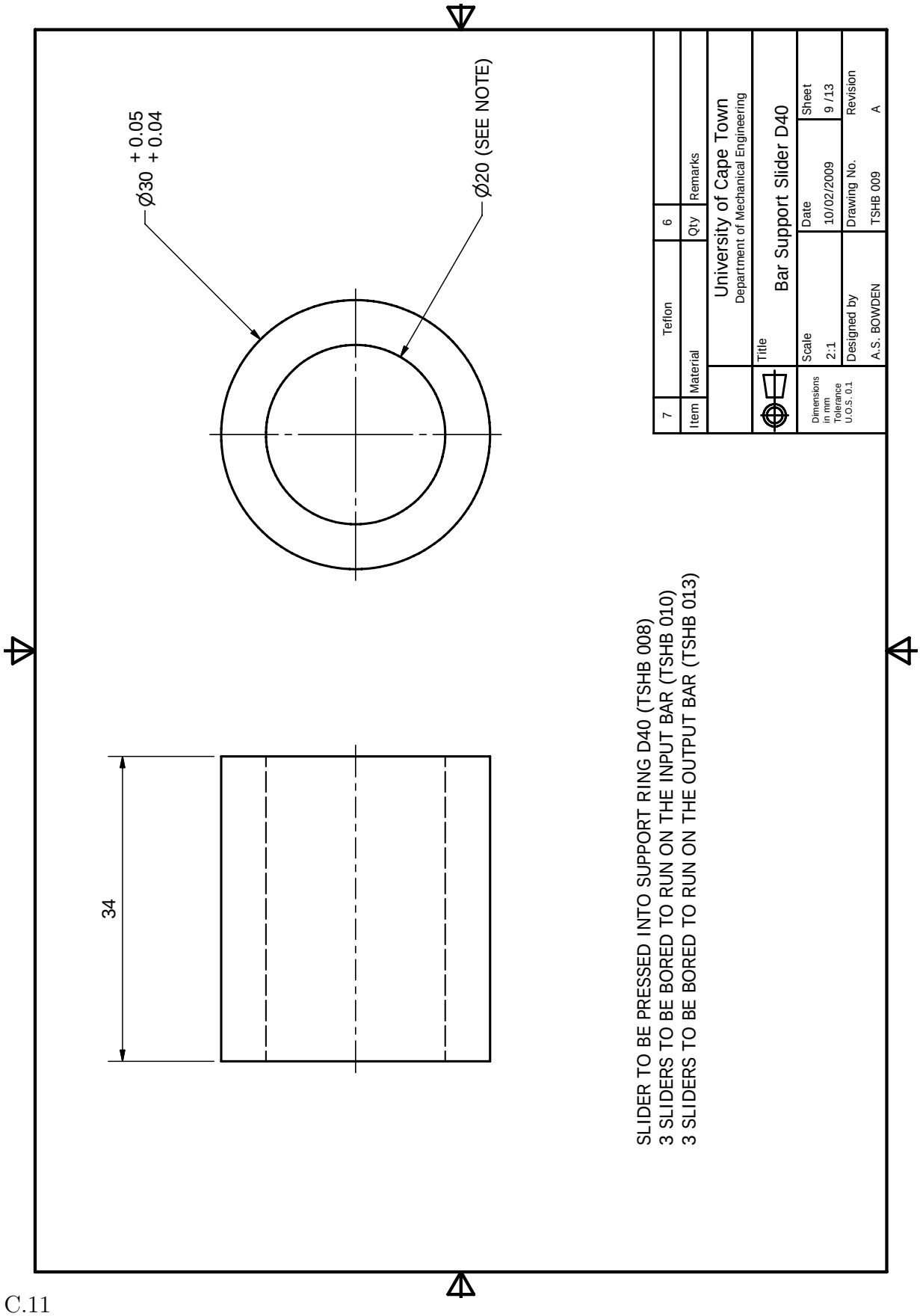
Ø30 + 0.05 + 0.04
Ø20 (SEE NOTE)
34
SLIDER TO BE PRESSED INTO SUPPORT RING D40 (TSHB 008)
3 SLIDERS TO BE BORED TO RUN ON THE INPUT BAR (TSHB 010)
3 SLIDERS TO BE BORED TO RUN ON THE OUTPUT BAR (TSHB 013)
7 Teflon 6
Item Material Qty Remarks
University of Cape Town
Department of Mechanical Engineering
Title
Bar Support Slider D40
Scale 2:1
Date 10/02/2009
Sheet 9 /13
Dimensions in mm
Tolerance U.O.S. 0.1
Designed by A.S. BOWDEN
Drawing No. TSHB 009
Revision A

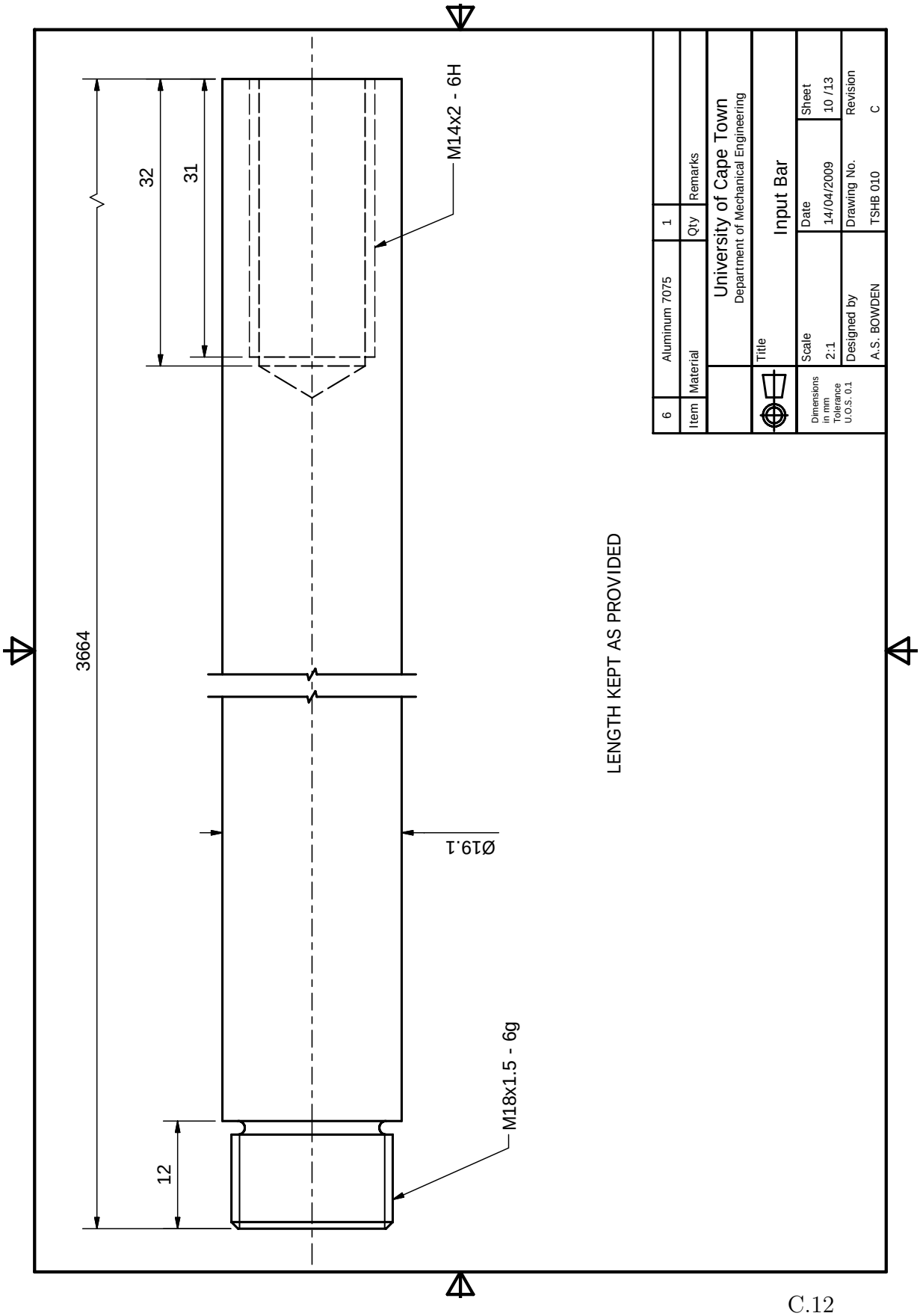
M14x2 - 6H
32
31
3664
Ø19.1
M18x1.5 - 6g
12
LENGTH KEPT AS PROVIDED
6 Item
Aluminum 7075 Material
1 Qty
Remarks
University of Cape Town
Department of Mechanical Engineering
Title
Input Bar
Scale 2:1
Date 14/04/2009
Sheet 10 /13
Designed by A.S. BOWDEN
Drawing No. TSHB 010
Revision C
Dimensions in mm
Tolerance U.O.S. 0.1

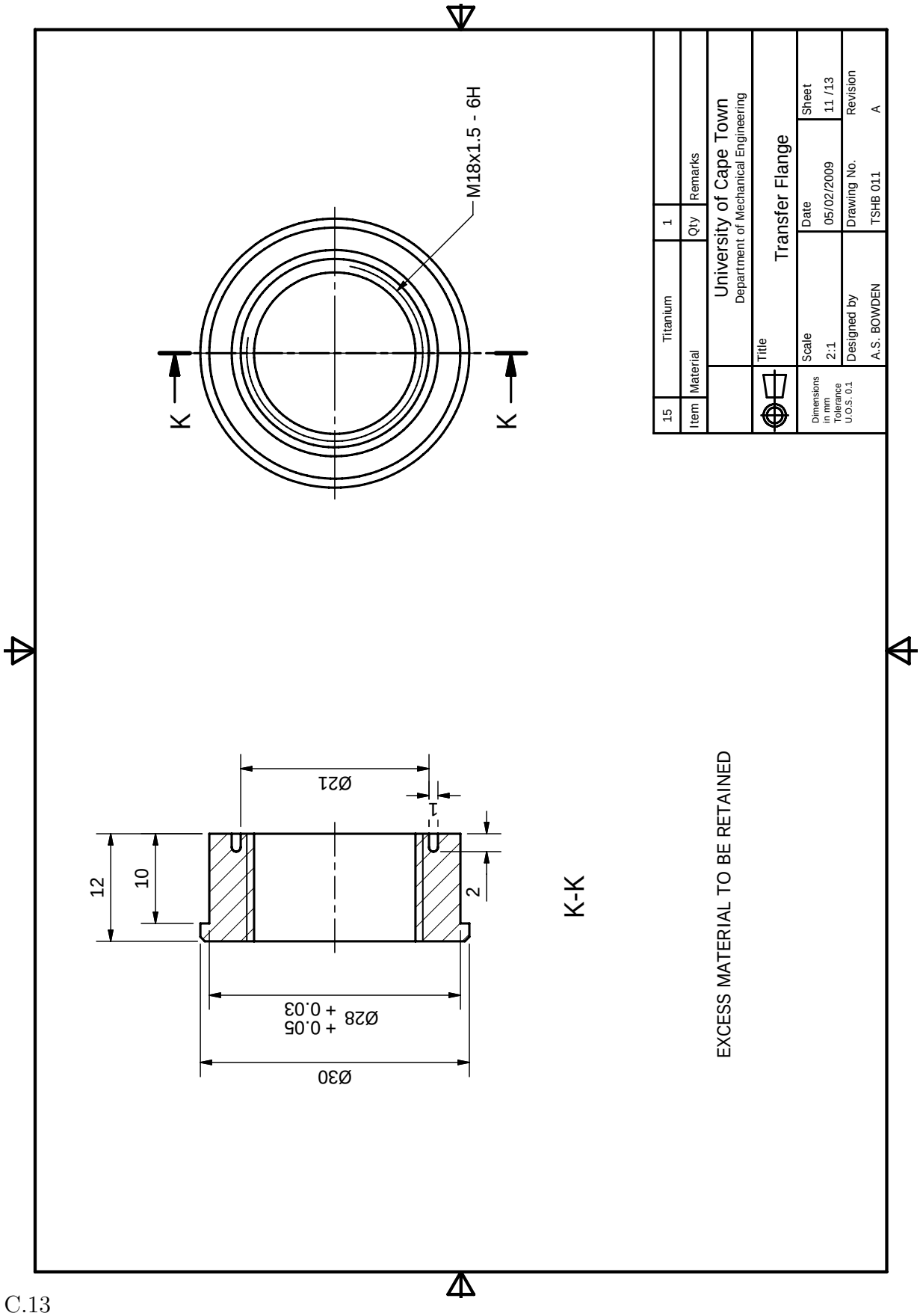
M18x1.5 - 6H
K
K
Ø21
1
12
10
2
Ø28 + 0.05 + 0.03
Ø30
K-K
EXCESS MATERIAL TO BE RETAINED
15
Item
Titanium
Material
1
Qty
Remarks
University of Cape Town
Department of Mechanical Engineering
Title
Transfer Flange
Scale
2:1
Date
05/02/2009
Sheet
11 /13
Designed by
A.S. BOWDEN
Drawing No.
TSHB 011
Revision
A
Dimensions in mm
Tolerance U.O.S. 0.1

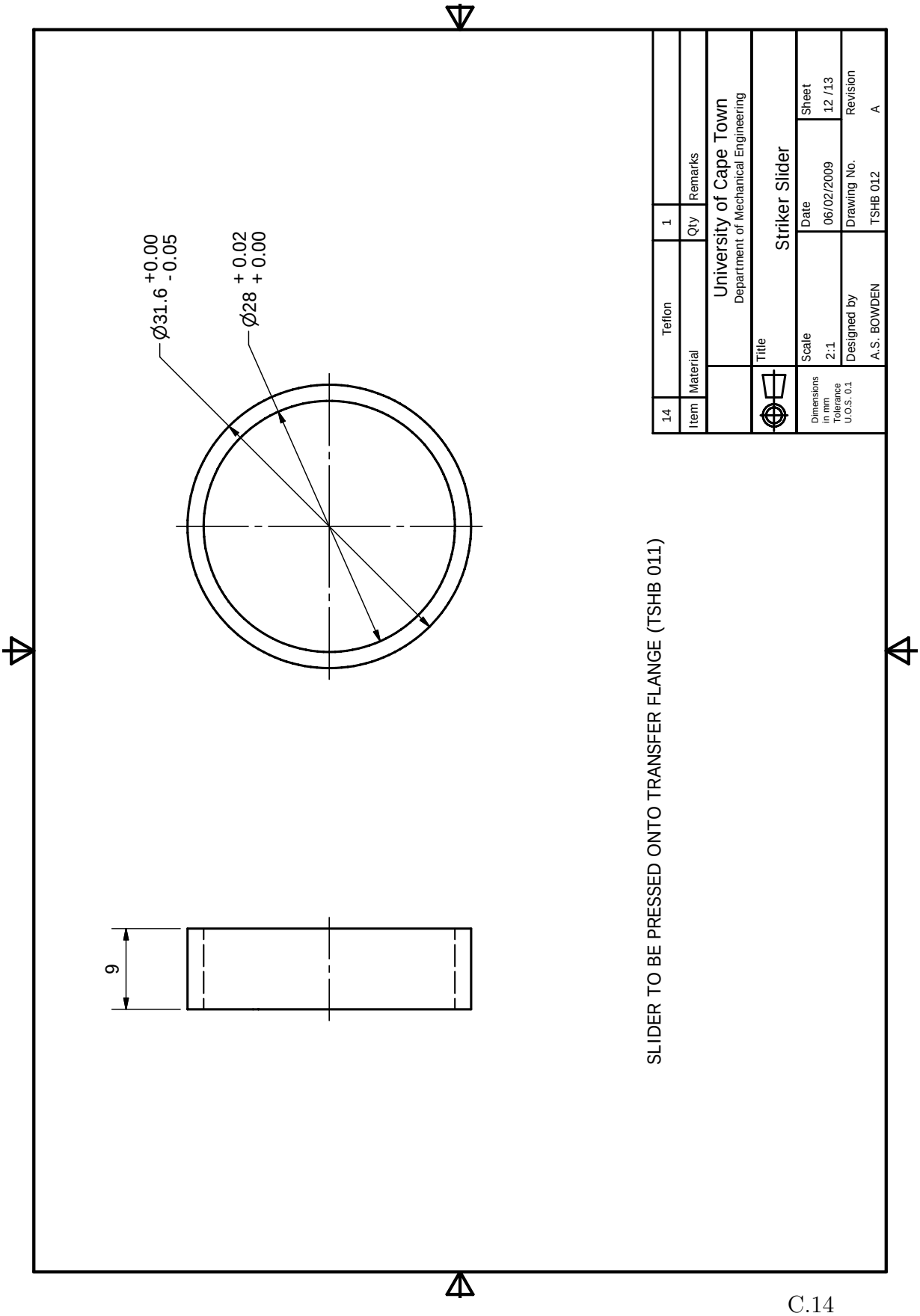
Ø31.6 +0.00 -0.05
Ø28 + 0.02 + 0.00
9
SLIDER TO BE PRESSED ONTO TRANSFER FLANGE (TSHB 011)
14 Teflon 1
Item Material Qty Remarks
University of Cape Town
Department of Mechanical Engineering
Striker Slider
Title
Scale 2:1
Date 06/02/2009
Sheet 12 /13
Designed by A.S. BOWDEN
Drawing No. TSHB 012
Revision A
Dimensions in mm
Tolerance U.O.S. 0.1

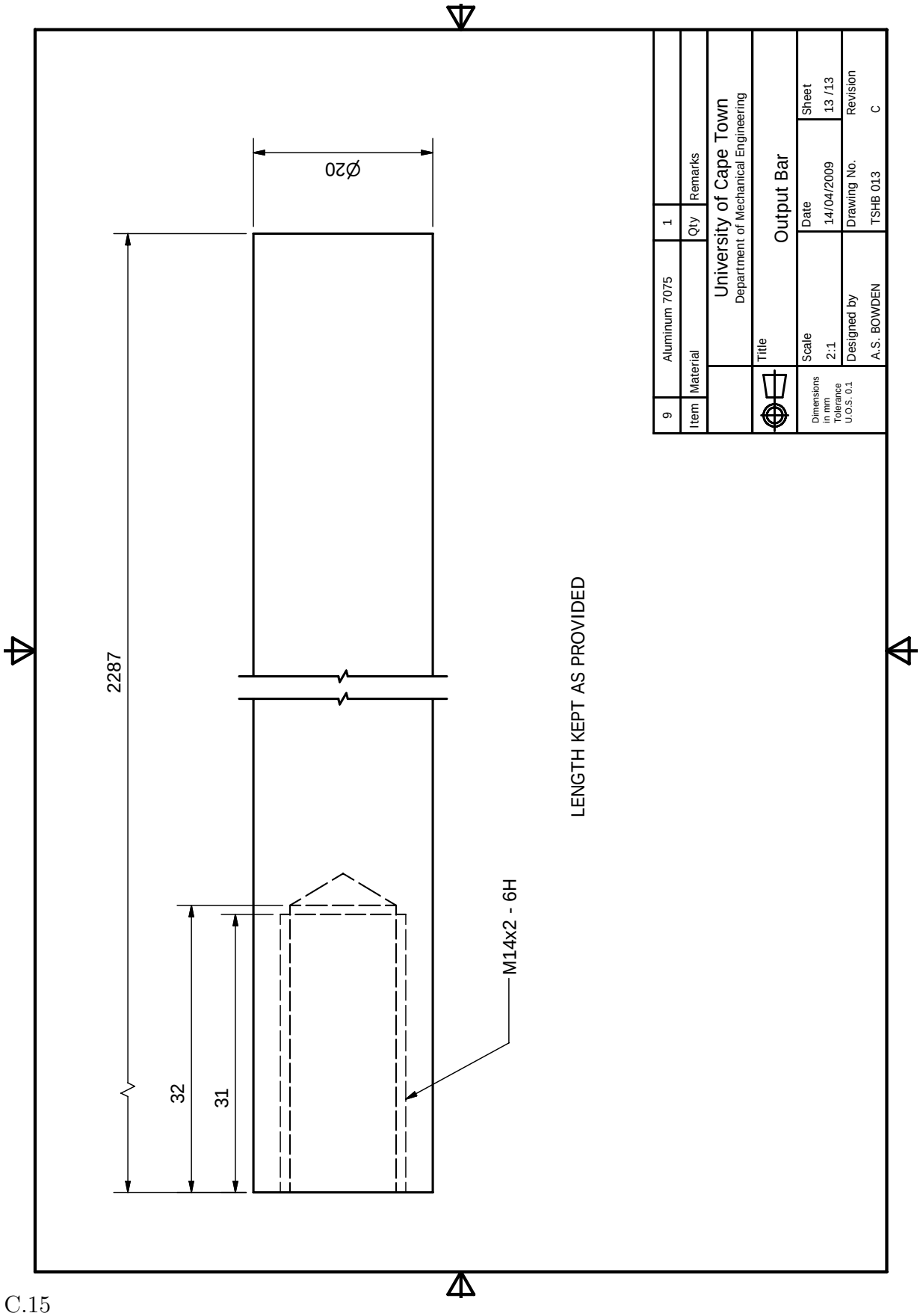
Ø20
2287
32
31
M14x2 - 6H
LENGTH KEPT AS PROVIDED
9
Item
Aluminum 7075
Material
1
Qty
Remarks
University of Cape Town
Department of Mechanical Engineering
Title
Output Bar
Scale
2:1
Date
14/04/2009
Sheet
13 /13
Designed by
A.S. BOWDEN
Drawing No.
TSHB 013
Revision
C
Dimensions in mm
Tolerance U.O.S. 0.1

C.2 Specimens

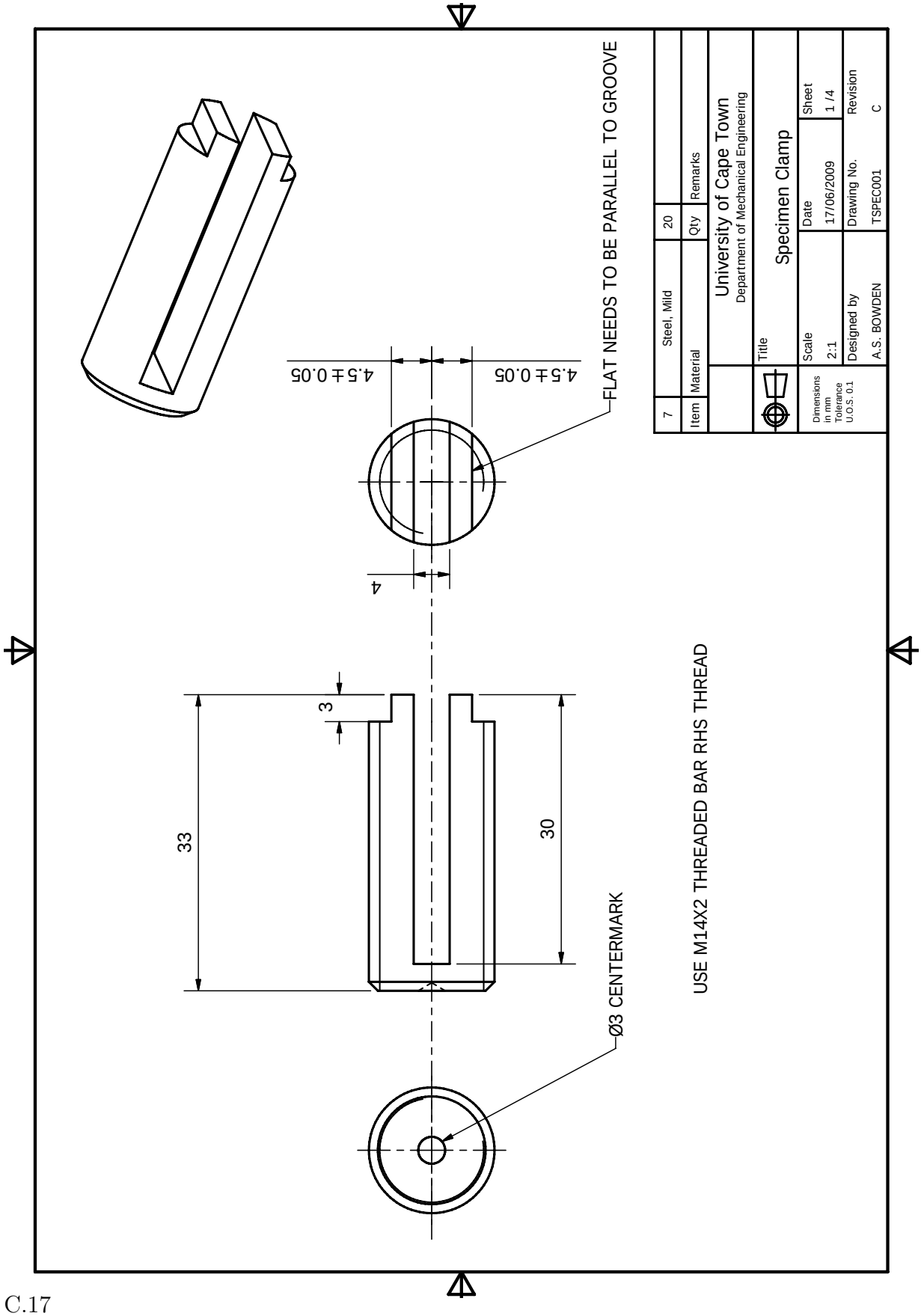
FLAT NEEDS TO BE PARALLEL TO GROOVE
4.5 ± 0.05
4.5 ± 0.05
4
3
33
30
Ø3 CENTERMARK
USE M14X2 THREADED BAR RHS THREAD
7
Steel, Mild
20
Item
Material
Qty
Remarks
University of Cape Town
Department of Mechanical Engineering
Title
Specimen Clamp
Scale
2:1
Date
17/06/2009
Sheet
1 /4
Designed by
A.S. BOWDEN
Drawing No.
TSPEC001
Revision
C
Dimensions in mm
Tolerance U.O.S. 0.1

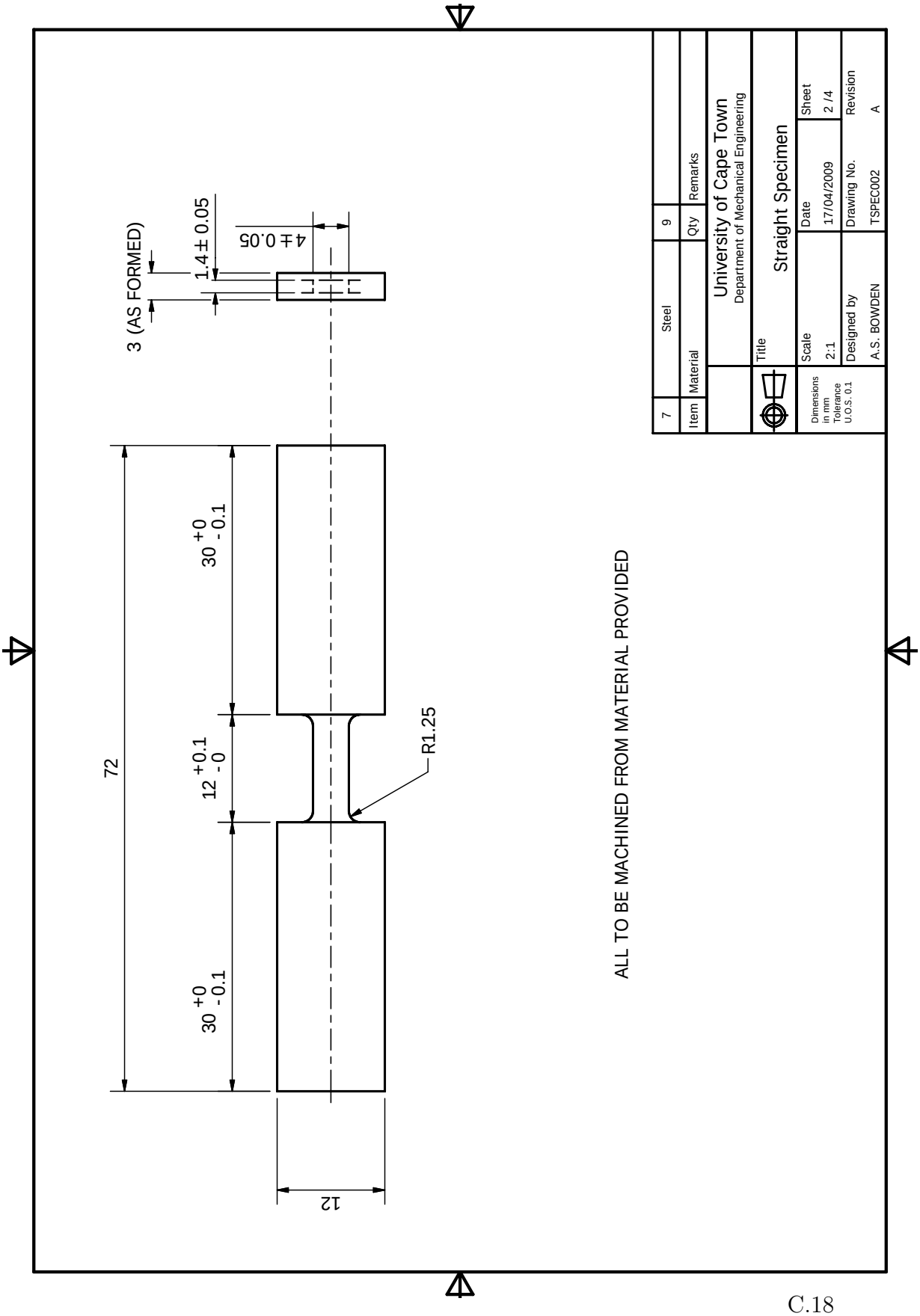
3 (AS FORMED)
1.4 ± 0.05
4 ± 0.05
72
30 +0 -0.1
12 +0.1 -0
30 +0 -0.1
R1.25
12
ALL TO BE MACHINED FROM MATERIAL PROVIDED
7
Item
Material
Steel
9
Qty
Remarks
University of Cape Town
Department of Mechanical Engineering
Title
Straight Specimen
Dimensions in mm
Tolerance U.O.S. 0.1
Scale
2:1
Date
17/04/2009
Sheet
2 /4
Designed by
A.S. BOWDEN
Drawing No.
TSPEC002
Revision
A

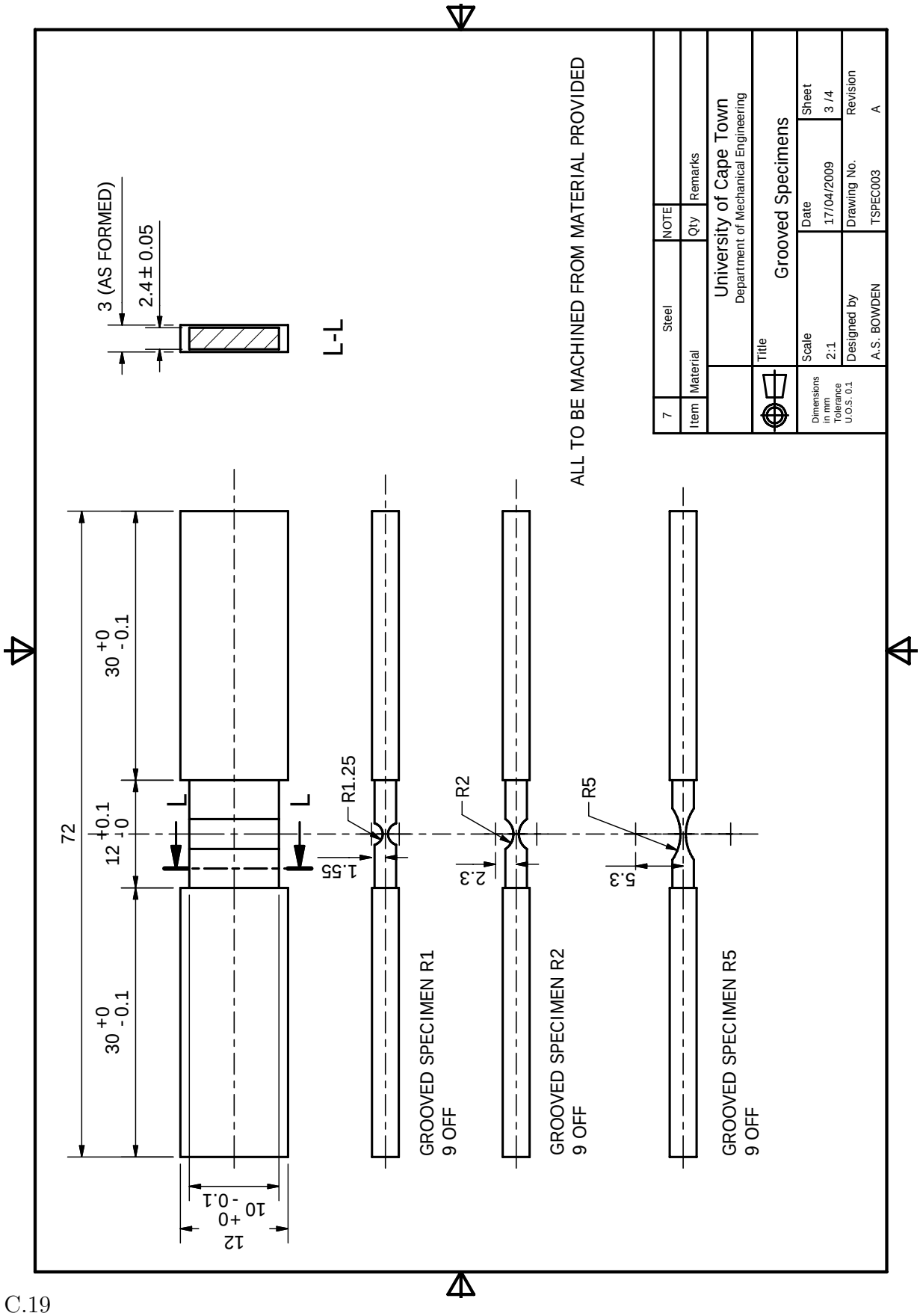
3 (AS FORMED)
2.4± 0.05
L-L
ALL TO BE MACHINED FROM MATERIAL PROVIDED
Item | Material | Steel | Qty | NOTE
7
Remarks
University of Cape Town
Department of Mechanical Engineering
Title
Grooved Specimens
Scale 2:1
Date 17/04/2009
Sheet 3 /4
Designed by A.S. BOWDEN
Drawing No. TSPEC003
Revision A
Dimensions in mm Tolerance U.O.S. 0.1
72
30 +0 -0.1
12 +0.1 -0
30 +0 -0.1
L
L
R1.25
R2
R5
1.55
2.3
5.3
12
10 +0 -0.1
GROOVED SPECIMEN R1
9 OFF
GROOVED SPECIMEN R2
9 OFF
GROOVED SPECIMEN R5
9 OFF

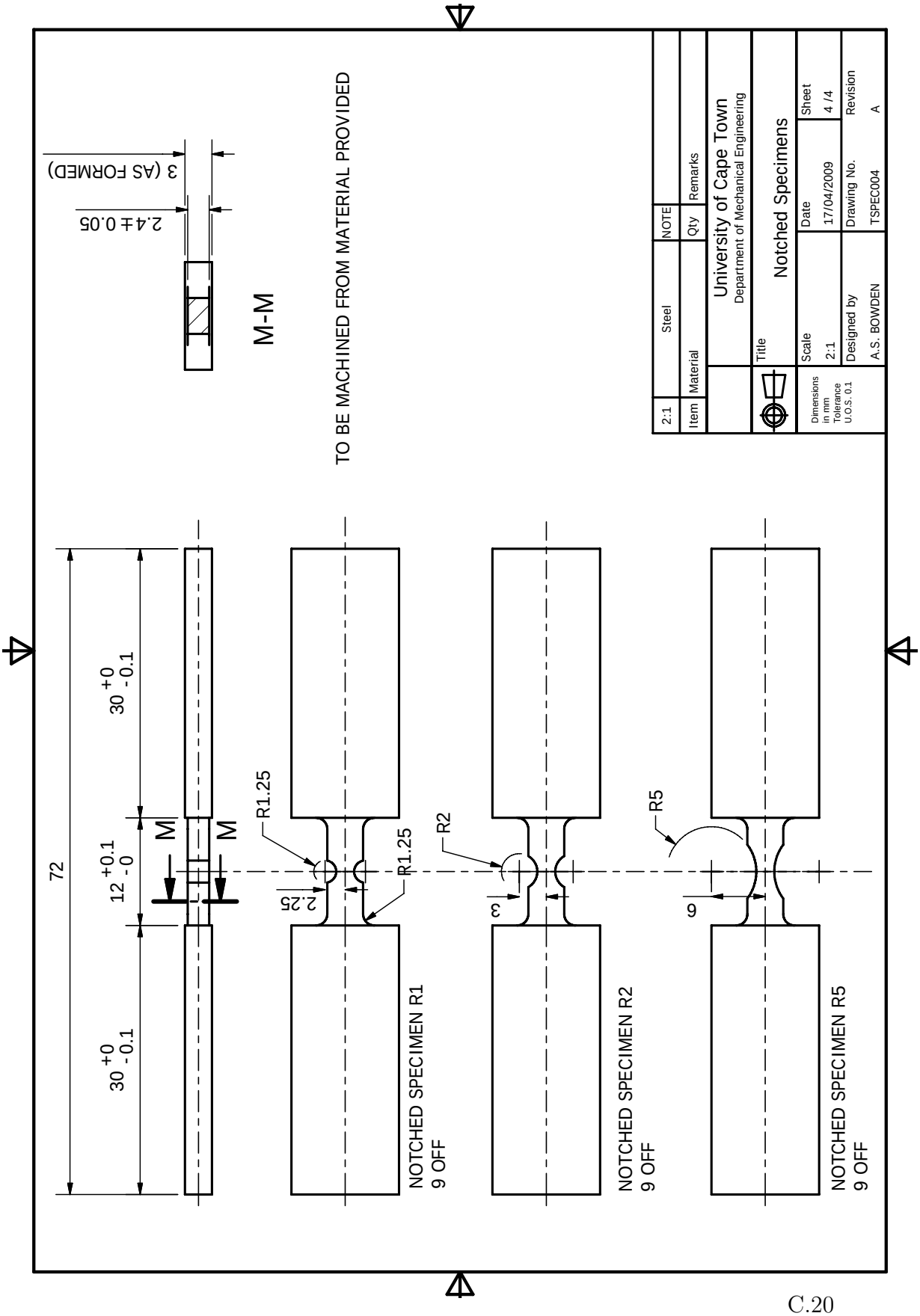
TO BE MACHINED FROM MATERIAL PROVIDED
M-M
2.4 ± 0.05
3 (AS FORMED)
2:1
Item
Material
Steel
NOTE
Qty
Remarks
University of Cape Town
Department of Mechanical Engineering
Title
Notched Specimens
Dimensions in mm
Tolerance U.O.S. 0.1
Scale
2:1
Date
17/04/2009
Sheet
4 /4
Designed by
A.S. BOWDEN
Drawing No.
TSPEC004
Revision
A
72
30 +0 -0.1
12 +0.1 -0
30 +0 -0.1
M
M
R1.25
R1.25
2.25
NOTCHED SPECIMEN R1
9 OFF
R2
3
NOTCHED SPECIMEN R2
9 OFF
R5
6
NOTCHED SPECIMEN R5
9 OFF

C.3 Glue Jig

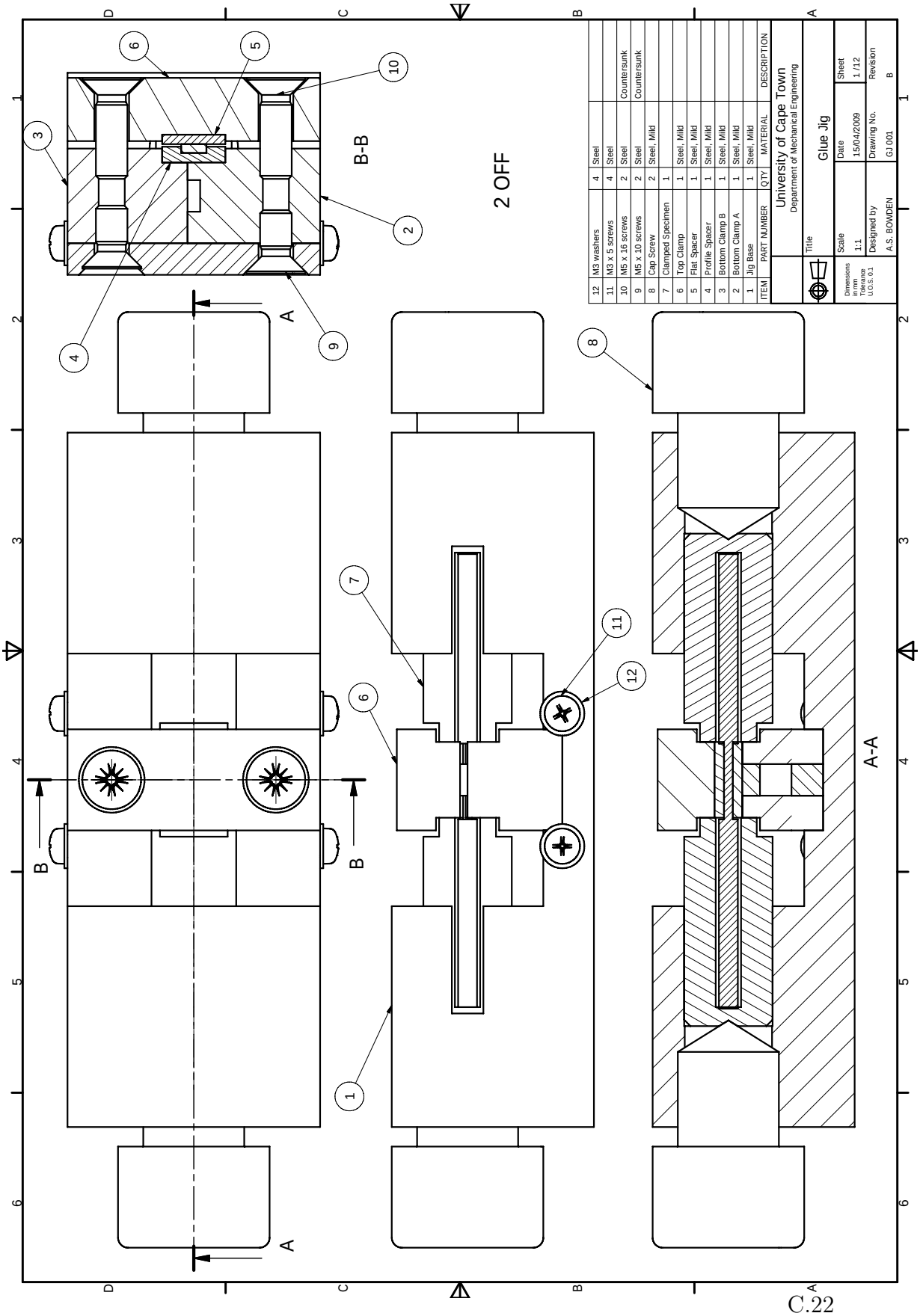
B-B
2 OFF
A-A
A
B
A
B
12 M3 washers 4 Steel
11 M3 x 5 screws 4 Steel
10 M5 x 16 screws 2 Steel Countersunk
9 M5 x 10 screws 2 Steel Countersunk
8 Cap Screw 2 Steel, Mild
7 Clamped Specimen 1
6 Top Clamp 1 Steel, Mild
5 Flat Spacer 1 Steel, Mild
4 Profile Spacer 1 Steel, Mild
3 Bottom Clamp B 1 Steel, Mild
2 Bottom Clamp A 1 Steel, Mild
1 Jig Base 1 Steel, Mild
ITEM PART NUMBER QTY MATERIAL DESCRIPTION
University of Cape Town
Department of Mechanical Engineering
Title
Glue Jig
Scale 1:1
Date 15/04/2009
Sheet 1 / 12
Dimensions in mm Tolerance U.O.S. 0.1
Designed by A.S. BOWDEN
Drawing No. GJ 001
Revision B

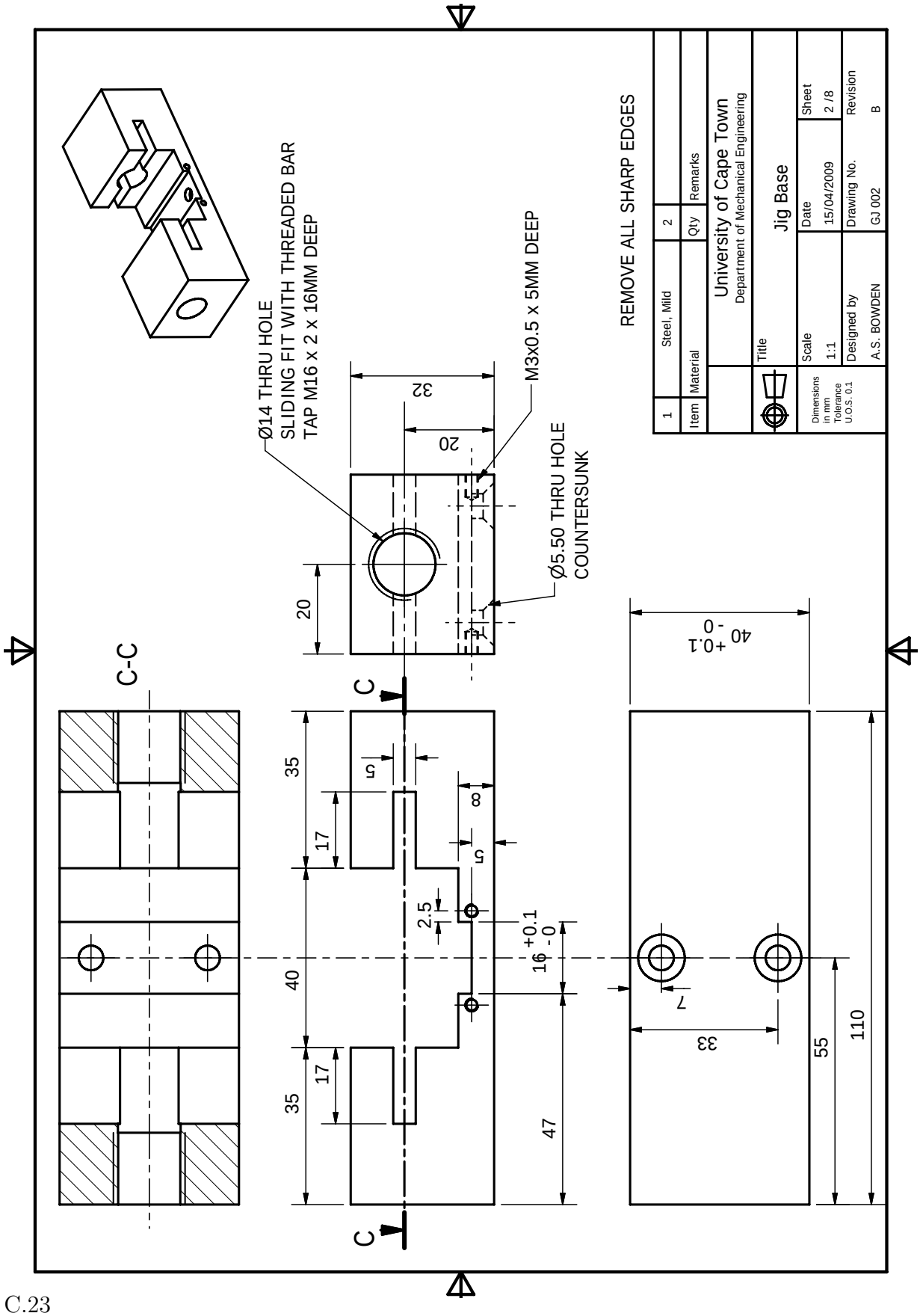
REMOVE ALL SHARP EDGES
Ø14 THRU HOLE
SLIDING FIT WITH THREADED BAR
TAP M16 x 2 x 16MM DEEP
M3x0.5 x 5MM DEEP
Ø5.50 THRU HOLE
COUNTERSUNK
C-C
C
C
32
20
20
35
17
5
8
5
2.5
40
35
17
16 +0.1 -0
47
40 +0.1 -0
7
33
55
110
1 Steel, Mild 2
Item Material Qty Remarks
University of Cape Town
Department of Mechanical Engineering
Title
Jig Base
Scale 1:1
Date 15/04/2009
Sheet 2 /8
Designed by A.S. BOWDEN
Drawing No. GJ 002
Revision B
Dimensions in mm
Tolerance U.O.S. 0.1

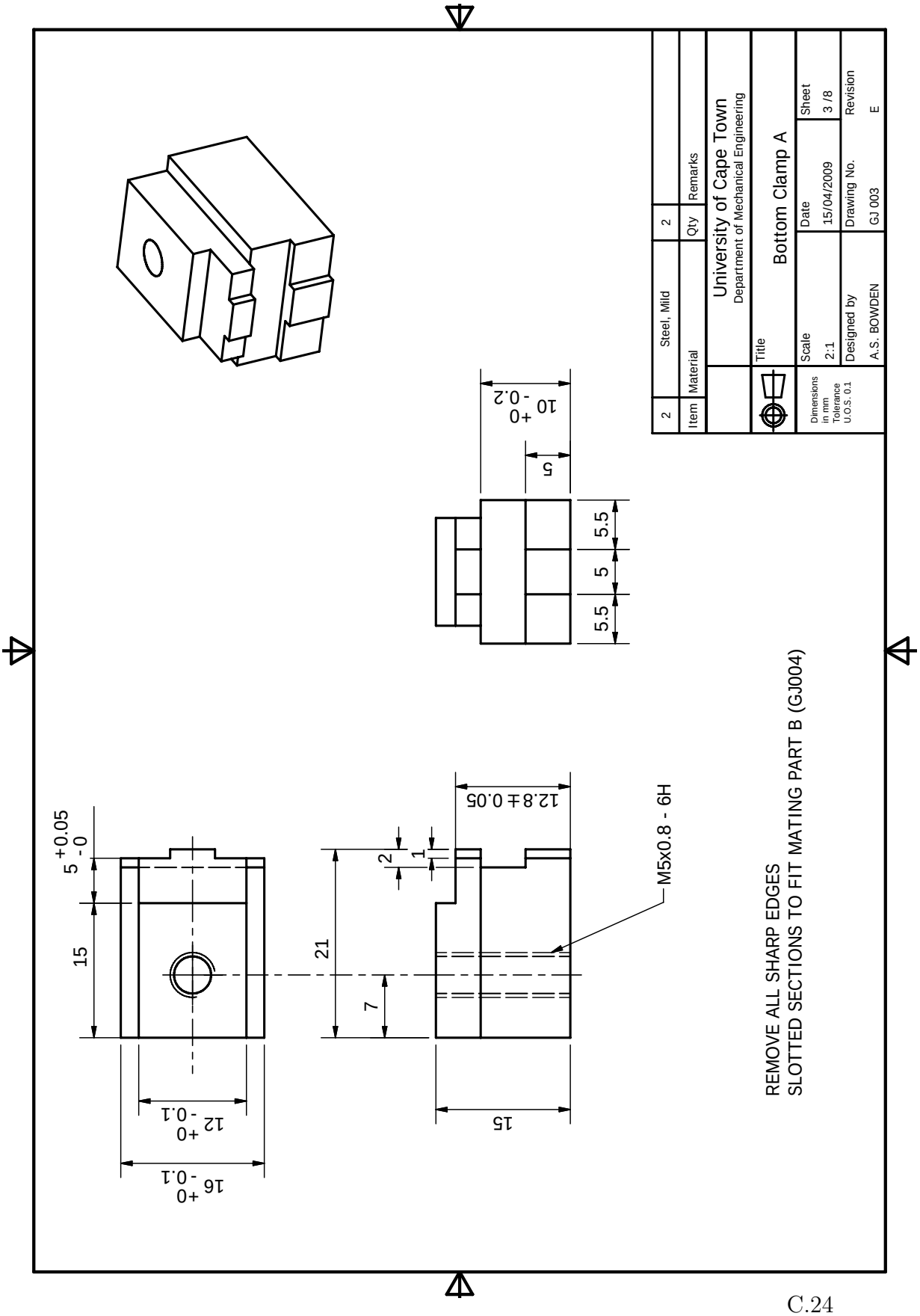
University of Cape Town
Department of Mechanical Engineering
Bottom Clamp A
Steel, Mild
Item
Material
Qty
Remarks
Scale 2:1
Date 15/04/2009
Sheet 3 /8
Designed by A.S. BOWDEN
Drawing No. GJ 003
Revision E
Dimensions in mm
Tolerance U.O.S. 0.1
REMOVE ALL SHARP EDGES
SLOTTED SECTIONS TO FIT MATING PART B (GJ004)
M5x0.8 - 6H
12.8±0.05
10 +0 -0.2
5
5.5
5
5.5
5 +0.05 -0
15
21
2
1
7
16 +0 -0.1
12 +0 -0.1
15

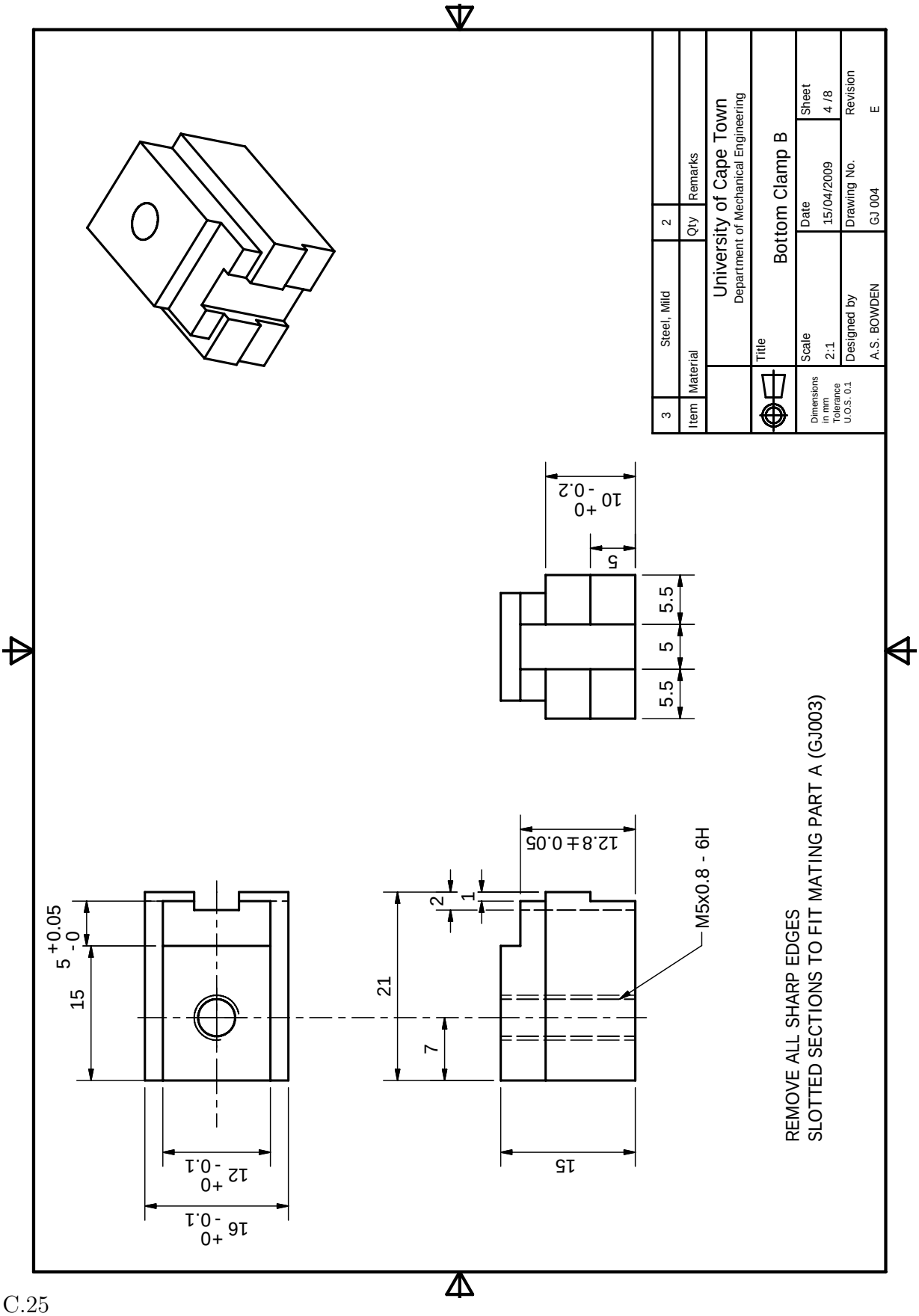
3 | Steel, Mild | 2
Item | Material | Qty | Remarks
University of Cape Town
Department of Mechanical Engineering
Title
Bottom Clamp B
Scale 2:1
Date 15/04/2009
Sheet 4 /8
Designed by A.S. BOWDEN
Drawing No. GJ 004
Revision E
Dimensions in mm
Tolerance U.O.S. 0.1
REMOVE ALL SHARP EDGES
SLOTTED SECTIONS TO FIT MATING PART A (GJ003)
M5x0.8 - 6H
12.8 ± 0.05
10 +0 -0.2
5
5.5
5
5.5
2
1
21
7
15
5 +0.05 -0
15
16 +0 -0.1
12 +0 -0.1

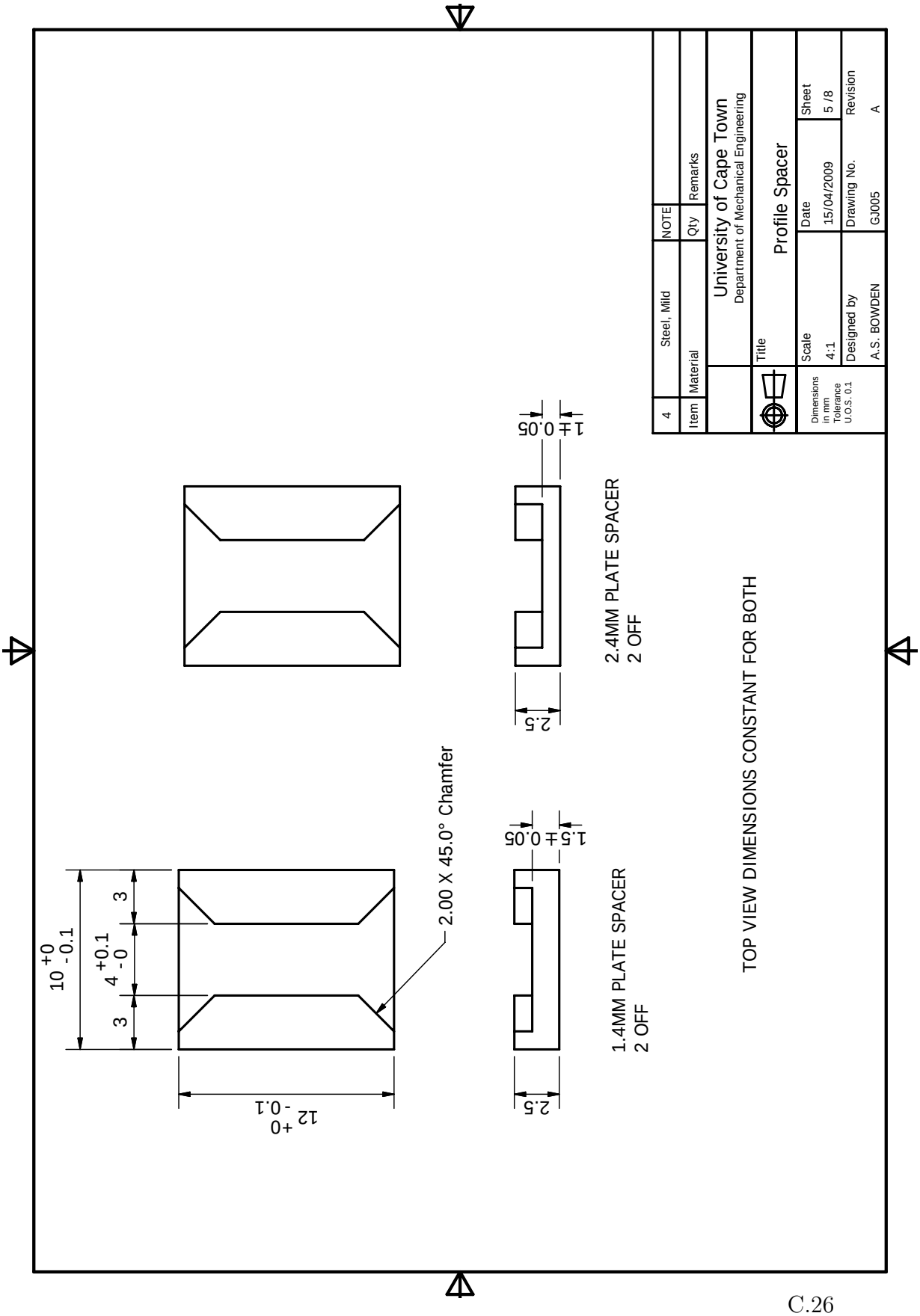
4
Item
Material
Steel, Mild
NOTE
Qty
Remarks
University of Cape Town
Department of Mechanical Engineering
Title
Profile Spacer
Scale
4:1
Date
15/04/2009
Sheet
5 /8
Designed by
A.S. BOWDEN
Drawing No.
GJ005
Revision
A
Dimensions in mm
Tolerance
U.O.S. 0.1
TOP VIEW DIMENSIONS CONSTANT FOR BOTH
2.4MM PLATE SPACER
2 OFF
1.4MM PLATE SPACER
2 OFF
2.00 X 45.0° Chamfer
1 ± 0.05
1.5 ± 0.05
2.5
2.5
12 +0 -0.1
10 +0 -0.1
4 +0.1 -0
3
3

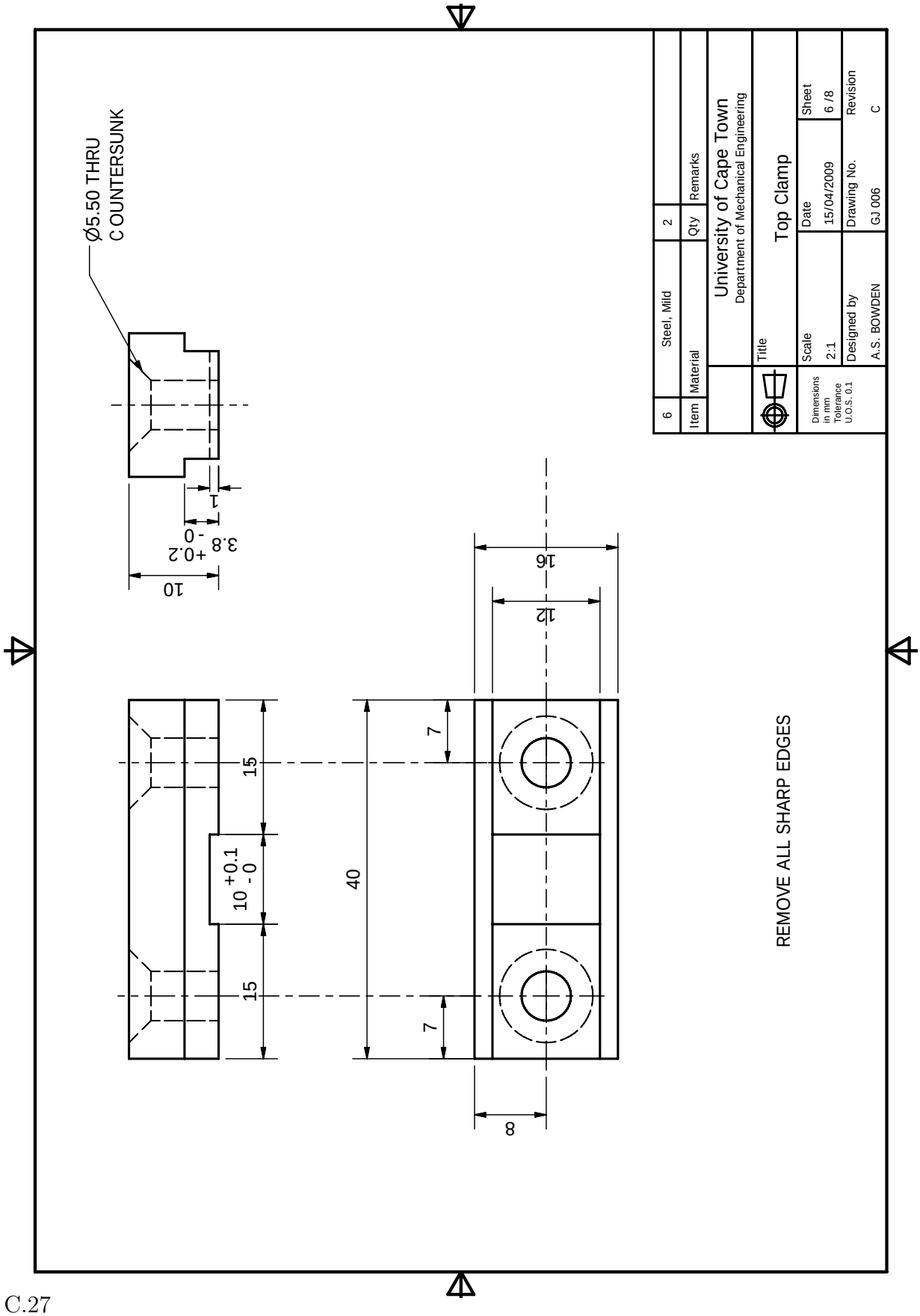
Ø5.50 THRU
C OUNTERSUNK
1
3.8 +0.2 -0
10
16
12
7
40
7
15
10 +0.1 -0
15
8
REMOVE ALL SHARP EDGES
6
Item
Material
Steel, Mild
2
Qty
Remarks
University of Cape Town
Department of Mechanical Engineering
Title
Top Clamp
Dimensions in mm
Tolerance U.O.S. 0.1
Scale
2:1
Date
15/04/2009
Sheet
6 /8
Designed by
A.S. BOWDEN
Drawing No.
GJ 006
Revision
C

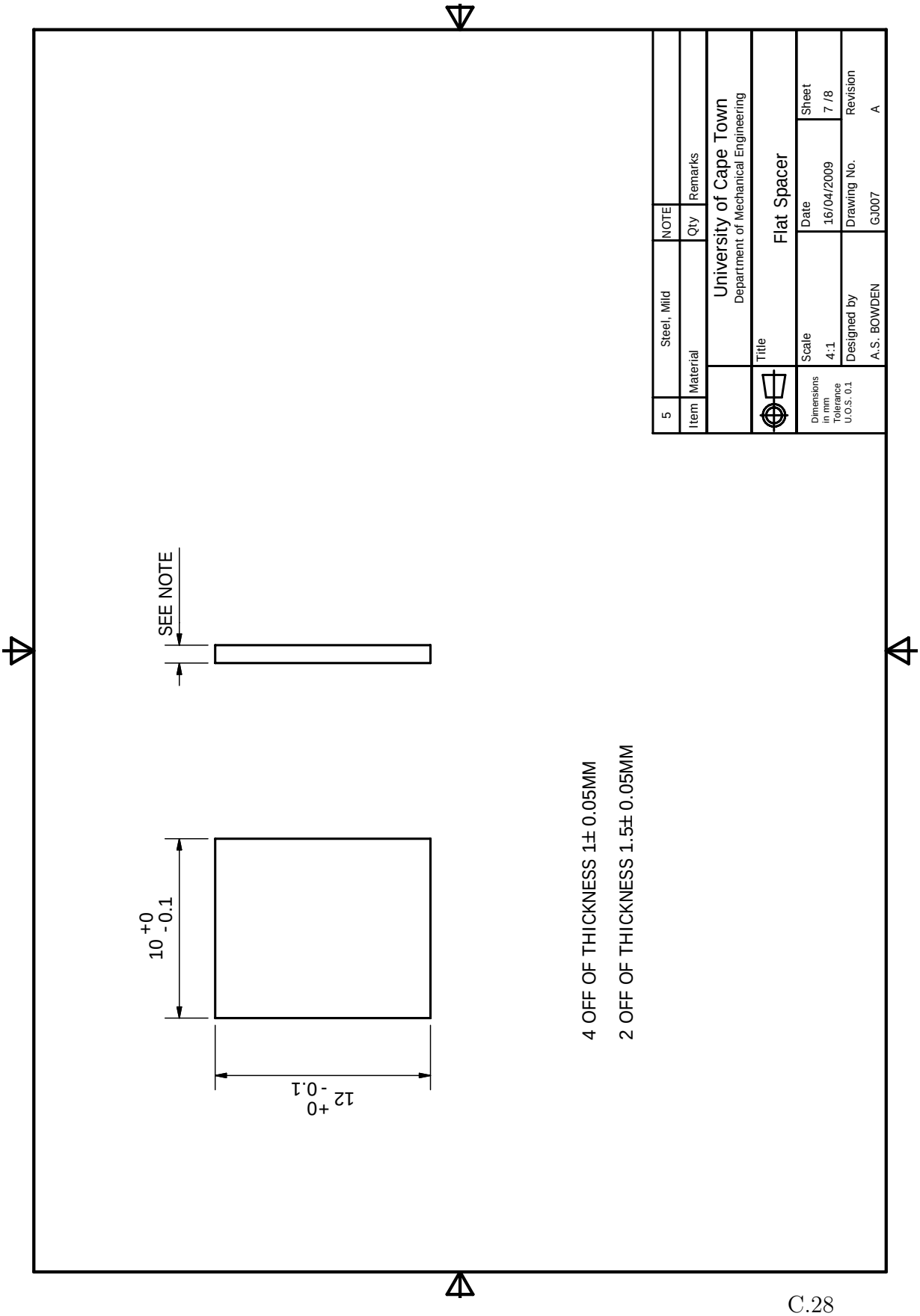
5
Item
Material
Steel, Mild
NOTE
Qty
Remarks
University of Cape Town
Department of Mechanical Engineering
Title
Flat Spacer
Scale
4:1
Date
16/04/2009
Sheet
7 /8
Designed by
A.S. BOWDEN
Drawing No.
GJ007
Revision
A
Dimensions in mm
Tolerance U.O.S. 0.1
SEE NOTE
10 +0 -0.1
12 +0 -0.1
4 OFF OF THICKNESS 1± 0.05MM
2 OFF OF THICKNESS 1.5± 0.05MM

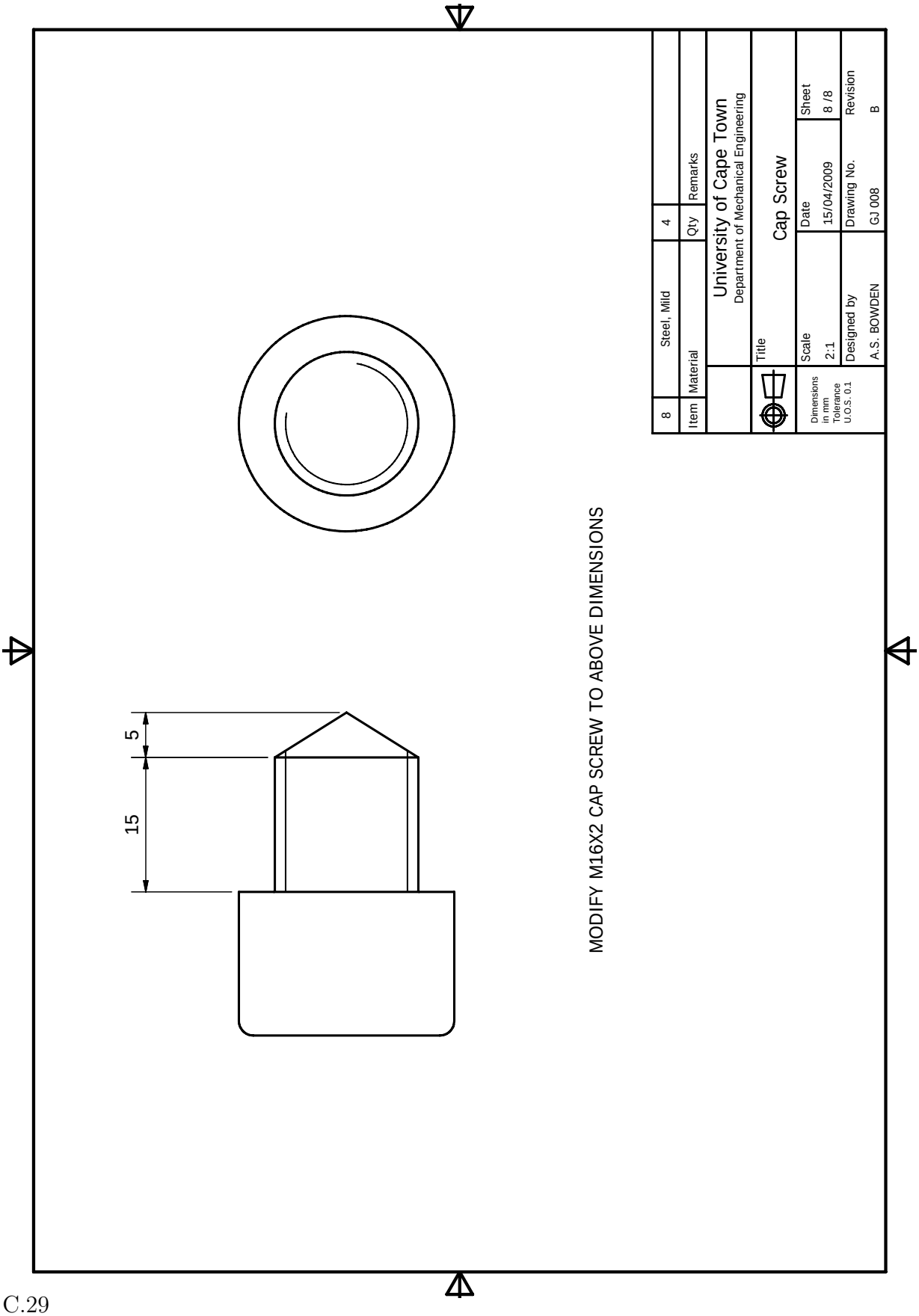
MODIFY M16X2 CAP SCREW TO ABOVE DIMENSIONS
5
15
8
Steel, Mild
4
Item
Material
Qty
Remarks
University of Cape Town
Department of Mechanical Engineering
Title
Cap Screw
Scale
2:1
Date
15/04/2009
Sheet
8 /8
Dimensions in mm
Tolerance U.O.S. 0.1
Designed by
A.S. BOWDEN
Drawing No.
GJ 008
Revision
B